2014

Action potentials as indicators of metabolic perturbations for temporal proteomic analysis

Aditya Reddy Kolli
University of Central Florida

ACTION POTENTIALS AS INDICATORS OF METABOLIC PERTURBATIONS FOR TEMPORAL PROTEOMIC ANALYSIS

by

ADITYA REDDY KOLLI
B.Pharmacy, Osmania University, Hyderabad, India, 2006

A dissertation submitted in partial fulfillment of the requirements
for the degree of Doctor of Philosophy
in the Department of Chemistry
in the College of Sciences
at the University of Central Florida
Orlando, Florida

Fall Term
2014

Major Professor: James J. Hickman

ABSTRACT

The single largest cause of compound attrition during drug development is due to inadequate tools capable of predicting and identifying protein interactions. Several tools have been developed to explore how a compound interferes with specific pathways. However, these tools lack the potential to chronically monitor the time dependent temporal changes in complex biochemical networks, thus limiting our ability to identify possible secondary signaling pathways that could lead to potential toxicity. To overcome this, we have developed an *in silico* neuronal-metabolic model by coupling the membrane electrical activity to intracellular biochemical pathways that would enable us to perform non-invasive temporal proteomics. This model is capable of predicting and correlating the changes in cellular signaling, metabolic networks and action potential responses to metabolic perturbation.

The neuronal-metabolic model was experimentally validated by performing biochemical and electrophysiological measurements on NG108-15 cells followed by testing its prediction capabilities for pathway analysis. The model accurately predicted the changes in neuronal action potentials and the changes in intracellular biochemical pathways when exposed to metabolic perturbations. NG108-15 cells showed a large effect upon exposure to 2DG compared to cyanide and malonate as these cells have elevated glycolysis. A combinational treatment of 2DG, cyanide and malonate had a much higher and faster effect on the cells. A time-dependent change in neuronal action potentials occurred based on the inhibited pathway. We conclude that the experimentally validated *in silico* model accurately predicts the changes in neuronal action potential shapes and proteins activities to perturbations, and would be a

powerful tool for performing proteomics facilitating drug discovery by using action potential peak shape analysis to determine pathway perturbation from an administered compound.

Dedicated to my parents

ACKNOWLEDGMENTS

First and foremost, I would like to thank Dr. James Hickman for giving me the opportunity to work in his laboratory. This dissertation would not have been possible without his continuous support, encouragement and confidence in my abilities. During my long research stint at UCF, which is a given in the field of interdisciplinary research, Dr. Hickman has provided me with the necessary time and freedom to pursue my research goals. His mentorship helped me steer my research while laying a strong foundation in fundamental methodologies to analyze and solve scientific problems. On a personal note, he was always there during the ups and downs of my graduate career. I could always walk up to him to get his advice, feedback or support. I consider myself fortunate to have him as my advisor.

I am deeply grateful to Dr. Peter Molar for his informative discussions and continuous guidance. He taught me the basic aseptic technique, cellular electrophysiology and helped me develop the neuronal module over time. Dr. Molnar had helped me understand the biophysical concepts for modeling the biophysical phenomena.

A special thanks to Dr. Vaibhav Thakore for his unconditional support and help in teaching me the essentials modeling. He had always been approachable for consultations and helped me understand the importance of building test cases and modular approaches for model development. Dr. Thakore helped me equip myself with the modeling tools that lead to an exponential increase in my learning abilities and modeling progress. Moreover, I thank him for motivating and giving me that extra-push which I needed to finish the project.

I thank Dr. Jerry Jenkins for helping me in developing the metabolic module by providing his key insights into the metabolic model. He had constantly analyzed my progresses, provided his valuable insight and mentored me during the development and optimization phases of the metabolic module. It was a great learning experience working with him.

I thank Dr. Frank Sommerhage and Dr. Nesar Akanda for providing the intrinsic details for patch clamp electrophysiology. I would also like to thank Maria Stancescu for preparing surface modified coverslips. I had enjoyed working with her on the characterization of the microfluidic system followed by testing drug effects.

I also thank Dr. Balaji Srinivasan for giving me an opportunity to write a review paper. His helpful inputs and direction not only helped me developing my scientific writing skills but also played a key role in helping me finish writing the dissertation in a short span of time. I also thank the past and present members of the hybrid systems laboratory for their support.

I acknowledge my committee members, Dr.Christian Clausen, Dr. Jack Ballantyne, Dr. Andre Gesquiere and Dr. Sumit Kumar Jha for their suggestions and encouragement.

Lastly and most importantly, I am grateful to have such a wonderful family and friends. Staying away from home was hard and I remember those long late night conversations with my family and friends that made me feel at home. They have always supported me at every stage of life and consider myself truly fortunate.

Sincerely,

Aditya Reddy Kolli

TABLE OF CONTENTS

LIST OF FIGURES

LIST OF TABLES

CHAPTER-1: INTRODUCTION

1.1. Proteomics

A good understanding of the factors affecting disease progression is essential for commencing treatments and making therapeutic monitoring decisions. The study of disease progression in humans has been accomplished through several approaches as listed in Figure 1 and includes genomics, transcriptomics and proteomics.

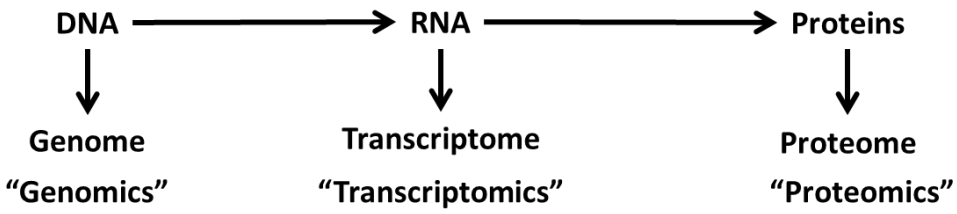

Figure 1: Biochemical contexts of different studies for disease progression

Deoxyribonucleic acid (DNA) contains all the necessary information required to build and maintain the cell. Great progress has been made to understand the structure of a DNA in identifying the genetic abnormalities caused in a specific disease condition [1]. Genes are expressed in varying combinations and nearly 21,000 genes have been identified and sequenced [2]. The complete set of DNA in a single cell of an organism is referred to as genome. Genomics is the study of structure and function of genomes. DNA transcribes into ribonucleic acid (RNA), followed by translation into a protein.

All genome sequences are now available and researchers are trying to determine the molecular and functional properties of each gene to understand the role of gene products in complex biological processes. The transcriptome is the set of all RNA molecules that include

messenger RNA (mRNA), ribosomal RNA (rRNA), transfer RNA (tRNA), and other non-coding RNA produced in the cells. The analysis of mRNA has become popular in recent years [3]. Several methods such as serial analysis of gene expression and DNA microarray technology are applied. However, the quantification of mRNA does not reflect the cellular proteins. Several factors including pH, hypoxia and drug administration define the expression and activity of proteins. The proteins interact and work in conjunction to maintain a functional biological system. Cells respond to stimuli by regulating the level and activity of cellular proteins the cell responds to any stimuli. Cellular processes are mediated through a large network of protein-protein interactions that are spatially and temporally regulated in the cell. A poor correlation has been shown between mRNA and protein expression levels [4].

Proteomics is the study of the expression, function and interactions of proteins in the proteome on a large scale [5]. The term proteomics was coined by Marc Wilkins during the 1990's, redefining the thought process of a biological working system. Proteomics offers a comprehensive analysis of a specific proteome, including abundances, variations and modifications in order to understand cellular processes. The phenotype of the cell is determined by the proteins that carryout cellular activities [6]. Each protein such as the membrane receptor, ion channel, transcription factor, kinases or chaperones has a specific function. Malfunction of the definitive proteins is the major cause of disease and serves as an indicator for the disease. Proteins are also the primary targets for several drugs [6]. Therefore, a logical step is to study the structure and functional properties of the working parts of the biological systems at different levels. Such a study would provide a comprehensive global comparison between different cell types, tissues, organs and the entire organism. More

importantly the study of proteomics enables us to grain a deeper insight into the mechanism of disease progression which could eventually help in developing a therapy.

Proteome is the expressed protein complement of a genome and represents the subset of all the gene products. A proteome is more complex than a genome, since any protein that is a product of a single gene can exist in multiple forms in the same cell or different types of cells due to post translational modifications. A proteome may vary with time and cellular requirements. For example, exposure of a cell to elevated temperatures causes an increase in expression of heat shock proteins. These changes affect the structure and function of the proteins. The survival of the cells is dictated by the gene expression and activity of their corresponding proteins. The proteome of the cell can comprise all the different forms of proteins and is complicated to study. Protein metabolism, the production and degradation of proteins is responsible for regulating the rate of cellular processes. Proteins after synthesis undergo major biochemical changes due to post translational modifications. Proteins are also involved in the energy metabolism networks in a cell. The life time and expression of proteins also varies, as some proteins may rapidly degrade, are only expressed in certain situations or a few may even last for a life time [7]. Proteins are synthesized and released into the cytosol or other compartments from the ribosomal machinery. There are two major mechanisms by which cells degrade proteins, namely, the lysosome and the proteasome. The degradation of cytosolic and nuclear proteins occurs within the proteasomes. In lysosome degradation, the entire protein enters the lysosome, followed by protein disassembly and degradation. The proteasome mechanism, unlike the lysosome system, is equipped to achieve metabolic balance. The rate of protein synthesis is determined by factors such as the amount of messenger RNA

(mRNA) and the rate of degradation by ubiquitination. Both lysosome and proteasome mechanisms are irreversible and do not respond to the rate of mass action kinetics of their products [7]. Posttranslational modification (PTM) is a step in protein biosynthesis where polypeptide chains undergo folding, cutting and other processes before becoming an active mature protein. Protein phosphorylation is a PTM of proteins in which a serine, a threonine or a tyrosine residue is phosphorylated by a protein kinase by the addition of a covalently bound phosphate group. Protein phosphorylation regulates protein functions by turning the control on/off during cell cycle, cellular signaling cascades and other cellular processes [1]. Proteins undergo wear and tear upon exposure to free-radicals and other biological agents leading to protein damage. External factors including environmental agents such as radiation, chemicals and drugs can lead to protein modification followed by inactivation. It is critical to maintain a balance between protein synthesis and degradation. The steady state of the cell reflects the ratio of the equilibrium constant between these two processes. Wheatley et al. has shown that 30 - 90% of all proteins are defective and improperly folded even after transferring to the endoplasmic reticulum [8]. When a change in the protein concentration occurs, either due to altered physiological process or an onset of a disease condition, a new steady state concentration is achieved by the cell [7].

The human genome project led to the classification of proteins encoded by the human genome and enabled the classification of genes based on their functions [2]. Table 1 lists the classification of proteins into functional categories based on human genome. The expression of different genes is required for the synthesis of different proteins in different functional categories. Proteins associated with intermediary and nucleic acid metabolism account for

about 15% of proteins in the proteome.

Table 1: Classification of proteins into functional categories based on human genome

Functional category	**% Genes**	**Functional category**	**% Genes**
Cell adhesion	1.9	Ion channel	1.3
Hydrolase	4.0	Motor	1.2
Carrier protein	0.7	Structural	1.0
Transcription factor	6.0	Protooncogene	2.9
Nucleic acid enzyme	7.5	Calcium binding	0.1
Signaling molecule	1.2	transporters	1.7
Receptor	5.0	Immunoglobulin	0.9
Kinase	2.8	Extracellular matrix	1.4
Regulatory molecule	3.2	Cytoskeletal	2.8
Transferase	2.0	Chaperone	0.5
Synthase	1.0	Lyase	0.4
Oxidoreductase	2.1	Ligase	0.2
Isomerase	0.5	Intracellular transporter	1.1
Miscellaneous	4.3	Unknown	41.7

The proteins involved in protein synthesis and turnover are about 15-20%. The signaling and DNA binding proteins constitute 20-25% of the proteins. Around 41.7% of the function of the genome is still unknown and determining their functionality is a challenge. It is important to identify and quantify huge variations in the protein profiles that are observed in different cell types.

Proteomics focuses on the interactions between multiple proteins as a part of a large-scale analysis and should be performed at a much higher level [1].The information from the functional characterization of a proteome will help us gain new insights into biology and medicine. Recent advances in the development of proteomic tools have allowed the evaluation of systemic changes in protein expression in responses to perturbations to a biological system [5]. In addition, proteomic biomarkers deliver a more reliable result when compared to traditional biomarkers since multiple interacting protein species are evaluated simultaneously in response to metabolic perturbation [5]. Proteomics is applied to characterize the behavior of the entire system rather than a single protein. Proteomics is a potential tool for drug discovery with an inception to identify novel biomarkers.

1.2. Applications of proteomics

Proteomics technology is advancing rapidly and could revolutionize our fundamental understanding of how a cell 'works' by identifying the responses to both internal and external stimuli. The major applications of proteomics are performing mining, profiling including steady state determination, mapping interaction and identifying protein modifications/functions [1]. These applications enable scientists to perform pathway analysis which involves examining

thousands of proteins simultaneously involved in several pathways.

Protein mining is the identification of all the proteins present in the sample followed by cataloging to determine how levels have changed in an experiment. Protein mining is performed to resolve numerous proteins and uses tools such as mass spectrometry (MS) in combination with software to determine the identity of the protein. Several approaches, each offering a set of advantages, have been adapted for protein mining and build a database. By combining the database and software tools, the protein of interest could be studied which otherwise could only be achieved by performing gene-expression analysis [1].

The largest application of proteomics is in profiling protein expression. Protein profiling facilitates the identification of the state of proteins in a biological sample or a cell exposed to physical/chemical stimuli and is mainly performed to compare the states of proteins in healthy vs. diseased cells. Protein profiling is an advanced form of protein mining and the obtained information could lead to identification of drug targets. Protein profiling is mostly conducted by employing two dimensional gel electrophoresis (2D-GE). Cancer proteomics relies on protein profiling to compare the transformed and non-transformed cells directly. Many novel tumor biomarkers and clues for cancer development have been identified. Protein profiling has been performed on several tissues such as breast, bladder, esophageal and prostate [3]. Protein microarrays are now widely used and are the fastest method to profile a protein.

Mapping the protein-protein interactions enable us to understand how protein interactions occur in living systems. The study of protein-protein interactions allows us to simultaneously assess the status of all the proteins in a pathway. Most of the cellular processes

occur in close association with other proteins. The process of cell growth, cell death and cell cycle are all regulated by signaling pathways through protein complexes. The interactions between protein networks dictate cellular functions such as cellular signaling and metabolic pathways. A majority of information has been obtained by performing *in-vitro* studies using single and purified proteins with a yeast two-hybrid system. Most proteomic techniques offer the ability to characterize multiple proteins interactions by pairing them. Multiple protein complexes have been identified and their role in cellular pathways has been determined. Protein-protein interaction is one of the most resourceful and demanding application of the pharmaceutical industry.

Identification of protein modifications allows us to map the structural and functional changes in proteins. Proteins undergo PTM in response to extracellular and intracellular signals. In addition, exposure to environmental hazards generates reactive species that may modify proteins. MS is a powerful tool for analyzing protein modifications. Antibodies are widely used for detecting protein modifications but with this method the precise sites where the modifications occur cannot be determined. Simultaneous characterization of the modified regulatory proteins during a signaling cascade is important. Analysis of protein function is performed to understand the molecular mechanisms underlying the biochemical process occurring in the cell. It includes the study of how proteins interact with other compounds or metabolites. The interactions of proteins occur at multiple stages such as with a single pathway, whole cells, tissues or an entire organism [9]. It is important to understand all these functions as several disease conditions arise as a consequence of alterations in protein functions. Furthermore, all the physiological functions such as signaling networks, energy production and

consumption of the cells are dependent upon the activity of the proteins.

1.3. Tools for proteomics

Several tools have been developed to systematically characterize and obtain a comprehensive profile of the functions in biological systems. Biochemical assays have reproduced some of the cellular pathways outside the cell but do not address the interactions with the myriad of other pathways within the cell [10]. Early stages of proteomics have heavily relied on biochemical assays but it is a very low throughput technology. Biochemical assays were also involved in studying gene regulation, especially the interactions between nucleic acids and proteins [11].

Imaging using high-throughput microscopic screening instruments have generated a large set of images by incubating cells with one or more fluorescent probes [12]. However, it is a difficult task to derive the patterns that link the generated images back to the biochemical reactions. Although fluorescent probes have supplied a wealth of information, they suffer from several draw backs such as toxicity due to photobleaching and triggering a cascade of signaling pathways due to the interaction of the probe with cellular proteins or metabolites. Live cells when exposed to an excitation light may be subjected to photodynamic effect, causing cellular damage by direct contact with molecular oxygen [13]. The optical resolution affected by the noise and photobleaching could alter the image quality leading to altered intracellular protein levels. Imaging is a powerful tool with high resolution and even small objects are identified. However, the images needs to be interpreted carefully as few images could be exaggerated and may not appear according to scale [13].

MS is the workhorse for performing proteomics and offers high sensitivity to detect digested or intact proteins [14]. Current modifications allow targeting the protein modification of interest such as phosphorylation, oxidation and ubiquination [15]. MS requires the proteins or peptides to be in gas phase for analyzing them. MS is used to detect and quantify proteins in biological matrix but is not yet capable of separating the complex protein mixtures from the unprocessed biological matrix [16]. Matrix assisted laser desorption/ionization (MALDI) is employed where the sample is dissolved into a matrix followed by exposure to laser [3]. The major advantage of MALDI is that no purification of the sample in 2D-gel is required to separate the proteins. A disadvantage of MALDI is that the matrix aids ionization and desorption when hit with a short laser pulse and can also cause a drift in the protein mass.

2D-GE is widely used and allows the separation of numerous proteins in a single experiment. 2D-GE can also determine the extent of a proteins expressions and changes in their expression levels from sample to sample. Several drug targets have been identified employing 2D-GE technique. Separated proteins may be identified using MS or by using antibodies. A multidimensional 2D-GE offers an advantage over the traditional gel electrophoresis by allowing the separation of several samples in a single experiment by comparing the controls with the diseased samples [15]. As an alternative to 2D-gel for protein quantification, isotope-coded affinity tags (ICAT) have been developed. ICAT relies on labeling proteins obtained from different sources with chemicals of different isotope composition. The application of different labels allows quantifying the difference using a mass spectrometer. The ICAT method also enables the detection of low concentration of proteins. The major drawback of profiling using the ICAT method is that the proteins must contain cysteine residues and these must be spaced

far enough apart for the proteases to cleave them. Liquid chromatography (LC) has advanced in the recent years and offers an advantage of separating proteins in the liquid phase. LC can be coupled to MS (LC-MS) for identifying and further characterizing the sample. The volume of sample required for LC is in the nanoscale, making it more useful to do proteomics in a microfluidic device. The major disadvantage of LC is that during the separation of small volumes, the flow rates are restricted [15].

Protein microarrays (PMAs) are powerful tools for capturing and measuring multiple proteins in a high throughput fashion for the study of potential biomarkers but are expensive [16]. In this method, cells are typically lysed and exposed to protein arrays along with specific antibodies. PMAs are designed specifically to 'catch' the protein of interest and characterize it. PMAs can be used in combination with other approaches to identify a specific protein. The changes in protein concentrations, modifications and interactions can all be studied using PMAs. Another major advantage of PMAs is that a specific set of proteins such as all the mitochondrial proteins can be targeted for analysis [15].

Nanoproteomics (NP) addresses the current limitations in selectively reaching a target protein *in vivo* by applying physical and biological barriers to detect low concentration targets [17]. NP offers rapid and miniaturized assay, real time analysis, low sample consumption and high sensitivity. However, the toxicity and biocompatibility of these techniques needs to be studied further [18].

Several reagents such as antibodies have been developed and characterized to improve proteomics but are limited to capturing and detecting a specific protein. Many other methods

such as immunoblotting, analytical ultracentrifugation, surface plasma resonance (SPR) and circular dichrosim are also employed to perform proteomics [15]. All these tools are excellent and powerful to perform proteomics but are incompetent to chronically monitor the interactions non-invasively.

1.4. Challenges in proteomics

The biggest challenge for proteomics lies in the proteome's complexity. A single gene encodes multiple proteins. The human genome contains 21,000 protein encoded genes that generate an estimated 250,000 to one million different proteins in a human cell [19]. The genome is a static blueprint of a cell whereas the proteome is dynamic and dependent on varying extracellular stimuli [20]. PTM leads to protein variability, causing different expression profiles and polymorphism that makes it difficult to detect [16]. The isolated proteins during cellular interactions must be in their native forms for an accurate analysis. In spite of the availability of several new advanced technologies, detection of low levels of proteins in a complex biological mixture still remains a challenge. Few eukaryotic cells have a low to high protein ratio of $1:10^6$, making it difficult to analyze and track the changes in the sample. Also, it is difficult to identify transcription factors, protein kinases and regulatory proteins as they are expressed in low number. Further purification or extractions methods may be employed to isolate the protein of interest from the proteome [3]. Also, certain protein extraction and separation techniques are skill-based and remain difficult to automate [21].

Most of the methods including 2D-GE or performing biochemical assays are not high-throughput. Performing an MS may require a substantial amount of time for data acquisition,

processing and analysis [3]. Quantification of hundreds of proteins can be achieved by performing MALDI time-of-flight MS (MALDI-TOF MS) but not all proteins in the sample can be detected, yielding a low-resolution analysis. A higher resolution of the sample can be obtained by using a MS/MS but it would require significant time and resources to interpret data. Performing a wide dynamic range of analysis has been another limitation of MS/MS [19]. Most of these systems are invasive, thereby activating other signaling pathways which lead to cellular apoptosis. Moreover, these systems detect only the end-point, cost ineffective, lack the capability for chronic monitoring of cellular functions interactions and are limited to the pathways being analyzed. Instead, a study of the entire biological system as a single entity is necessary and would provide profound insights.

1.5. Systems biology driven proteomics

Systems biology employs a centralizing approach to characterize biological systems, where the interactions described mathematically to establish a computable model. Systems biology aims to increase our understanding and predicting the behavior of a biological system. The key utilities of model building are (1) to organize information from different sources into a cohesive model, (2) to determine what species and interactions play a vital role a specific pathway of interest or the entire cell, (3) identification of new inter-dependencies on cellular process and (4) to learn all the quantitative features on a large scale. System biology based tools are now widely used to perform drug discovery due to the physiological relevance of results and the ability to perform high content screening. These tools aid in analyzing cellular pathways providing a deeper understanding of several biochemical processes including metabolic

pathways [22].

Most biological systems behavior cannot be limited to a single molecule or pathway instead they result due to the interactions occurring at different levels among different cellular compartments. Modeling of the reconstructed system, if possible at different levels, would allow performing simulations and predicting hypothesis. The earlier stages of the developed systems could be small containing few proteins representing a signaling pathway and eventually lead to a whole-cell model [23]. Since systems biology is hypothesis driven, the model is validated by perturbations and validating with the experimental datasets. A dynamic analysis of the changes in the model enables the identification of changes in protein activity. In modeling biological systems, cellular networks are divided into signaling, regulatory and metabolic that responds to perturbations and alters cellular activities. Currently, a biological system is best characterized using metabolic models [24]. The basis of reconstruction and development of cellular networks is well documented and have also received much interest. Analysis of these networks can be aimed at performing a quantitative or qualitative analysis [25]. For example, a boolean network can be implemented to perform quantitative and kinetic models for quantitative analysis of cellular signaling pathways.

Proteomics was identified as an essential discipline for building precise network models [23]. Proteomic analysis and Systems Biology have come closer during the past decade and present a promising approach to unveil functions of proteins in complex cellular networks. Proteomic analysis by employing systems biology would be a powerful tool. It has become obvious that protein analysis needs to be performed on a large- scale as the rate of drug

attrition has increased. The complex dynamics of proteins makes it difficult to study. Proteins are the actual effectors for maintaining cellular hemostasis by driving the cellular pathway and cannot be simply be studied by looking at a gene, mRNA or in fact a single protein. A large amount of experimental data is being generated using several tools such as PMAs, imaging and LC-MS/MS [24]. The data obtained from all the proteomic tools can be integrated into a single system for further analysis. Proteomic tools can be applied to study the protein-protein interactions and protein functions as a result of perturbations in biological process on a large scale. Most of the limitations and challenges of the proteomic tools could be addressed by coupling existing tools and data to systems biology driven models. However, none of the current standalone tools or tools coupled to systems biology can monitor the cellular pathways or the dynamic changes that a protein undergoes in response to perturbations [23].

1.6. Motivation

A system capable of determining temporal profiles of living cells to perturbations of a compound as it interacts with a cell over a period of time providing a rich set of information that could be captured non-invasively would be beneficial [26,27]. Such system would provide insight into the mechanistic details of cellular pathways, predict the response of proteins interactions in cellular systems to multiple perturbations beyond those from which models are derived and guide the design of perturbations for a desired response. Tools based on monitoring the state and activities of the excitable cells are frequently used to quantify the physiological responses to external stimuli [28,29].

Neurons exhibit an action potential (AP) that gives complex information about the internal/external environment of excitable cells. The AP shape contains a significant amount of information, as it is dependent on concerted action of ion channels located on cell membrane that are tightly regulated by receptors and intracellular messenger systems [30,31]. Ion channels are regulated by all common intracellular mechanisms including phosphorylation and second-messenger dependent systems [32] as intracellular ions play the significant role of second messengers in cells [33]. The membrane electrical activity is highly dependent on the state, physiology and pathophysiology of the cells [34]. The AP generation and shape are determined by Na^+, K^+, Ca^{2+}, ATP, other second messenger dependent channels and pumps [35-37]. Calcium [38], sodium [39], and potassium [40] channel modulators have been shown to affect the shape of cellular action potentials [27].

Cellular metabolism and membrane electrical properties are tightly integrated. The changes in AP are characteristic to the biochemical pathway affected by chemical or biological entities [26,27,41]. Deconvolution is the quantitative determination of underlying ionic currents of AP which would not only enable the detection of altered pathways but also potentially differentiate compounds with different mechanisms of actions [27,41]. Cellular electrophysiology is the gold-standard technique for measuring ionic currents of an excitable cell and the electrical components in the cell membrane, including primary ion channels. The information obtained from the system is highly complex in nature and needs to be deconvoluted using an *in silico* tool to gain a deeper understanding on the dynamics of the physiological processes [26].

1.7. Previously developed models

Previously developed models of cellular pathways in cells have been effective in modeling pathways and enhancing drug discovery. Techniques for network modeling of cellular pathways span a wide spectrum of complexity. Models of signaling pathways have been reconstructed by combing and analyzing information available in the public domain, including DNA sequence data, protein sequence data, literature, pathways recorded in public databases, gene expression data, mass spectrum data and metabolic profiles. However, these networks often have delivered several false positives or false negatives due to noise and incomplete data.

The great majority of cell models were also tailored towards one or two specific cell activities, mostly carbon flux, respiration, signaling, gene activation and electrophysiology. Computational models incorporating ion channels to represent whole-cell AP models relate the changes in membrane potential to the sum of inward and outward ionic currents. They typically consisted of 10-70 differential equations with multiple parameters. Gleeson et al. introduced NeuroML, which offers a multilayer approach of electrophysiological features from individual cells with selected ion channels to morphologically reconstructed multi-compartment neurons forming networks with others [42]. However, the modeled neurons were limited to their electrophysiological function since metabolic events were not included. Lewis *et al*. modeled complex signaling interactions between astrocytes and motor neurons by including metabolic pathways for each cell type [43]. Zhou et al. published their comprehensive work on the electrophysiological activity of cardiac myocytes and influences of the mitochondrial TCA cycle [44]. Masson et al. explored the link between electrical activity and insufficient metabolic energy by merging the classical Hodgkin-Huxley conductance model [45]. Their model provided

theoretical basis to study the dependence of cellular bioenergetics on membrane electrical activity. The metabolic model was not detailed enough to perform analysis of cellular pathways. Cortassa et al. developed a computational model by integrating cardiac electrophysiology, contraction and mitochondrial bioenergetics to obtain a greater insight into their interactions and dependencies [46]. The model lacked the detailed glycolytic and pentose phosphate pathway along with the deconvolution module to predict the responses of action potentials.

Experimentally validated models have already been developed which are coupled to the electrophysiological properties of the cell membrane to complex intracellular pathways [47,48]. These models have been used to predict the physiological changes in the intracellular mechanisms such as gene expression, activation of secondary messenger systems and phosphorylation [49]. Several publications from leading groups in systems biology are all extraordinary milestones towards large-scale and whole-cell modeling. A first 'real' whole-cell model of *Mycoplasma genitalium* was built by combining all the molecular components to study the unexplored cellular behavior [50]. However, experimentally validated computational models including all major functions and organelles of mammalian cells, especially neurons, are currently not available.

A popular way to develop more complex and comprising models is to extend existing pathway models with further reactions and species or in some cases the combination of two or more existing models. The latter approach comes with challenges as the employed models were usually proposed by different groups, which used different time frames, units, and often worked with pathways of different cell types if not species. In our previous work, we have

demonstrated the use of neuronal cells as sensor elements for toxin detection [27,41]. The interrupted AP showed differences we believe could vary depending upon the pathway being inhibited by a compound, protein or gene.

1.8. Objectives of dissertation

The objective of this dissertation is to develop and experimentally validate an *insilico* tool that would predict action potential time-series by enabling chronic monitoring of intracellular networks and intracellular proteins activities.

To achieve the aforesaid objectives the following tasks have been performed

1. The basal metabolism of NG108-15 cells has been determined by performing biochemical measurements.
2. The NG108-15 cellular metabolic model was reconstructed and experimentally validated by employing the biochemical measurements.
3. A neuronal module for deconvolution of neuronal action potentials was constructed and the electrophysiological parameters were extracted.
4. The effects of inhibition of cellular proteins involved in energy producing metabolic pathways were evaluated by measuring the biochemical and electrophysiological changes in NG108-15 cells.
5. A coupled neuronal-metabolic model including the sub-cellular compartment was built to generate a series of action potentials followed by predicting the changes in intracellular ion concentrations and protein activities.

6. An experimental validation of neuronal-metabolic model was performed by simulating multiple scenarios of inhibiting cellular proteins involved in cellular bioenergetic pathways for predicting protein activities and action potential time-series.
7. An in-depth analysis of predicted temporal activities of cellular proteins during metabolic perturbations was carried out to evaluate the model predictive capabilities.

1.9. Dissertation outline

This dissertation describes development and experimental validation of neuronal metabolic model.

Chapter 2 provides the theory behind the cellular metabolic pathways and general approach for model development is discussed. The ionic basis of membrane electrical properties, cellular electrophysiological techniques and the theory behind Hodgkin-Huxley model are explained.

Chapter 3 describes the experimental methods employed in measuring the effects metabolic inhibitors. This chapter includes details of the modifications of surfaces, cell culture, biochemical assays and patch clamp electrophysiology protocols that were utilized.

Chapter 4 illustrates the development of neuronal-metabolic model. The coupling of different intracellular pathways including the metabolic reactions was explained. The chapter also includes the reconstruction and a detailed description of biophysical components involved in neuronal module. The integration of both the modules followed by methodologies employed for parameter estimation is described. The chapter also included a detailed description on how

experimental conditions were simulated

Chapter 5 provides a discussion on the results obtained from the model. The basal metabolic properties of NG108-15 cell are presented. The calibration of model to steady state using the experimental data is explained. The deconvolution of action potentials to extract the ion channel parameters has been described in detail. Also, a discussion on how the neuronal-metabolic model was simulated to steady state and perturbations induced were estimated is provided. The experimental validation of simulated results for all the drugs and drug combinations including the characteristic analysis of action potential time series data is presented. The predicative capabilities of the model are demonstrated in this chapter.

Chapter 6 concludes the dissertation by outlining the outcomes from the model and the future work involved in developing the model is discussed in detail.

CHAPTER-2: THEORY

In this chapter the cellular metabolism and membrane electrical properties were reviewed. An understanding of the fundamental theory behind the biochemical and biophysical interactions occurring during cellular function is a prerequisite. The core cellular pathways involved in energy metabolism followed by describing the basics of modeling and kinetic analysis are presented. The second half of the chapter describes the characterization of membrane electrical properties following the description of the measurement techniques and their mathematical basis.

2.1. Cellular Metabolism

Cellular metabolism plays a vital role in cellular functions. The metabolic reactions can be categorized into two broad categories, namely degradation and synthetic pathways. The biochemical reactions occurring in a pathway are organized, localized and regulated in a cell [51]. The rates of intracellular enzymes i.e., regulatory proteins dictate cellular activities. The protein activities are modified in a cell to maintain a favorable environment for obtaining highly efficient cellular processes. At steady state, a cell requires carbon for biosynthesis and ATP for cellular functions [51]. These requirements are met by central metabolic pathways that include glycolysis, pentose phosphate pathway (PPP), mitochondria and endoplasmic reticulum.

2.1.1. Glycolysis and PPP

The glycolytic pathway is one of the core metabolic process during which one molecule

of glucose is converted into two molecules of pyruvate by producing ATP. Glycolysis is also known as the Embden-Meyerhof pathway that has two phases [51]. In phase one, conversion of glucose into fructose-1,6-bisphosphate is catalyzed by hexokinase (HK), phosphogluccose isomerase (PGI) and phosphofructokinase (PFK). HK and PFK consume two molecules of ATP to mediate conversions. During the second phase of glycolysis, fructose-1,6-biphosphate is further metabolized into pyruvate by consuming two ADP molecules and produces four molecules of ATP. The fate of pyruvate is dependent on cellular oxygen utilization. In hypoxia conditions, pyruvate generated gets converted into lactate and is transported by monocarboxylate transporters (MCT) [52]. In contrast, during normoxia pyruvate enters the mitochondria and gets further metabolized to generate ATP. Additionally, the glycolytic enzymes such as HK, glyceraldehyde 3-phosphate dehydrogenase (GAPDH) and enolase have been shown to be multifunctional as they play a role in cellular transcription [52].

The pentose phosphate pathway (PPP) is an alternative pathway for metabolizing carbon entering glycolysis. The end product of PPP, ribose-5-phosphate, is utilized in the synthesis of nucleic acids. PPP generates NADPH that is utilized for ATP production. The activity of PPP differs from cell-to-cell. For example, muscle cells lack PPP as they utilize carbohydrates for energy generation whereas red blood cells lack mitochondria forcing the cell to completely rely in PPP for NADH generation [53]. On the other hand, neurons, which are of interest here, have been shown to possess active PPP [54]. The PPP and glycolysis are interconnected. The enzyme transketolase in PPP mediate the conversion of xylulose-5phosphate to glyceraldehyde-3-phosphate. The produced glyceraldehyde-3-phosphate enters the second phase of glycolysis directly to generating pyruvate and ATP [52].

2.1.2. Mitochondria

Mitochondria are considered as the power house of the cell. Two major mitochondrial pathways namely, the TCA cycle and electron transport chain generate ATP. Pyruvate generated during glycolysis is transported into mitochondria by monocarboxylate transporters present on the mitochondrial membrane. Pyruvate is converted into mitochondrial acetyl-CoA which acts as the starting point for the TCA cycle. The acetyl group from Acetyl-CoA is transferred to oxaloacetate to generate citrate. A series of cyclic reactions convert citrate to oxaloacetate by performing two decarboxylations and four steps of oxidation to form malate followed by regenerating oxaloacetate. The ATP production from the TCA cycle occurs during the conversion mediated by succinyl-CoA lyase [53]. The TCA cycle generated NADH and $FADH_2$ are transported by succinate dehydrogenase (SDH) to the electron transport chain for ATP production. The TCA cycle generates precursors for biosynthesis of several amino acids. The major sites of regulations of TCA cycle were citrate synthase, isocitrate dehydrogenase and α-ketoglutarate dehydrogenase. The TCA cycle is also sensitive to the buildup of metabolites by lowering its activity [53].

The electrons generated in glycolysis are transported into mitochondria by the malate-aspartate shuttle (MAS) or glyceraldegyde-3-phosphate shuttle (G3P). The expression and efficiency of these shuttles varies in different cell types [51]. MAS and G3P transport 6 and 3 electron equivalents respectively. The electrons from NADH and $FADH_2$ are passed into the inner mitochondrial membrane by complexes I, III and IV. The electrons then move towards oxygen and protons from the cytosol are consumed to increase the pH in the mitochondrial membrane creating a potential difference. The protons move through F_1F_0-ATPase to

synthesize ATP. The mitochondrial ATP is transferred into the cytosol by the adenine nucleotide transporter [53].

2.1.3. Endoplasmic reticulum

The endoplasmic reticulum (ER) has several functions including folding and transport of proteins. The ER also acts as stress modulator by altering intracellular calcium levels. The intracellular calcium levels in a cell are maintained at low concentrations when compared with sodium and potassium concentrations. The low calcium concentrations are necessary as several proteins get activated or deactivated from calcium binding. Thus, cellular calcium concentrations must always be maintained in homeostasis and in check to avoid activation of unwanted signaling cascades [55]. The intracellular calcium concentrations are maintained by two mechanisms, buffering and sequestering. Buffers are calcium-binding proteins that absorb 95-99% of free cytosolic calcium [55]. Calcium sequestering usually occurs in the ER.

The ER consists of three major channels that mediate calcium fluxes. The sarco/endoplasmic calcium ATPase (SERCA) pump moves cytosolic calcium into the ER against the concentration gradient by consuming cellular ATP. To generate feedback and maintain homeostasis, cells have inositol triphosphate (IP_3) and ryanodine (RyR) receptors. A negative and positive feedback is obtained from channels when calcium is bound to them. These receptors have been shown to control several cellular processes such as cell cycle and membrane electrical activity [55].

2.1.4. Metabolic alterations in cancer cell

Cancer cells have exhibited aerobic glycolysis i.e., higher glycolytic activity compared to normal cells even in the presence of sufficient oxygen. This phenomenon was first described by Otto Warburg in the year 1930. The prime cause for metabolic alterations was due to lowered mitochondrial activity and was resolved by Warburg in 1956. This effect of cells possessing aerobic glycolysis was termed as the 'Warburg effect'. The Warburg effect was considered as one of the prominent symptoms in cells with altered metabolic activities. Researchers have rationalized this effect to describe (a) defective mitochondria, (b) adaption to hypoxia, (c) oncogenic signaling and (d) overexpression of cellular proteins [52].

Impaired mitochondrial function forces the cell to depend on glycolysis for ATP generation. Mitochondrial damage was assumed as low levels of ATP were being produced. Analysis of mitochondrial DNA (mtDNA) levels revealed high mutations in cancer cells [52]. Several factors such as reactive oxygen species (ROS) and low levels of chaperones could cause mutations [52]. Hypoxia has been shown to directly modulate energy metabolism. Tumors have been shown to have a restricted supply of oxygen creating a hypoxic environment that would increase glucose utilization and lactate production leading to acidification. It's well established that inhibiting glycolytic activity with 2-deoxy-glucose (2DG), Oxamate or 3-bromopyruvate has a significant effect on cancer cells [52,56,57].

The enzymes that play a vital role in TCA cycle dependent ATP production are fumarate hydratase (FH) and succinate dehydrogenase (SDH). Studies have showed that inhibiting SDH caused accumulation of succinate and suppresses the TCA cycle activity [52]. SDH is an

important enzyme as it is involved in both the TCA cycle and electron transport chain. A loss in SDH activity would arrest mitochondrial energy metabolism completely. Cancer cells have been shown to possess increased ROS levels. It is possible that increased ROS levels may lower or inhibit ROS-sensitive enzymes [52].

2.1.5. Metabolic Modeling

Metabolic modeling employs systemic integration of experimental knowledge into a mathematical framework that enables the prediction of dynamic behavior in cellular machinery. Currently metabolic models are largely validated based on constrained-based approaches. Most metabolic models are usually aimed at the identification of molecular targets for controlling cellular activities. Models based on ordinary differential equations (ODEs) have been successful at determining cellular fluxes, metabolite concentrations and protein activities. An ODE for a certain component (C) is usually represented by determining the rate of production ($v_{production}$) and consumption ($v_{consumption}$) as shown in equation 1.

$$\frac{d}{dt}[C] = v_{production} - v_{consumption} \quad (1)$$

The rate of production and consumption depends on kinetics of proteins involved in pathways. The basic kinetic method that describes the activity of most proteins is Michaelis-Menten kinetics. Proteins are complex and so it their activity. A biochemical determination of protein activities and estimation of their kinetics has enabled the derivation of kinetics of specific proteins or a common kinetic equation for describing a set of proteins [58,59].

Several tools, such as Pathways Tools [60], have been developed to implement and

model the kinetics of a set of proteins. The initial conditions were usually estimated using experimental data. The numerical equations can then be solved using an ODE solver. Due to a large interest in model development, a Systems Biology Markup Language (SBML) has been developed to exchange models of different biochemical networks [61]. Parameter estimation currently is one of the biggest challenges in systems biology. An increase in the number of interactions exponentially increases the parameter estimation space. To overcome this several strategies have been proposed. A toolbox (COBRA) in MATLAB has been developed by constraint-based modeling for quantitative prediction of cellular networks [62]. The model predictions obtained from COBRA have delivered the best set of parameters and when evaluated the model predications were accurate [62].

2.2. Cellular electrophysiology

The flow of ions across the membrane creates a voltage difference called biopotential. The changes in the biopotential may occur due to several factors such as temperature, pH, ionic concentrations or extrinsic current [63]. Cellular electrophysiology is the study of membrane electrical properties of a cell. The goal of performing electrophysiology is to detect electrical signals generated by excitable cells such as neurons, muscle, cardiac, pancreatic and sensory neurons. Cellular electrophysiology involves measuring changes in voltage or current across the membrane. A voltage clamp recording is performed to measure changes in sodium and potassium currents by holding voltage constant and a current clamp is obtained by holding current constant thereby measuring changes in membrane potential.

2.2.1. Ionic basis of action potentials

Cells at rest have a certain potential called a resting membrane potential, due to difference in ionic concentrations across the membrane. The intracellular potassium concentration is about 10-14 times higher compared to the extracellular potassium concentration leading to a negative reversal potential. The concentrations of sodium and calcium are very low intracellular and high extracellularly generating a positive reversal potential. The plasma membrane contains 'open' potassium channels that allow the passage of potassium ions. The resting membrane potential is mainly determined by the movement of potassium ions since it is occurring down the concentration gradient through the open potassium channels. The resting membrane potential of a typical cell is about -60 mV to -70 mV and the reversal potential of potassium is close to the resting potential. A change in resting membrane potential always changes the intracellular potassium concentration and reversal potential [64].

An action potential (AP) represents changes in cellular membrane potentials generated when a required strength of electric current is passed through the membrane of an electrically excitable cell. Different cells exhibit action potentials of different shapes including a variation in AP amplitude and time course. The time course of AP's varies from 1 ms in neurons to 5s in cardiomyocytes [63]. AP is a cyclic process where membrane depolarization, hyperpolarization and resting membrane potential cycle are a result of alterations in ion permeability.

During an AP, an initial depolarization changes the conformation of voltage-gated sodium channels and allows an influx of sodium ions. The propagation of this AP depolarizes the

adjacent region thereby opening voltage-gated sodium channels and increasing the sodium influx. A combination of factors established due to differences in ionic concentrations and resting membrane potential drives sodium ions into the cell. As more sodium ions enter the cell, the membrane is depolarized, further causing a larger influx of sodium and the permeability of sodium in that specific region increases. But when the reversal potential of sodium matches the cellular membrane potential, the sodium influx ceases [64]. During the closure of voltage gated sodium channels, voltage gated potassium channels open leading to an increased potassium permeability. The potassium efflux causes the membrane to repolarize back to the resting membrane potential. The voltage-gated calcium channels are also opened simultaneously with potassium channels and closed upon reaching resting membrane potential. Upon reaching the resting membrane potential the sodium, potassium and calcium ion channels close [64].

Action potentials cause characteristic changes in membrane potentials by rearranging ionic balances across the membrane. The movement of ions across the membrane generates a change in voltage. Although the changes in voltage are significant, the actual number of ions that move across the membrane are very small compared to number of ions in the total volume of the cytosol. The ionic fluxes during AP were measured initially by performing an experiment on giant squid axons. The movement of ions across the membrane was characterized by using radioactive sodium and potassium. It was found that depending on the size of a neuron, during single AP generation about one potassium ion per 300,000 in the cytosol is exchanged for extracellular sodium. So the changes in the total cytosolic ionic concentrations during an AP are negligible [64].

2.2.2. Measurement techniques

Several techniques such as patch-clamp, extracellular recordings and planar patch clamp are employed for performing cellular electrophysiology. Each technique offers a set of advantages and disadvantages. Both intracellular and extracellular recordings have been performed to study membrane activity. During patch clamp electrophysiology, the recordings are usually performed by patching cell using a sharp electrode to measure changes in membrane potential. Several variations in patch clamp techniques have been exercised depending on the study. An on-cell patch is performed where patch membrane is kept intact and currents are measured without disturbing intracellular pathways. Another variation is an inside-out patch. During an inside out-patch, the cell is patched and pipette is withdrawn quickly to exposing intracellular contents of the cell to external environment. A whole-cell patch is the most common patch employed during patch clamp electrophysiology. Patch clamp techniques enables measurements of single ion channel properties. The principle behind patch clamp relies on the high-resistance seal formed between sharp electrode and cell membrane. The resistance of the seal varies from patch-to-patch but usually a giga-ohm seal is necessary to maintain a stable patch. During a whole-cell patch, a small surface of the cell membrane is drawn into the pipette, and by applying suction the membrane is broken enabling access into the whole-cell. A ground electrode lies in the extracellular chamber acting as a reference electrode. The electrodes are connected to an amplifier for detecting and measuring changes across cellular membrane. An outside-out patch is formed by patching a cell and slowly withdrawing the pipette along with a bleb of cellular membrane containing the ion channel of interest. The activity of ion channels in the bleb can then be measured. Perforated patch clamp

employs rupturing the cell membrane by incorporating a small amount of antibiotic. A giga-ohm seal is formed during perforated patch by just touching pipette to the membrane. Since the membrane is not ruptured, a long term measurements can be performed.

Patch clamp electrophysiology is the gold standard for measuring membrane electrical activity. It is a short term and technique driven. To overcome this microelectrode arrays have been developed and are capable of measuring electrical activity over long periods. Optical measurement systems based on changes in emitted fluorescence signal upon incorporation of a dye are also used. The fluorescent probes are voltage sensitive and emit fluorescence when a change in voltage occurs. The changes in fluorescent intensities need to be tracked and processed for quantifying. To perform high throughput electrophysiology, the planar patch clamp technique has been developed. During planar patch clamp, cells are suspended in a solution and added to a chip containing micro pipettes. Suction is applied in the micropipettes to create a seal followed by record membrane electrical activities.

2.2.3. Hodgkin-Huxley model

Hodgkin & Huxley's mathematical description of AP formalism is the most widely used to describe an AP and relies on the opening and closing of channels, selectively allowing ions to move across the membrane [65]. A series of voltage clamp experiments were performed and the experimental data was fitted to obtain sodium conductance of voltage gated sodium channels consisting of activation 'm' and inactivation 'h' gates. The potassium conductance was also determined which consisted of a single activation gate 'n'. The ionic conductances were obtained from,

$$g_{Na} = g_{max} m^3 h \tag{2}$$

$$g_K = g_{max} n^3 \tag{3}$$

Where g_{max} is the maximum conductance of ion channel. The exponents on m, n and h were determined by obtaining a fitting of the model to experimental data. The gating variables were postulated and determined for voltage-gated time constants i.e., τ_m , τ_h and τ_n. The leak conductances were incorporated to account for small conductances in the membranes. The ODE's for the HH model are given by,

$$\frac{C\, dV}{dt} = -g_{Na} m^3 h(V_m - V_{Na}) - g_K n^4 (V_m - V_K) - g_{leak}(V_m - V_{leak}) + I_{app} \tag{4}$$

$$\frac{dn}{dt} = \alpha_n(1 - n) - \beta_n n \tag{5}$$

$$\frac{dm}{dt} = \alpha_m(1 - m) - \beta_m m \tag{6}$$

$$\frac{dh}{dt} = \alpha_h(1 - h) - \beta_h h \tag{7}$$

The model could mimic the neuronal dynamics accurately but were computationally inefficient for parameter estimation and model simulation [66]. To create a more accurate estimation of parameters, a functional form for the voltage dependence of the rate constants that takes into account more realistic effect of the electrical field on the ion channel protein was developed by Destexhe et al. [67]. Mohan et.al have developed a linear thermodynamic formalism that was then used to describe the voltage and time dependence of the ionic conductance, which eliminated the need for 'guessing' the function for the voltage-dependence

of rate constants and the same form could be used for characterization of all ion channels [27].

CHAPTER-3: EXPERIMENTAL METHODS

In this chapter, the methodology implemented to perform experiments is described in detail. NG108-15 cells, a neuroblastoma-glioma hybrid neuronal cell line were used for developing and charactering the model. The NG108-15 cell line was developed by fusing a mouse N18TG2 neuroblastoma cell with a rat C6-BU-1 glioma cell in the presence of an inactivated Sendai virus. The NG108-15 cells line was developed in 1971 by Bernd Hamprecht [68]. These cells do not form synapses and possess functional properties of neurons making them ideal for performing high-throughput drug screening and pathway analysis. A combination of biochemical and electrophysiological measurements were performed to characterize and develop the model.

3.1. Surface modification

Glass coverslips (22 mm × 22 mm, Thomas Scientific) were coated with N-1[3-(trimethoxysilyl) propyl] diethylenetriamine (DETA) according to previously published protocols [10]. The protocol involved cleaning coverslips using a mixture (1:1) of hydrochloric acid and methanol followed by soaking it in concentrated H_2SO_4 for 30 min. The cover slips were rinsed with deionized (DI) water for 30 min, immersed in boiling in deionized water for 30 min, rinsed with acetone and placed in an oven at 70 ^{o}C for 20 min to allow drying. The cleaned surfaces were treated with a 0.1% (v/v) mixture of organosilane in toluene to form a thin film of DETA (United Chemical Technologies., Bristol, PA). The DETA coated coverslips were heated to a temperature just below the boiling point of toluene, rinsed with toluene, reheated to a

temperature just below the boiling point again and then oven dried [27]. The DETA surface was analyzed using contact angle measurements and X-ray photon spectroscopy (XPS) [69].

3.2. Preparation of culture medium and patching Solutions

3.2.1. Culturing and differentiation medium

NG108-15 culturing medium was prepared by adding 50ml of 10% fetal bovine serum (FBS) (Gibco, NY, USA) and 10ml of hypoxanthine-aminopetrin thymidine (HAT) medium supplement (Sigma-Aldrich Corp, St.Louis, USA) to 500ml of Dulbecco's modified eagle's medium (DMEM, Gibco). The differentiation medium was prepared by adding 10 ml of B27 (Gibco) to 500ml of DMEM (Gibco) media. The prepared medium was sterilized by filtration and stored at 4 ^{o}C.

3.2.2. Intracellular patch solution

Intracellular solution was prepared by dissolving 4-(2-hydroxyethyl)-1-piperazineethanesulfonic acid (HEPES) and ethylene glycol tetraacetic acid (EGTA) in water. The mixture was sonicated to ensure that EGTA is completely dissolved. Following sonication, NaCl, KCl, $MgCl_2$ and $CaCl_2$ were added to the solution. DI water was added to make up the volume to 50 mL. The osmolarity of the solution was verified using an osmometer (Fiske) and adjusted to 280-290 mOsm by adding HEPES. The pH of the solution was adjusted to 7.2 at room temperature. The prepared solution was aliquoted into 1mL vials and stored at 4 ^{o}C. The osmolarity was checked prior to performing the experiment. The composition of the solution is listed in Table 2.

Table 2: Composition of intracellular patch solution

Compound	Concentration (mM)
Sodium chloride	10
Potassium chloride	140
Magnesium chloride	2
Calcium chloride	0.5
Ethylene glycol tertaacetic acid	1
HEPES buffer	10

3.3. NG108-15 cell culture

The NG108-15 cell line (passage number: 16) was obtained from Dr. M. W. Nirenberg, National Institute of Health (NIH) and was sub-cultured according to previously published protocols [27,41]. A vial of NG108-15 cells stored under liquid nitrogen was thawed and immediately resuspened in 9ml of culturing medium. The medium with the cells was centrifuged at 1000 RPM for 5 min. The supernatant was removed and the cells were resuspened in 1ml of fresh culturing medium. A cell count was performed using tryphan blue in a hemocytometer. During resuspension, cells were mixed slowly to avoid cell damage and care was also taken to avoid bubbles. The suspension containing cells was then added to a T-75 flask (Corning, NY, USA) containing 20ml of fresh differentiation medium. The flask was placed in a

standard cell culture incubator at 37 ^{o}C for 72 hours to achieve 90% confluency (Figure 2).

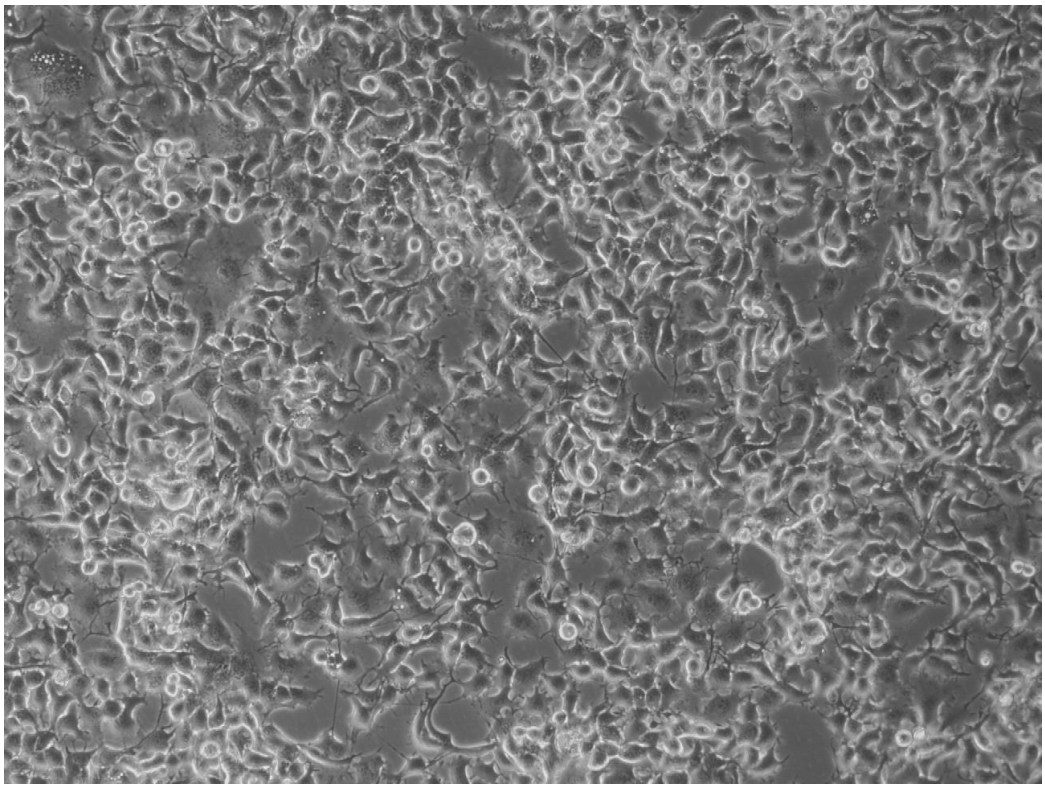

Figure 2: A representative image of NG108-15 cells after reaching 90% confluency on Day 3.

DETA coated cover slips were sterilized by rinsing with ethanol in a biosafety hood. The coverslips were allowed to dry in the hood and transferred to 6-well plates (Corning, NY) followed by the addition of 3ml of fresh differentiation media. The plates were placed in the incubator for 20 min. Cells were collected from the T75 flask by removing the culturing media and adding 10ml of fresh differentiation media. The flask was tapped to detach the cells. The medium with cells was centrifuged for 5 min at 1000 RPM. The supernatant were removed and resuspened in 1ml of fresh differentiation medium. Cell count was performed using tryphan blue in a hemocytometer. The cell mixture was diluted and plated at different densities. Cells were plated at 4×10^5 cells per well for patch clamp electrophysiology and 8×10^5 to 1×10^6 cells

per well for biochemical assays. A half media change was performed every 2 days. The morphology of cells was examined every day and experiments were performed after 4 days (Figure 3).

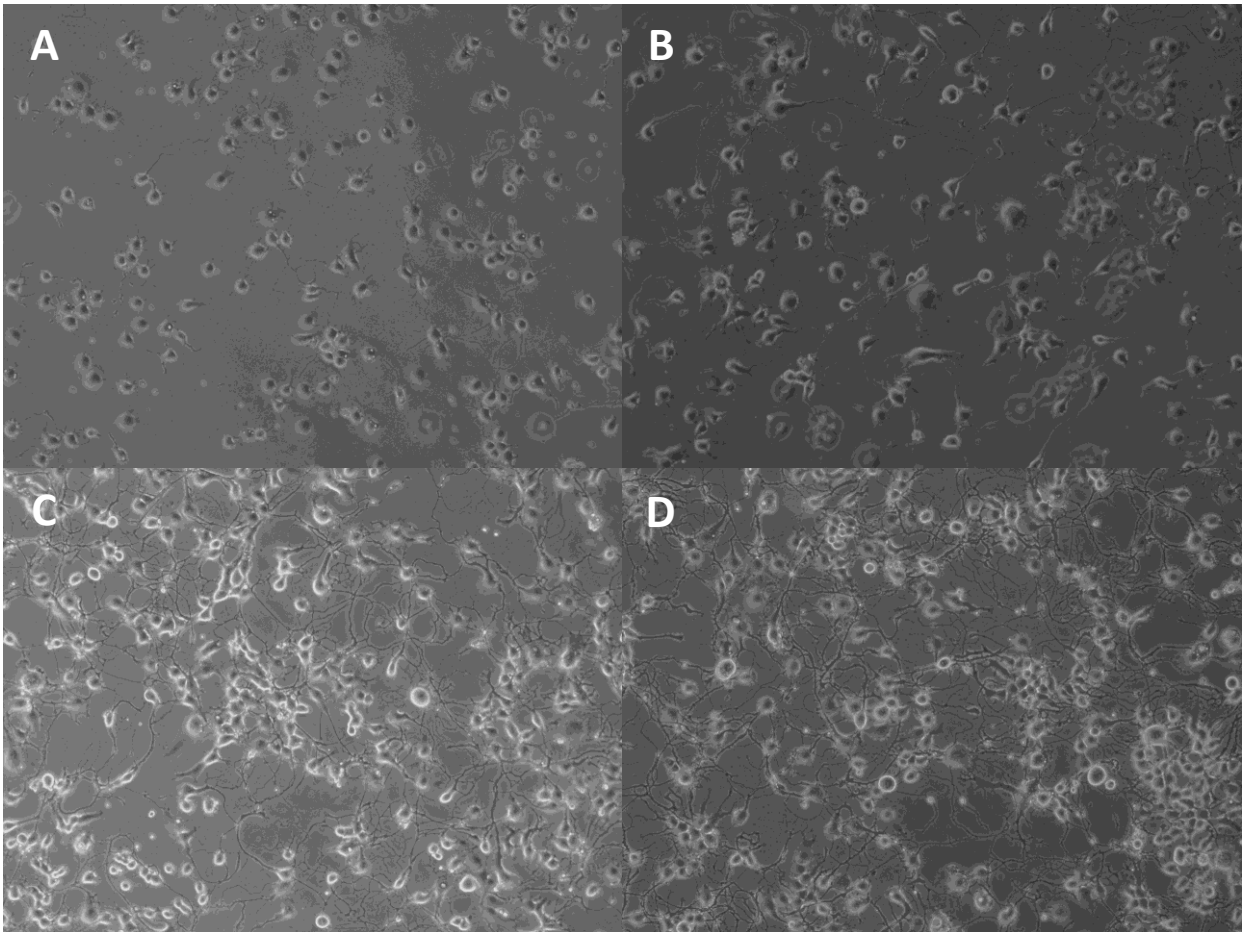

Figure 3: Differentiation of NG108-15 cells. The morphology of cells on DETA coated coverslips on DIV-1 (A), 3 (B), 4 (C) and 5 (D) is shown at 10x

3.4. Biochemical assays

The basal metabolism of the NG 108-15 cells was determined by performing biochemical assays on day four. The rate of glucose uptake, lactate production, ATP and ADP concentrations were determined.

3.4.1. Glucose assay

The differentiation medium was taken out from the 6 well plate and 1ml of fresh differentiation medium or differentiation medium containing drug was added. Samples were collected every 20 min and the glucose concentration was analyzed using a colorimetric assay kit. (Biovision, Inc; Catalog #K606-100). A sample of 4 µL was diluted by adding 16µL of assay buffer solution and 2µL of the diluted sample was further diluted to total volume of 50µL/well.

The glucose standard curve was prepared by diluting the glucose standard to 1nmol/µL by adding 10µL of the glucose standard to 990µL of glucose assay buffer. Various volumes, namely 0, 2, 4, 6, 8 and 10 µL of the above solution were added into each well individually. The volume was adjusted to 50µL/well with glucose assay buffer to generate 0, 2, 4, 6, 8 and 10 nmol/well of the glucose standard.

Enough reagents for the number of assays to be performed were pre-mixed. For each well, a total 50µL reaction mix was prepared by adding 46µL glucose assay buffer, 2µL glucose probe and 2µL glucose enzyme mix. Then 50µL of glucose reaction mix was added to each well to obtain 100µL per well. The plate/reaction was then placed in an incubator at 37^0C for 30 min. The absorbance was measured at 570nm using a Synergy HT mulitwell plate reader (BioTek Instruments, Inc.). A calibration curve was performed simultaneously and the background was corrected using the blank (Figure 4).

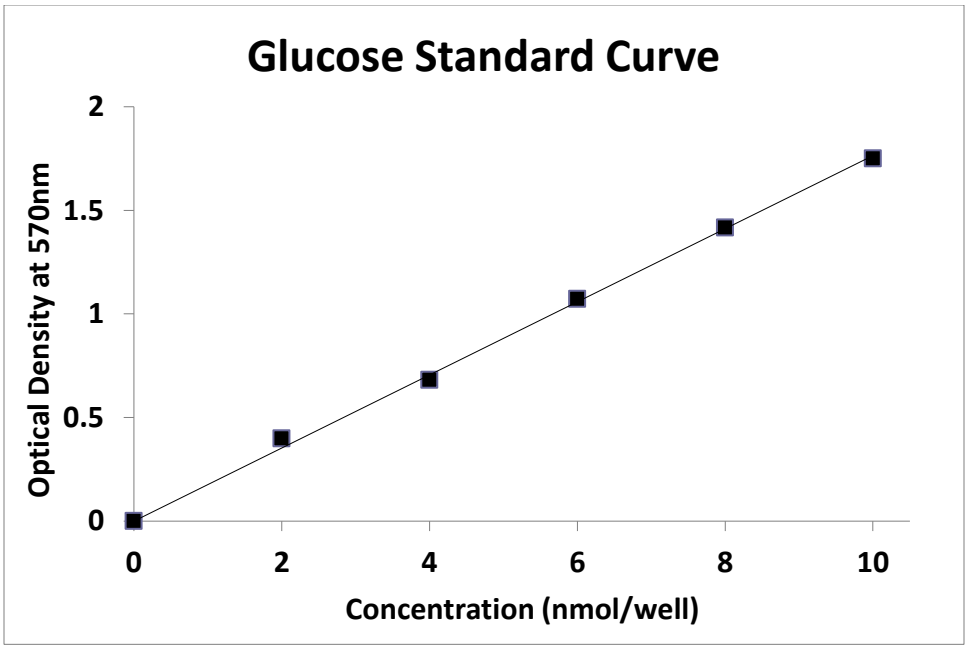

Figure 4: Glucose assay standard curve

The concentrations of the samples were determined by the following equations:

$$C = \frac{Sa \times D}{Sv} \tag{8}$$

Where, C = Actual concentration from the graph; Sa = Sample amount (in nmol) from standard curve; Sv = Sample volume added to the sample wells; D = Dilution factor

Calculation of Flux per minute per cell (Fmc),

$$Fmc = \left[\left(\frac{C2 - C1}{T2 - T1}\right)\left(\frac{1}{Cc}\right)\right] \tag{9}$$

Where, C2 = Concentration of glucose present at time (T2), C1 = Concentration of glucose present at time (T1) and Cc = Cell count.

3.4.2. Lactate assay

Samples were collected every 20 min and the lactate concentration was analyzed using a colorimetric assay kit (Biovision, Inc; Catalog #K606-100). Samples were collected simultaneously while performing the glucose assay. A sample of 4 µL was diluted by adding 16µL of assay buffer solution and 2µL of the diluted sample was further diluted to total volume of 50µL/well.

The lactate standard curve was prepared by diluting the lactate standard to 1nmol/µL by adding 10µL of the lactate standard to 990µL of lactate assay buffer and it was mixed well. Various volumes, namely 0, 2, 4, 6, 8 and 10 µL of the above solution were added into each well individually. The volume was adjusted to 50µL/well with glucose assay buffer to generate 0, 2, 4, 6, 8 and 10 nmol/well of the lactate standard.

Sufficient reagents for the number of assays to be performed were pre-mixed. For each well, a total 50µL reaction mix was prepared by adding 46µL lactate assay buffer, 2µL lactate probe and 2µL lactate enzyme mix. Then 50µL of lactate reaction mix was added to each well so that each well totaled 100µL in volume. The plate/reaction was then placed in the incubator at 37^0C for 30 min. The absorbance was measured at 570nm using as Synergy HT mulitwell plate reader (BioTek Instruments, Inc.). A calibration curve was performed simultaneously and the background was corrected using the blank (Figure 5).

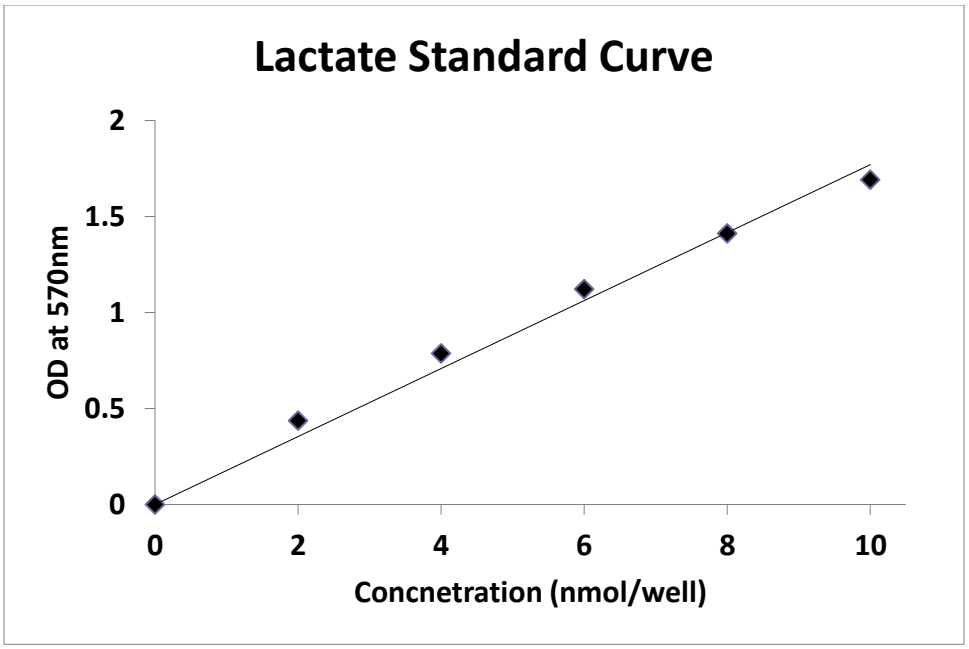

Figure 5: Lactate assay standard curve

Calculation of the Unknown concentration using linear trend:

$$C = \frac{Sa \times D}{Sv} \tag{10}$$

Where, C = Actual concentration from the graph; Sa = Sample amount (in nmol) from standard curve; Sv = Sample volume added to the sample wells; D = Dilution factor

Calculation of Flux per minute per cell (Fmc),

$$Fmc = \left[\left(\frac{C2 - C1}{T2 - T1}\right)\left(\frac{1}{Cc}\right)\right] \tag{11}$$

Where, C2 = Concentration of glucose present at time (T2), C1 = Concentration of glucose present at time (T1) and Cc = Cell count.

3.4.3. ATP assay

On day 4, differentiation medium was replaced with the either fresh or drug containing medium. Cells were incubated and samples were collected for every 20 min and 60 min. Cells were rinsed twice and collected by trypsinization. The detached cells were resuspended in extracellular solution and cell count was performed. Cells were centrifuged and 100uL of ATP assay buffer was added to the cells followed by adding 20 µL of PCA and 5 µL of neutralization solution (Deproteinizing Sample Preparation Kit, Biovision, Inc, Catalog#: K808-200). The sample was then frozen until all the remaining samples were collected. 50 µL of the sample was analyzed using the ATP assay kit (Biovision, Inc; Catalog #K354-100).

The ATP standard curve was prepared by diluting the ATP standard to 1nmol/µL by adding 10µL of the ATP standard to 990µL of ATP assay buffer. Various volumes, namely 0, 2, 4, 6, 8 and 10 µL of the above solution was added into each well individually. The volume was adjusted to 50µL/well with ATP assay buffer to generate 0, 2, 4, 6, 8 and 10 nmol/well of the ATP standard.

Reagents for the number of assays to be performed were pre-mixed. For each well, a total 50µL reaction mix was prepared by adding 44µL ATP assay buffer, 2µL ATP probe, 2µL ATP developer min and 2µL ATP converter. Then 50µL of ATP reaction mix was added to each well so that each well totaled 100µL in volume. The plate/reaction was then placed in the incubator at 37^0C for 30 min. The absorbance was measured at 570nm using as Synergy HT mulitwell plate reader (BioTek Instruments, Inc.). The calibration curve was performed and the background was corrected by subtracting the value from the 0 lactate control from all readings

(Figure 6).

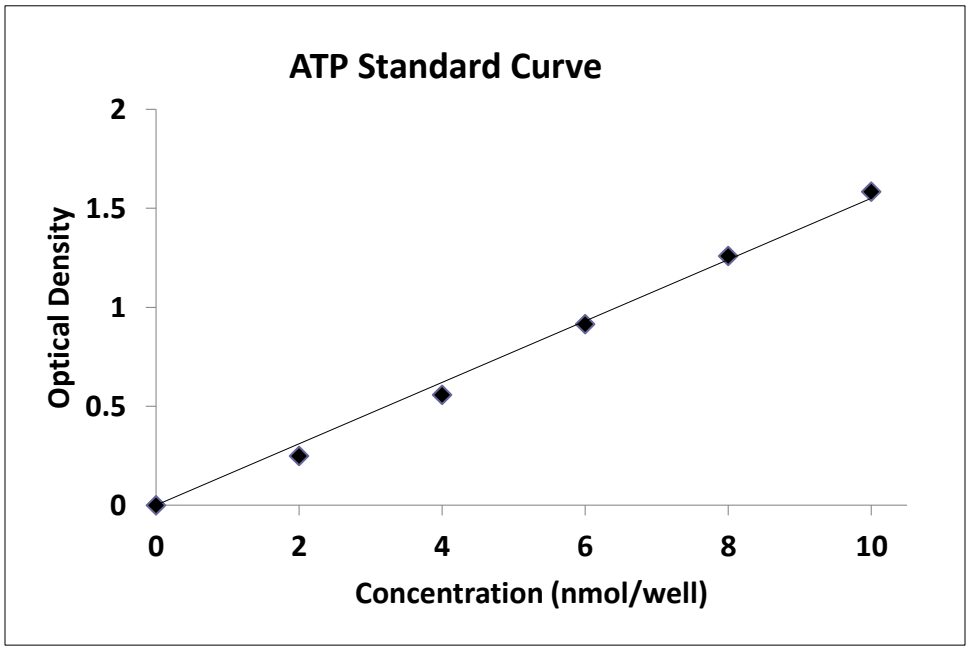

Figure 6: ATP assay standard curve

Calculation of the ATP concentration(C) using linear trend:

$$C = \frac{Sa \times D}{Sv} \tag{12}$$

Where, C = Actual concentration from the graph, Sa = Sample amount (in nmol) from standard curve, Sv = Sample volume added to the sample wells, D = Dilution factor, Total cell volume = number of cells × cell volume.

Dilution factor (D) was calculated as,

$$D = \frac{Total\ cell\ volume}{Total\ cell\ volume + PCA + Neutalization\ solution} \tag{13}$$

3.4.4. ADP assay

An ADP assay was performed in parallel with the ATP assay. On day 4, differentiation medium was replaced with either fresh or drug containing medium. Cells were incubated and samples were collected for every 20 min and 60 min. Cells were rinsed twice and collected by trypsinization. The detached cells were resuspended in extracellular solution and cell count was performed. Cells were centrifuged and 100µL of ADP assay buffer was added to the cells followed by adding 20µL of PCA and 5µL of neutralization solution (Deproteinizing Sample Preparation Kit, Biovision, Inc, Catalog#: K808-200). The sample was then frozen until all the remaining samples were collected. 50uL of the sample was analyzed using the ADP assay kit (Biovision, Inc; Catalog #K355-100).

The ADP standard curve was prepared by diluting the ADP standard to 1nmol/µL by adding 10µL of the ADP standard to 990µL of ADP assay buffer and it was mixed well. Various volumes, 0, 2, 4, 6, 8 and 10 µL, of the above solution was added into each well individually. The volume was adjusted to 50µL/well with ADP assay buffer to generate 0, 2, 4, 6, 8 and 10 nmol/well of the ADP standard.

Required quantity of reagents for the number of assays to be performed was pre-mixed. For each well, a total 50µL reaction mix was prepared by adding 44µL ADP assay buffer, 2µL ADP probe, 2µL ADP developer min and 2µL ADP converter. Then 50µL of ATP reaction mix was added to each well so that each well totaled 100µL in volume. The plate/reaction was then placed in the incubator at 37^0C for 30 min. The absorbance was measured at 570nm using as Synergy HT mulitwell plate reader (BioTek Instruments, Inc.). The calibration curve was

performed and the background was corrected by subtracting the value from the blank from all readings (Figure 7).

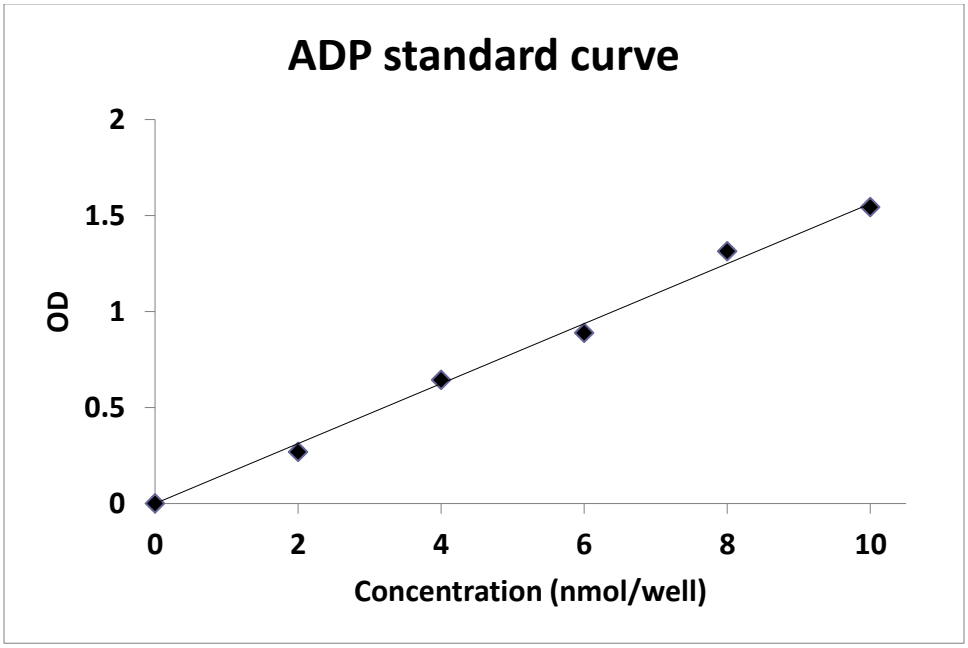

Figure 7: ADP assay standard curve

Calculation of the ADP concentration(C) using linear trend:

$$C = \frac{Sa \times D}{Sv} \tag{14}$$

Where, C = Actual concentration from the graph; Sa = Sample amount (in nmol) from standard curve; Sv = Sample volume added to the sample wells; D = Dilution factor; Total cell volume = number of cells × cell volume.

Dilution factor (D) was calculated as,

$$D = \frac{Total\ cell\ volume}{Total\ cell\ volume + PCA + Neutalization\ solution} \quad (15)$$

3.5. Patch clamp electrophysiology

Patch clamp electrophysiology was performed on the NG108-15 cells to collect parameters for the model. Whole cell recordings were performed to assess changes in cellular membrane electrical activity. The instrumentation and the methodology to record cellular electrical activity are described in the following sections.

3.5.1. Instrumentation

The experimental setup for performing patch clamp electrophysiology is shown in figure 2A. It consists of a a Zeiss Axioscope 2 FS plus upright microscope (Figure 8B) which was mounted on a Gibraltar platform with motors for movement in X and Y directions (Figure 8B). The whole system was mounted on a vibration-isolation table to avoid unwanted vibrations during recording. A Faraday cage was also installed round the system and grounded to protect the interior against external electric fields and electrostatic discharges. Micromanipulators were used to precisely manipulate the patch pipette at a micrometer resolution. The pipette holder was attached to the headstage (Figure 2B) and was also equipped with a flexible tube to control pressure.

The electrodes were prepared using a Shutter 97 pipette puller (BF150-86-10; Sutter, Novato, CA) as shown in Figure 8B. The voltage clamp and current clamp measurements were performed on a Multiclamp 700B amplifier (Axon Instrument, Foster City, CA, USA) as shown in

Figure 2C. An Axon Digidata 1322A (Figure 8C) interface was used to filter the signals at 2 kHz and digitized at 20 kHz. The probe from Axon Digidata 1322A was connected to the micromanipulators and pipette holder. All data acquisition was performed using pClamp 10 software (Axon Instruments, Foster City, CA, USA).

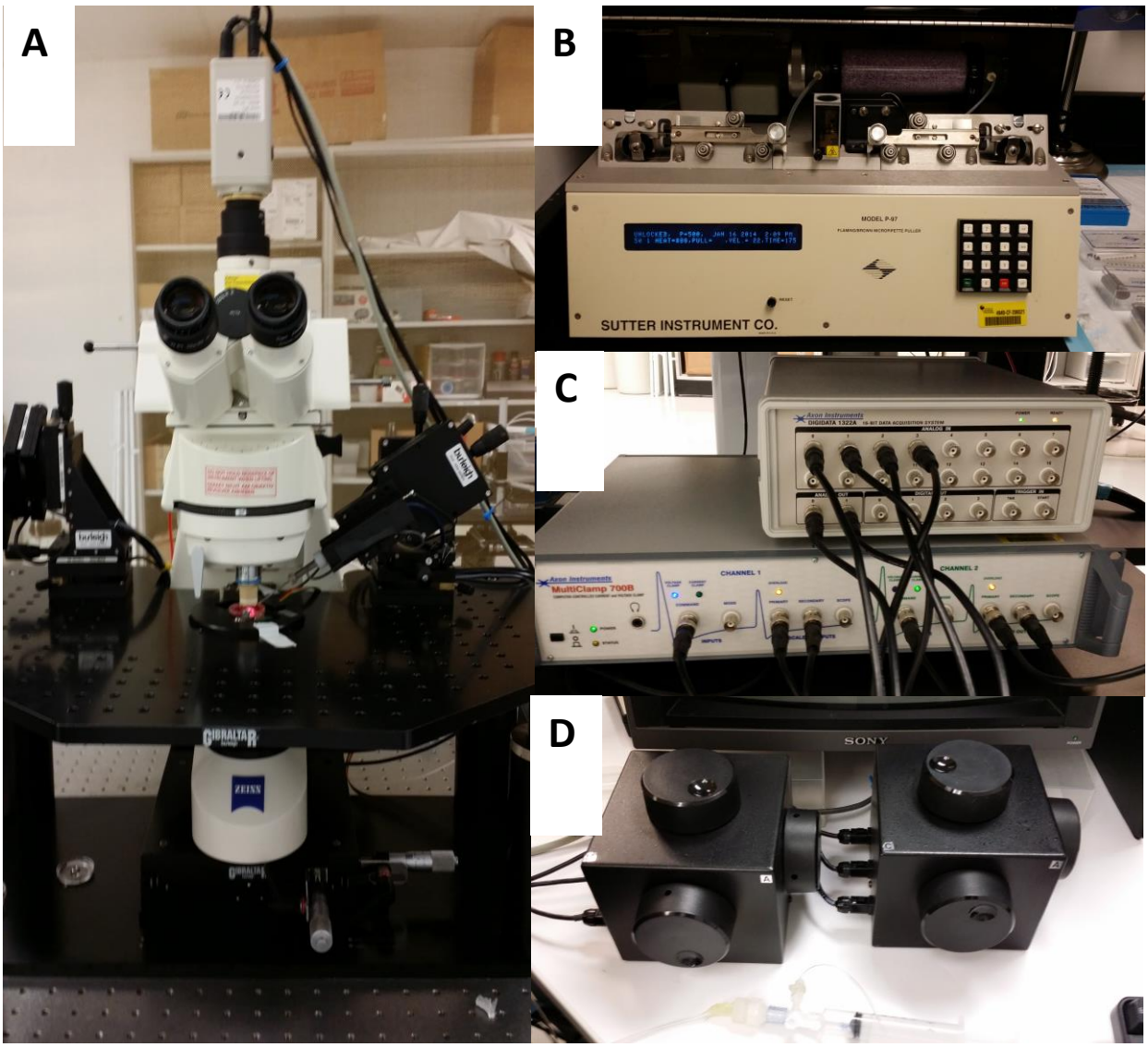

Figure 8: Set up of the electrophysiology rig having the microscope mounted on a gibraltor stage (A). Pipette puller (B), Amplifier (C), micromanipulator (D) is also shown

3.5.2. Whole cell recordings

Whole-cell patch recordings were performed on the stage of a Zeiss Axioscope 2 FS Plus upright microscope (Axiovert 200, Carl Zeiss, Göttingen, Germany). The recordings were obtained at room temperature (21-25 ^{o}C) in the recording chamber containing differentiation medium. The recording chamber was continuously perfused with the differentiation medium. To investigate the effect of the drugs on action potential, metabolic inhibitors were added to the medium. Patch pipettes (4–6 MΩ resistance) were prepared from borosilicate glass with a Sutter P97 pipette puller and filled with intracellular solution.

The cell to be patched was observed under a 40X objective. The electrode was positioned till the tip was bright on the monitor and immerse in the patch chamber (Figure 9). The pipette offset was compensated. The objective was lowered followed by the electrode until one could see the electrode was above the cell (Figure 10). The Seal Resistance was recorded and the electrode was pushed towards the cell membrane. The pipette then touched the cell and an increase of 0.5mohms was observed. The initially applied pressure was removed and gentle suction was applied by mouth. If required, constant pressure was applied to form a seal. The image of the cell was saved. A holding potential of -70mV (in Multiclamp) was applied to form the gigaohm seal. The leakage current on the amplifier was less than 30pA. The gigaohm-seal formed was recorded and the pipette capacitance (fast & slow) was compensated. A short slight suction 'Kiss' was applied to open the cell membrane and the capacitive transient was observed. The membrane resistance was recorded and the seal test window was switched off.

The membrane potential was checked by switching to I=0 mode. The whole cell

parameters (click Auto) followed by leak subtraction (auto) were compensated. The stability of the patch was checked by clicking on membrane test and results were saved. The gain and Bessel were set to 5 and 3 respectively. The ionic currents were measured in voltage clamp mode using 10mV voltage steps from a holding potential of -85mV. By holding the voltage constant the changes in current was measured in voltage clamp mode. A p/6 protocol was implemented upon compensating for the whole cell capacitance and series resistance. The access resistance of the patched cells was less than 20 MΩ. Experimental parameters such as membrane resistance, membrane capacitance, resting membrane potential and injected stimulus current were noted. The protocol in clampex was then initiated. The membrane test was again performed and the results were saved.

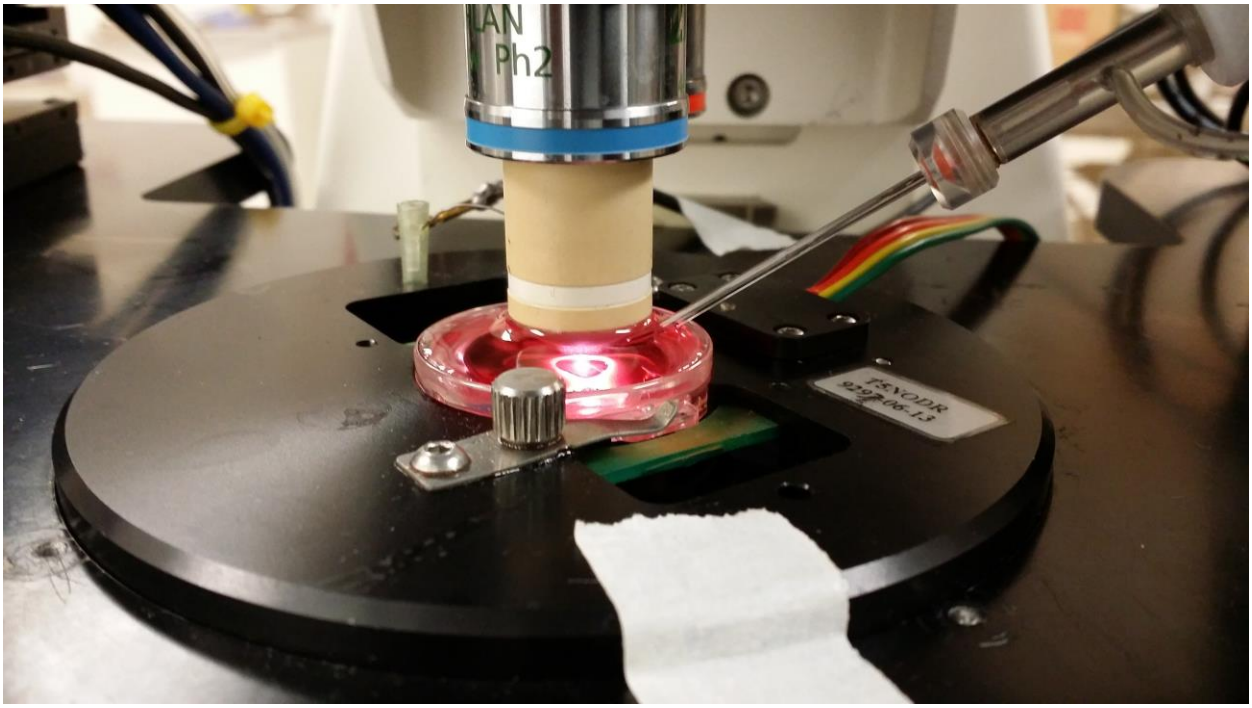

Figure 9: An image showing the glass electrode, ground electrode, patching chamber, objective lens on an electrophysiology rig

The action potentials were recorded by switching to IC mode and by compensating for bridge balance. The holding current was adjusted to get a membrane potential of -70mV. A 2 ms depolarizing current injections was injected to initiate action potentials. The perfusion system was switched to add the drug. The APs were continuously recorded until either the patch was lost or the cell could no longer generate an AP. The membrane test was checked and results were saved.

Figure 10: Picture of NG108-15 cell during electrophysiological recording

A voltage clamp recording was again performed at the end to see the effects of drugs on VC recording. All the recordings were corrected for a junction potential that developed during the interface between the patch electrode and the bath solution. The Multiclamp 700B files were also saved for extraction of any other parameters, if necessary. Data was saved and imported into MATLAB using a custom code for parameter estimation.

CHAPTER-4: MODEL DEVELOPMENT

The neuronal-metabolic model was built in a top-down approach by integrating the ensemble metabolic model to a modified Hodgkin Huxley based neuronal module. The models were implemented with physiological compartments, including physiological volumes. The metabolic compartments were nested in the cytosolic volume and the total cellular volume was nested in the extracellular volume. The compartments were implemented as volumetric ratios as shown in Table 3.

Table 3: Volumetric ratios of nested cellular compartments

Compartment	**Volumetric ratio**	**Reference**
Total Intracellular volume	1	Estimated
Bulk cytosolic space	0.65	[70]
Sub-cellular space	0.02	[70]
Mitochondria	0.05	[71]
Endoplasmic reticulum	0.1	Estimated
Others (Nucleus, Lysosomes)	0.28	Estimated

A modular approach was utilized during model reconstruction. The model development was completed in 3 major developmental stages, (1) reconstruction of a neuronal metabolism, (2)

development of neuronal module and (3) the integration of models for predicting effects of metabolic perturbations. Each of these modules is described in the following sections.

4.1. Reconstruction of metabolic model

The metabolic module for NG108-15 cells includes the core metabolic pathways for carbon metabolism and cellular bioenergetics and was reconstructed by combining glycolysis [72], mitochondria [59] and endoplasmic reticulum [73,74] modules. The model was reconstructed in MATLAB Simbiology. Simbiology allows for rapid expansion of the model by facilitating the addition of other cellular processes through Systems Biology Markup Language (SBML). It also provides access to several solvers for simulation of dynamic models of cellular process. The equations can be programmed directly in MATLAB but Simbiology enables us to implement it in a graphic user-interface (GUI) by creating a diagram for visualization. The data can be imported and exported easily from Simbiology. Moreover, it is backed up by the entire MATLAB suite which can help perform various analyses using any custom code. A detailed list of reactions, fluxes, parameters and metabolite concentrations are depicted in the Appendix.

4.1.1. Glycolysis model

The glycolysis module was adapted from a comprehensive model of energy and redox metabolism for human erythrocytes [58]. This mathematical model converts glucose to lactate through a series of 13 reactions, from hexokinase to lactate dehydrogenase via 2,3-biphosphoglyceate shunt involving 19 reactants (Figure 11). Glycolysis requires oxidized Nicotinamide adenine dinucleotide (NAD^+) and reduced Nicotinamide adenine dinucleotide

(NADH). The NADH is utilized by the cells and is recycled back to NAD^+. Several reactions are capable of performing this conversion and one of them is the lactate dehydrogenase (LDH) that converts pyruvate into lactate. The lactate is then transported out of the cell via the monocarboxylate transporters (MCT). The MCT's are also equipped to transport pyruvate.

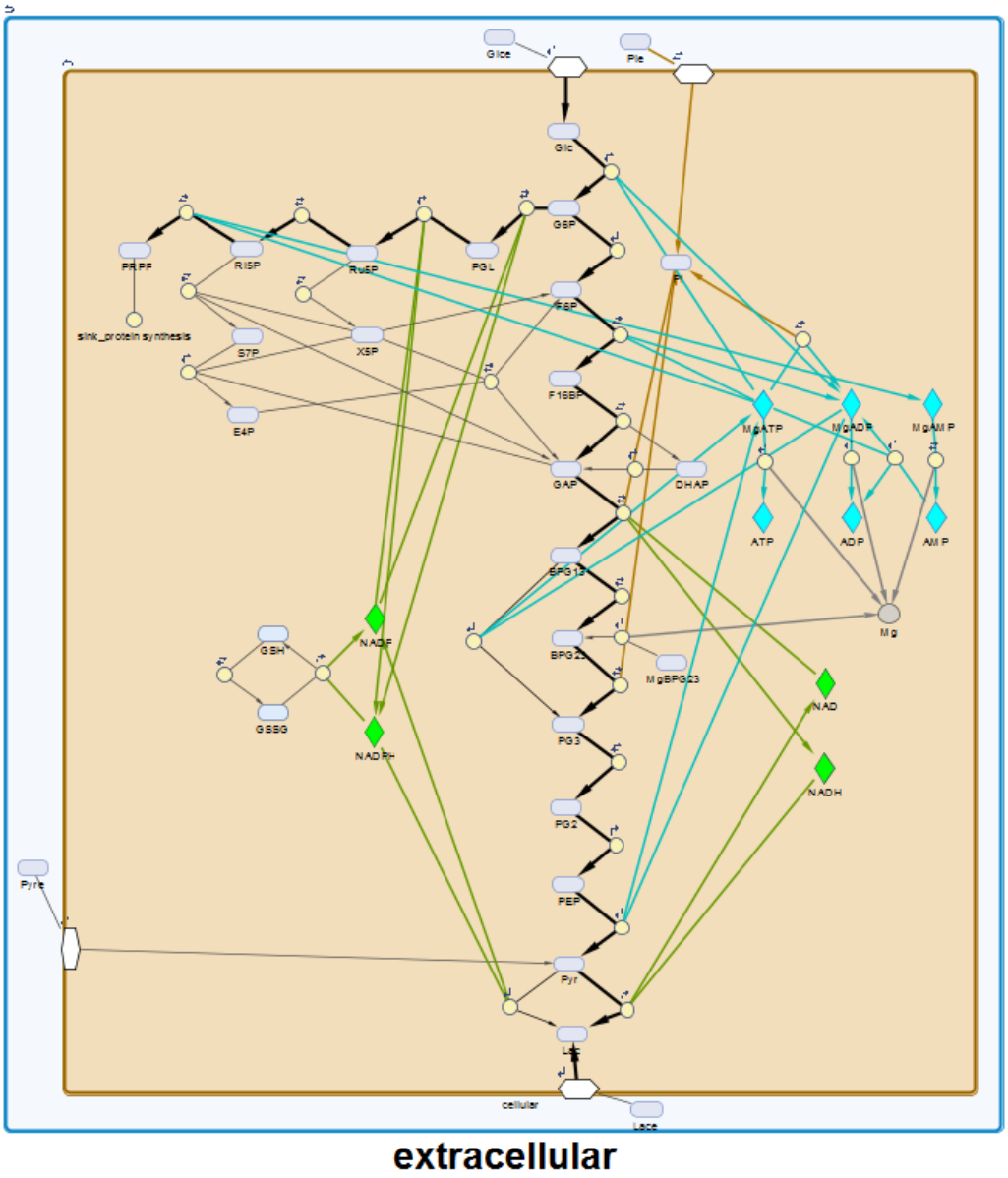

Figure 11: Glycolytic module consisting of glycolysis, pentose phosphate pathway and glutathione

In addition, the glycolytic module also contains ten other reactions that include glutathione oxidation, glutathione reduction and pentose phosphate pathway (PPP). The glutathione reduction and oxidation dictates the conversion of Nicotinamide adenine dinucleotide phosphate (NADPH) to NADP thereby influencing the lactate dehydrogenase enzyme activity. The glutathione process has been lumped together into a generalized reaction. A sink for phosphoribosylpyrophosphate (PRPP) has been included for the consumption of carbon entering the PPP to avoid the accumulation of intracellular metabolites. The ATP dependent exchangers were incorporated and calibrated to match the activities obtained from the neuronal module. A generalized ATP consumption reaction has been implemented to represent all the other ATP utilizing pathways. The total adenine concentration has been maintained constant by including the conservation condition and an adenine kinase reaction that mediates the conversion of ADP to AMP and ATP [72]. The total adenine nucleotides including the NAD^+ and NADH, NADP and NADPH and FAD^+ and $FADH_2$ were held constant. The temporal behavior of the metabolite concentration is based on ordinary differential equations. All the rate equations have a general form as described in equation 16,

$$v = V_{max} \times r(X) \times \left(\prod_i x_i^{c^+{}_{ij}} - \frac{1}{q} \prod_i x_i^{c^-{}_{ij}} \right) \tag{16}$$

Where c^+ and c^- are the positive and negative elements of the stoichiometric matrix, q is the equilibrium constant and r(X) is the regulatory function for saturation, allostery, etc [58]. Earlier models have described the HK, PFK, PK, DPGM, DPG, G6PD, 6PGD and GSSR to be completely irreversible. An increase of backward fluxes by several orders of magnitude due to high

accumulation of metabolites was avoided by using rate equations based on equation 16. The equilibrium constants and kinetic equations were taken from several other sources [58]. The equations for AK, PGK and enolase were based on data from previously published results [58]. AK and PGK were considered to have a random BiBi mechanism. PGM and enolase are based on an UniUni mechanism [58].

4.1.2. Mitochondrial model

The mitochondrial model was adapted from a cardiac mitochondrial metabolism model and consists of 22 reactions involving 27 reactants [59]. The total mitochondrial volume was set to be 5% of the total cell volume [71]. The model incorporates the main mitochondrial electrophysiological and metabolic process including the oxidative phosphorylation and matrix-based process in mitochondria (Figure 12). The reaction rates of the enzymes in the TCA cycle namely, citrate synthase, isocitrate dehydrogenase, α-ketoglutarate dehydrogenase and malate dehydrogenase have been implemented as described and implemented as described by Cortassa et al [59]. Sensitivity to calcium is also incorporated for IDH and KDGH. The TCA cycle in the model can be divided into two pathways, the tricarboxylate (oxaloacetate to α-ketoglutarate) and the dicarboxylate (α-ketoglutarate to oxaloacetate) pathway. Acetyl-CoA and oxaloacetate react and produce α-ketoglutarate (αKG), NADH, and CO_2. αKG serves as a substrate of the dicarboxylate pathway producing OAA that resupplies and initiates the tricarboxylate pathway.

The mitochondrial model involves the complete oxidation of acetyl CoA to generate NADH and ATP. Acetyl CoA is the point of convergence for carbohydrate, amino acid and fatty

acid metabolism. The oxidation of acetyl CoA produces NADH and FADH2, which are oxidized to propel oxidative phosphorylation. The model includes both the explicit electrical gradient ($\Delta\Psi_m$) and the proton gradient across the mitochondrial inner membrane established by oxidative phosphorylation. The protons from NADH and $FADH_2$ are oxidized pumping protons across the mitochondrial inner membrane establishing a proton motive force and proton gradient. The large $\Delta\Psi_m$ of the inner mitochondrial membrane determines the electrochemical transport of ions across, including calcium influx and efflux. The proton motive forces drive the phosphorylation of matrix ADP to ATP by F_1F_0-ATPase. The F_1F_0-ATPase activity accounts for the reversibility of the enzyme when the $\Delta\mu_H$ collapses.

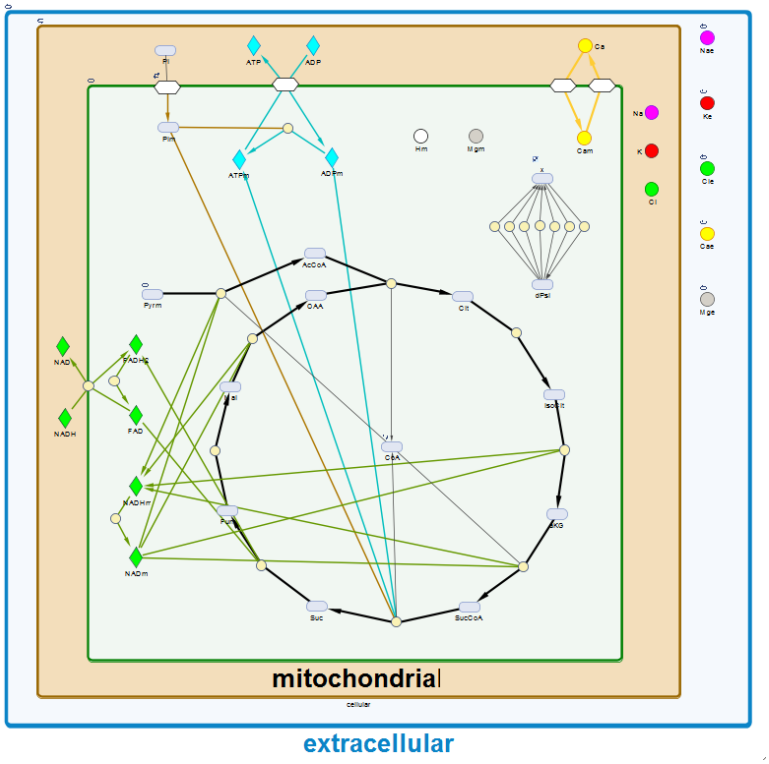

Figure 12: Diagram showing mitochondrial module in Simbiology

The Adenine Nucleotide Transporter (ANT) transports the ATP from the inner

membrane of the mitochondria to the cytosol and reaction was implemented. The model also incorporates a proton leak that influences the mitochondrial membrane potential and proton motive force that follows a thermokinetic formulation. The mitochondrial membrane potential is determined by,

$$\frac{\mathrm{d}\Delta\Psi_{\mathrm{m}}}{\mathrm{dt}} = \frac{V_{He} + V_{He(F)} - V_{Hu} - V_{ANT} - V_{H_{leak}} - V_{NaCa} - 2V_{uni}}{C_{mito}} \quad (17)$$

Where, $V_{He}, V_{He(F)}, V_{Hu}, V_{ANT}, V_{H_{leak}}, V_{NaCa}\ and\ V_{uni}$ are the rates of NADH oxidation, FADH2 oxidation, F_1F_0-ATPase , adenine nucleotide transporter, sodium-calcium exchanger and calcium uniporter. The redox (Ares), phosphorylation (AF1) potentials and the proton motive force ($\Delta\mu_H$) are the driving forces. The coefficients in the equations and the rate constants of are obtained from Cotrassa et.al [59]. In addition, the model considers the explicit dependence of the TCA cycle dehydrogenases on mitochondrial calcium concentration. The influx of calcium through the Ca^{+2} uniporter and the Na-dependent Ca^{+2} efflux driven by Na^{+}/Ca^{+2} antiporter determines the mitochondrial calcium concentration. The phosphate transport into the mitochondria also has the general form described in equation 16.

4.1.3. Endoplasmic reticulum Model

The endoplasmic reticulum (ER) model was included to study the effect of calcium on cellular dynamics. The ER model consists for the IP_3 receptor, sarcoplasmic reticulum calcium ATPase (SERCA) and a calcium leak (Figure 13). These pumps were implemented as described in Chen et.al [74]. The activation/inhibition of the general plasma membrane receptor has been coupled with the activation of phospholipase C (PLC), which converts phosphatidylinositol 4,5-

biphosphate (PIP2) to inositol 1,4,5-triphosphate and diacylglycerol (DAG). The rate equation for the hydrolysis of PIP_2 and IP_3 and DAG by PLC was implemented using Michaelis-Menten kinetics and multiplied by its Boolean value. Therefore, when the Boolean value is zero, the reaction rate is zero, and when the Boolean value is one, the reaction rate is given by equation 18,

$$v = V_m * \left(\frac{[PIP_2]}{K_m + [PIP_2]}\right) \tag{18}$$

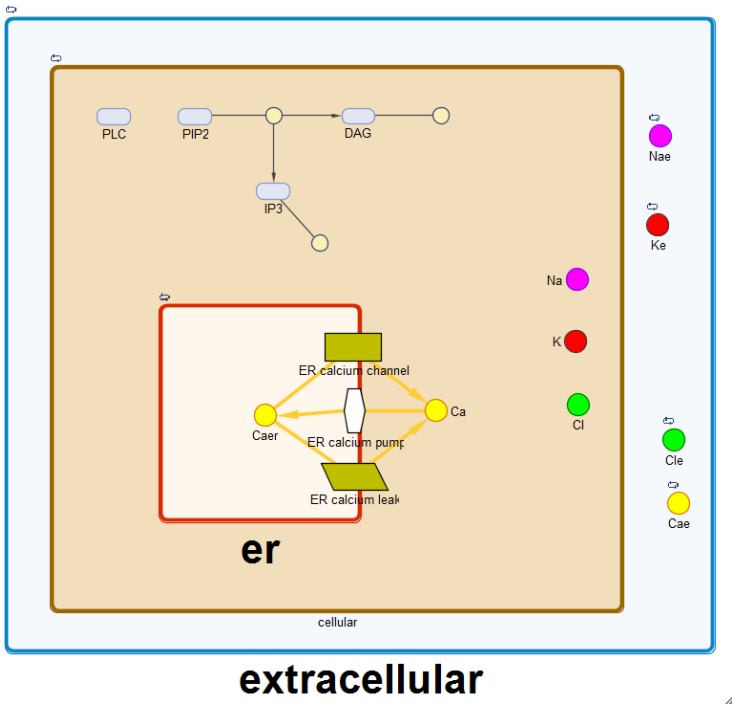

Figure 13: Implemented endoplasmic reticulum module in Simbiology

A simple rate equation was implemented for IP_3 and DAG consumption, which used mass action kinetics IP_3 then, activates IP_3R calcium channels on the endoplasmic reticulum membrane, through which endoplasmic reticulum calcium is released into the cytosol. While the flux of calcium to and from the mitochondria has been addressed by the implementation of

the mitochondrial metabolism model [59], the ER calcium flux has been addressed by implementing reactions as described in Marhl et al. [73]. The IP_3 calcium channel kinetics was modified as described by Chen et al and includes a dependence of IP_3 that was absent in the channel reaction rate as described by Marhl et al.

4.1.4. Ensemble metabolic model

The glycolysis and the mitochondrial model were coupled by including the reactions for pyruvate transport into mitochondria followed by conversion of acetyl Co-A by pyruvate dehydrogenase (Figure 14). The rate equation for pyruvate transport into mitochondrial space had the general form previously described in equation 16,

$$v = V_{max}\left([Pyr]_{cell} - \frac{[Pyr]_{mito}}{K_{eq_{PT}}}\right) \tag{19}$$

Where, $K_{eq_{PT}}$ is the equilibrium constant for pyruvate transport, $[Pyr]_{Mito}$ and $[Pyr]_{cell}$ are the concentrations of pyruvate in the mitochondria and cytosol. The rate equation for pyruvate dehydrogenase was implemented using the irreversible mass action kinetics as described by Nazaret et al. [75] and is shown below.

$$v = K_{PDH}\left([Pyr]_{Mito} - \frac{[AcCoA]_{mito}}{K_{eq_{PDH}}}\right)[CoA]_{mito}\,[NAD]_{mito} \tag{20}$$

Where, K_{PDH} is the Michaelis constant for PDH, $K_{eq_{PDH}}$ is the equilibrium constant for PDH, $[Pyr]_{Mito}$, $[AcCoA]_{mito}$, $[CoA]_{mito}$and $[NAD]_{mito}$are the concentrations of pyruvate, Acetyl-CoA, CoA and NAD in mitochondria.

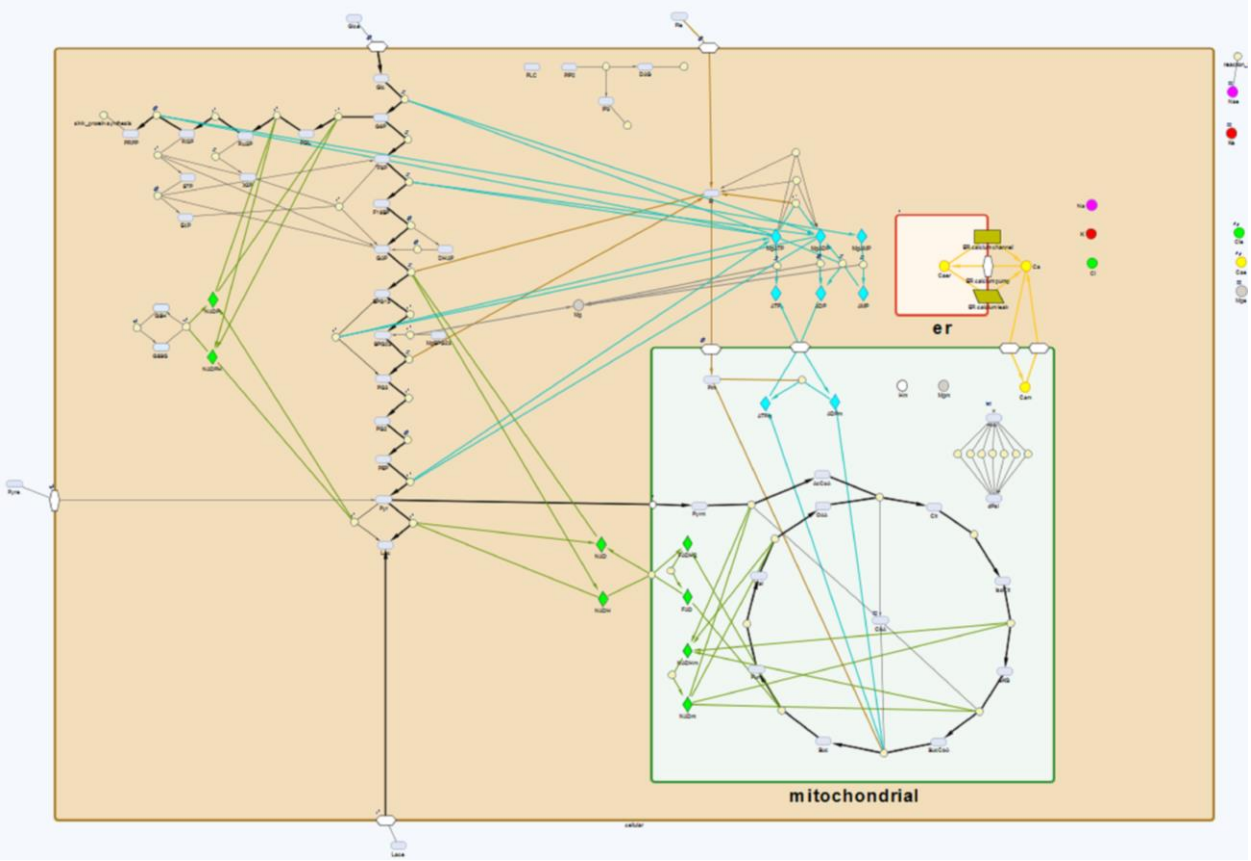

Figure 14: Reconstructed NG108-15 metabolic model in MATLAB Simbiology

The Glycerol-3 Phosphate (G3P) shuttle for transferring the NADH equivalents into the mitochondria was incorporated using irreversible mass action kinetics. The shuttle is irreversible and not as efficient as the malate-aspartate shuttle (MAS). It can generate only 1.5 ATP compared to 2.5 ATP transferred by MAS [51]. The reducing equivalents of NADH are transferred to glycerol-3 phosphate which is converted to dihydroxyacetone phosphate on the mitochondrial membrane by mitochondrial glycerol-3phosphate dehydrogenase. Thus the reducing equivalents are transferred to FAD to form $FADH_2$ in the mitochondria which are further oxidized to generate the required proton motive force for ATP production.

The cytosolic ATP and ADP levels are linked to the mitochondrial Adenine Nucleotide

Transporter activity. The ATP consumption by the ATP-dependent pumps was incorporated and matched to the activity of that obtained in the neuronal module. The generalized ATPase reaction was also included to represent all the other ATP consuming processes in the cell. The general ATPase reaction will further be categorized upon incorporation of other modules and ATP dependent reactions. The mitochondrial calcium uptake and release was tied to the cytosolic calcium concentration. The cytosolic calcium concentration is again dependent on the calcium fluxes from the endoplasmic reticulum and the neuronal module. The phosphate transport into the cell and mitochondria was implemented based on equation 16.

The cellular volume of NG108-5 cells was calculated using the equation of volume for a sphere. A radius of 22.5µm was used and is within the experimentally observed range published by American Type Culture Collection (ATCC) and also in agreement with the cell volume reported by Dubois el al. [76].

4.1.5. Parameter estimation for metabolism model

The rate equations in the metabolic model contain several parameters such as V_{max}, K_m, K_i etc. The values of the parameters are dependent on mutations, binding of effectors, lack of cofactors, etc.. In the glycolytic module only specific parameters such as the maximum activity V_{max} is considered to alter as it reflects the concentration of the enzymes and the structural modifications of the enzyme [58]. The V_{max}'s for the set of glycolytic, PPP, pyruvate transport and lactate transport reactions were scaled directly. The mitochondrial module has no V_{max}'s but instead the mitochondrial enzyme concentration (E) is altered directly.

The flux of all the reactions in the metabolic reaction was obtained by forcing the model to a steady state. The steady state fluxes were set to obey the flux balance condition as shown below to represent the conservation of mass for reaction system. In steady state, the dependent change of metabolic concentrations in equation 21 is zero. The sundials solver was used with an absolute tolerance of 1.0e-8 and a relative tolerance of 1.0e-5. Sundials solver was recommended by MATLAB for running simulations that use rules and events.

$$\sum_{j=1}^{r} N_{ij}\, V_j = \sum_{j=1}^{r} N_{ij} \left(V_j^{(+)} - V_j^{(-)} \right) = 0 \tag{21}$$

Optimization was performed using built-in MATLAB optimization routines. The function '*fmincon'* computes a constrained minimum of a function by varying the variables within specific bounds. Metabolites fluxes have been included as constraints in FBA. The fluxes of glucose uptake and lactate release were constrained during parameter estimation. The intracellular levels of ATP and ADP were also constrained during flux balance analysis by applying sum of squared residuals.

Model optimization was carried out by applying the weighted least squares fitting method. The least square method minimizes the summed square of residuals. The residuals are the difference between simulated values and experimental values,

$$r_n = S_n - E_n \tag{22}$$

The fit was improved by incorporating an additional scaling factor (weight) in the fitting process. The error estimate with weighted least-squares regression was determined by

$$ssr = \sum_{n} w(r)^2 \tag{23}$$

Where, the simulated flux is given by S and the experimental flux by E. The influence of parameter estimate is response is determined by weight w. An arbitrary weight has been implemented to prioritize parameters during estimation. The algorithm implemented during parameter extraction is shown in Figure 15.

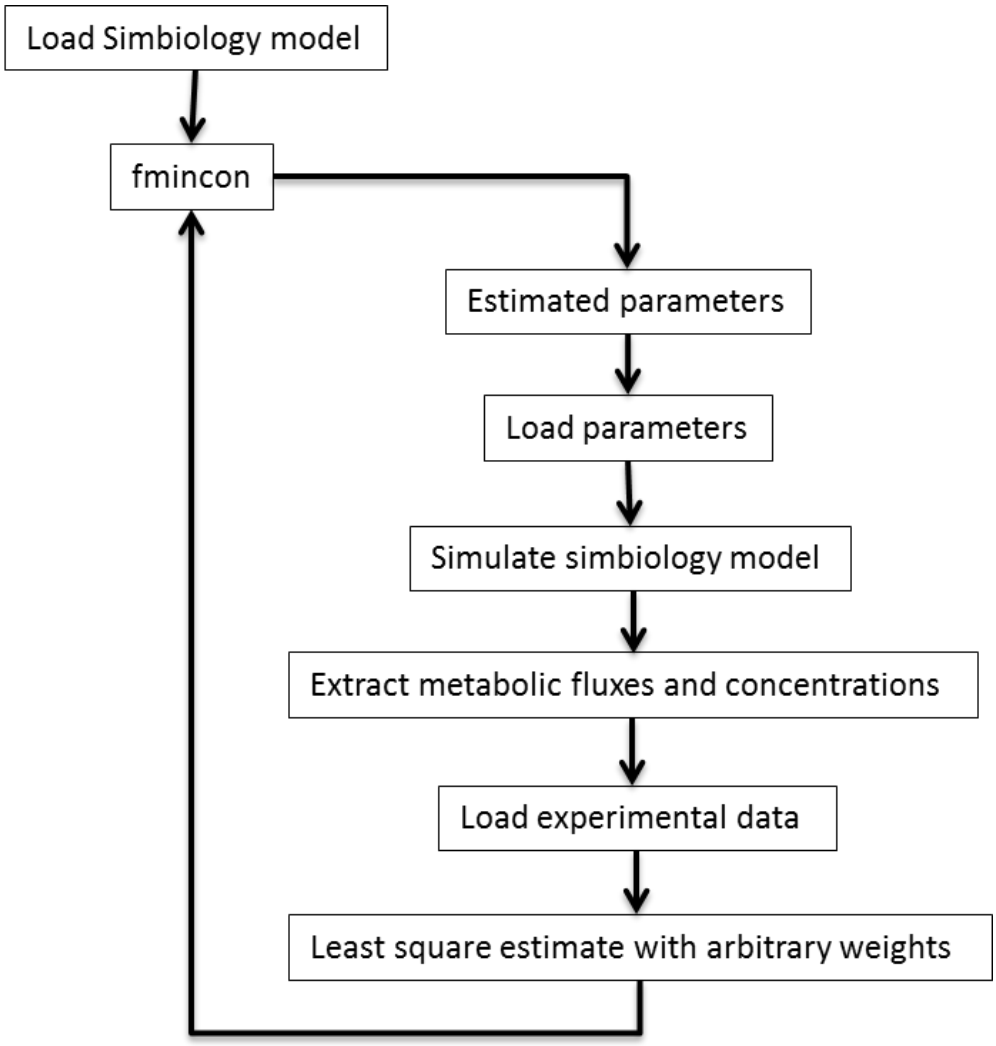

Figure 15: Flowchart for estimation of metabolic model parameters

4.2. Development of neuronal module

The neuronal module was implemented on the cell membrane (Figure 16). The ions move from the extracellular space to the sub-cellular space and from the subcellular space to the bulk cytosol. A modified Hodgkin-Huxley formulation based on incorporating a thermodynamic approach was employed to implement the neuronal module. The rate of change in membrane potential (V_m) was determined using,

$$\frac{dV}{dt} = \frac{-I_{ion} + I_{stim}}{C_m} \tag{24}$$

Where, C_m is the membrane capacitance, I_{stim} is the stimulus current and I_{ion} is the sum of all the ionic currents.

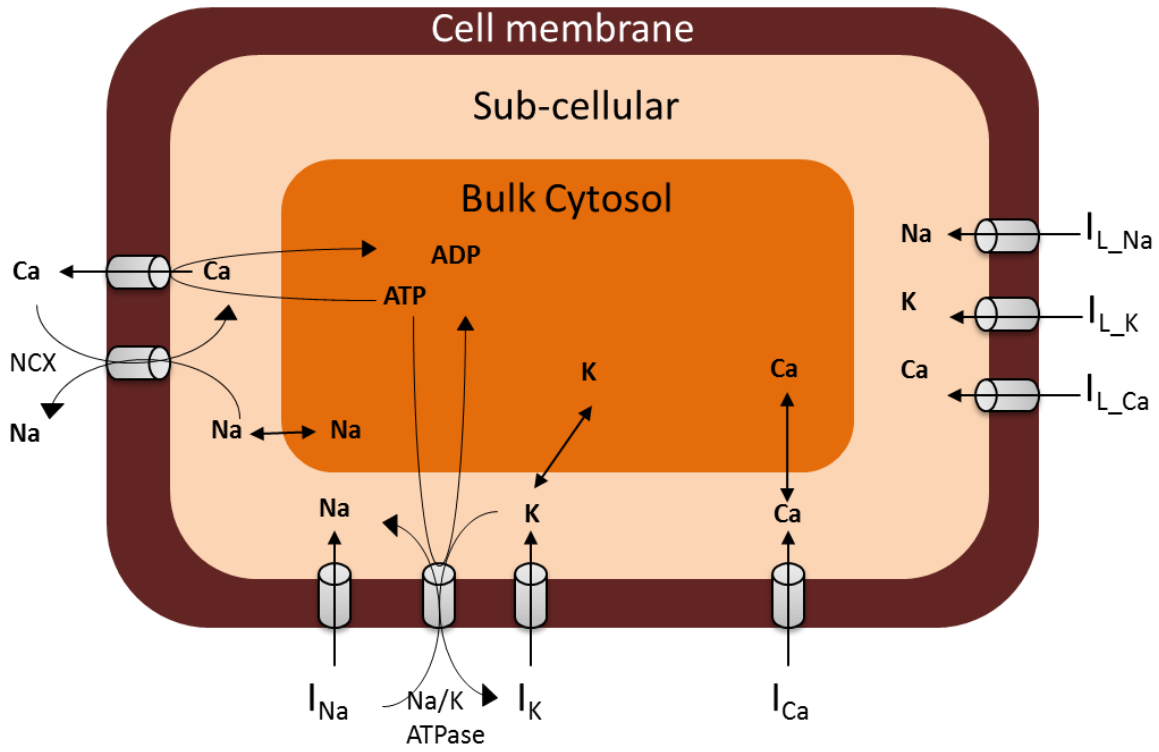

Figure 16: Schematic representation of neuronal module

The total ionic current I_{ion} and the leakage current I_L were defined as,

$$I_{ion} = I_{Na} + I_K + I_{Ca} + I_{K_{ATP}} + I_{NaKATPase} + I_{NCX} + I_{CaATPase} + I_{L_{Na}} + I_{L_K} + I_{L_{Ca}} + I_{L_{Gen}} \quad (25)$$

Where, $I_{Na}, I_K \; and \; I_{Ca}$ is the current generated from the voltage gated sodium, potassium and calcium channels, $I_{K_{ATP}}$ is from ATP-dependent potassium channel, $I_{NaKATPase}$ is from the sodium-potassium exchanger, $I_{CaATPase}$ is from the calcium pump, I_{NCX} is from the sodium calcium exchanger. $I_{L_{Na}} + I_{L_K} \; and \; I_{L_{Ca}}$ are the specific ionic leakages for sodium, potassium and calcium ions. $I_{L_{Gen}}$ represents the general leak. The method for determination of all the ionic currents is described in the following sections.

4.2.1. Voltage gated channels

The voltage gated sodium, potassium and calcium ion channels were implemented using the thermodynamic formulation [27]. These gates are controlled and activated by changes in membrane potential. A simple two state (open/close) formalism is adapted to describe the channel activation and inactivation. The voltage gated ionic currents are given by

$$I_{Na} = g_{Na} m^3 h (V_m - V_{Na}) \quad (26)$$

$$I_K = g_K n^4 (V_m - V_K) \quad (27)$$

$$I_{Ca} = g_{Ca} e^3 (V_m - V_{Ca}) \quad (28)$$

Where g_{Na}, g_K, g_{Ca}, V_{Na}, V_K and V_{Ca} are maximum ion channel conductance and reversal

potentials of sodium, potassium and calcium respectively. The dynamics of gating variables m, h, n, and e with their steady state values m_∞, h_∞, n_∞, and e_∞ as and the respective voltage dependent time constants τ'_S are given by,

$$\frac{dm}{dt} = \frac{m_\infty - m}{\tau_m} \tag{29}$$

$$\frac{dh}{dt} = \frac{h_\infty - h}{\tau_h} \tag{30}$$

$$\frac{dn}{dt} = \frac{n_\infty - n}{\tau_n} \tag{31}$$

$$\frac{de}{dt} = \frac{e_\infty - e}{\tau_e} \tag{32}$$

The voltage dependent steady state parameters and their respective time constants were determined using the general formula,

$$m_\infty = \frac{1}{1 + e^{-zF(V_m - V_{1/2})/RT}} \tag{33}$$

$$\tau_m = \frac{A}{e^{(zF\xi/RT)(V_m - V_{1/2})}\cosh(zF(V_m - V_{1/2})/2RT)} \tag{34}$$

Where, z is relates to the number of moving charges during the opening and closing of the ion channels, $V_{1/2}$ is the half activation/inactivation potential of an ion channel; A is related linearly to the activation or inactivation time constant, ξ is the asymmetric position of the moving charge in the cell membrane, R is real gas constant, F is Faraday's constant, T is temperature, R_m is membrane resistance and V_m is the resting membrane potential.

The reversal potentials were calculated as follows,

$$V_{Na} = 59.16 \log_{10}\left(\frac{[Na]_{out}}{[Na]_{in}}\right) = 65\ mV \tag{35}$$

$$V_K = 59.16 \log_{10}\left(\frac{[K]_{in}}{[K]_{out}}\right) = -85\ mV \tag{36}$$

$$V_{Ca} = \frac{59.16}{2} \log_{10}\left(\frac{[Ca]_{out}}{[Ca]_{in}}\right) = 124\ mV \tag{37}$$

Where the Na^+, K^+ and Ca^{+2} are the intracellular and extracellular ionic concentrations. The resting membrane potential was back calculated from the experimental holding potentials using the reversal potentials and the maximum ionic conductance using equation 38.

$$V_m = \frac{g_{Na}V_{Na} + g_kV_K + g_{Ca}V_{Ca} + g_{leak}V_{leak}}{g_{Na} + g_K + g_{Ca} + g_{leak}} \tag{38}$$

4.2.2. ATP dependent potassium channel

An ATP-dependent potassium channel was incorporated and is activated when the cellular ATP decreases. The equation has been adapted from Cunningham et al. [77] and is defined as,

$$I_{K_{ATP}} = g_{K_{ATP}}\, z(V_m - V_K) \tag{39}$$

$$z = \frac{1}{1 + \left(\frac{[ATP]}{k_{12}}\right)^{\gamma}} \tag{40}$$

Where, $g_{K_{ATP}}$ is the maximum conductance of z is the gating variable, [ATP] is the ATP

concentration, k_{12} is 0.06, V_K is the reversal potential of potassium and the hill coefficient (γ) is 1.

4.2.3. ATP dependent sodium-potassium pump

The sodium potassium exchanger has been implemented as described by Kager et al. [78] to restore the balance for sodium and potassium ions. The pump contributes an electrogenic factor as it transports 3 Na^+ in exchange for 2 K^+ by consuming ATP. The ATP dependence was incorporated for ATP consumption and to determine its activity based on changes in intracellular ATP levels [79].

$$A_{pump} = \left(\left(1 + \frac{K_{mK}}{[K_o]}\right)^{-2}\right) \times \left(\left(1 + \frac{K_{mNa}}{[Na_i]}\right)^{-3}\right) \times \left(\left(1 + \frac{K_{ATP}}{[ATP]}\right)^{-1}\right) \quad (41)$$

$$I_{K_{ATPase}} = -2 * I_{max}^{NKA} * A_{pump} \quad (42)$$

$$I_{Na_{ATPase}} = 3 * I_{max}^{NKA} * A_{pump} \quad (43)$$

The pump is modeled using the above modified rate equation where K_{mK} is 3.5 mM/L, K_{mNa} of 10 mM/L and K_{ATP} = 5 mM [78,79]. I_{max}^{NKA} is the maximal flux generated by the pump to compensate the leaks and other pumps to obtain a steady state at rest. The literature reported value for I_{max}^{NKA} is 0.013 mA/cm^2[78].

4.2.4. Sodium-calcium exchanger

The sodium calcium exchanger (NCX) transports 3 Na^+ in exchange for Ca^{+2} and is electrogenic. The exchanger was implemented using the formulation as described by

Courtemanche et al. [80,81].

$$K_b = e^{\left(\frac{\gamma V_m F}{RT}\right)} \tag{44}$$

$$K_{qa} = e^{\left(\frac{(\gamma-1) V_m F}{RT}\right)} \tag{45}$$

$$A_{NCX} = \frac{([Na]_i^3 \times [Ca]_o \times K_b) - \left([Na]_o^3 \times [Ca]_i \times K_{qa}\right)}{\left(K_{m_{Na}}^3 + [Na]_o^3\right)\left(K_{m_{Ca}} + [Ca]_o\right)\left(1 + 0.1K_{qa}\right)} \tag{46}$$

$$I_{Na_{NCX}} = -3 * I_{max}^{NCX} * A_{NCX} \tag{47}$$

$$I_{Ca_{NCX}} = 2 * I_{max}^{NCX} * A_{NCX} \tag{48}$$

Where, $K_{m_{Na}}$ is 87.5 mM, $K_{m_{Ca}}$ is 1.38 mM, I_{max}^{NCX} is the maximal flux, and the voltage dependence parameter γ is 0.35.

4.2.5. ATP dependent calcium pump

The ATP dependent calcium pump has been incorporated as described by Kager et al. [81]. The ATP dependence was incorporated to calculate ATP consumption.

$$A_{Caatp} = \left(\left(1 + \frac{K_{mCa}}{[Ca_i]}\right)^{-1}\right) \times \left(\left(1 + \frac{K_{m_{ATP}}}{[ATP]}\right)^{-1}\right) \tag{49}$$

$$I_{Ca_{ATPase}} = I_{max}^{Caatp} * A_{Caatp} \tag{50}$$

Where, K_{mCa} is 6.9 μM [81] and $K_{m_{ATP}}$is 2.5 mM (estimated). I_{max}^{Caatp} is the maximal flux for the Ca-ATPase pump and is estimated to simulate steady state.

4.2.6. Leakages

Specific ionic leakages were implemented as described by Kager et al. [78].

$$I_{L_{Na}} = g_{leak_{Na}}(V_m - V_{Na}) \tag{51}$$

$$I_{L_K} = g_{leak_K}(V_m - V_K) \tag{52}$$

$$I_{L_{Ca}} = g_{leak_{Ca}}(V_m - V_{Ca}) \tag{53}$$

$$I_{L_{gen}} = g_{leak_{gen}}(V_m - V_{leak}) \tag{54}$$

The $g_{leak_{Na}}$, g_{leak_K} and $g_{leak_{Ca}}$ are the maximum leak conductance of sodium, potassium and calcium ions. The maximum leak conductance and reversal potential for general leak are determined by choosing the holding potentials of -85 and -80 mV. At these potentials the cell is hyperpolarized and has no significant contribution from the voltage gated ion channels. The maximum leak conductance of leakage is,

$$g_{Leak_{gen}} = \frac{(5 - R_m)\,(I_{85} - I_{80})}{(5\,R_m)} \tag{55}$$

The $I_{85}\ and\ I_{80}$ are the total ionic currents at the holding potential of -85 and -80 mV. R_m is the membrane resistance. The leakage reversal potential was determined using,

$$V_{leak} = \frac{I_{ionic}^{V_m}}{g_{leak_{gen}}} + V_m \tag{56}$$

$$I_{ionic}^{V_m} = I_{Na} + I_K + I_{Ca} + I_{K_{ATP}} + I_{NaKATPase} + I_{NCX} + I_{CaATPase} + I_{L_{Na}} + I_{L_K} + I_{L_{Ca}} \quad (57)$$

The reversal potential for leakage was calculated based on the fact that the membrane current at resting membrane potential was zero. The membrane resistance and resting membrane potential were experimentally determined.

4.2.7. Ionic concentrations

The ionic currents were converted into chemical units to determine the changes in the ionic concentrations. Ionic concentration was obtained by multiplying ionic current in pA with a surface factor (F_S). The surface factor was determined by,

$$F_S = \frac{Current}{Faraday * Cell\ Volume} \quad (58)$$

$$F_S = \frac{10^{-12}\ \frac{mol\ C}{s}}{96485\ \frac{C}{s} * (50 \times\ 10^{-15})\ m^3}$$

$$F_S = 2.073 \times 10^{-7} \frac{mol}{m^3\ ms}$$

The model was compartmentalized and the diffusion of ions was considered to take place from the center of the sub-cellular space to the center of the bulk cytosolic space. The diffusion of ion (I) is given by [70],

$$J_{I(C_1-C_2)} = D_{I(C_1-C_2)} A \frac{[I]_{C_1} - [I]_{C_2}}{\Delta x_{C_1-C_2}} \quad (59)$$

Where, the ion diffuses a distance (x) through area (A) from the center of one compartment (C1) to another compartment (C2). The parameters (Table 4) were obtained from the Rabbit ventricular myocyte [70]. The diffusion distance of 0.45 from the subcellular space to middle of the bulk cytosolic space was calculated assuming a length of 1.8 m. The distance determines the transfer functions for the ionic fluxes between compartments. The lumped nature of the compartments was thereby adjusted to the physical geometry [70].

Table 4: Parameters for flux determination

Parameter	Value	Reference
Cell length	100 μm	[70]
Cell radius	10 μm	[70]
Sub-cellular space depth	45 nm	[70]
Area (Subcell - bulk)	3.01×10^{-6} cm^2	[70]
D_{Na} (Subcell - bulk)	1.09×10^{-5} cm^2/s	[82]
D_K (Subcell - bulk)	1.96×10^{-5} cm^2/s	[83]
D_{Ca} (Subcell - bulk)	1.22×10^{-6} cm^2/s	[82]
Distance (Δx)	0.5 μm	[70]

The changes in the subcellular space and bulk cytosol sodium concentration was determined using the equation,

$$\frac{d}{dx}[Na]_{Subcell} = \frac{-I_{Na}^{total} F_S + J_{Na}([Na]_{Bulk} - [Na]_{Subcell})}{V_{Subcell}} \quad (60)$$

$$\frac{d}{dx}[Na]_{Bulk} = \frac{J_{Na}([Na]_{Subcell} - [Na]_{Bulk})}{V_{Bulk}} \quad (61)$$

The changes in the subcellular space and bulk cytosol potassium concentration was determined using the equation,

$$\frac{d}{dx}[K]_{Subcell} = \frac{-I_{K}^{total} F_S + J_{K}([K]_{Bulk} - [K]_{Subcell})}{V_{Subcell}} \quad (62)$$

$$\frac{d}{dx}[K]_{Bulk} = \frac{J_{K}([K]_{Subcell} - [K]_{Bulk})}{V_{Bulk}} \quad (63)$$

The changes in the subcellular space and bulk cytosol calcium concentration was determined using the equation,

$$\frac{d}{dx}[Ca]_{Subcell} = \frac{-I_{Ca}^{total} F_S + J_{Ca}([Ca]_{Bulk} - [Ca]_{Subcell})}{V_{Subcell}} \quad (64)$$

$$\frac{d}{dx}[Ca]_{Bulk} = \frac{J_{K}([Ca]_{Subcell} - [Ca]_{Bulk})}{V_{Bulk}} \quad (65)$$

Where, I_{Na}^{total}, I_{K}^{total} and I_{Ca}^{total} are the total specific currents generated by the movement of sodium, potassium and calcium respectively. $V_{Subcell}$ and V_{Bulk} are the volumes of the sub-compartments.

4.2.8. Parameter estimation for electrophysiological recordings

The coupled ordinary differential equations were numerically integrated in MATLAB using a built-in differential equation solver 'ode15s' to solve a set of differential equations. A relative tolerance of 10^{-5} and an absolute tolerance of 10^{-6} were used. A custom graphical user interface (GUI) was created in MATLAB for parameter estimation and all the ion channels of the neuronal module including the leakage correction were incorporated.

The experimentally measured voltage clamp and current clamp were imported into MATLAB for deconvolution. The initial fitting parameters were obtained from the previously published average values [27,78]. The potassium currents in the voltage clamp recordings were fitted followed by calcium and sodium currents. A simultaneous fit was then performed on the voltage gated ion channels to obtain a first estimate for ion channel parameters. Using the obtained ion channel parameters and to avoid numerous solutions considering the large set of parameters being fitted, a second optimization was performed to extract a quasi-unique set of parameters by fitting the simulated action potentials to experimental measurements. The fittings were not sufficiently optimized to balance the ionic concentrations and could not produce a steady state. So, a third optimization routine was performed by optimizing the activities of pumps, exchangers and specific leakages. The I_{max} for ion exchanges and g_{max} for specific ionic leakages were determined. The action potential time series data was then fitted to further validate the experimental action potentials. The second and third steps of the optimization routines were repeated to fit the experimental recordings.

The optimization was performed using built-in MATLAB optimization routines. The

function *'fmincon'* computes a constrained minimum of a function by varying the variables within specific bounds. This was carried out in combination with the sum of squared residuals (ssr) as described in the following equation,

$$ssr = \sum_{n} (S(t_n) - E(t_n))^2 \quad (66)$$

Where, the simulated value is given by S and the experimental value by E at time t_n.

4.3. Integration of neuronal and metabolic models

The model was numerically integrated using MATLAB (2014a) in a modular approach. It was modeled and simulated using a desktop computer running Windows 7 on a 2.95GHz Intel Core2-Quad CPU and 8GB RAM. The obtained results were analyzed and plotted in MATLAB.

The neuronal module and the metabolic model were coupled to form the neuronal-metabolic model. The models were interfaced to exchange the intracellular ATP, ionic concentrations and the membrane potentials. Additional ATP consumption reactions such as NaK-ATPase and Ca-ATPase were incorporated into the metabolic model. The activity of these reactions was matched to that of the neuronal model. The metabolic model can sense only the bulk cytosolic concentrations. The neuronal module coupled to the deconvolution algorithm extracted the ion channel parameters which were then imported into the neuronal-metabolic model. The neuronal module calculates currents and the changes in the ionic concentrations. The obtained concentrations were fed into the metabolic model. The metabolic model was simulated following the determination of the metabolic activity. The new metabolite and ionic

concentrations were again feed into the neuronal module.

The action potential was simulated for every one second. The ionic exchangers usually restored the ionic balances within a few milliseconds. Stimulating an action potential every one second gives the ionic exchanges ample time to restore ion balances. The model was simulated to simultaneously generate a series of action potentials and run the metabolic model to determine the intracellular fluxes and changes in ionic concentrations. The model also predicted the changes in intracellular protein activities and metabolic concentrations. To simulate drug effects, the event created in Simbiology was turned 'on' and the model was simulated. The simulation results were compared to the experimentally determined values.

4.4. Simulating experimental conditions

To simulate the drug effects an event was created in the metabolic model (Simbiology-MATLAB) to introduce a drug effect that inhibits the enzyme activity. The inhibitors tested (Table 5) only bind and inhibit the enzymes in the metabolic pathway. The inhibitors do not bind to ion channels, so the ion channel parameters were held constant while fitting the drug induced time-series data. The only parameters allowed to change are the reversal potentials for the ion channels and cellular ATP concentrations in the neuronal module. So when fitting the effects of ion channel inhibitors, the ion channel parameters can be changed as they bind to the ion channel directly, thereby modifying its properties.

The V_{max} of the targeted enzyme was reduced, using a scaling factor. The scaling factor allows a function for the dose-response curve, describing the effect of a compound on the

enzyme [84]. The scaling factor 'b' typically relates the drug concentration [D] according to,

$$b = \frac{1}{1 + \left(\frac{[D]}{IC_{50}}\right)^{n}} \tag{67}$$

Where IC_{50} is the drug concentration at which a 50% reduction in the enzyme activity is observed, which n is the Hill coefficient of the dose-response curve and is often assumed to be one as one drug molecule is necessary to inhibit the enzyme [84]. The IC_{50} values were obtained by fitting the model to metabolic experimental data.

The neuronal-metabolic model was simulated to predict the changes in cellular metabolism and action potentials. The specific V_{max}'s or the enzyme concentration that were reduced to simulate the drug effects are listed below.

Table 5: List metabolic inhibitors and their targets

Drug	**Enzyme**
2DG	Hexokinase
Cyanide	Mitochondrial Oxidative Phosphorylation
Malonate	Succinate Dehydrogenase
2DG + Cyanide	Hexokinase and Oxidative Phosphorylation
2DG + Malonate	Hexokinase and Succinate Dehydrogenase

CHAPTER-5: RESULTS

The results obtained from the experiments and computational model are analyzed in this chapter. The basal metabolism was evaluated for calibrating the metabolic model to steady state. The core energy producing metabolic pathways namely glycolysis, mitochondrial TCA cycle and the electron transport chain were inhibited using 2DG, cyanide and malonate. A combinational inhibition of these pathways was also performed to experimentally validate the metabolic and electrophysiological responses. The neuronal-metabolic model was simulated to predict the metabolic fluxes and action potential time-series. The simulation data was compared to the experimental measurements. The results presented in this chapter demonstrate the predictive capabilities of the model.

5.1. Bioenergetics of NG108-15 cells

The NG108-15 cells were obtained by fusing mouse N18TG2 neuroblastoma and rat C6-BU-1 glioma cells in presence of sendai virus. During the fusion process reprogramming of core cellular metabolic pathways may occur. The reprogramming of cellular metabolic pathways impacts cellular functions and bioenergetics. To characterize and quantify NG108-15 cellular bioenergetics, the basal metabolism was determined by measuring the glucose utilization, lactate secretion, cellular ATP and ADP levels.

5.1.1. Glucose and lactate flux

The carbon flux was determined by measuring glucose uptake and lactate release. The

glucose uptake was found to be 495.19 ± 63.72 pM/hr/cell and is in close range to that found in glioblastoma cells previously [85]. The lactate flux was determined to be 851.05 ± 74.72 pM/hr/cell. The rates of lactate production are consistent with the expected flux for glioma cells [86]. The measurement of carbon flux revealed that 85% of the carbon entering the cell was ending up as lactate and only 15% of carbon is being utilized by other pathways in the cell. The glycolytic and lactate fluxes remained steady over time (Figure 17). The carbon flux was compared to Murine hybridoma cell line. Murine hybridoma cell had a glucose uptake of 380 nmol/hr/10^6 cells and a lactate release of 630 nmol/hr/10^6 cells indicating a carbon flux of 83% into lactate production [87].

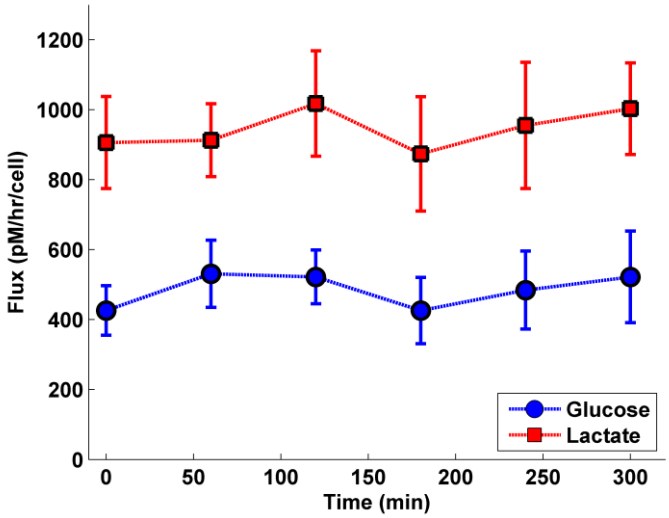

Figure 17: Measured glucose uptake (O) and lactate output (□) flux of NG108-15 cells

Lactate excretion causes the cell to waste three carbons that can either be incorporated into macromolecular precursor biosynthesis or get utilized in ATP production [88]. The increased lactate excretion elevates carbon uptake and simultaneously increases the pentose phosphate pathway activity. The elevated carbon utilization and lactate production regardless

of the availability of oxygen suggests the presence of aerobic glycolysis. This phenomenon was found by Otto Warburg and termed as 'the Warburg effect'. The effect was mostly found in cancer cells with lower mitochondrial respiration rates. This elevated glycolysis helps the cell to maintain higher proliferation rates or in differentiation mode enables the cell to produce neuronal process faster compared to primary neurons. Moreover, a sufficient amount of energy for maintaining cellular functions is produced by glycolysis in cancer cells.

5.1.2. ATP and ADP concentrations

Cellular ATP levels act as an indicator of cellular health and any disruption in cellular pathways may lead to impaired cellular bioenergetics. The assay kits measure the total cellular ATP and ADP levels including free and Mg-bound ATP/ADP. The intracellular ATP and ADP levels in NG108-15 cell were found to be 0.22 $\pm$ 0.03 mM and 0.11 $\pm$ 0.02 mM respectively. The ATP and ADP levels were stable over time (Figure 18) matching the literature reported values [89].

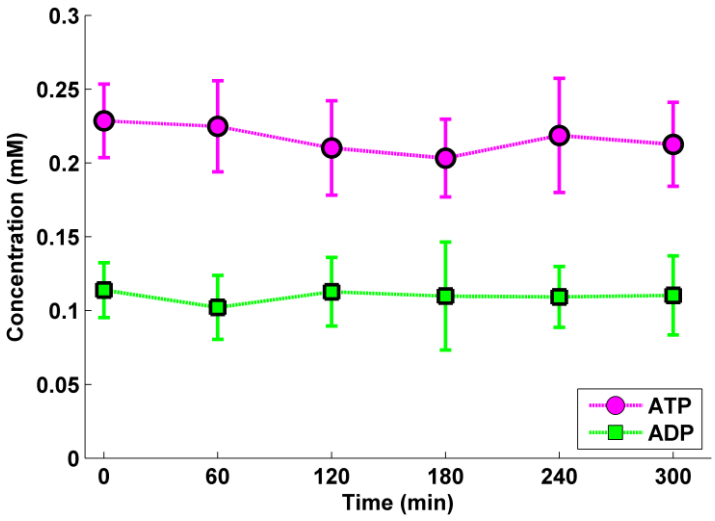

Figure 18: Measured intracellular ATP (O) and (□) ADP levels in NG108-15 cells

A literature search on intracellular ATP levels in different cell lines has shown that they possess lower levels (Table 6). Furthermore, most cell lines depend on aerobic glycolysis, an inefficient pathway for ATP production. The alterations in cellular bioenergetic pathways produce different metabolites supporting rapid cell growth and proliferation [88]. Normal cells utilize the nutrients efficiently and cell lines have no selective pressure to optimize their metabolism for ATP production. Glycolysis is an inefficient mode of ATP generation compared to mitochondrial pathway. The intracellular ATP/ADP ratio is also maintained at steady state and determines which pathway the cell adapts for ATP production. A lower ATP/ADP ratio has been shown to favor glycolysis and a higher ratio would favor mitochondrial ATP production [88]. A slight change in cellular ATP/ADP or ADP/AMP ratio may impair cellular homeostasis and trigger apoptosis [90].

Table 6: Literature reported cellular ATP levels in different cell lines

Cell type	**Origin**	**ATP** **(nmol/106 cells)**	**ADP** **(nmol/106 cells)**	**ATP/ADP ratio**	**Reference**
HeLa	Cervical cancer cells (glycolysis dominated)	5.2	1.64	3.2	[91]
BSC-40	Kidney epithelial cell line (oxidative phosphorylation dominated)	9.47	1.08	8.8	[91]
SH-SYSY	Human dopaminergic neuroblastoma cell line	1.33	0.24	5.5	[92]
NG108-15	Hybrid neuroblastoma and glioma cell	8 - 10	-	-	[89,93]
NG108-15	Hybrid neuroblastoma and glioma cell	10 + 0.83	5.13 + 0.44	1.9	Measured values

5.2. Deconvolution of Electrophysiological Recordings

5.2.1. Thermodynamic dependent Hodgkin-Huxley Model

To deconvolute the electrophysiological recordings the neuronal model was constructed in a modular approach. The basic voltage gated ion channels were modeled by incorporating the thermodynamic dependences and simulated using previously published ion channel parameters [27]. The voltage clamp and the current clamp recordings were simulated for a NG108-15 cell.

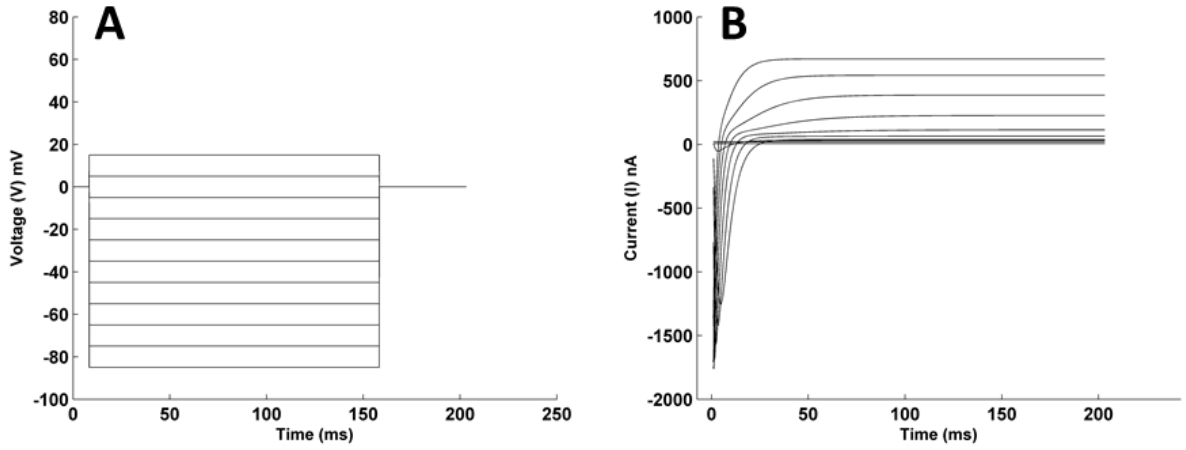

Figure 19: Voltage clamp simulation. (A) The voltage steps protocol used during a voltage clamp recording. (B) Simulated voltage clamp recording for NG108-15 cell

During a voltage clamp recording, the voltage was held constant at different 'steps' (Figure 19A) and the changes in the current were recorded (Figure 19B). The voltage dependence on the ionic current is demonstrated by plotting the current-voltage relationship (Figure 20). The properties of NG108-15 cells were demonstrated by varying the current during incremental impositions of voltage or the responses of voltage to current injections through a whole-cell patch. The IV-curve for NG108-15 defines the input resistance.

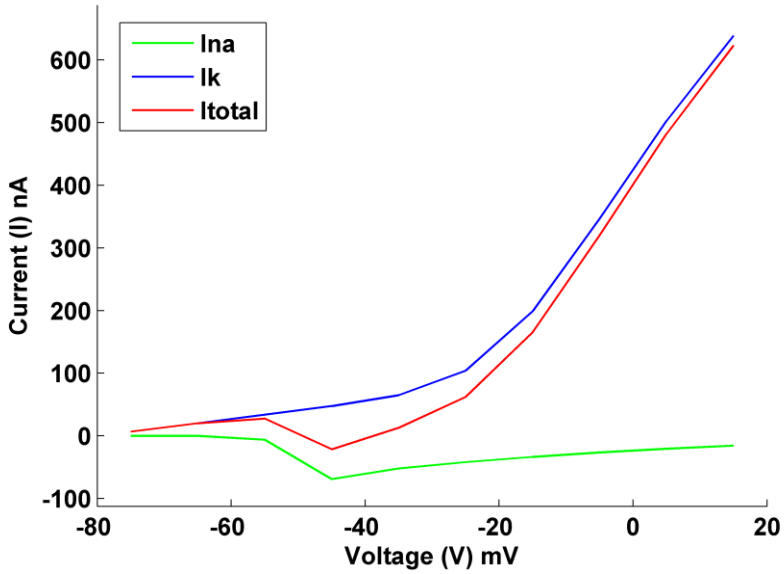

Figure 20: IV Curve for NG108-15 cell showing the changes in sodium (green), potassium (blue) and total current (red) at different voltages

The current clamp recording was also simulated to generate an action potential using the same parameters by application of a stimulus current (Figure 21).

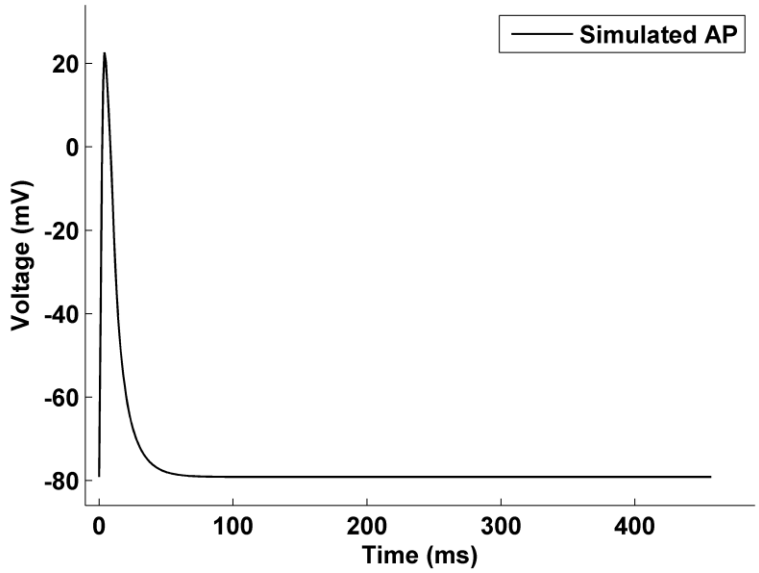

Figure 21: Simulated current clamp recording showing an action potential

The activation and inactivation of gates determines the generation of action potentials. The probabilities during NG108-15 action potential are shown in the Figure 22. At rest, the activation variable for sodium (*m*) is small and inactivation variable (*h*) for sodium is large. The activation of potassium (*n*) and calcium (*e*) are also small. When a stimulus is applied, the membrane depolarizes causing an increase in *m* leading to the peak in action potential. The activation of potassium gate (n) also increases and *h* decreases. The activation of the calcium gate (e) also takes place during the action potential generation. The gates h and n slowly return to their initial state when compared to other gates where as other gates act rapidly (Figure 22).

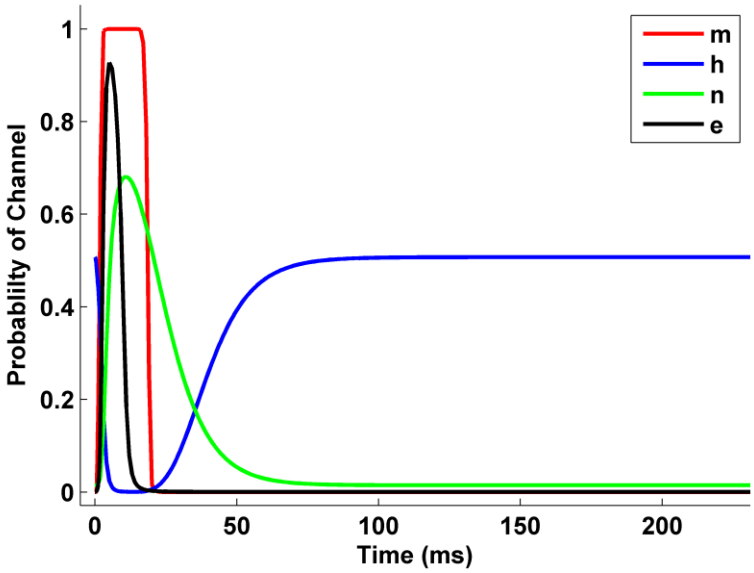

Figure 22: The activation and inactivation of voltage gated ion channel gates during an action potential

5.2.2. Modeling ionic exchangers, pumps and leaks

The ATP dependent potassium channel (K_{ATP}) has emerged as an important ion channel especially in neurodegenerative diseases and acute brain ischemia adapting to changes in metabolic activity. The probability of activation and inactivation depends on the intracellular

ATP levels directly coupling the metabolic activity and membrane electrical activity. The channel was modeled and simulated to visualize the changes in action potential peak shape due to changes in cellular ATP concentration (Figure 23).

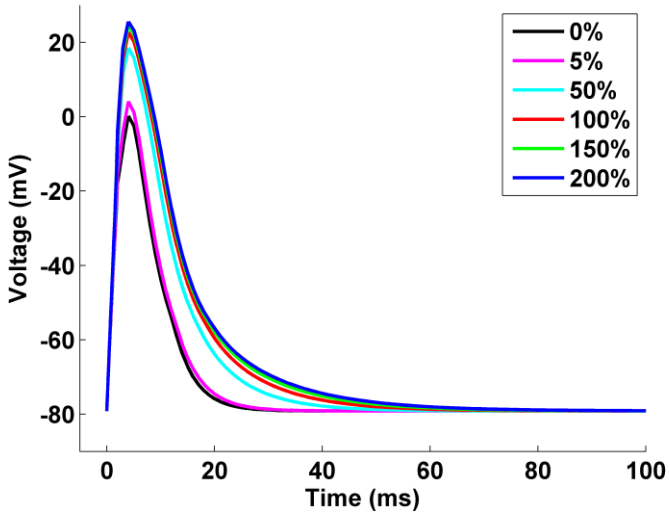

Figure 23: Effect of cellular ATP levels on action potential peak shape

The resting membrane potential is mainly determined by the ionic pumps and leakages. The sodium and potassium ion leaks are counterbalanced by the Na/K-ATPase pump. The ATP dependent sodium potassium exchanger is a major pump responsible for maintaining sodium and potassium homeostasis. The current generated by moving three sodium ions out and two potassium ions against the concentration gradients has been added to the respective total specific ionic currents. At rest, the pump balances the sodium (Figure 24) and potassium (Figure 25) fluxes of the ion channels and leaks. A stoichiometric balance of intracellular potassium and sodium ions was not achieved by Na/K-ATPase pump alone. Additional ionic pumps have been incorporated to maintain cellular ionic concentrations (Figure 26).

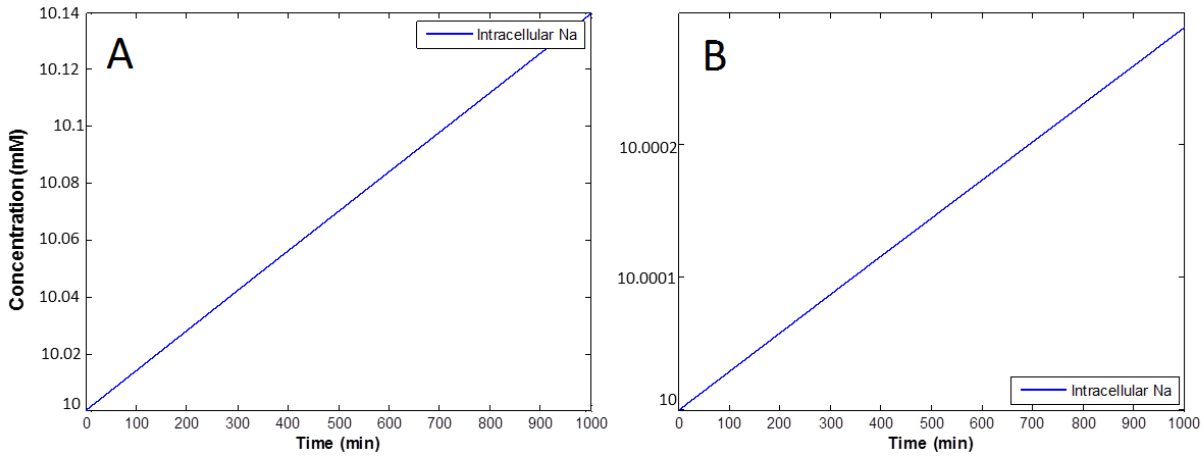

Figure 24: Restoration of intracellular sodium concentration by Na/K-ATPase pump. (A) Without Na/K-ATPase and (B) with Na/K-ATPase

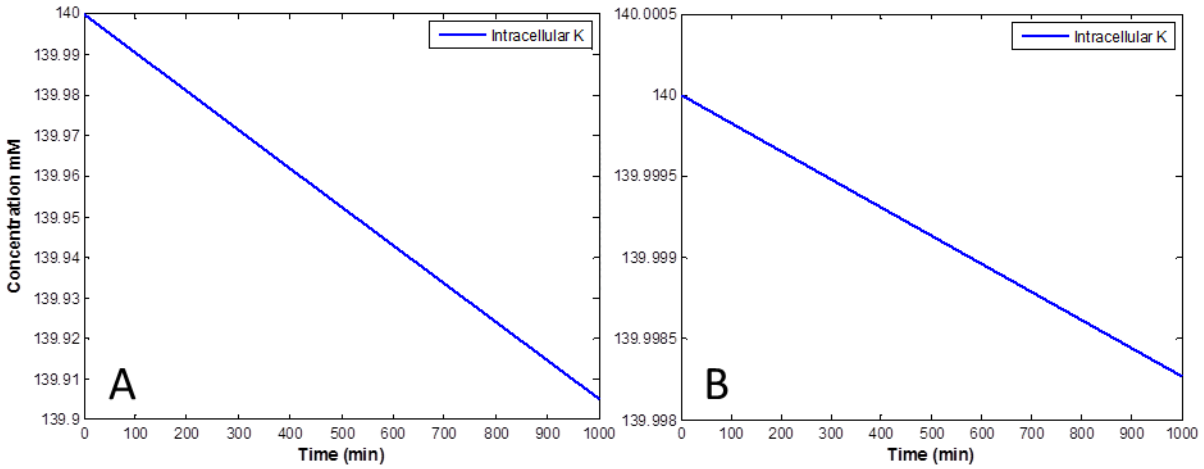

Figure 25: Restoration of intracellular potassium concentration by Na/K-ATPase pump. (A) Without Na/K-ATPase and (B) with Na/K-ATPase

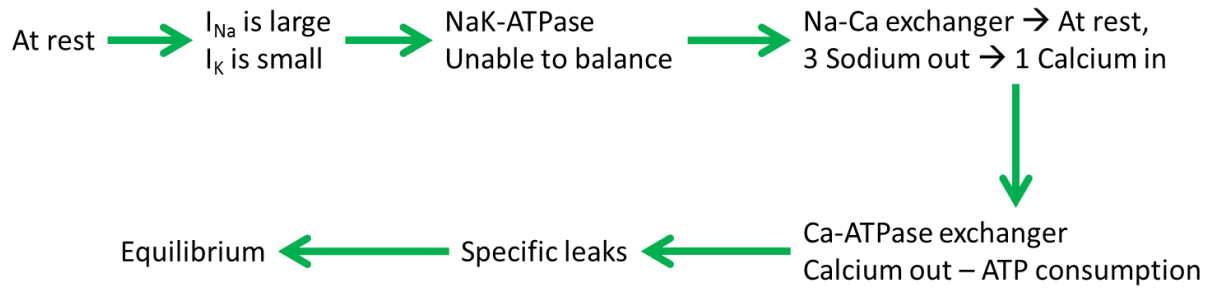

Figure 26: Rationale for implementation of other ionic pumps

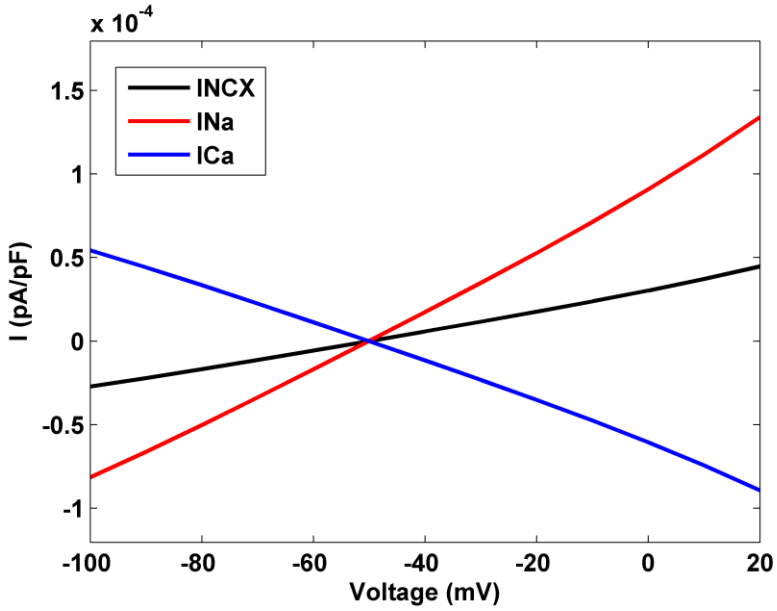

Figure 27: Sodium-calcium exchanger currents mediated by changes in membrane potential

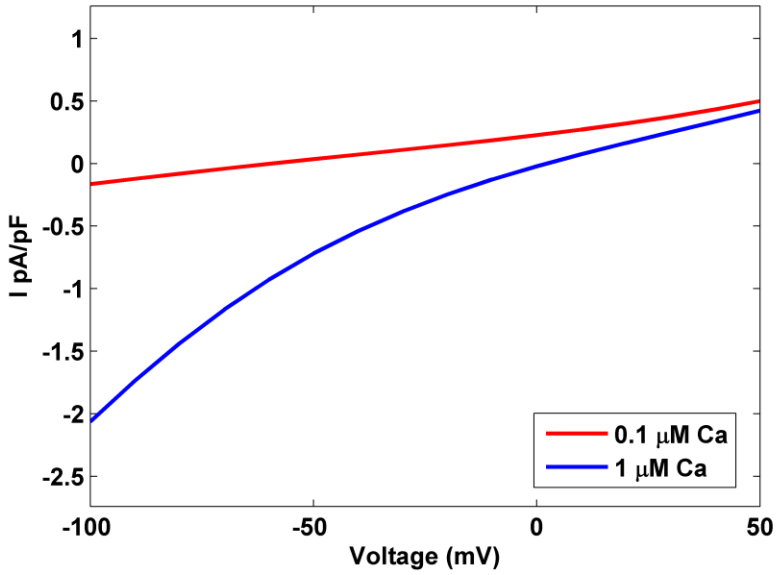

Figure 28: Remodeled the IV curve for sodium calcium exchanger showing the exchanger activity for different calcium concentrations

The sodium calcium exchanger (NCX) activity is dependent on the membrane potential and intracellular calcium concentration. NCX exchanges one calcium ion for three sodium ions

and has an electrogenic contribution to the membrane electrical properties. At rest, the exchanger activity is reversed transferring three sodium ions out and one calcium ion thereby generating a very small sodium and calcium current (Figure 27). The membrane depolarization reverses the pump activity again resulting in an outflow of calcium and influx of sodium [81]. A shift in curve representing the calcium influx and efflux is observed (Figure 27). The pump activity depends on the intracellular calcium concentration. Two intracellular calcium concentrations were used to model validate the exchanger activity (Figure 28). The slope of the curve varies with the increased calcium concentration leading to a faster extrusion of intracellular calcium ions. The activity from Courtemanche et al. [80] and Kager et al. [81] has been reproduced to validate NCX and adapted into the neuronal module.

The ATP dependent calcium pump (Ca-ATPase) transports intracellular calcium ions against the concentration gradient by consuming intracellular ATP. The pump activity increased with an accumulation of intracellular calcium (Figure 29). Kager at al. have assumed an unlimited availability of cellular ATP and modeled the pump [81]. Since ATP could be a limiting factor in the model, ATP dependence has been incorporated so that the pump could lower the extrusion of calcium ions upon lowering the intracellular ATP levels. The ATP dependence has been modeled to match the Ca-ATPase activity previously reported by Kager et al. (Figure 30). The activity of pump is made very sensitive to intracellular ATP levels so a slight decrease in ATP concentration would lower the pump activity and lead to an accumulation of intracellular calcium.

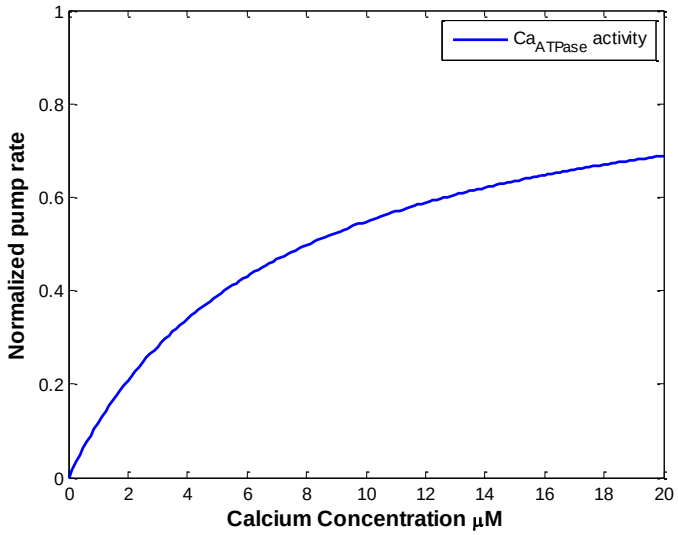

Figure 29: Calcium dependence on Ca-ATPase pump

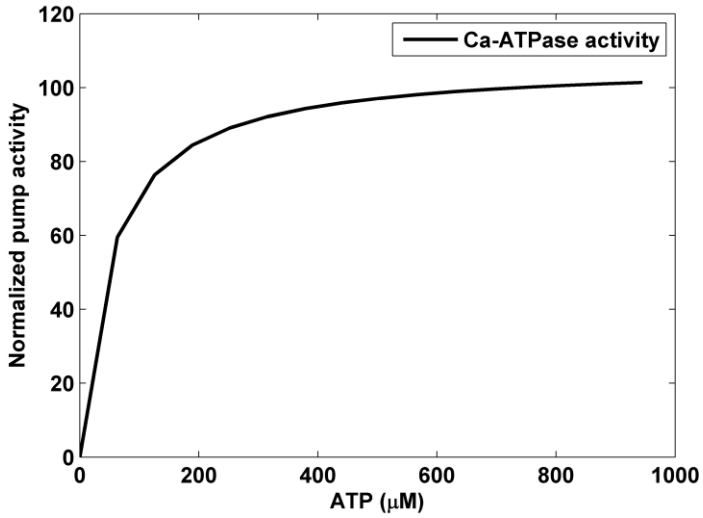

Figure 30: ATP dependence on Ca-ATPase pump

Specific ionic leakages were implemented to represent all the other sodium, potassium and calcium ion channels [78]. The ions diffuse long the diffusion gradient and the ionic exchangers restore the altered intracellular levels. All the equations were implemented and the steady state was simulated using the experimental holding potential. The holding potential was

varying due to the experimental conditions. The resting membrane potential was calculated as shown in Figure 31A. The sodium, potassium and calcium ionic concentrations were at steady state when the model was simulated for 40 min (Figure 31). The parameter estimation for I_{max} of all the pumps and conductance for leakages was performed to simulate steady state. Model was compartmentalized by incorporating the ionic fluxes of subcellular space and bulk cytosol. The fluxes were simultaneously determined while generating the action potential.

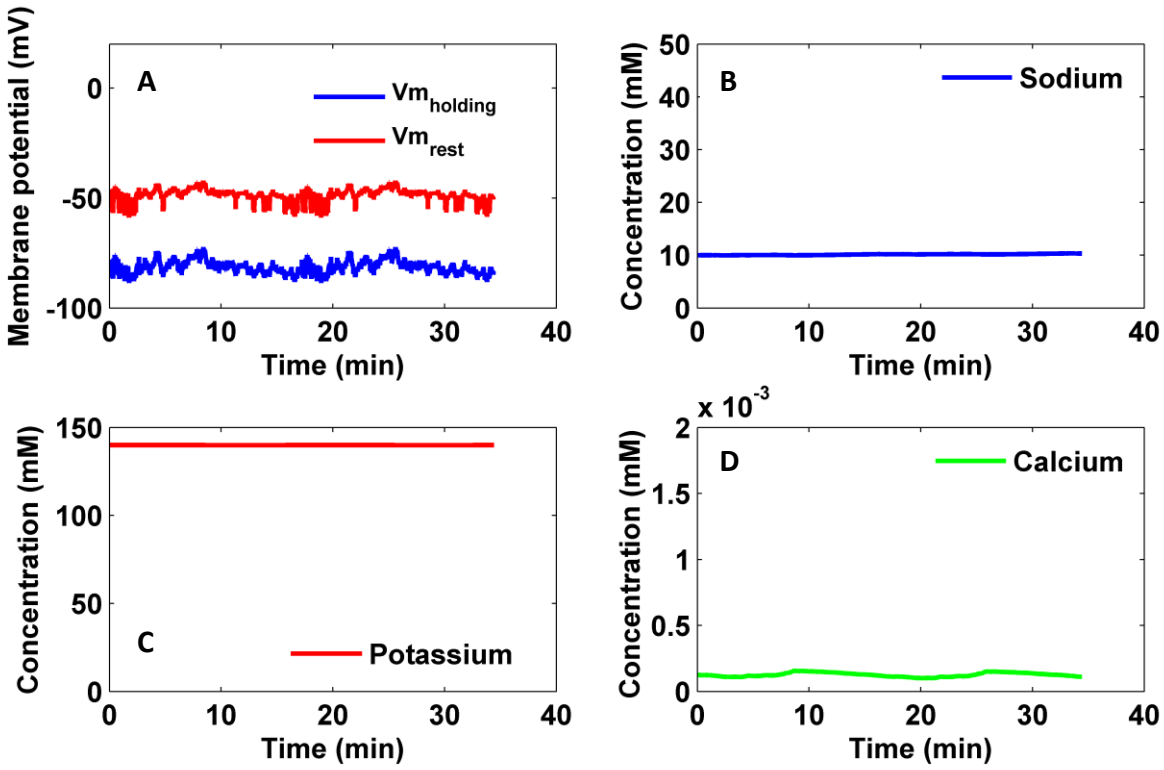

Figure 31: Calibration of the neuronal module to simulate steady state. (A) The resting membrane potential (red line) of the cell is determined based on holding potential (blue line). The changes in (B) sodium, (C) potassium and (calcium) concentrations are simulated

5.2.3. Extraction of electrophysiological parameters

NG108-15 cells were observed to be fully differentiated on day-4 in serum-free differentiation medium and were patched to record their electrophysiological activity (Figure 32). Voltage clamp and current clamp data were imported into Matlab and fitted using the custom graphical user interface. The curves were fitted after an initial 0.1ms delay to eliminate the effect of experimental artifacts. The voltage clamp recordings were fitted initially and an agreeable fit was obtained to the sodium, potassium and calcium ion channel data (Figure 32).

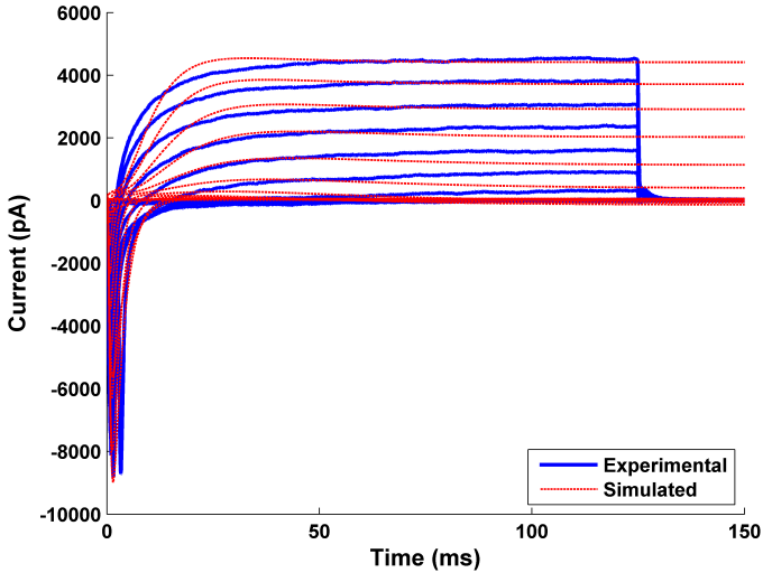

Figure 32: Simulated (red) voltage clamp were fitted to an experimental (blue) recording

Ion channel parameters were then automatically fitted using the fitting algorithm that converged in less than 4 minutes. Weighted least square error function was applied to quantify the difference between the simulated and the experimentally recorded data [27]. The implemented error function is:

$$\text{Least square: } E_{L_{square}} = \sum_{n} (S(t_n) - E(t_n))^2$$

Weighted least square: $E_{WL_{square}}=E_{L_{square}}$ if $t_n<30ms$ and $E_{WL_{square}}=5\times E_{L_{square}}$ if $t_n\geq 30ms$

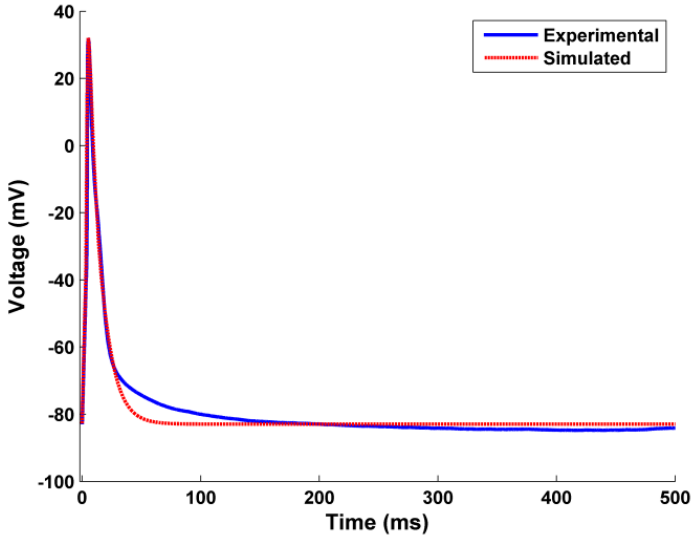

Figure 33: Simulated (red) action potentials were fitted to experimental (blue) action potential recording

The action potentials (Figure 33) were evoked with a short 2 ms current injection in current clamp mode at holding potential. The following parameters were obtained from the patch-clamp recordings and used in the modeling: membrane resistance, resting membrane potential, membrane capacitance and injected current. The maximum conductance of the leakage current was calculated form the resting membrane potential in the model. The earlier averaged ion-channel parameters were used as initial values for AP fitting. Using the voltage dependent sodium, potassium and calcium ion channels, ATP-dependent potassium channel, ATP-dependent exchangers, sodium-calcium exchanger and specific leakages an excellent fit to the entire AP was obtained (Figure 33). The first action potential was fitted simultaneously with the voltage clamp recording and the extracted parameters were fed into the coupled neuronal-metabolic model.

The model showed a sharp rise in the subcellular ionic concentrations of sodium (Figure

34), potassium (Figure 35) and calcium (Figure 36) ions. However, the bulk cytosolic concentrations did not change significantly.

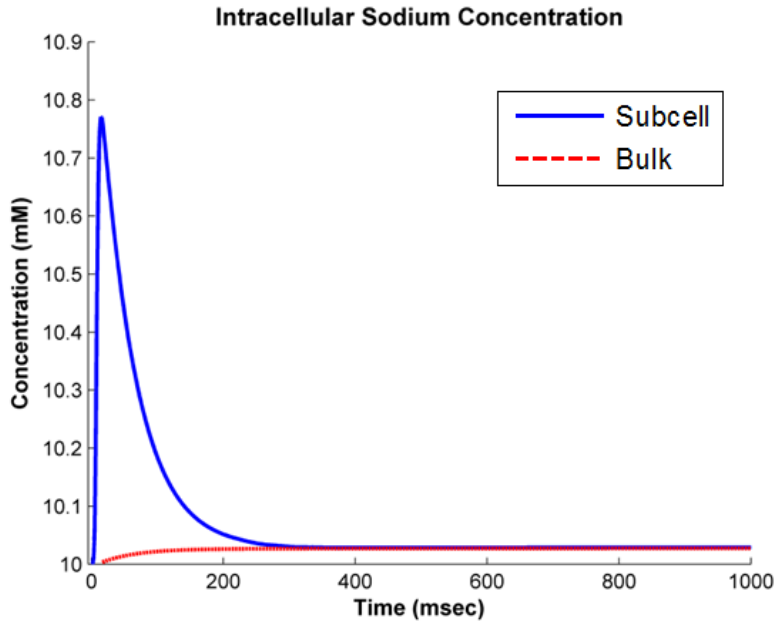

Figure 34: Simulated changes in subcellular and bulk cytosolic sodium concentration during action potential

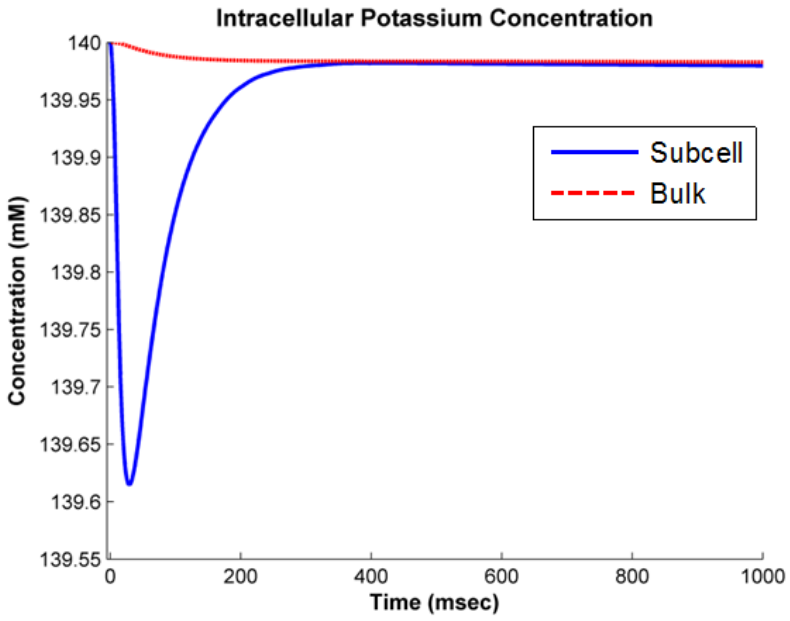

Figure 35: Simulated changes in subcellular and bulk cytosolic potassium concentration during action potential

These results were observed to be in agreement with the physiological observations. It is well

known that during action potential generation and propagation, the ionic concentrations close to the membrane change rapidly causing the membrane potential to alter. The bulk intracellular ionic concentrations do not change significantly. The ion channels on the plasma membrane only sense the ionic concentrations close to the membrane and act rapidly to restore the ionic balances.

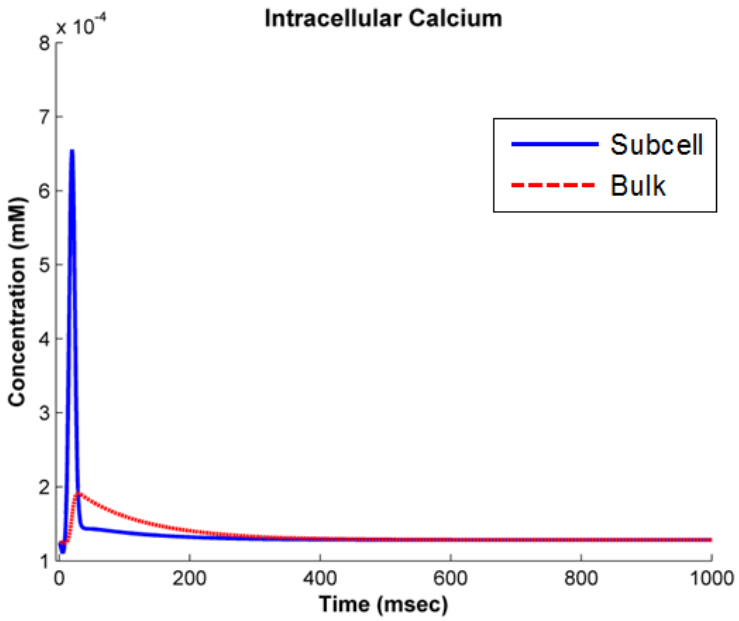

Figure 36: Simulated changes in subcellular and bulk cytosolic calcium concentration during action potential

The sodium and calcium buffering takes place in the cell [70]. To keep the model simple, buffering systems have not been included. A sudden rise in ionic concentration leads to an increased activity of the exchangers and pumps to extrude and restore the intracellular ionic concentrations. The diffusion of ions takes place from the subcellular space to the bulk cytosol initially and when the pumps are reestablishing the sub-cellular concentrations, the bulk cytosolic concentrations also slowly reached the initial values.

5.2.4. Statistical analysis

Ion channel parameters were extracted by fitting the voltage clamp recoding and the initial action potential of a total of forty nine data sets. Several fitting parameters were applied in fitting the action potentials. Each dataset produced a different set of parameters. Statistical analysis was performed to determine the variations in fitting parameters. A box plot has been created to visualize the skewness of parameters and to identify outliers. The box plot of voltage-gated sodium channel parameters is shown in Figure 37.

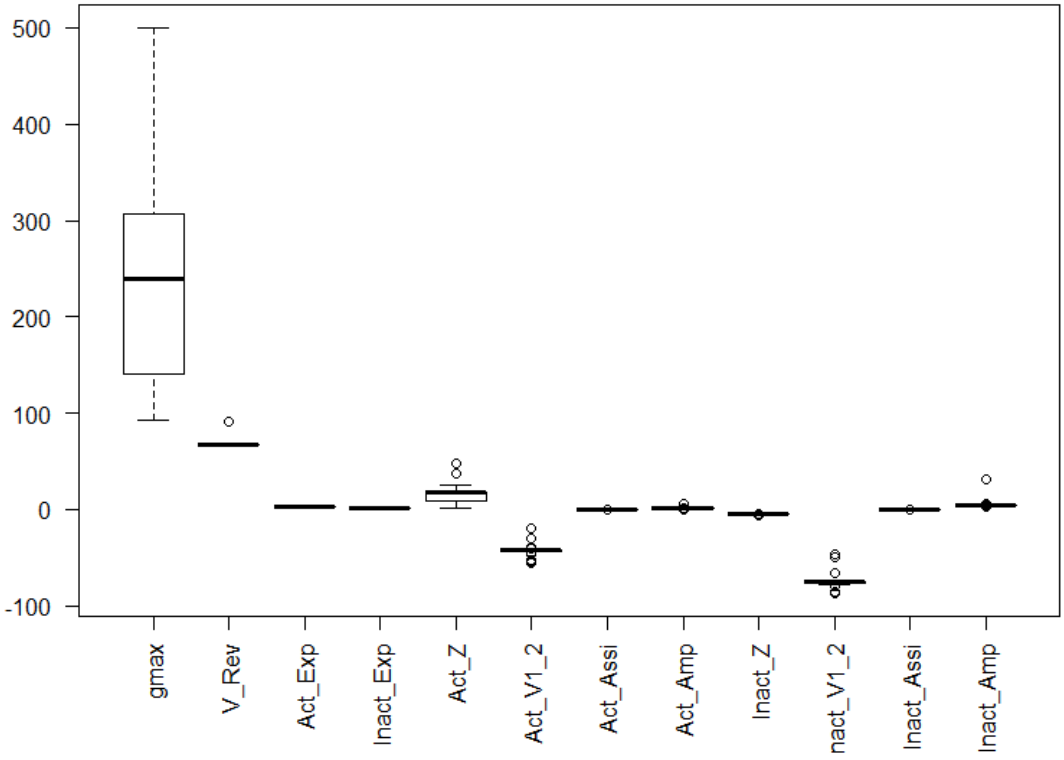

Figure 37: Box plot for voltage gated sodium channel parameters

The maximum conductance of sodium channel has a wide range and is much higher than the conductance of other ion channels. These conductances are unique for a particular cell to support its cellular functions. The variations in voltage thresholds and time constants for

channel activation and inactivation vary the ion channel conductance [94]. Moreover the location where the cells are patched can also cause variations. The activation and inactivation parameters are used to fit the exponential and sigmoidal functions of Hodgkin-Huxley model. No large change was found in these parameters while fitting it to the experimental data. The estimated half-activation potential was -43.41 ± 6.47 mV and was agreement with that found in neuronal models. The experimentally determined half-activation potential from central neurons is -60 mV [95]. The variations could be due to the different resting membrane potentials of the cells (Figure 41C).

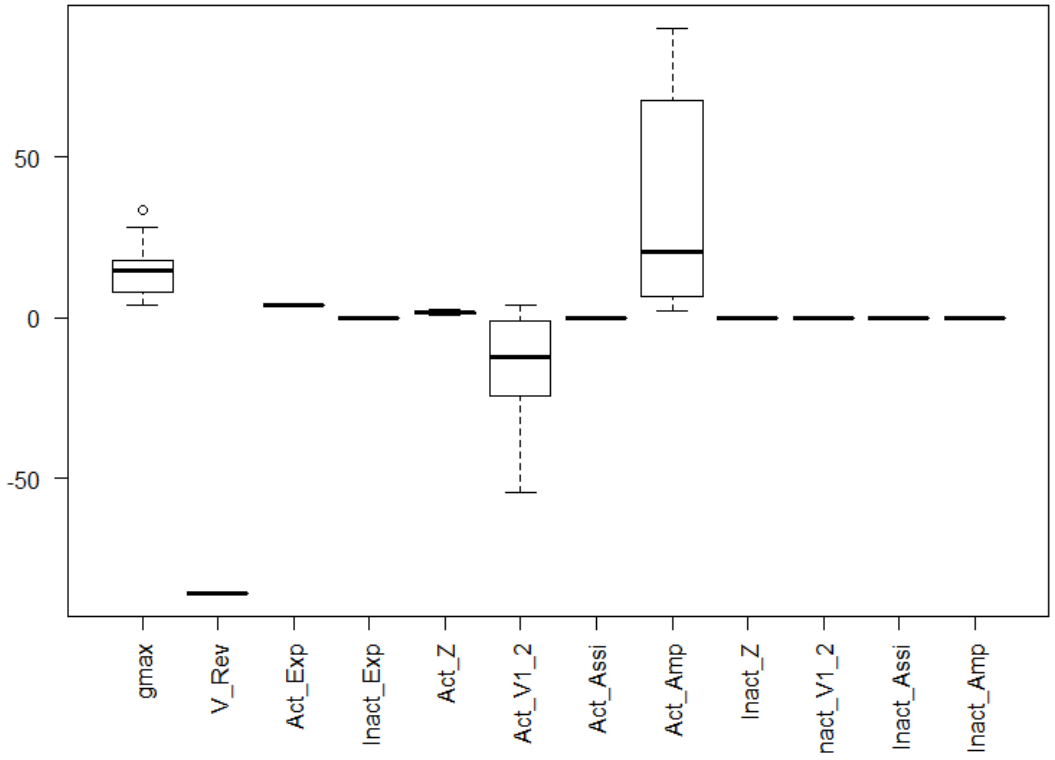

Figure 38: Box plot for voltage gated potassium channel parameters

The box plot of potassium channel parameters showed the variability in activation amplitude, half-activation potential and the maximum conductance (Figure 38). The half-

activation potential of cortical pyramidal neurons was found to be -24.5mV and was close to the fitted result of -16.04 ± 9.62 mV for NG 108-15 cells [96]. The activation time constant (Act_amp) has a higher standard deviation but the box plot shows that 25% of the values are in the 3rd quartile close to 22 ms. The maximum conductance (g_{max}) for voltage gated potassium channel is very low compared to the sodium channel.

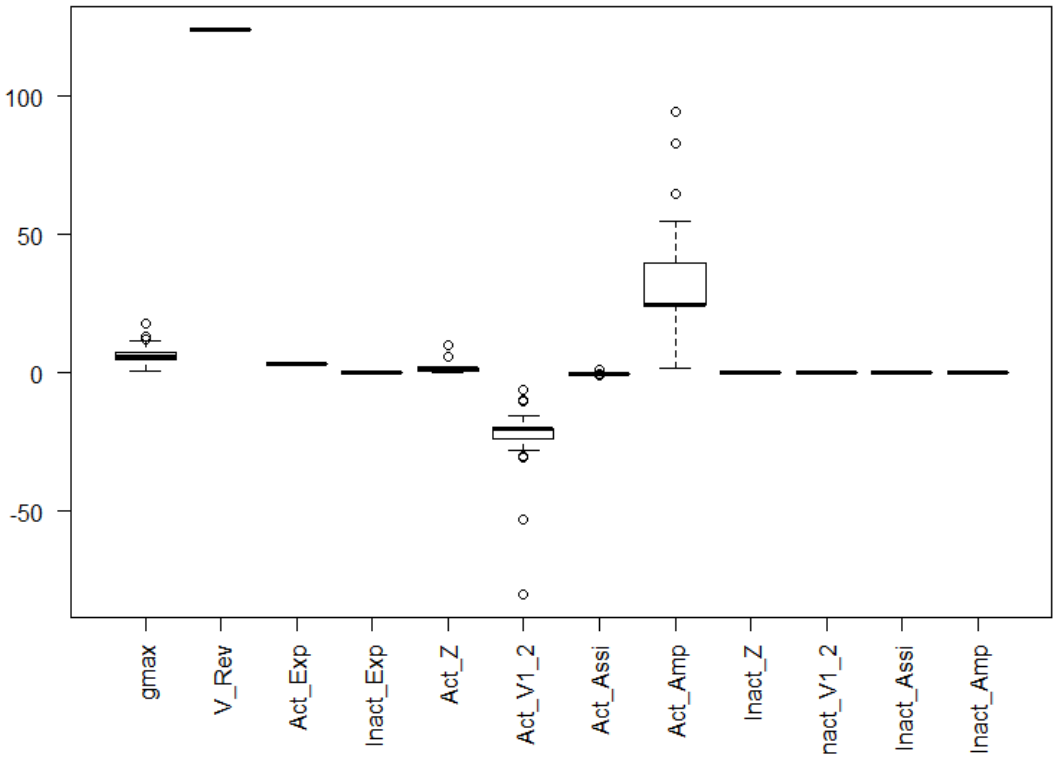

Figure 39: Box plot for voltage gated calcium channel parameters

Similarly, the calcium parameters showed slight variations (Figure 39). The activation time constant and half-membrane potential had a few outliers. The fitted g_{max} of voltage gated calcium channel for NG108-15 cells is 6.77 ± 3.69 mS and is in agreement with the earlier reported values [27]. Few recordings had a higher calcium conductance causing a 'hump' in action potential. The calcium entering the cell acts as serves as secondary messenger during AP.

A list of all the ion channel parameters with the standard deviations is given below in Table 7 and 8.

Table 7: Average electrophysiological parameters for NG108-15 cells obtained from fitting to voltage clamp and current clamp recordings. Data are mean + SD (n = 49)

Ion channel Parameters	**Sodium**	**Potassium**	**Calcium**	**Leak**
Conductance (g)	241.21 ± 104.08	14.62 ± 7.43	6.77 ± 3.69	3.24 ± 2.34
Reversal potential (V_{Rev})	67.85	-85.61	124.05	- 53 ± 86
Activation exp (m,n,e)	3	4	3	-
Inactivation exp (h)	1	-	-	-
Activation q (q)	14.92 ± 8.97	1.61 ± 0.42	1.71 ± 1.67	-
Half activation potential ($V_{1/2}$)	-43.41 ± 6.47	-16.04 ± 9.62	-25.41 ± 14.44	-
Act.assim (ξ)	-0.43 ± 0.08	-0.04 ± 0.22	-0.17 ± 0.05	-
Act.Ampl (A)	0.83 ± 0.77	35.39 ± 30.38	32.19 ± 18.29	-
Inactivation q (q)	-4.66 ± 0.4	-	-	-
Inact. Half-activation	-73.9 ± 7.07	-	-	-
Inact. Assim	0.36 ± 0.04	-	-	-
Inact.Ampl	4.95 ± 4.38	-	-	-

Table 8: Activities of exchangers and leaks

	NaK-ATPase	Ca-ATPase	NCX	K-ATP	Na leak	K leak	Ca leak
Imax	1520 ± 351	1700 ± 147	502 ± 55	-	-	-	-
Conductance	-	-	-	2.54 ± 1.98	0.39 ± 0.21	4.2 ± 1.6	0.12 ± 0.2

The I_{max}'s for the exchangers also varied from cell to cell as the membrane potential, capacitance and fluxes varied (Table 8). The fitted I_{max} for Na/K-ATPase is close to that reported in the literature for neurons [78,79]. The Ca-ATPase was slightly higher than the Na/K-ATPase as NG108-15 cells have higher intracellular calcium levels similar to cancer cells. The cellular resting membrane potential was determined based on separation of potassium ions since the cellular membrane has higher permeability towards potassium. The potassium leak conductance is higher compared to the sodium and calcium leak conductances.

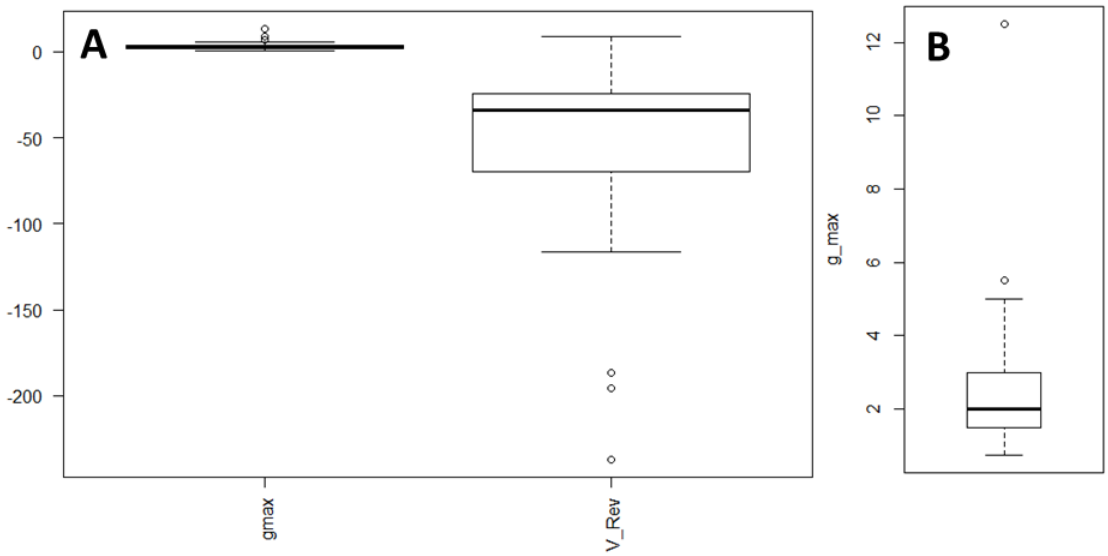

Figure 40: Box plot for (A) leakage currents and (B) maximum conductance of ATP dependent potassium channel

The maximum conductance and reversal potential for general leak have also been analyzed (Figure 40A). The implementation of ion channels in the model lead to a decrease in leakage conductance. The maximum conductance of the ATP dependent potassium channel was 2.54 $\pm$ 1.98 (Table 8) and is higher than that of primary cortical neurons [77]. The sensitivity of K_{ATP} channel varies from cell to cell [97]. A decrease in cellular ATP level causes the K_{ATP} channel to activate and prevents the potassium ions to move across the membrane. The experimental membrane resistance is 0.64 + 0.30 GΩ and the membrane capacitance which is indicative of the cell size is 69.19 + 37.87 pF. The resting membrane potential (RMP) of the patched cells was -43.88 + 5.99 mV with 25% of the recordings in the third quartile showing a RMP of -47 mV (Figure 41C). The resting membrane potential of NG108-15 cell has been reported to range from -33.2 to -47 mV [98,99].

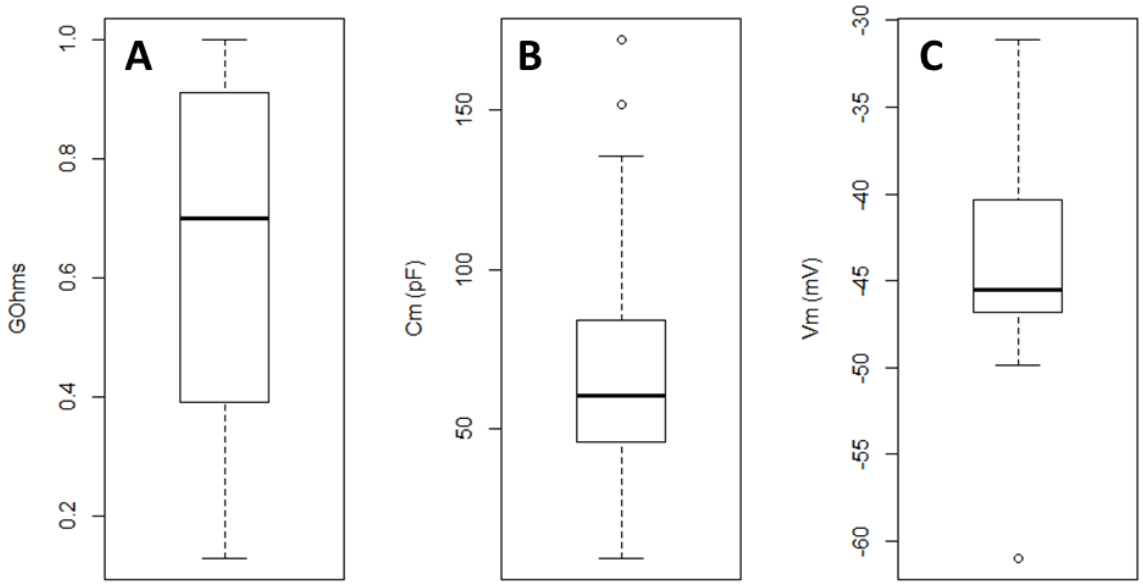

Figure 41: Box plot for experimentally obtained (A) membrane resistance, (B) membrane capacitance and (C) resting membrane potential

5.3. Steady state analysis

Modeling cellular metabolic pathways integrates all the information into a functional networking model that simulates all the intracellular interactions. The aim is to construct and validate the model to predict cellular protein activities, fluxes, metabolite concentrations and action potentials at steady state.

5.3.1. Forcing metabolic model to steady state

The method for reconstructing large models is to obtain a validated model and recalibrate it to match the experimental data for the cell type of our interest. The cellular pathways possess a very complex feedback and feed-forward interactions that control the overall flux and must be maintained continuous check [100]. This means that the relative ratios of kinetic constants are important and any disruptions in the balance will render the model causing an accumulation of intracellular metabolites. In reality, cell controls the flux by adjusting protein concentrations. Metabolic genes are typically located in blocks within the genomes and are expressed together. In our model, we are essentially altering the V_{max} of the reactions to mimic the changes in protein concentration within a cell as a means of controlling flux [58,72,101].

The glycolytic model derived from red blood cell [72] was more favorable as it utilizes glucose as the primary source of carbon. This is important because glucose is the major source of carbon in brain and neuronal glycolysis is regulated by hexokinase [54]. In addition, the glycolytic model consists of the PPP that is active in brain [54]. Red blood cells lack mitochondria forcing them to completely rely on glycolysis for carbon and ATP [102]. Since the

glycolytic module from red blood cells has higher a glycolytic activity, we have lowered the V_{max} of the glycolytic enzymes between 1-100% to match the experimentally measured data [58,101]. Similarly, the mitochondrial model obtained from cardiac cell provides 90% of the energy from mitochondrial oxidative phosphorylation and is highly active [103]. The TCA cycle activity was lowered by altering the enzyme concentrations. The total concentration of the TCA cycle metabolites was conserved [59] to match the experimental data.

The ensemble metabolic model was calibrated by scaling a set of pathways simultaneously. At steady state, the rate of production and consumption of all metabolic concentrations is balanced and equals zero. A fitting algorithm was written to fit the model to experimental data in a modular approach. The fitting algorithm scaled the pathways by computing the range of possible fluxes for each pathway that enables a close-to-optimal fit with the experimental data. The fitting algorithm also iteratively performed the metabolic flux analysis while constraining the flux through each pathway. The metabolic model was constrained to match the glucose and lactate flux to 495 and 851 pM/hr/10^6 cells respectively. The total cellular ATP and ADP levels were constrained to 220 and 110 μM. The reassembled model attained steady state after running it for 120 min (Figure 42 and Figure 43).

The initial concentrations of all species in the metabolic model were then changed to run the model in steady state from beginning. The overall adenosine pool was kept constant. The ATP/ADP and ATP/AMP ratios were 2.2 and 5 respectively. The Na/K-ATPase and Calcium-ATPase activity were tied matched to the activities obtained from the neuronal module and later integrated in the coupled model.

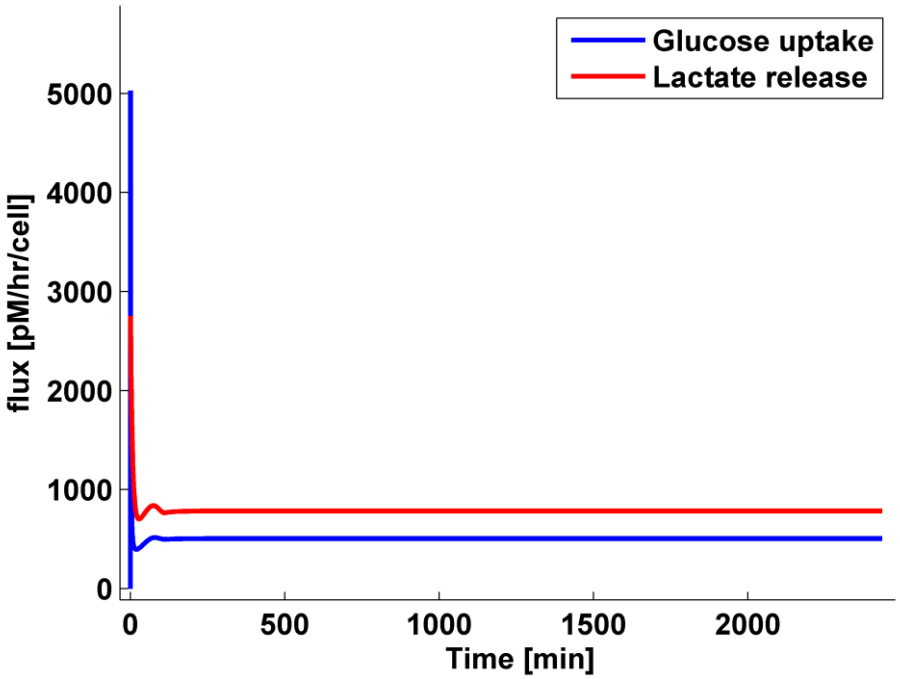

Figure 42: Simulating glucose uptake and lactate release to steady state

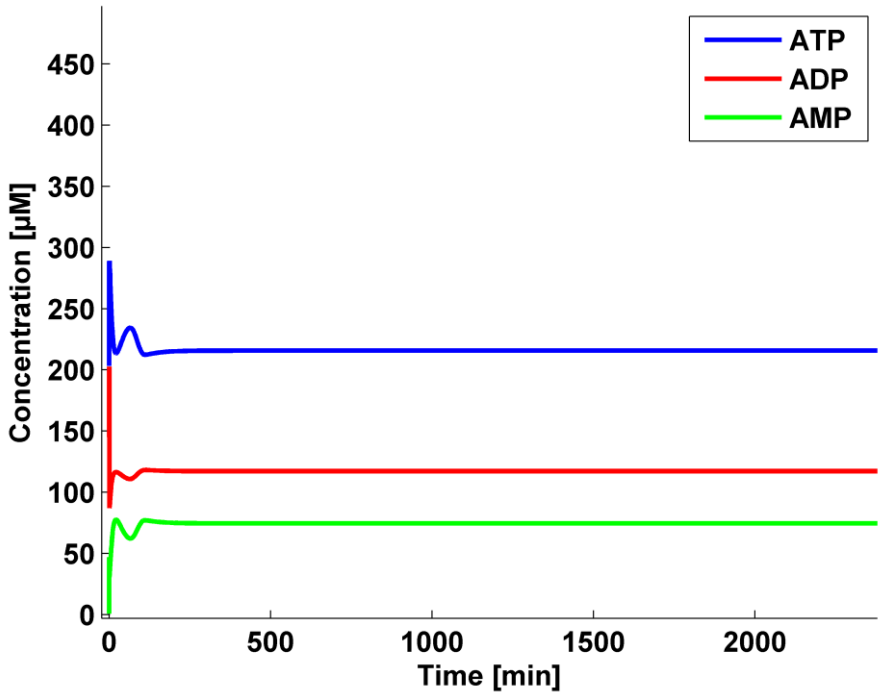

Figure 43: Simulated steady state of intracellular adenosine levels

The metabolic flux analysis of NG108-15 cells showed that 83.09 % of carbon ends up in lactate production, 14.76% enters the mitochondrial TCA cycle, 2.02% is used by pentose phosphate pathway (PPP) for PRPP synthesis and 0.13% is secreted out of cells as pyruvate (Figure 44). The activity of pentose phosphate pathway in cancer cells or cell lines has been shown to vary depending on the cellular activity that ranges from 0.1 % to 11% and considering that NG108-15 cells were in differentiation stage 2% seems to be reasonable. The transport of pyruvate into extracellular space is very less as most of it got converted into lactate or entered mitochondria.

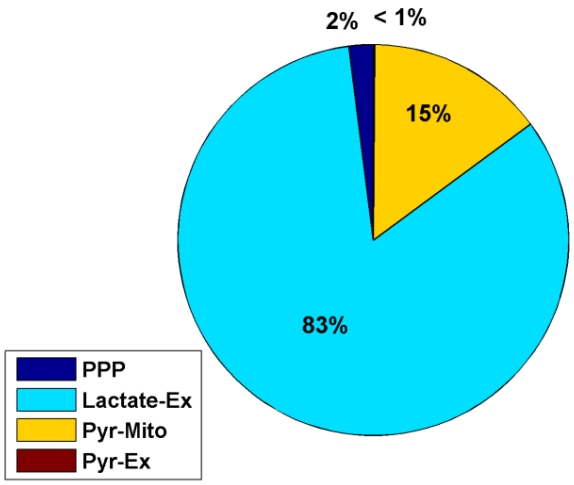

Figure 44: Fate of carbon in NG108-15 cell

Analysis of the ATP production by NG108-15 cell showed that 81.3% of ATP is being produced by glycolysis and only 18.7% of ATP is being contributed by the mitochondria towards the total cellular ATP concentration (Figure 45). Due to the increased carbon flux through glycolysis, NG108-15 cells produced more ATP from glycolysis and less from mitochondria. The total concentrations of ATP and ADP represented in the figure include free and magnesium

(Mg)-bound ATP and ADP. The total magnesium concentration has been held constant in the model.

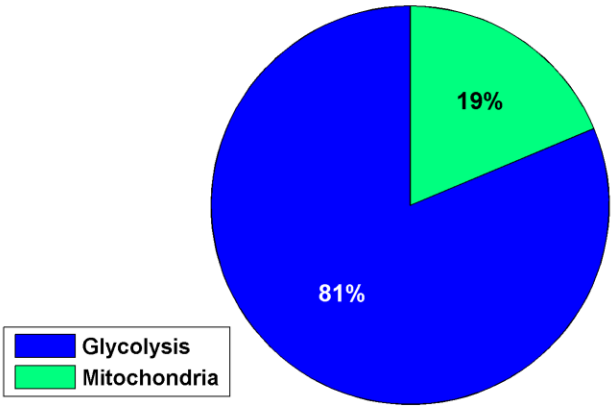

Figure 45: ATP Production by different pathways in NG108-15 cell

During steady state, the rate of ATP production is equivalent to ATP utilization. The analysis of ATP utilization revealed that 45% of total cellular ATP is used back in glycolysis to mediate the conversions by hexokinase and phosphofructokinase enzyme (Figure 46). Although the net production of ATP is more by glycolysis, 45% is a significant amount that is being used back. A higher utilization of ATP by glycolysis also enables the cells to consume more glucose which would be available for both glycolysis and pentose phosphate pathway. The ATP dependent sodium-potassium and the ATP-dependent calcium exchangers consumed 17 and 11% of the total cellular ATP respectively. The PPP and AK consumed less than 2% of the total ATP levels. The general ATPases representing all the other ATP-dependent process consumed 26% of the ATP (Figure 46).

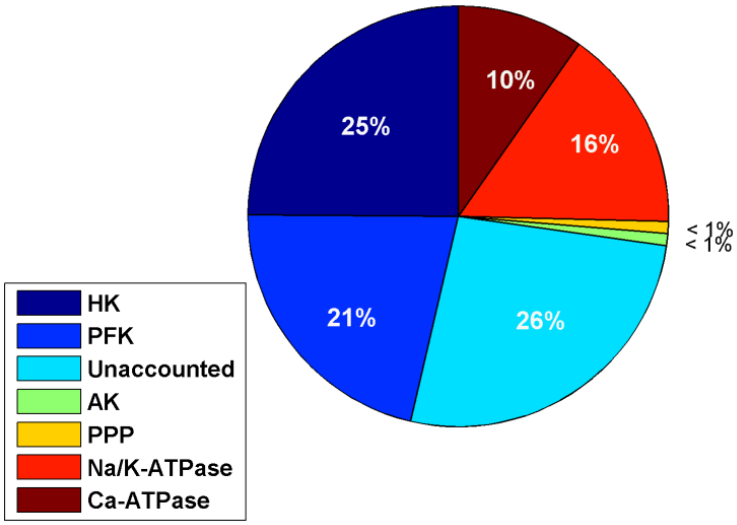

Figure 46: ATP utilization by different cellular processess in NG108-15 cell

NG108-15 cells lack glutamate [104] indicating the absence or a non-functional malate-aspartate-shuttle. The other shuttle capable of transferring the high-energy electrons generated in the glycolytic pathway into mitochondria and simultaneously active in brain could be the Glyceraldehyde-3-phosphate shuttle (G3P shuttle) [102]. The G3P shuttle transfers four high-energy electrons from the cytosol to mitochondrial electron transport chain by the flavin nucleotides. The efficiency of G3P shuttle is lower compared to malate-aspartate shuttle (MAS). MAS transfers six high-energy electrons into mitochondria. The activity of NAD/NADH recycling was compared as it determines the activity of glycolysis and mitochondria. The glycolytic lactate dehydrogenase has recycled 93% of NAD/NADH and 7% was recycled by mitochondria (Figure 47). The lower mitochondrial recycling of NAD/NADH demonstrates that not too many electrons are entering the mitochondria leading to a lower mitochondrial membrane potential generation. This lowered membrane potential reduced the drive for ATP synthase and resulted in lower mitochondrial ATP production.

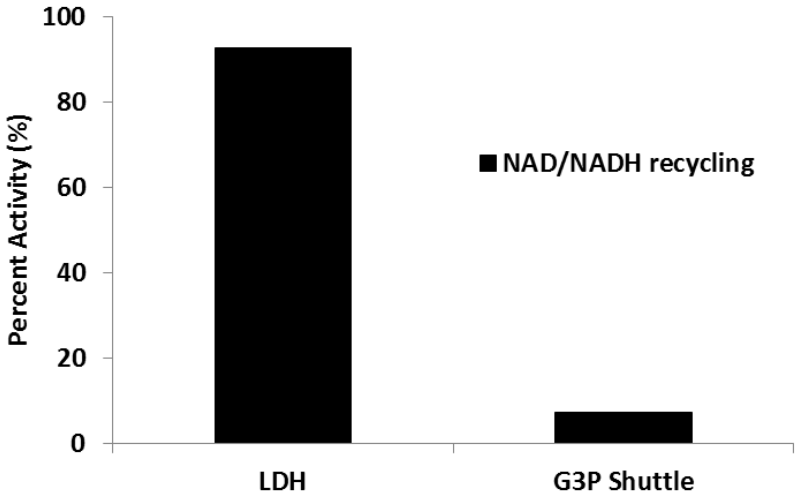

Figure 47: Predicted NAD/NADH recycling between glycolytic lactate dehydrogenase (LDH) and glycerol-3-phosphate (G3P) shuttle

5.3.2. Simulating neuronal-metabolic model to steady state

Cellular membrane properties are sensitive to changes in cellular metabolism especially in neurons. So, the calibrated metabolic model was coupled to neuronal module for building the neuronal-metabolic model. The coupled model was simulated to steady state and the activities of ATP-dependent pumps were matched. The extracted parameters (Table 7 and Table 8) including ion pumps and leaks parameters were exported into the neuronal-metabolic model for simulating steady state. The neuronal-metabolic model is simulated to continuously generate action potentials and predict the changes in the intracellular ionic concentrations. The model-generated action potentials were in good agreement with the experimentally obtained recordings (Figure 48A). The coupled model was simulated for 80 min and only the first 1000 action potentials generated a time span of 12 min are shown here.

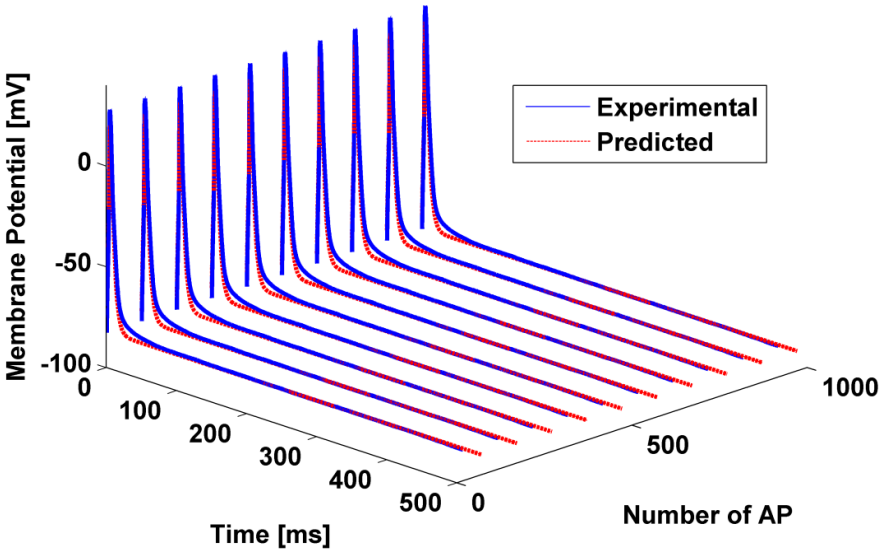

Figure 48: Simulated (red) and measured (blue) action potentials of NG108-15 cell

The sub-cellular ionic concentrations of all ions change rapidly during AP generation and reaches back to a steady state. Moreover, the bulk cytosolic concentrations have increased slightly and reached steady state. Simulating multiple action potentials also caused the sub cellular sodium (Figure 49- blue), potassium (Figure 50- red) and calcium (Figure 51- pink) concentrations to spike along with the action potential. The exchangers sensed a rapid increase in subcellular ionic concentration and extruded increased concentrations from the cell to restore ionic balance. A certain amount of ions also diffused into the cell increasing intracellular concentrations. The altered concentrations sodium (Figure 49 – green), potassium (Figure 50 - green) and calcium (Figure 51- gold) were also determined. The change in bulk concentration is small and usually assumed to be negligible. The metabolic model senses changes in bulk cytosolic concentrations and alters the metabolic activity. The rate change of concentrations usually varies by the membrane electrical activities and cell types [105].

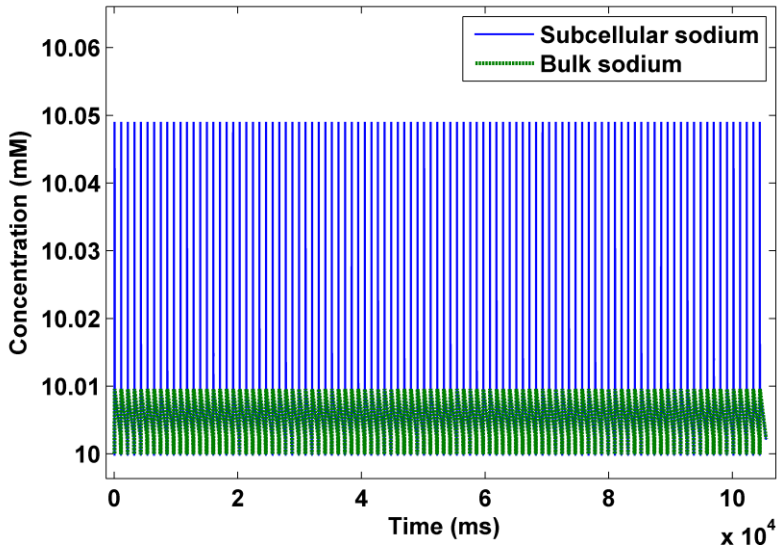

Figure 49: Predicted changes in subcellular and bulk cytosolic sodium concentrations during action potentials

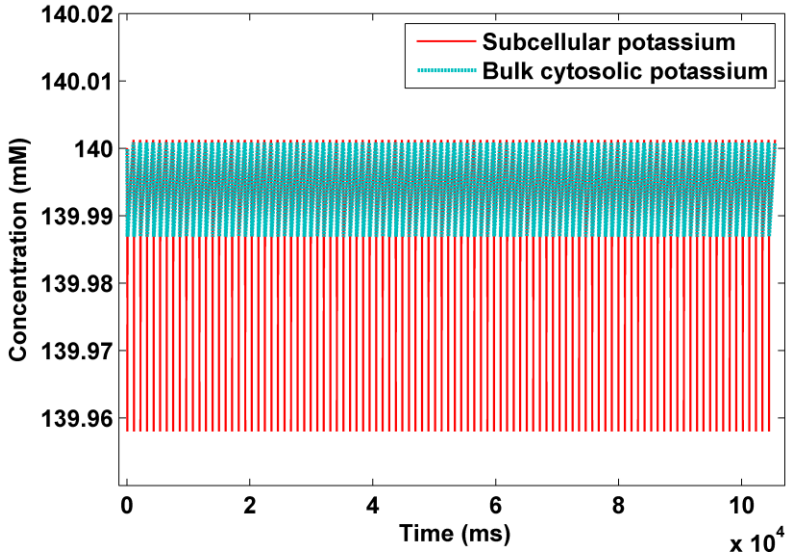

Figure 50: Predicted changes in subcellular and bulk cytosolic potassium concentrations during action potentials

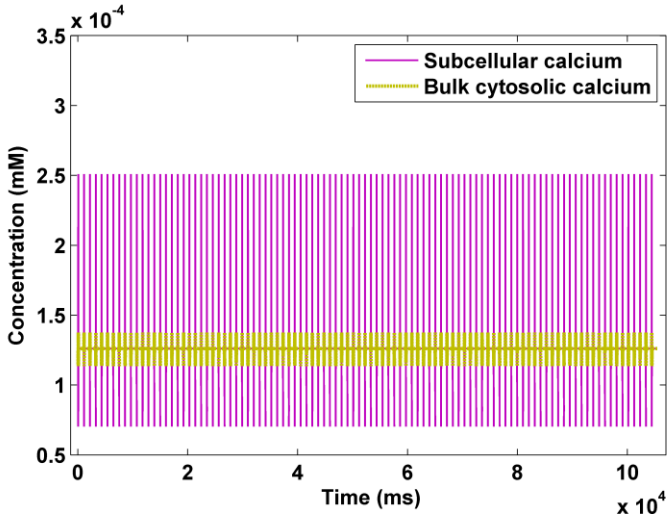

Figure 51: Predicted changes in subcellular and bulk cytosolic calcium concentrations during action potentials

The fluxes obtained from the neuronal-metabolic model was also extracted and compared to the experimentally determined values. An excellent fit was obtained to glucose and lactate flux (Figure 52). The intracellular ATP and ADP levels were also in agreement with the measured values (Figure 53).

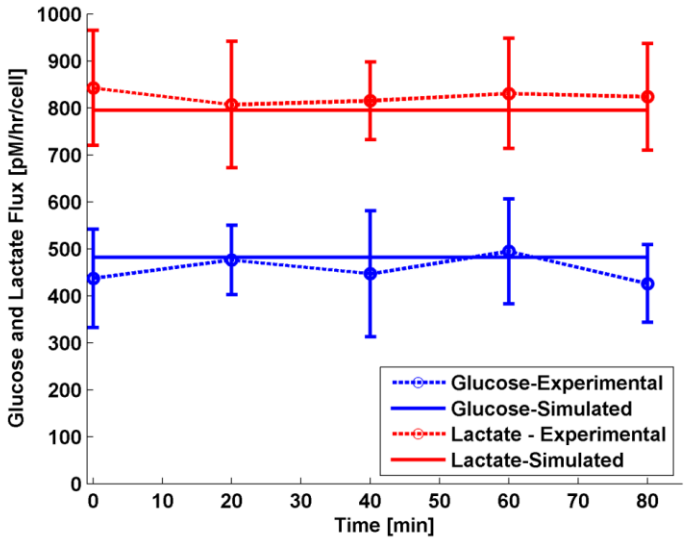

Figure 52: Compared glucose (blue) and lactate (red) flux obtained from neuronal-metabolic model (solid line) to experimental values (dotted line)

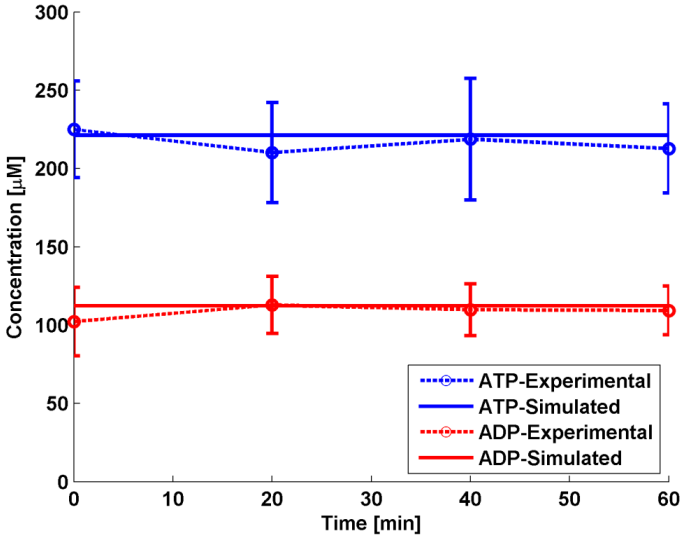

Figure 53: Compared ATP (blue) and ADP (red) flux obtained from neuronal-metabolic model (solid line) to experimental values (dotted line)

The low levels of intracellular pyruvate levels were predicated by the model (Figure 54). The lower pyruvate levels enable cells to avoid cell death by inhibiting the HDAC1/HDAC3 [106]. The extracellular and mitochondrial levels of pyruvate levels are low compared to the cytosolic levels. However, most of the pyruvate ended up as lactate due to elevated glycolysis.

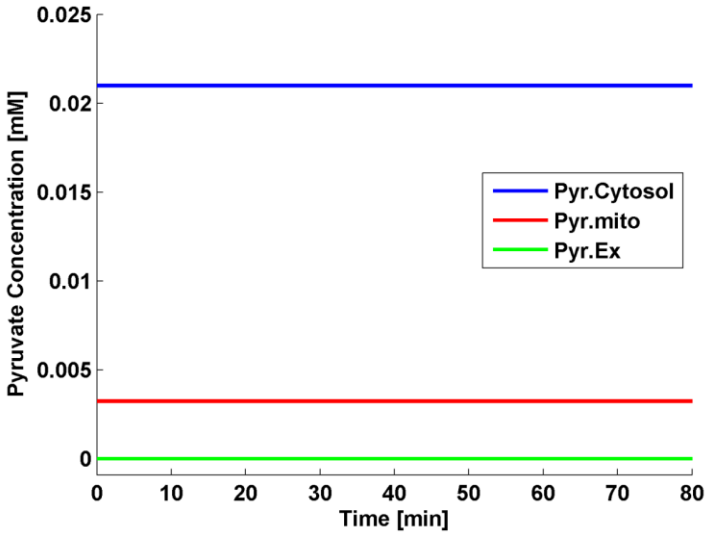

Figure 54: Predicted extracellular (green), mitochondrial (red) and cytosolic (blue) pyruvate concentrations

Phosphoribosyl pyrophosphate (PRPP) in pentose phosphate pathway is a precursor for several biomolecules. The predicted PRPP levels are in close range to that found in B16 melanoma cells [107]. PRPP transfers a high energy phosphate for the phosphorylation of purines bases and synthesis of purines, pyrimidines and pyridine nucleotides.

A proton gradient is established across inner mitochondrial membrane as a result of transport of electrons by cytochrome complexes. The mitochondrial membrane potential of NG108-15 cells was found to be -122 mV (Figure 55) and was in range as with the other neuroblastoma cell lines [108]. This potential difference drives the ATP synthesis by F_1F_0ATPase pump. The redox mechanisms have a huge effect on the cellular metabolic activities. The metabolic activities, ATP levels and redox levels are tightly integrated into the model. The redox mechanism is sensitive to alterations in glycolytic enzyme activities. The intracellular metabolite concentrations are dependent on changes in protein activities.

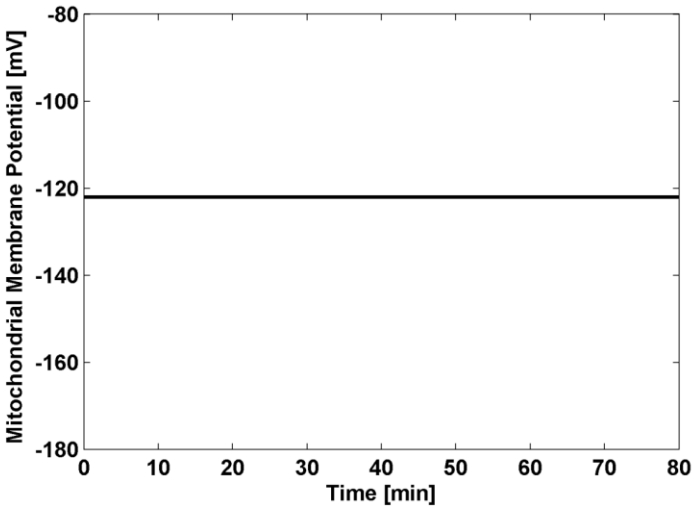

Figure 55: Predicted mitochondrial membrane potential of NG108-15 cell

The metabolite concentrations and flux rates in the model were at steady state and the protein functions were dependent on the maximum activity of the enzymes. The activities of

these enzymes lie mostly at plateau. An increase or decrease in protein activity will determine the metabolite concentration and will also restore the model back to original steady state upon perturbations in metabolite levels. The stability of metabolic activity is not only due to the stoichiometry of metabolites but due to regulatory protein mechanisms.

5.4. Perturbing glycolysis

The first rate limiting step in glycolysis is the ATP dependent conversion of glucose to glucose-6-phosphate (G6P). The phosphorylation converts non-ionic form of glucose to anionic G6P. G6P act as the entry point for PPP and glycolysis. Several studies have shown that hexokinase plays a crucial role in initiating and maintain high glycolytic rates in rapidly proliferating cells [52]. To inhibit the glycolytic pathway, cells were treated with 2-Deoxy-glucose (2DG). The molecular structure of 2DG is similar to glucose and the cell transports it through the glucose transporters. 2DG is an effective glycolytic inhibitor as it not only competes with cellular glucose for phosphorylation but also directly decreases cellular ATP levels by consuming ATP during the conversion to 2-deoxyglucose-6-phosphate (2DG6P). The metabolite 2DG6P cannot be further metabolized down the glycolysis and get accumulated in the cell [105]. Moreover, neuronal cells lack glycogen stores and they depend on glycolysis as a source for carbon and energy production making glycolytic inhibition more pronounced.

To determine and experimentally validate the metabolic perturbations induced by glycolysis, the NG108-15 were exposed to 2DG followed by determining the metabolic activity and electrophysiological changes. To mimic the experimental conditions, the hexokinase enzyme was inhibited in the neuronal-metabolic model using an event in Simbiology.

5.4.1. Analysis of carbon flux

The scaling factor 'b' for inhibiting the hexokinase activity was estimated by predicting the IC_{50} values. The simulated lactate flux was initially fitted to experimentally measured values (Figure 56– red line) for determining the scaling factor (and IC_{50}). The rapid decline of glucose flux during the first 20 min shows that NG108-15 cells are sensitive to 2DG treatment due to elevated glycolytic activity. A 60 min exposure to NG108-15 cells decreased the lactate flux by 68%. The lactate flux has remained constant after 60 min and reached a plateau. The lactate flux obtained from the metabolic model gave a good fit to experimental measurements. The model predicted a decline in glucose flux upon inhibiting hexokinase activity (Figure 56 - blue line). A 60 min exposure of 2DG leads to a 61% decrease in glucose flux into the cell. The model predicts that a prolong exposure of 2DG has further lowered the glycolytic flux. The glucose uptake rates were not determined as the assay kit was detecting both glucose and 2DG.

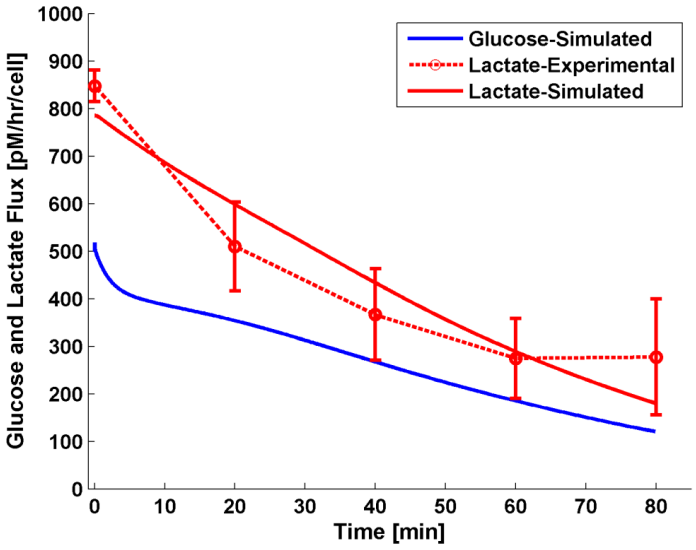

Figure 56: Predicted glucose uptake and lactate flux of 2DG compared to experimental data

The metabolic flux analysis of carbon usage by NG108-15 cell upon exposure to 2DG is shown in Figure 57. The amount of carbon that ended up as lactate decreased from 83% to 66%. The overall carbon flux into all the pathways decreased. But due to lowered carbon usage by glycolysis during 2DG treatment, the mitochondrial carbon usage has increased from 15% to 33%. (Figure 44 and 57).

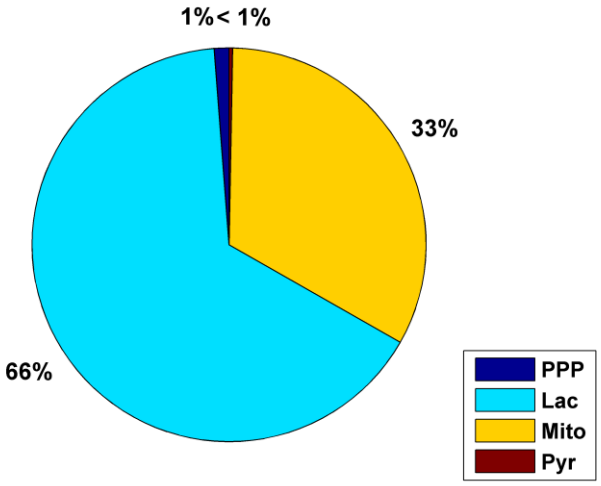

Figure 57: Carbon flux analysis of NG108-15 cell exposed to 2DG

The cellular pyruvate levels were also analyzed to examine the amount and rates of pyruvate flux into different pathways. Inhibition of glycolysis reduced the cytosolic pyruvate flux significantly and provoked a decrease in transport of pyruvate into mitochondria (Figure 58). Moreover, an external supply of pyruvate could have significantly delayed the effect of glycolysis inhibition [105].

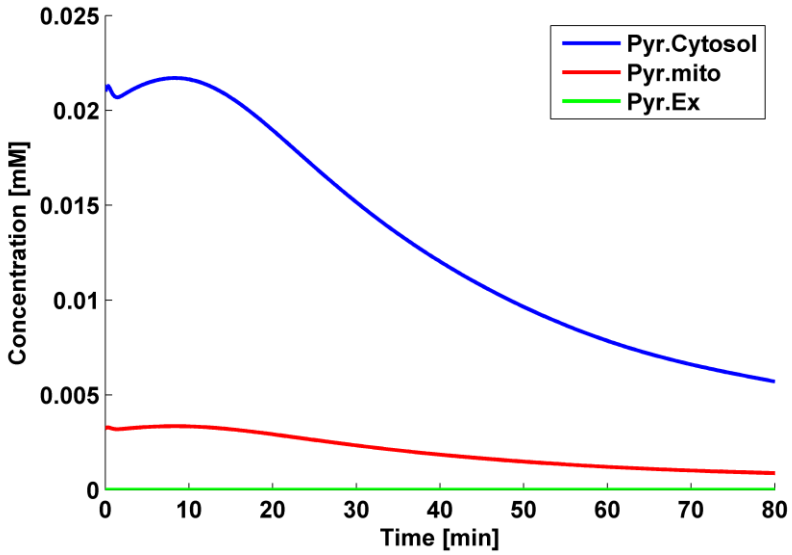

Figure 58: Predicted pyruvate flux during simulating the effects of 2DG

5.4.2. ATP production and utilization

The exposure of 2DG decreased carbon flux into the cell resulting in a lowered cellular ATP levels. The model predicted intracellular ATP (Figure 59) and ADP levels (Figure 60) were in agreement with the experimentally measured ATP and ADP levels. Since the adenosine level in the model is conserved, a decrease in ATP and ADP levels caused the cellular AMP levels to rise (Figure 61). The conversion of ATP, ADP to AMP is mediated by the enzyme Adenylate kinase (AK). After 20 min, the cellular ADP level predicted by the model decreased faster compared to the experimental measurements. It may be due to the production of adenosine by cells or other mechanisms that are currently not accounted in the model. The overall trend of changes in the adenine nucleotide predicated by the model is in good agreement with the experimentally determined values.

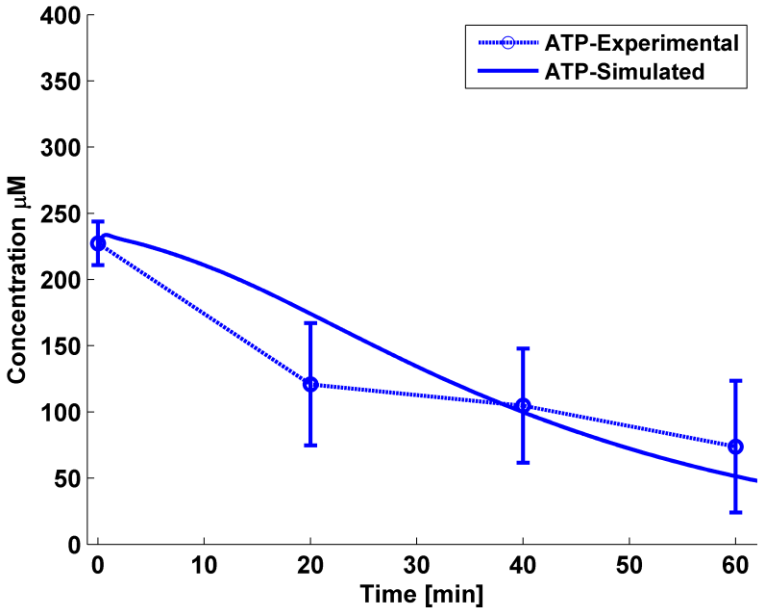

Figure 59: Predicted (solid line) and experimentally (O-dotted line) measured ATP production exposed to 2DG

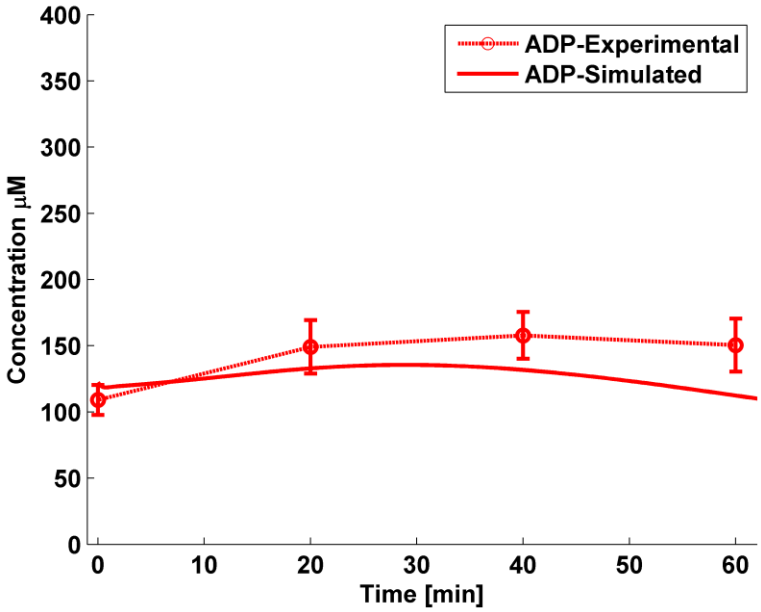

Figure 60: Predicted (solid line) and experimentally (O-dotted line) measured ADP production exposed to 2DG

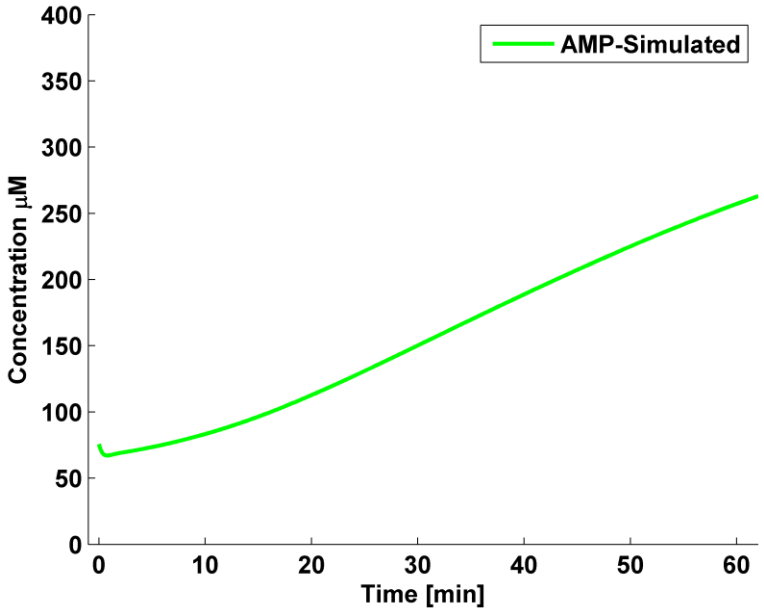

Figure 61: Predicted (solid line) AMP levels exposed to 2DG

The ATP production by individual pathways exposed to 2DG were analyzed. The over all ATP production by both glycolysis and mitochondria has decreased. But the percent amount of ATP produced by glycolsyis has lowered from 81% to 60% (Figure 62). The mitochondrial ATP production has increased from 19% to 40%. The increase in mitochondrial activity is due to the inhibitoion of glycolysis which focred the cell to rely on mitochondrial ATP generation to meet its cellular requirments.

The usage of ATP by difference cellular pathways was also evaluated simulaneously (Figure 63). The total ATP usage by cellular pathways went down. The ATP utilized in glycoslysis ishas reduced from 46% to 41%. The ATP consumption by general ATPases, NaK-ATPase, PPP and AK were 29%, 11%, 18% and 1% respectively. The lowered carbon influx into mitochondria has decreased the generation of protons necessary for maintaining the required mitochondrial

membrane potential for driving ATP synthase. The simulated mitochondrial membrane potential (ΔΨ) changed from -120mV to -107 mV (Figure 64). The decline in ΔΨ was not suffieicent enough inhibiting ATP generation infact a higher amount of mitochondrial ATP were synthesised and transported into cytosol by Adenine nucleotide transloactor (ANT). The ANT is responsible for exporting ATP from mitochondrial matrix and importing ADP from cytosol.

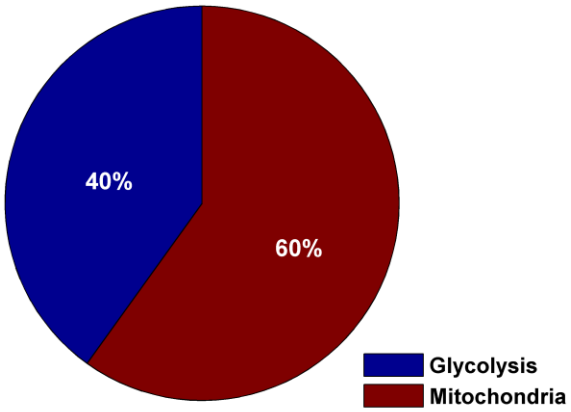

Figure 62: Predicted ATP production by NG108-15 cell upon exposure to 2DG

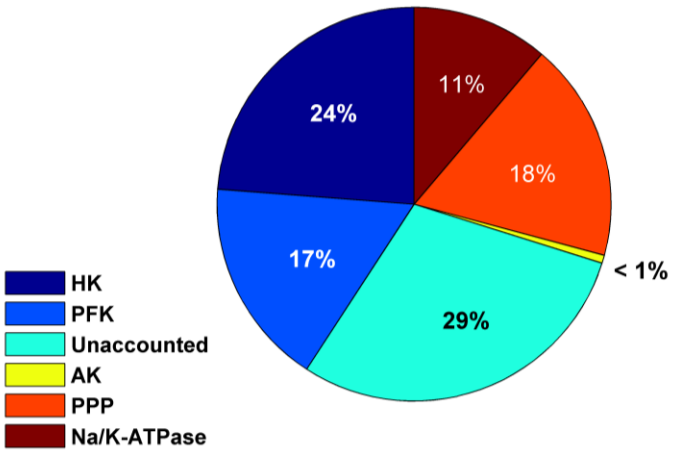

Figure 63: Predicted ATP utilization by NG108-15 cell upon exposure to 2DG

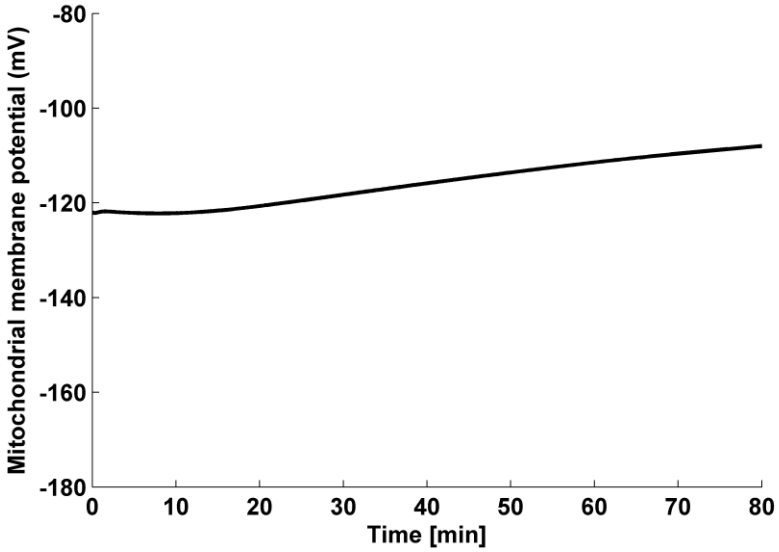

Figure 64: Predicted mitochondrial membrane potential of NG108-15 cell exposed to 2DG

5.4.3. Predicting action potentials and ionic concentrations

The neuronal-metabolic model predicted the changes in action potential peaks shapes as the cellular metabolism was being affected. The experimentally measured action potentials exposed to 2DG were compared to model generated action potentials and were in good agreement (Figure 65). The entire action potential time series was matched to experimental recordings to validate model predictions. The evaluation of time series data is crucial as most of the drugs reduced might cause similar effects in AP but the time scale of those effects would be significantly different.

Inhibiting glycolysis caused a compelling change in intracellular ATP levels. Reduction of intracellular ATP levels lead to decreased ATP-dependent electrogenic pump activity and also activated ATP dependent potassium channel. The changes in membrane electrical activity cause changes in intracellular ionic concentrations. The intracellular accumulation of sodium (Figure

66) and calcium (Figure 68) followed by a decline in potassium (Figure 67) concentration was observed.

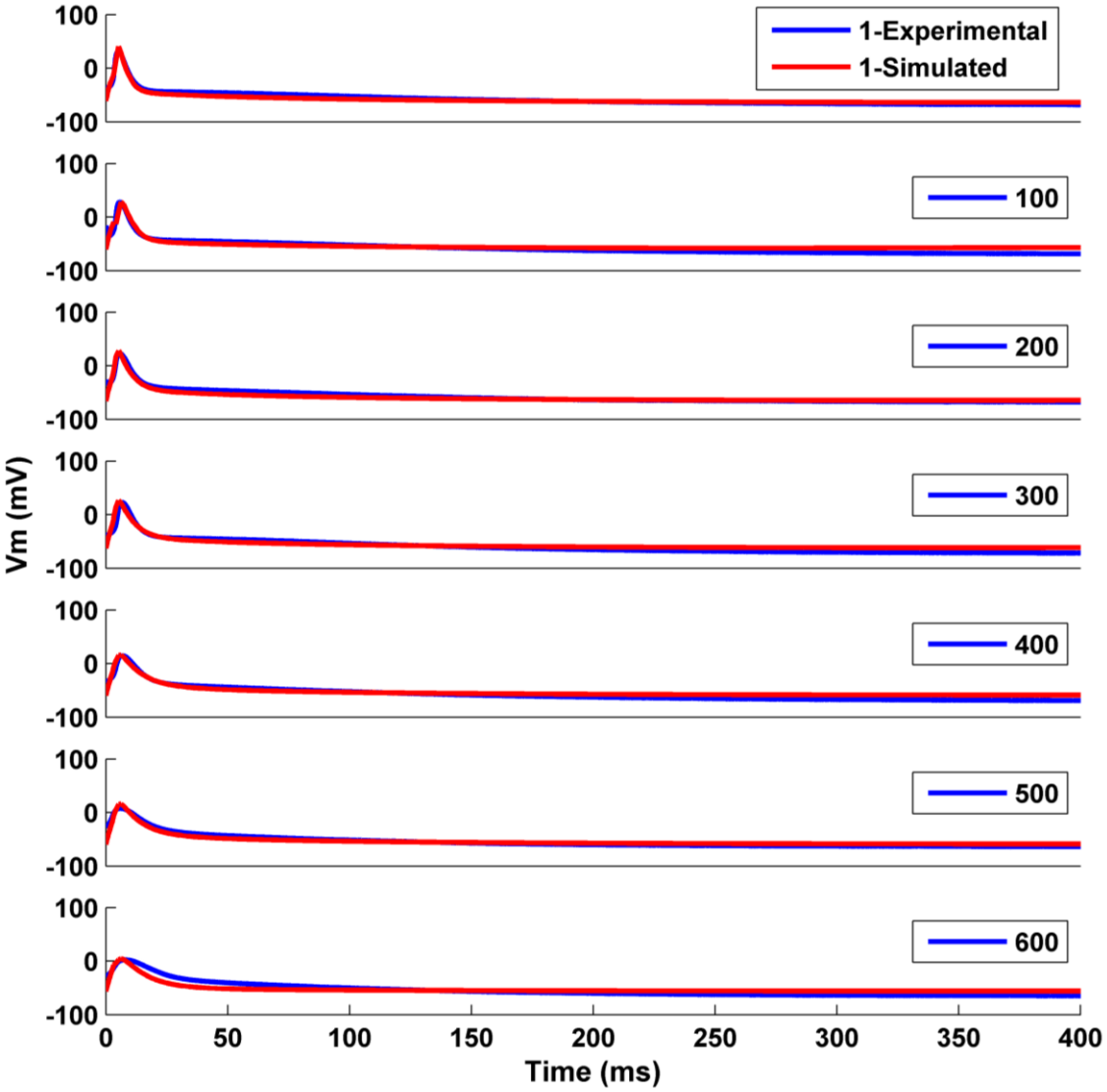

Figure 65: Predicted (red) action potential time series compared to experimental (blue) recordings when treated with 2DG

The sodium, potassium and calcium concentrations reached to 13.82, 132.8 and 0.085 mM respectively after 17 min. It has been found that neurons are more sensitive and loose cellular homeostasis than glial cells upon exposure to metabolic perturbations [105]. The

simulation showed the calcium concentration has increased rapidly after 15 min (Figure 68) and is in agreement with the literature reported changes [105].

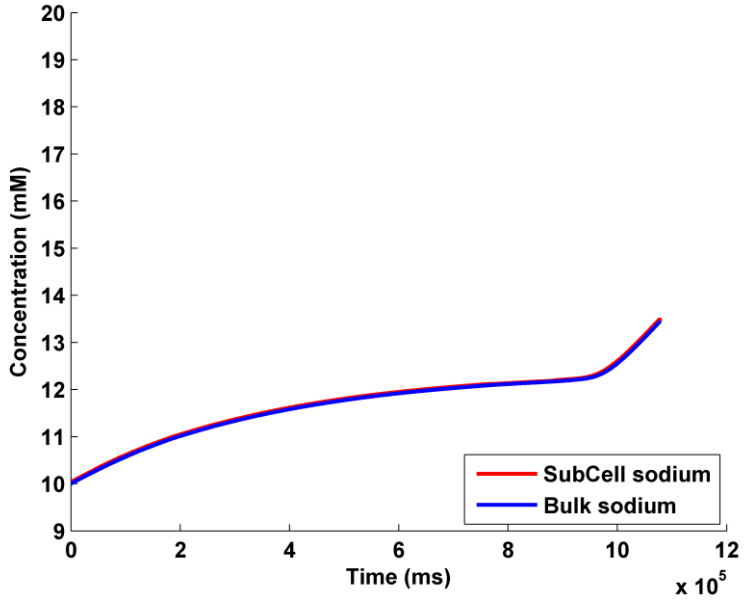

Figure 66: Predicted 2DG induced changes in subcellular and bulk cytosolic sodium concentrations

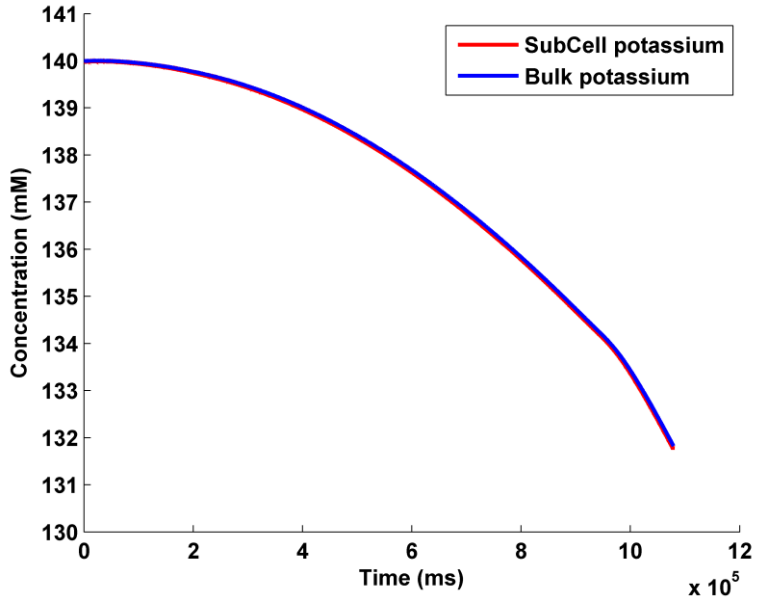

Figure 67: Predicted 2DG induced changes in subcellular and bulk cytosolic potassium concentrations

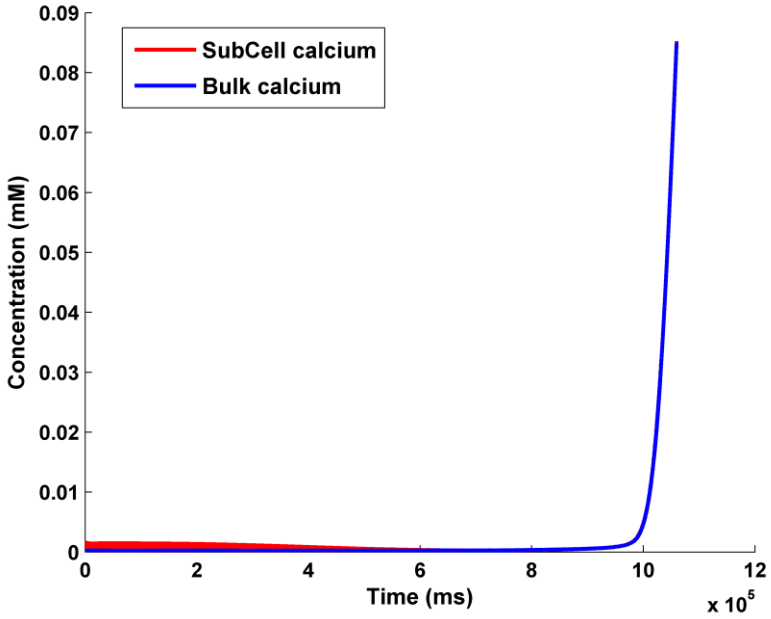

Figure 68: Predicted 2DG induced changes in subcellular and bulk cytosolic calcium concentrations

5.5. Perturbing mitochondrial electron transport chain

The mitochondrial electron transport induced perturbations were studied by inhibiting oxidative phosphorylation reaction using cyanide. Cyanide is a potent reversible inhibitor of mitochondrial cytochrome oxidase and causes sudden death by acting on central nervous system. Cyanide predominately inhibits the consumption of oxygen required for ATP production. Although cyanide inhibition is reversible, a prolong exposure will lower cellular ATP levels inducing an irreversible damage to cell. The biochemical events during cyanide exposure have been studied on a wide variety of cells including neurons and NG108-15 cells [89]. To determine and experimentally validate the metabolic perturbations induced by electron transport chain, the NG108-15 were exposed to cyanide followed by determining the metabolic activity and electrophysiological changes.

To mimic the experimental conditions, the oxidative phosphorylation in the mitochondria was inhibited in neuronal-metabolic model by creating an event in Simbiology. Simultaneously, even the contribution of oxidative phosphorylation towards mitochondrial membrane potential was inhibited.

5.5.1. Analysis of carbon flux

The scaling factor 'b' for inhibiting oxidative phosphorylation was estimated by predicting the IC_{50} values. The IC_{50} values were obtained by fitting the simulated lactate flux to experimental data (Figure 69– red line). The model showed a decreased glucose flux into the cell upon inhibiting mitochondrial activity (Figure 69 - blue line). The lactate flux obtained from the metabolic model gave a satisfactory fit to experimental measurements. The experimental and simulated results showed an initial increase in lactate production by NG108-15 cell.

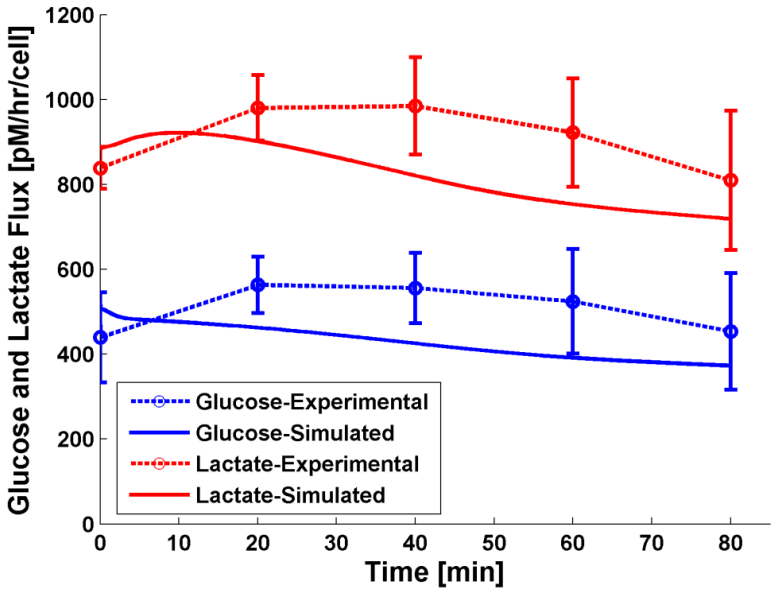

Figure 69: Cyanide treated simulated glucose uptake and lactate flux compared to experimental data

The increase in lactate production was due to the inhibition of mitochondrial process forcing the cell to rely on glycolysis for ATP production. The mitochondrial pyruvate levels have increased during the first couple of minutes as the mitochondria were unable to metabolize pyruvate through TCA cycle (Figure 70 – red line). The mitochondrial pyruvate levels have increased to 203% whereas the cytosolic levels have lowered by 14% after a 5 min exposure to cyanide. The prolonged exposure has caused the cytosolic pyruvate levels to lower as pyruvate was used during glycolysis to generate lactate and ATP (Figure 70 –blue line). The reduction in cytosolic levels of pyruvate caused the mitochondrial pyruvate to be transported back to into cytosol for ATP generation. The overall cytosolic pyruvate levels were reduced by 35% and the mitochondrial pyruvate levels were reduced by 24% after 80 min.

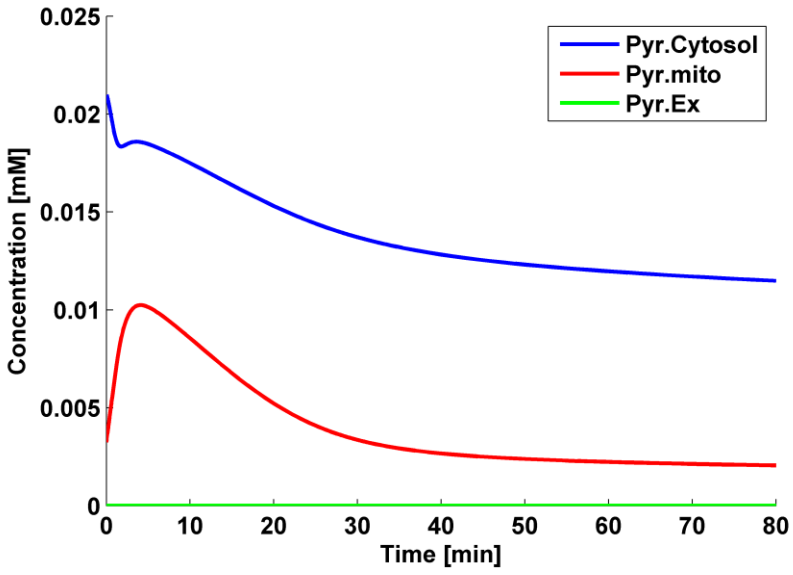

Figure 70: Simulated pyruvate fluxes during cyanide treatment

The metabolic flux analysis of carbon utilization showed that carbon utilization by glycolysis has increased from 83% to 88% upon exposure to cyanide (Figure 71). The

mitochondrial carbon utilization decreased from 15% to 10%. No significant change in PPP was observed as the glycolytic metabolites were deplting faster leaving no excess metabolities to enter PPP. The transport of pyruvate into the extracellular space was less than 1%. These results indicate a shift in metabolic activity from mitochondria to glycolysis occurs during hypoglycemia.

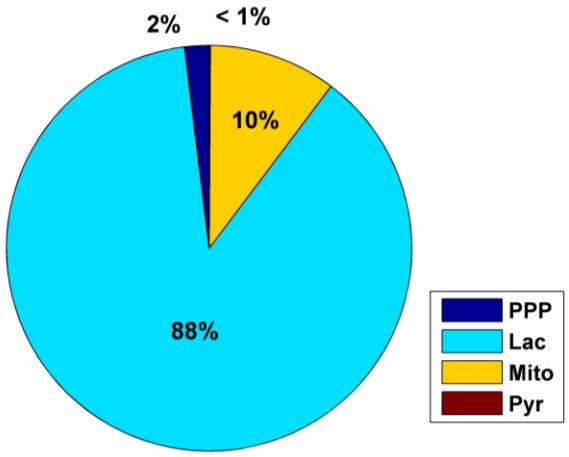

Figure 71: Predicted carbon utilization by NG108-15 cells during cyanide treatment

5.5.2. ATP production and utilization

The contribution of ATP production by mitochondrial oxidative phosphorylation was determined by treating cells with cyanide, a respiratory chain inhibitor. Treatment with cyanide not only eliminates the utilization of pyruvate but also other endogenous fuels such as amino acids and fatty acids that may contribute high energy electrons for ATP synthesis [105]. The ATP production during cyanide treatment was measured and compared to simulated values. The model accurately predicted change in cellular ATP (Figure 72) and ADP (Figure 73) levels. These results were in accordance with the cyanide effects tested by Ray et al. [89]. Glycolysis alone could not maintain the cellular ATP level and the rate of decline in cellular ATP was slow

compared to 2DG treatment. The AMP levels slightly increased as the cellular ATP and ADP were converted by AK (Figure 74). A 60 minute exposure of cyanide lowered the cellular ATP levels to 148 ± 29 µM. The ADP levels did not change significantly and remained at 109 ± 15 µM indicating the conversion of cellular ATP to AMP.

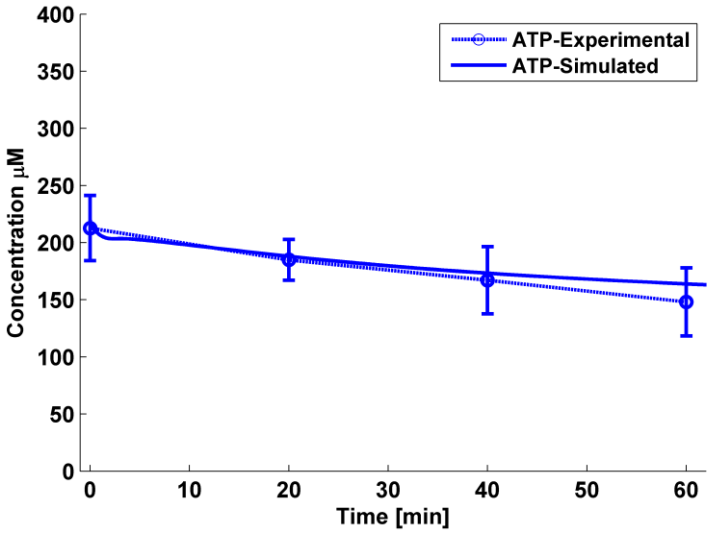

Figure 72: Predicted (solid line) and experimentally (O-dotted line) measured ATP production exposed to Cyanide

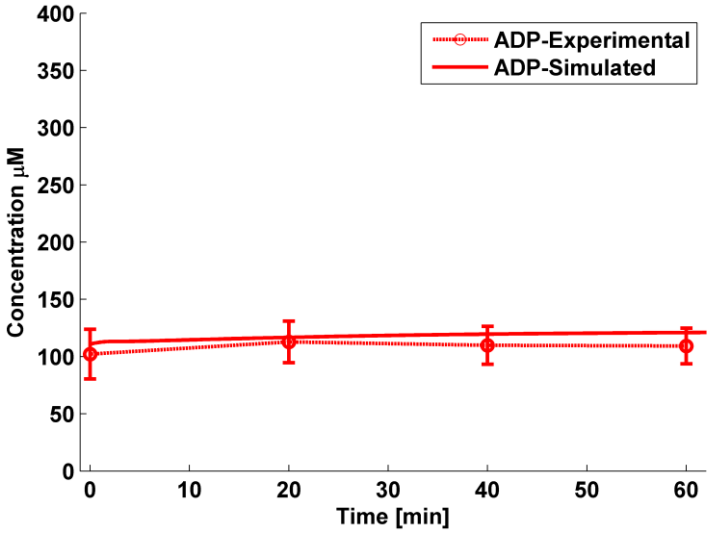

Figure 73: Predicted (solid line) and experimentally (O-dotted line) measured ADP production exposed to Cyanide

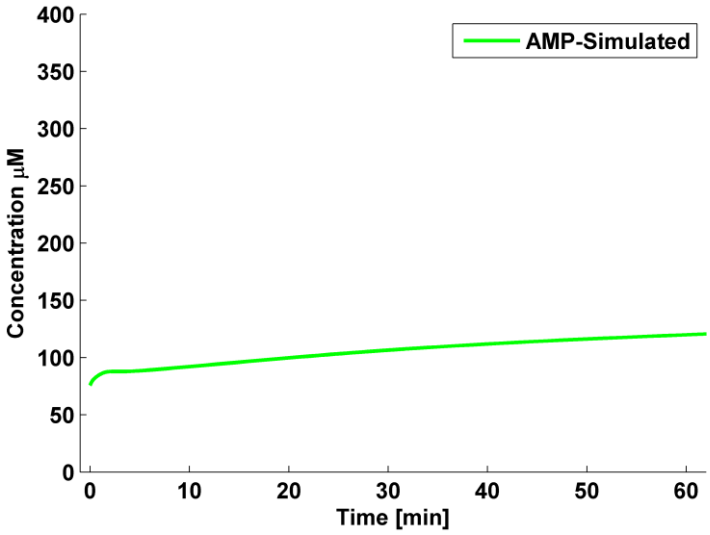

Figure 74: Predicted AMP levels exposed to 2DG

The ATP production by individual pathways exposued to cyanide was analyzed. The total production of ATP by both glycolysis and mitochondria has declined but the percent amount of ATP produced by glycolsyis has increased from 81% to 85% (Figure 75). The mitochondrial ATP production has decreased from 19% to 15%. Inhibition of mitochondria has focred the cell to rely on glycolysis for ATP generation. The ATP generated by glycolysis was sufficient enough for cellular functions. The ATP utilization by difference cellular pathways was determined (Figure 76). The ATP utilization by glycoslysis has increased from 41% to 49%. The ATP consumption by general ATPases, NaK-ATPase, Ca-ATPase, PPP and AK was 25%, 15%, 10%, < 1% and < 1%. The activity of general ATPases decreased by 4%. The carbon influx into mitochondria has decreased and lower number of protons were generated by TCA cycle.

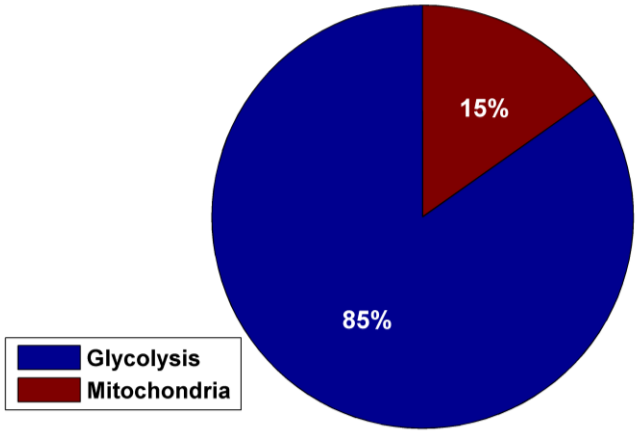

Figure 75: Predicted ATP production by NG108-15 cell upon exposure to Cyanide

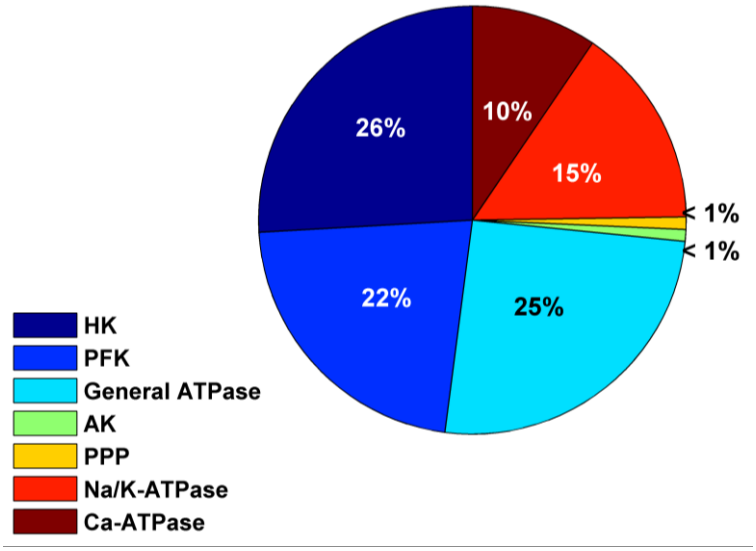

Figure 76: Predicted ATP utilization by NG108-15 cell upon exposure to Cyanide

Since the activity of glycolytic enzymes has not decreased significaantly, the NAD/NADH recycling has elevated and electrons are probably being transported into the mitochondria by the G3P shuttle thereby enabling the maintainence of mitocondrial membrane potetnial. The simulated mitochondrial membrane potential ($\Delta\Psi$) changed from -121 mV to -100 mV within 2 minutes due to usage of the existing electrons and slowly reached back to -110mV as the

electrons from glycolysis were transferred into mitochondria (Figure 77).

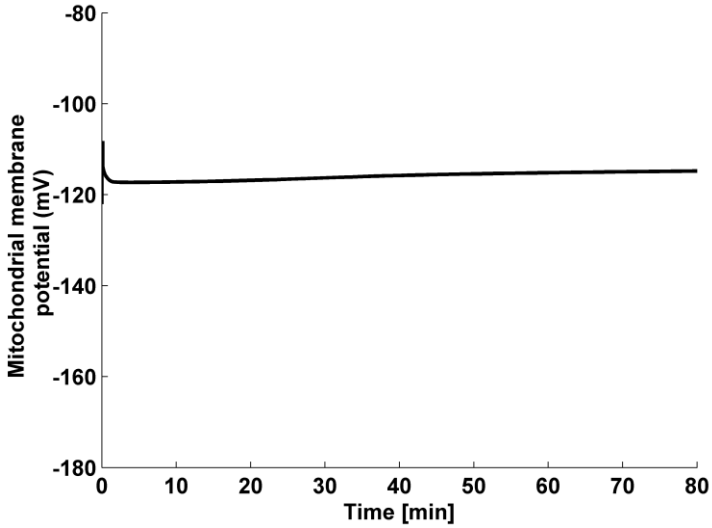

Figure 77: Predicted mitochondrial membrane potential of NG108-15 cell exposed to Cyanide

5.5.3. Predicting action potentials and ionic concentrations

The neuronal-metabolic model generated action potentials and predicted the changes in action potential peaks shapes as the cellular metabolism was inhibited. The action potential time series obtained from the model was plotted against the experimental recordings to validate the model. The measured action potentials matched the simulated action potentials (Figure 78). A visual analysis showed no change in the action potential peak shapes as the cellular ion channels and ATP dependent exchangers were functional. The required amount of ATP was being generated by glycolytic pathway. A detailed analysis of action potential time series has been performed in chapter 5.9.

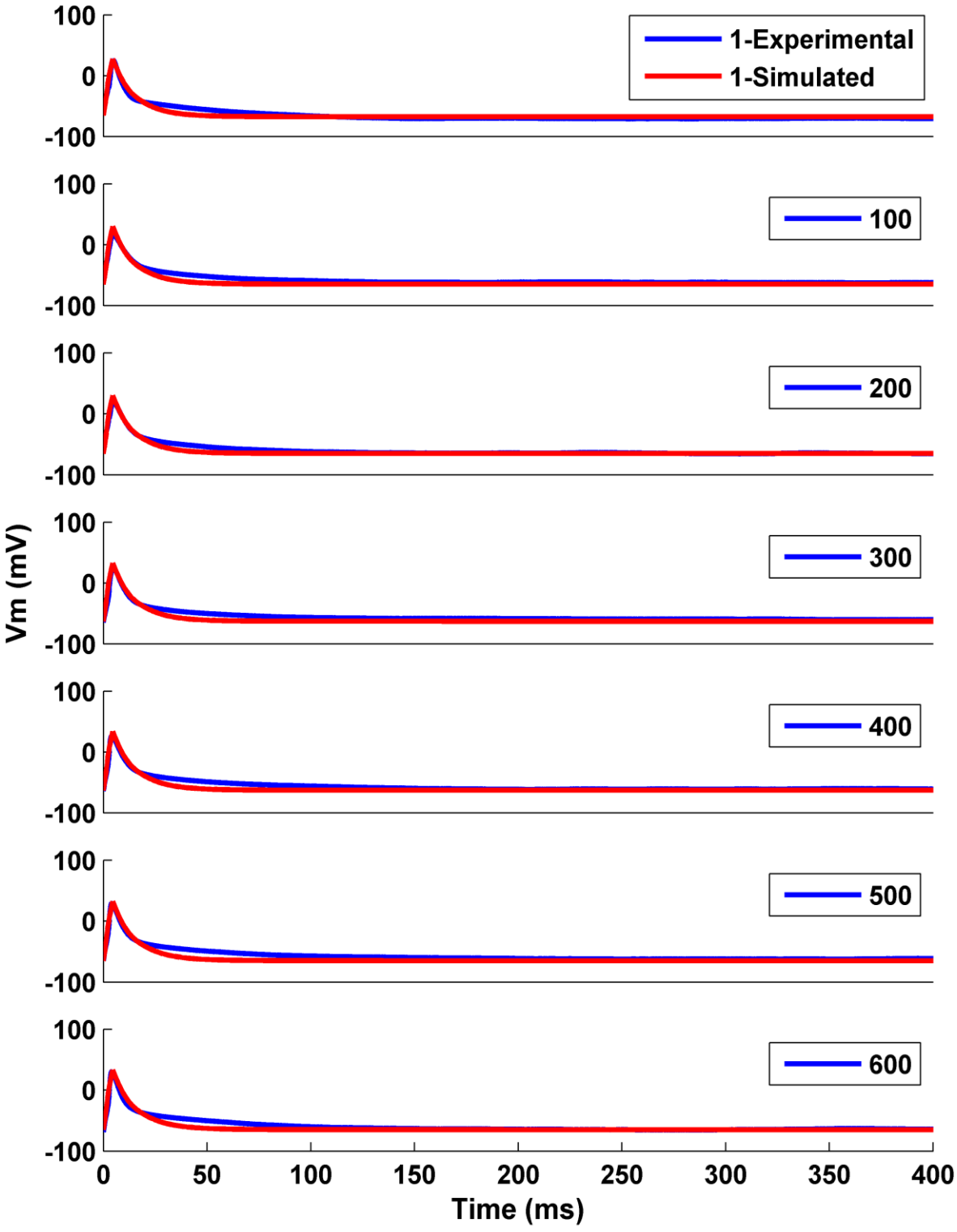

Figure 78: Predicted (red) action potential time series compared to experimental (blue) recordings when treated with cyanide

Inhibiting mitochondrial membrane potential has slightly reduced cellular ATP levels. The electrogenic ATP-dependent exchangers activity were unaffected (Figure 76) and have been successful at restoring ionic concentrations (Figure 79, Figure 80 and Figure 81). The sodium, potassium and calcium concentrations reached to 10.78, 138.1 and 0.125 mM respectively after 17 min. The action potential peak shape has not significantly altered. The change in intracellular ionic concentrations less initially as the cellular ATP levels were not lowered. After 17 min of exposure to cyanide, the ATP levels slightly reduced and the intracellular ionic concentrations were altered. The changes in sodium, potassium and ATP concentrations lead to a rapid rise in intracellular calcium concentration. The changes in the subcellular space are swift and achieved equilibrium with the bulk cytosolic concentrations. The above results obtained from simulating neuronal-metabolic model and experiments suggests that NG108-15 cells are insensitive to cyanide.

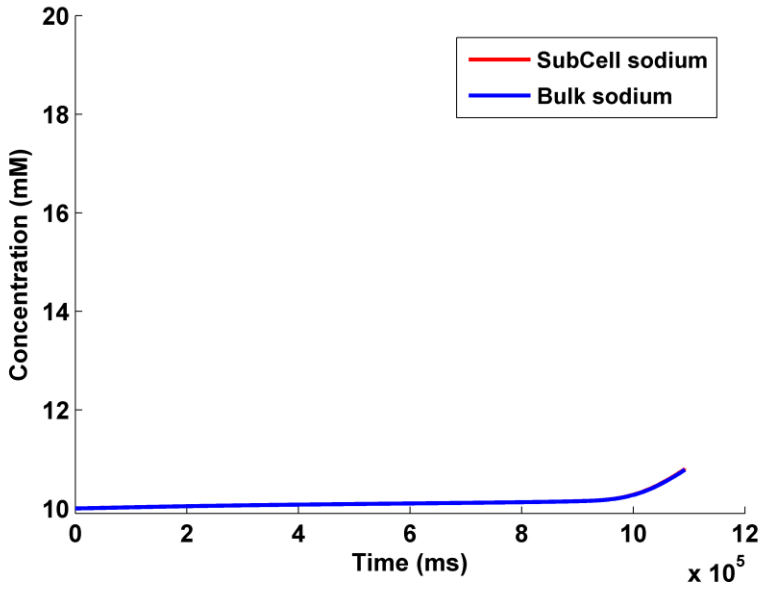

Figure 79: Predicted cyanide induced changes in subcellular and bulk cytosolic sodium concentrations

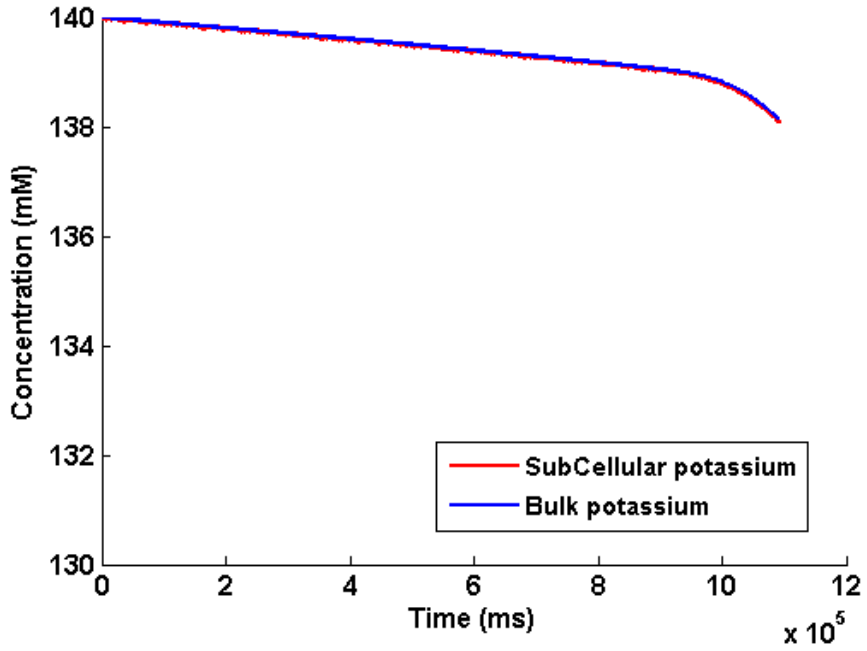

Figure 80: Predicted cyanide induced changes in subcellular and bulk cytosolic potassium concentrations

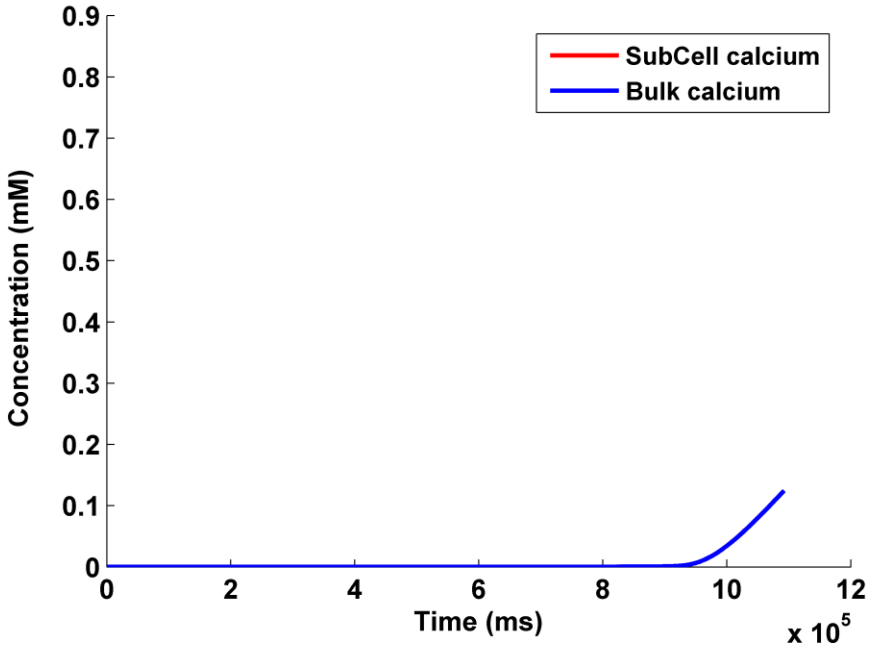

Figure 81: Predicted cyanide induced changes in subcellular and bulk cytosolic calcium concentrations

5.6. Perturbing mitochondrial TCA cycle and electron transport chain

Succinate dehydrogenase (SDH) was inhibited to investigate metabolic perturbations induced by mitochondrial TCA cycle and electron transport chain. SDH is the only enzyme that couples mitochondrial TCA cycle and electron transport chain. SDH is complex-II in the electron transport chain and does not pump protons directly across inner mitochondrial membrane. Complex-II transfers reducing equivalents through co-enzyme Q10 that gets re-oxidized by complex-III in inner mitochondrial membrane. Malonate is a competitive inhibitor of SDH and causes an accumulation of succinate in mitochondria. Malonate has been shown to induce *in vivo* and *in vitro* neuronal toxicity in a dose-dependent manner [109].

To investigate the metabolic perturbations induced by malonate, NG108-15 cells were exposed to Malonate followed by determining the metabolic activity and electrophysiological changes. To simulate experimental conditions, SDH enzyme in TCA cycle was inhibited in the neuronal-metabolic model by creating an event in Simbiology. The inhibition factor was predicted by fitting the model to experimental lactate flux. The IC_{50} values obtained are used for simulating the neuronal-metabolic model.

5.6.1. Analysis of carbon flux

The carbon flux into the cell has increased upon treating cells with malonate. A 20 min exposure of malonate has increased the glucose flux into cell by 30% (Figure 82 – blue line). The increased glycolytic flux subsequently resulted in an elevated lactate flux. The lactate flux was increased by 22.5% (Figure 82 – red line). The model also predicted an overall increase in glucose and lactate flux which is in agreement with the experimentally determined values

(figure 82). The increased glucose and lactate flux were lowered by 10% and 6% respectively after 60 min exposure. The mitochondrial flux decreased and an increase in cellular glycolysis was observed indicating that the cell was probably running at its maximum glycolytic capacity.

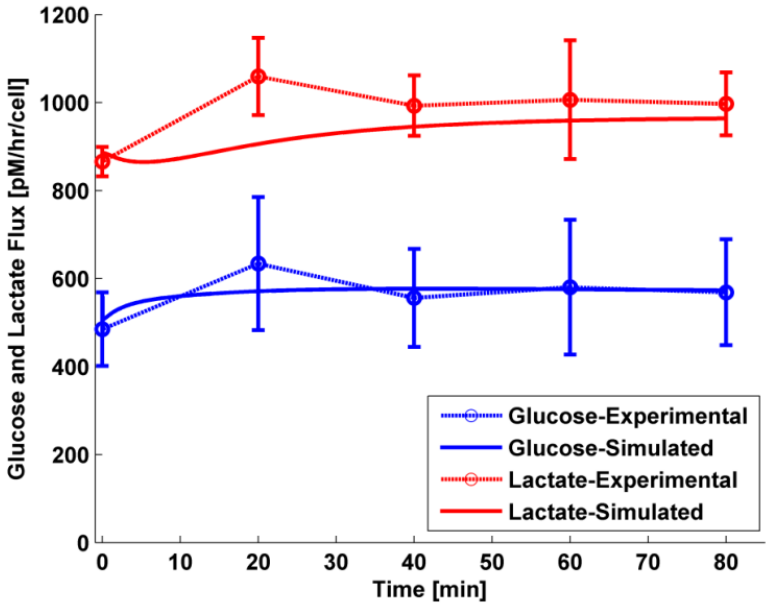

Figure 82: Simulated glucose uptake lactate release flux compared to experimental data by treating NG108-15 cells with malonate

The pyruvate flux was analyzed to track the flow of carbon into different pathways over time (Figure 83). A 9x increase in mitochondrial pyruvate concentration was observed upon a 30 min exposure to malonate. Similarly, the cytosolic pyruvate has also increased as the pyruvate was not metabolized in TCA cycle leading to a build-up in mitochondria and cytosolic compartments. The pyruvate levels were slowly reaching back to steady state adjusting to the perturbations caused by malonate. Due to increased requirement of pyruvate in glycolysis, a very small amount of carbon is exported out of the cell as pyruvate. Further analysis of the carbon flux into different pathways was performed. The glycolytic flux has increased by 2%. The

mitochondrial flux has decreased only by 2% since the pyruvate was getting accumulated in the mitochondrial compartment as shown in Figure 83. The carbon flux into PPP and extracellular pyruvate remained unaltered when compared with controls (Figure 44).

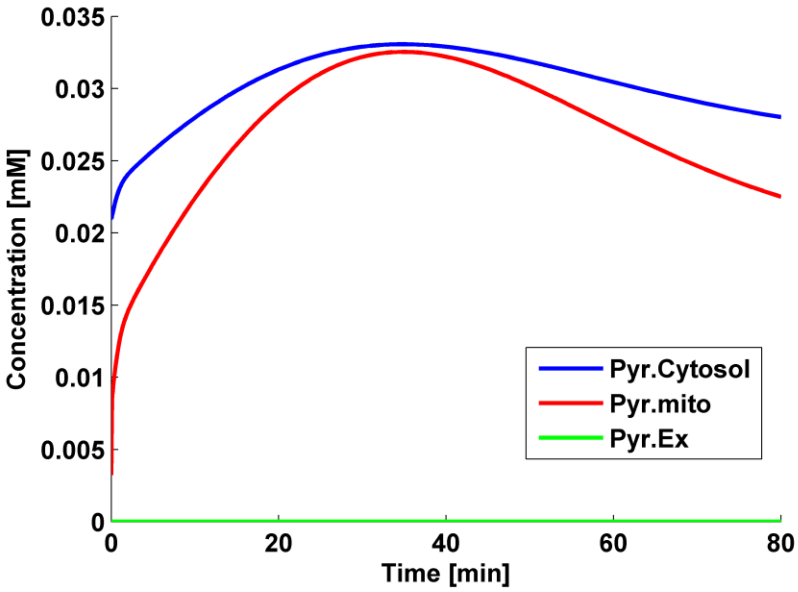

Figure 83: Analysis of pyruvate concentrations in cytosol, mitochondria and extracellular compartments during malonate treatment

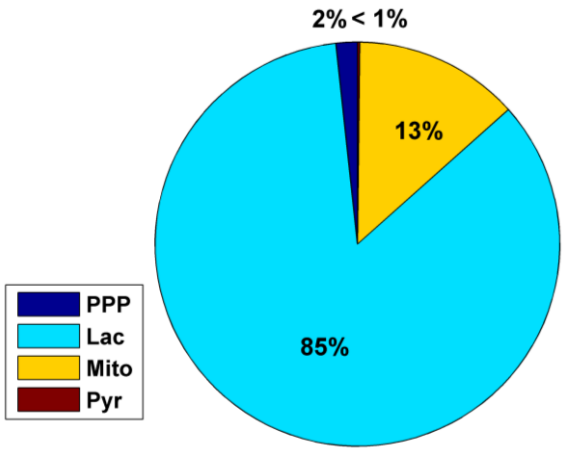

Figure 84: Analysis of carbon fluxes for cells exposed to malonate

5.6.2. ATP production and utilization

The changes in ATP and ADP levels were measured by exposing cells to malonate. The experimentally determined and simulated results of ATP (Figure 85) and ADP (Figure 86) measurements were in good agreement. The predicted AMP levels have also increased when treated with malonate (Figure 88). A 60 min exposure to malonate caused cellular ATP levels to decline by 22%. The reduction in ATP levels increased the ADP and AMP levels by 37% and 47% respectively. The adenine nucleotide levels were conserved in the model and their levels are governed by AK.

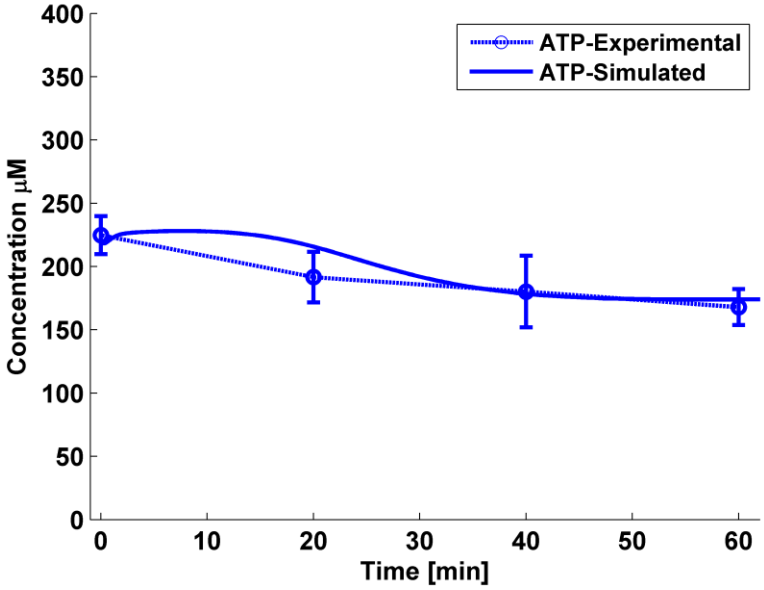

Figure 85: Experimental and predicted changes in intracellular ATP concentration during malonate treatment

The rate of decline in ATP production was slightly less compared to cells treated with cyanide. The protons generated from elevated glycolysis were transferred into the mitochondria by G3P shuttle. The transferred protons contribute towards the mitochondrial membrane potential. The mitochondrial membrane potential was reduced from -121 mV to -

117 mV (Figure 87). The mitochondrial membrane potential has been shown to be lowered by decrease in the cellular ATP production during malonate treatment in neurons. But due to the altered metabolic activity the mitochondrial membrane potential was not significantly altered.

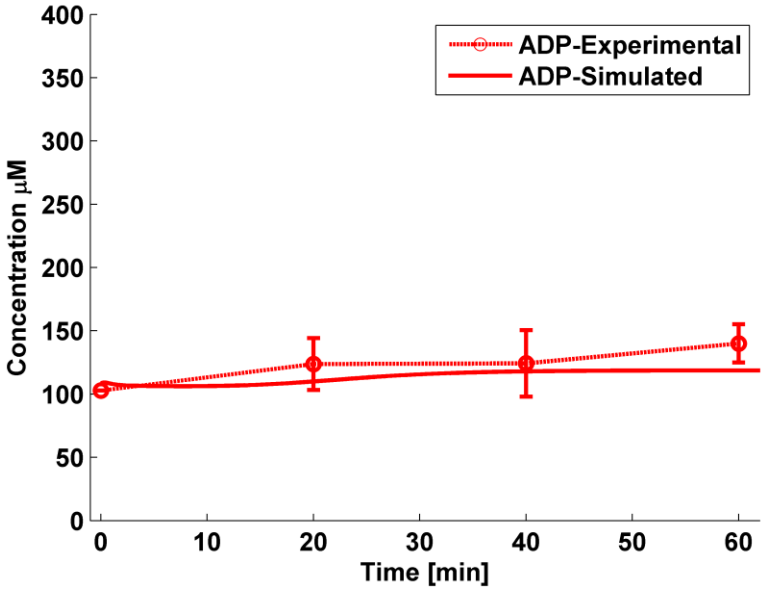

Figure 86: Experimental and predicted changes in intracellular ADP concentration during malonate treatment

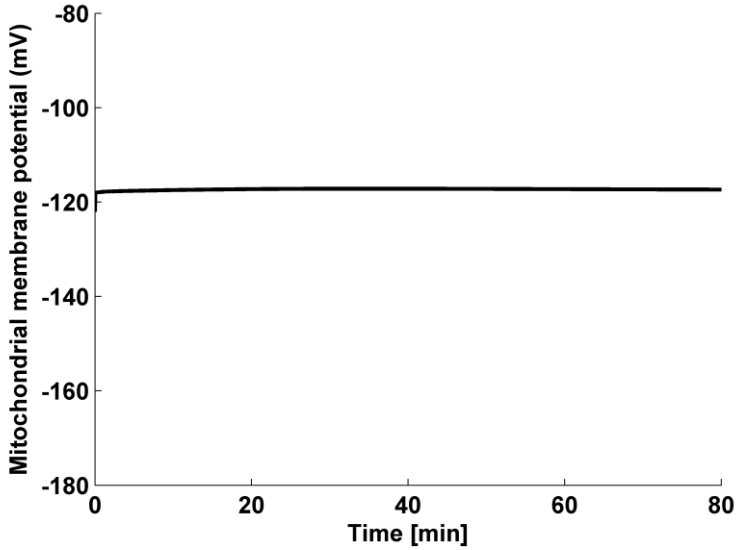

Figure 87: Mitochondrial membrane potential of NG108-15 cell during treatment with malonate

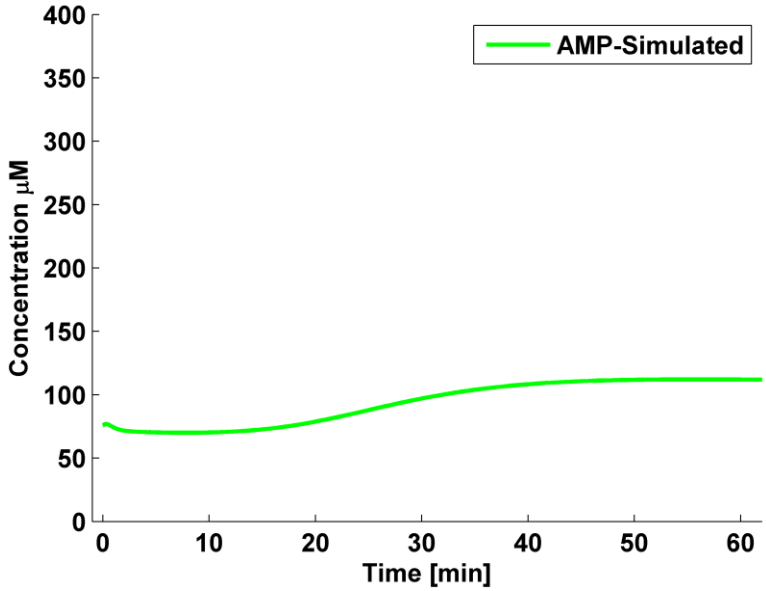

Figure 88: Predicted changes in intracellular AMP concentration during malonate treatment

A complete analysis of cellular ATP production and utilization was performed to gain metabolic insights and identify protein activities. Since the mitochondrial membrane potential was not altered significantly, the mitochondrial ATP production declined by 2% and simultaneously the ATP production increased by 2%.

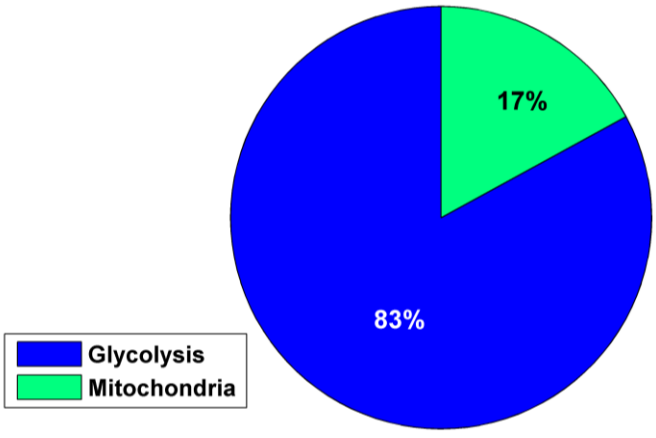

Figure 89: Analysis of ATP production pathways during malonate treatment

The ATP utilization by glycolysis increased by 7% as glucose uptake was heighted. Despite a decrease in cellular ATP level, a sufficient amount of ATP was still being synthesised by the cell to carryout the necessary functions. The ATP utilization flux by Ca-ATPase, NaK-ATPase, general ATPase, AK and PPP were 10%, 15%, 26%, <1% and <1%.

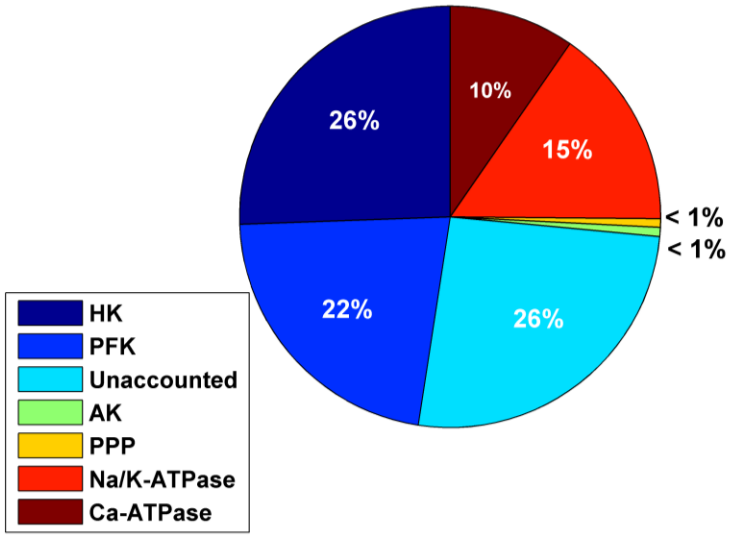

Figure 90: ATP utilization by different pathways upon exposure to malonate

5.6.3. Predicting action potentials and ionic concentrations

The model generated action potentials (AP's) were compared to experimentally determined action potentials. The simulated AP's were in good agreement with the experimental recordings (Figure 91). The action potential peak height was maintained as the ion channels and exchangers were functional. The rate of decline in membrane resistance was estimated and included in the model during action potential simulation. The action potential parameters were not altered as malonate does not bind to ion channels and only the reversal potentials of all ions are allowed to change.

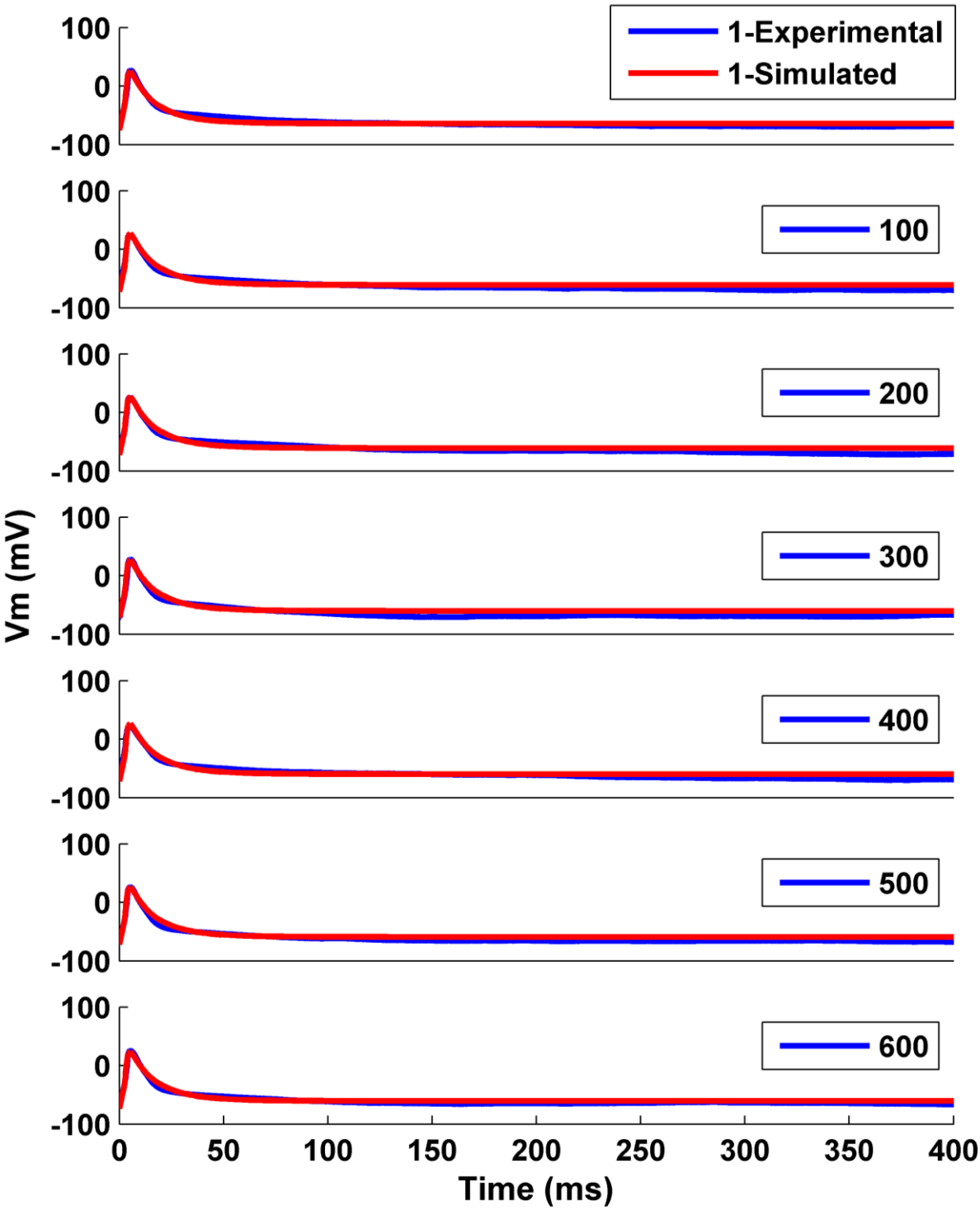

Figure 91: Simulated (red) and experimental (blue) malonate treated action potential time series

The neuronal and metabolic modules are driven by changes in the cellular ATP and ionic concentrations. The model predicted ATP concentrations were analyzed during malonate treatment. The intracellular sodium concentration increased by 1.7 mM (Figure 92) and potassium concentration decreased by 18.6 mM (Figure 93). The calcium concentrations did not change significantly (Figure 94). The subcellular calcium concentrations reached a maximum of 8.48×10^{-4} mM. The maximum flux of ionic concentrations depends on the fitting parameters obtained during action potential deconvolution. The intracellular ionic concentrations were slowly altered and no rapid change was observed as cellular ATP levels were slowly lowered. A rapid significant decline might have caused intracellular ionic concentrations to rise quickly.

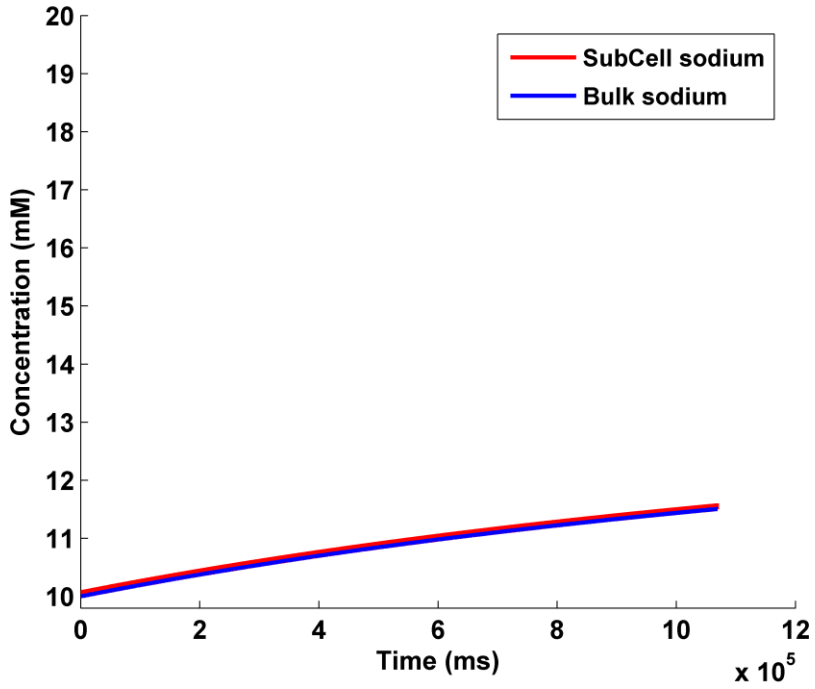

Figure 92: Predicted changes in subcellular (red) and bulk (blue) cytosolic sodium concentrations in NG108-15 cells exposed malonate

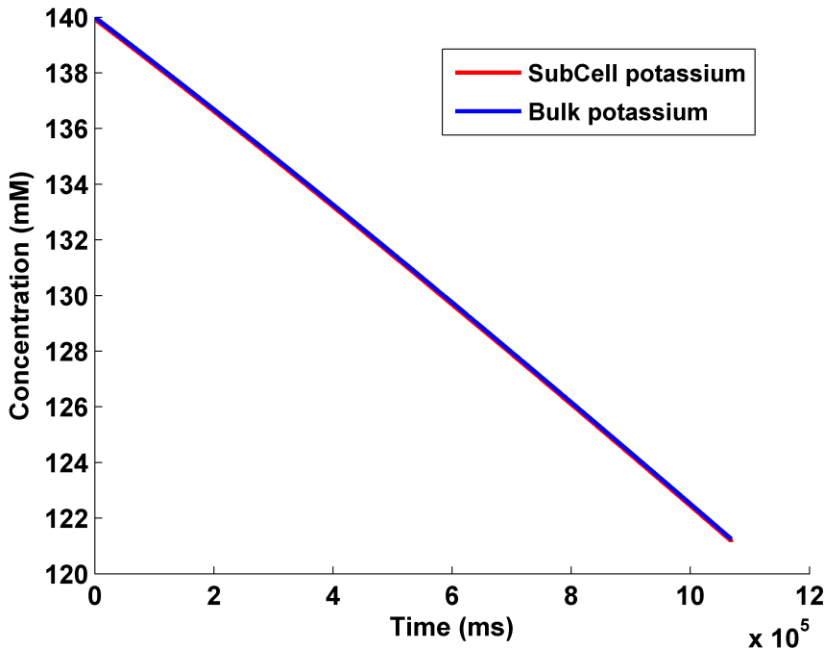

Figure 93: Predicted changes in subcellular (red) and bulk (blue) cytosolic potassium concentrations in NG108-15 cells exposed malonate

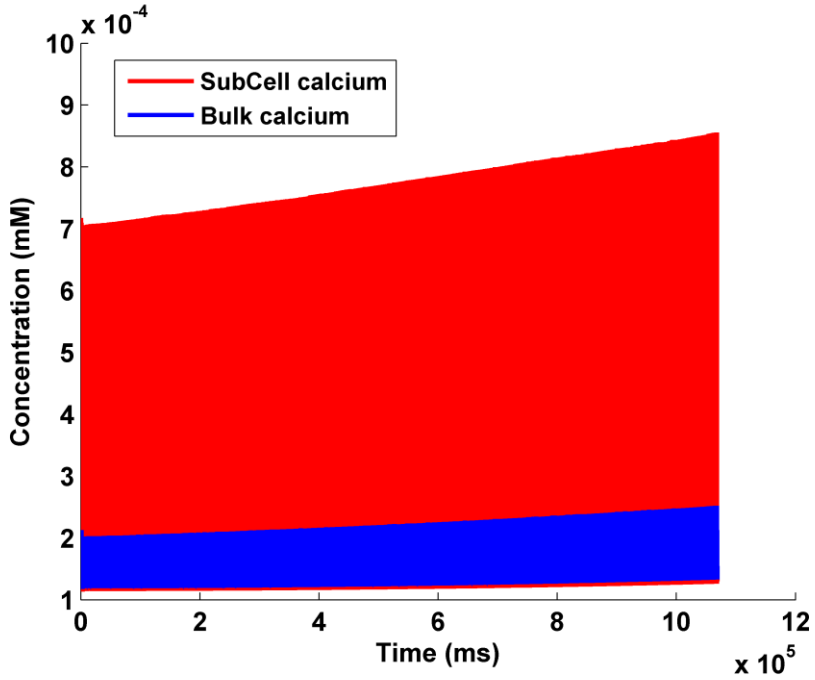

Figure 94: Predicted changes in subcellular (red) and bulk (blue) cytosolic calcium concentrations in NG108-15 cells exposed malonate

5.7. Perturbing glycolysis and mitochondrial electron transport chain

Most diseases such as cancer are being treated with some combination of surgery, radiation and/or multiple drug treatment. Drug treatment mainly involves using drugs that kill rapidly dividing cells. Cellular pathways in cancer cells are modified and certain pathways are over expressed. The rationale behind using such treatment is to use a combination of drugs that inhibit cellular pathways at multiple points. NG108-15 cells are insensitive to mitochondrial inhibitors, so a combinational treatment with a glycolytic inhibitor was tested to increase the sensitivity. Cells were treated with 2DG and cyanide simultaneously to induce metabolic perturbations in glycolysis and the mitochondrial pathways. The metabolic perturbations were validated by determining the metabolic and neuronal responses.

5.7.1. Analysis of carbon flux

The cellular glucose uptake and lactate production were measured by exposing the cells to 2DG and cyanide. These drugs significantly inhibited glycolysis and mitochondrial oxidative phosphorylation and lowered the carbon fluxes in the cell. A rapid decline in cellular glucose consumption and lactate production was observed within the first 20 min (Figure 95). The glucose and lactate fluxes were lowered by 66% and 72%, respectively, in 20 min. The decline was much faster than the standalone treatment of either drug. Prolonged exposure to 2DG and cyanide has further decreased the carbon fluxes and a complete inhibition of glucose flux was observed after 80 min. Inhibition glycolysis caused a decline in cytosolic pyruvate concentrations in 4 min (Figure 96). The pyruvate levels in the mitochondria have rapidly increased reaching a peak concentration of 0.02 mM.

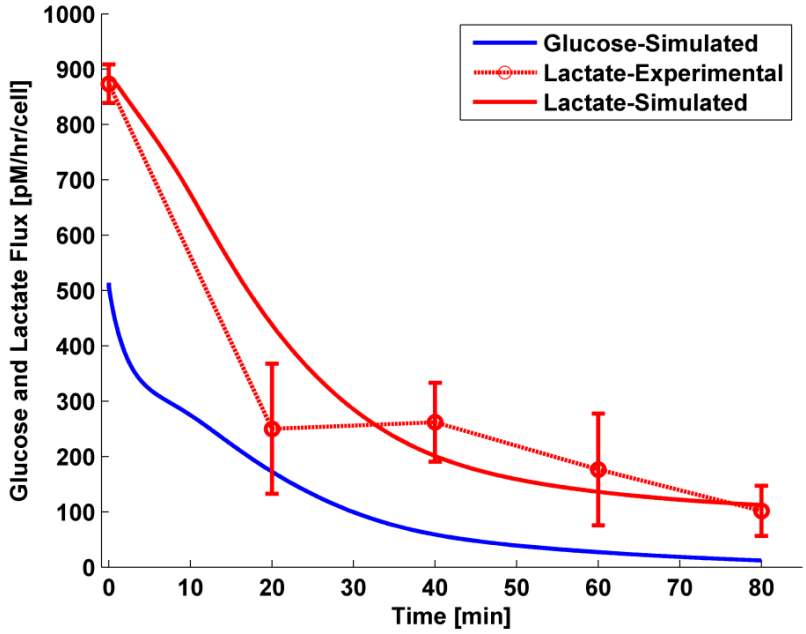

Figure 95: Experimental lactate production compared to the model generated lactate and glucose flux during combinational treatment with 2DG and cyanide

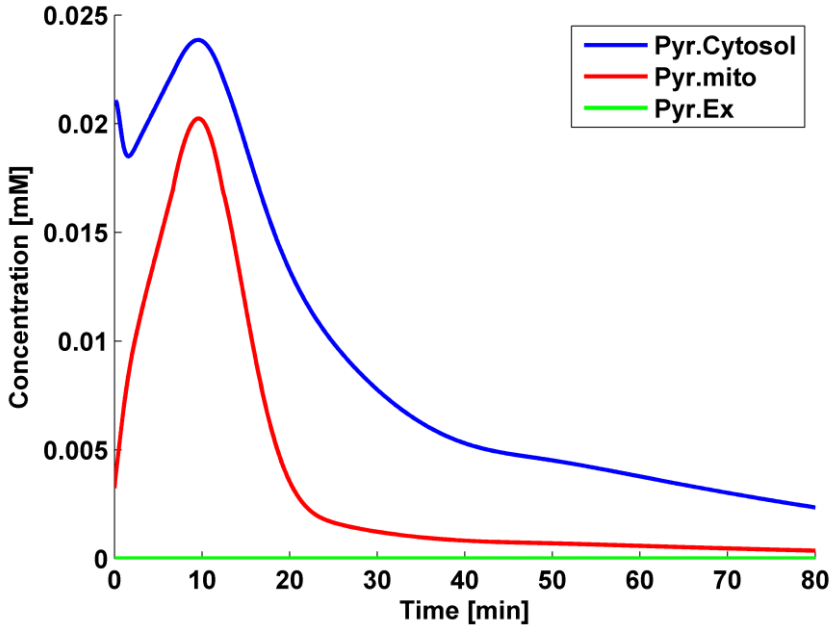

Figure 96: Predicted cytosolic, mitochondrial and extracellular concentrations of pyruvate in NG108-15 cell exposed to 2DG and Cyanide

The increased mitochondrial pyruvate levels were accumulated and transported back to the cytosol causing the cytosolic pyruvate concentrations to rise. Since carbon influx has been inhibited, the cellular metabolite levels got exhausted. This expedited depletion of the glycolytic metabolites forced the carbon flux towards lactate production. The cytosolic pyruvate decreased as it was converted to lactate and simultaneously the accumulated mitochondrial pyruvate was transported into the cytosol (Figure 96).

The flux balance analysis of carbon into different pathways was performed (Figure 97). The global fluxes have decreased and the ratio of carbon fluxes had also changed. The mitochondrial flux of carbon was lower than the lactate flux. The carbon in glycolysis and the mitochondria were 94% and 5% respectively. The PPP flux has also been lowered to 0.57%. The extracellular flux of carbon as pyruvate was less than 0.3%. The combinational treatment had a larger effect on glycolysis and significantly lowered its activity. Metabolic perturbations induced by inhibition of glycolysis and mitochondrial respiration had a huge effect on cellular functions.

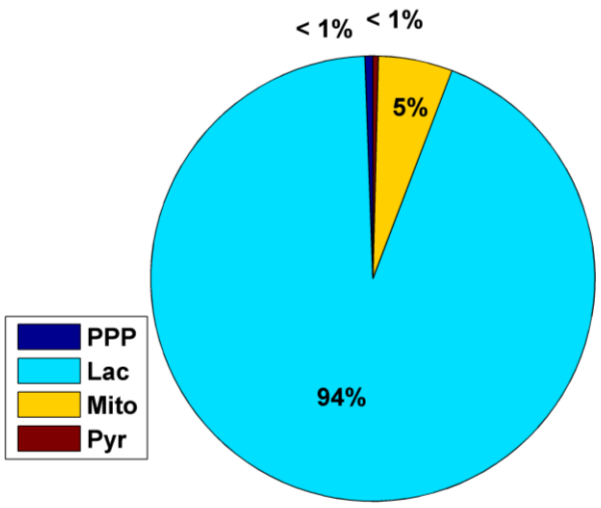

Figure 97: Flux balance analysis of carbon usage by different pathways during 2DG and cyanide treatment

5.7.2. ATP production and utilization

The changes in ATP and ADP levels in cells exposed to a combinational treatment of 2DG and cyanide were assessed by experimental determination at different time intervals. The simulated ATP (Figure 98) and ADP (Figure 99) concentrations were compared to experimentally determined values. A 20 min exposure of 2DG and cyanide lowered the ATP levels to 32%. Prolonged exposure beyond 20 min caused cellular ATP levels to decrease further down to 18%. The ADP levels increased by 36% during the first 20 min and were decreased by 18%, almost reaching the initial concentrations. The predicted AMP levels increased from 75 µM to 345 µM (Figure 100).

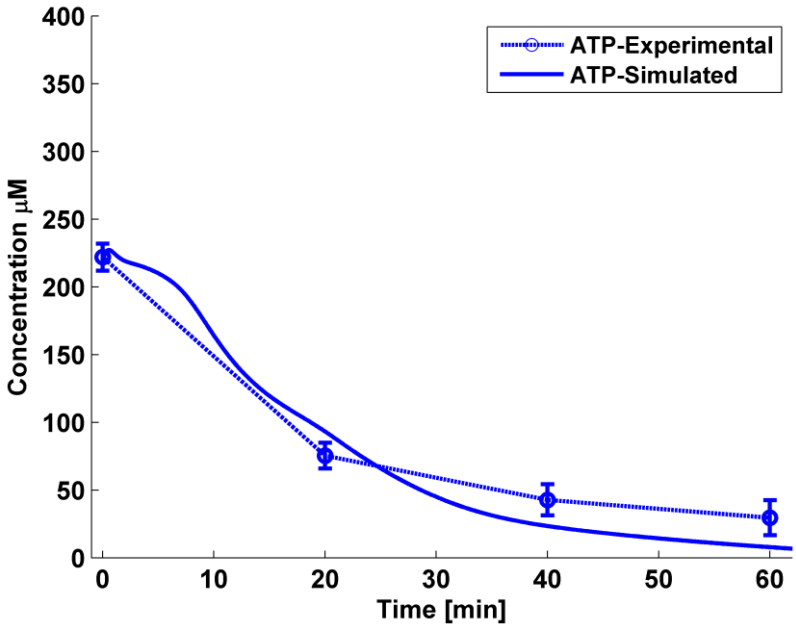

Figure 98: Measured and simulated ATP concentrations in NG108-15 cell exposed to a combinational treatment of 2DG and Cyanide

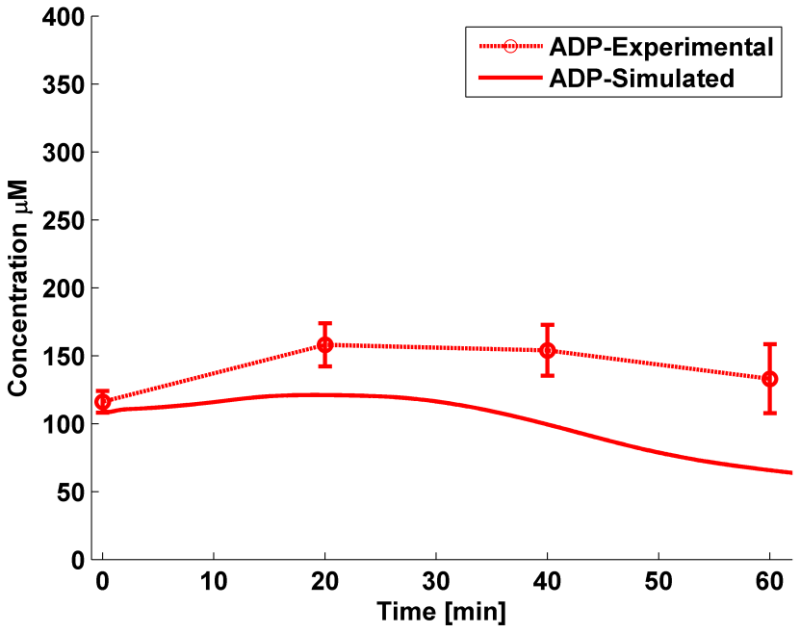

Figure 99: Measured and simulated ADP concentrations in NG108-15 cell exposed to a combinational treatment of 2DG and Cyanide

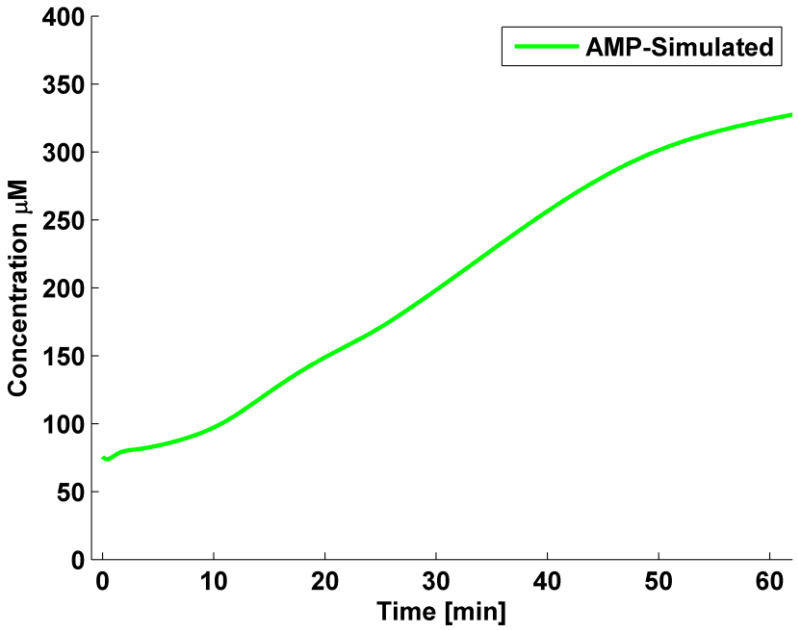

Figure 100: Simulated AMP concentrations in NG108-15 cell exposed to a combinational treatment of 2DG and Cyanide

The mitochondrial membrane potential depolarized from -121 mV to -88 mV (Figure 101). An initial small transient was observed lowering the potential to -113 mV due to the aberrant arrest of mitochondrial respiration by cyanide. As carbon flux was inhibited by metabolic inhibitors, the generation of protons required to maintain mitochondrial membrane potential had decreased. This decrease in mitochondrial membrane potential resulted in a decline in mitochondrial ATP generation mechanisms.

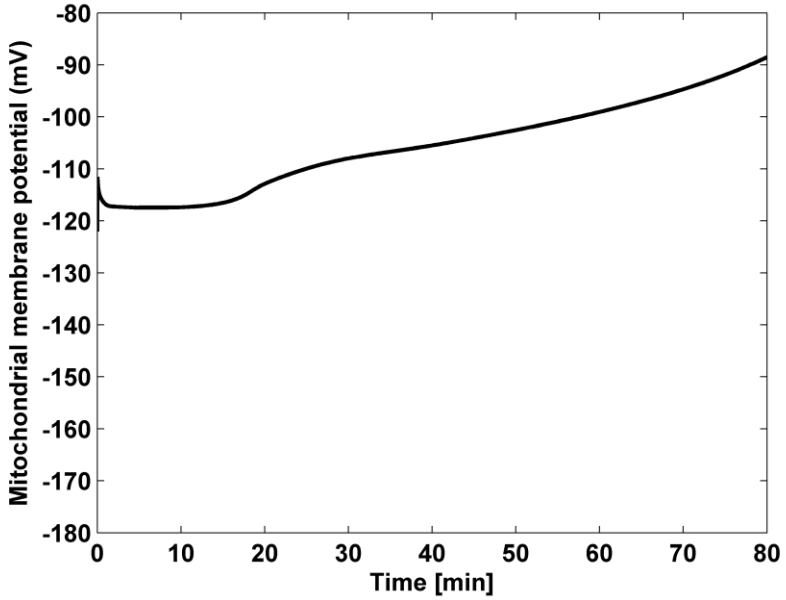

Figure 101: Predicted changes in mitochondrial membrane potential of NG108-15 cell exposed to 2DG and cyanide

The flux balance analysis was perfomed on the ATP production and utilization of different pathways during treatment with 2DG and cyanide. The analysis indicated an overall reduction in cellular ATP generation. After 80 min of combinational treatment, the glycolytic and mitochondrial ATP production were 93% and 7% respectively (Figure 102). The utilization of ATP by different pathways has shown that only 27% of ATP was used back again in cellular glycolysis pathway (Figure 103). The reduction in ATP levels have also decreased the conversion

of glucose by hexokinase. The NaK-ATPase and Ca-ATPase were utilized appromimately 14 and 22% of cellular ATP, respectively, to restore cellular homeostasis. The general ATPases were utilizing around 36% of ATP. The ATP usage by PPP and AK was lowered and consumed less than 1% of ATP.

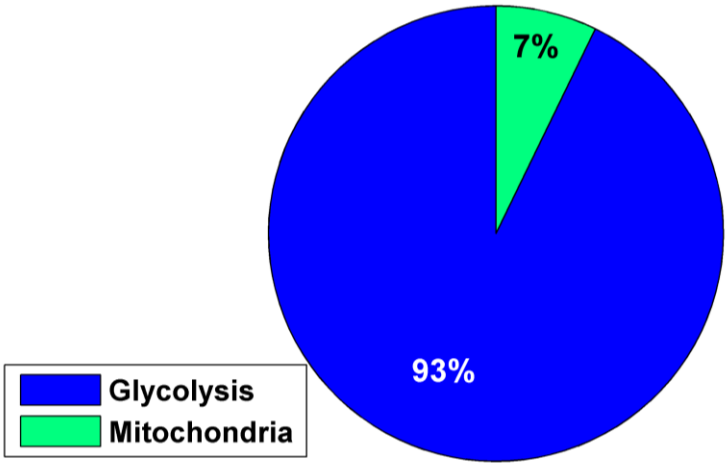

Figure 102: Analysis of ATP production by glycolysis and mitochondrial process during 2DG and Cyanide

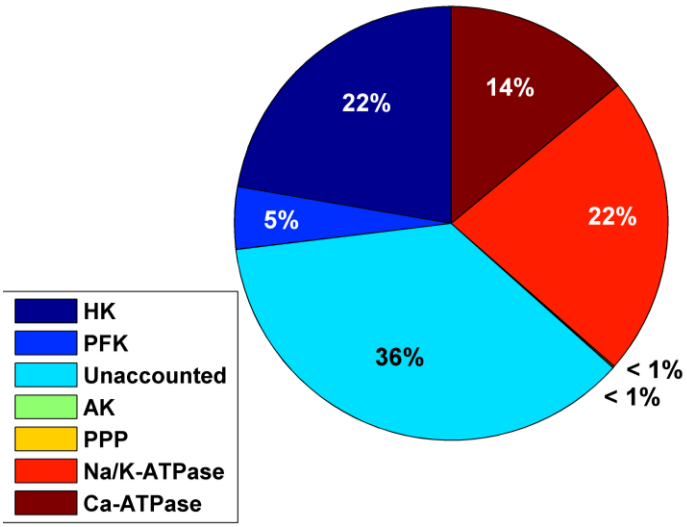

Figure 103: ATP utilization by different cellular process exposed to 2DG and cyanide

5.7.3. Predicting action potentials and ionic concentrations

The model generated action potentials during metabolic perturbation induced by 2DG and cyanide were significantly altered. The simulated action potentials were compared to the experimental measurements (Figure 104) and an excellent fit was obtained between them.

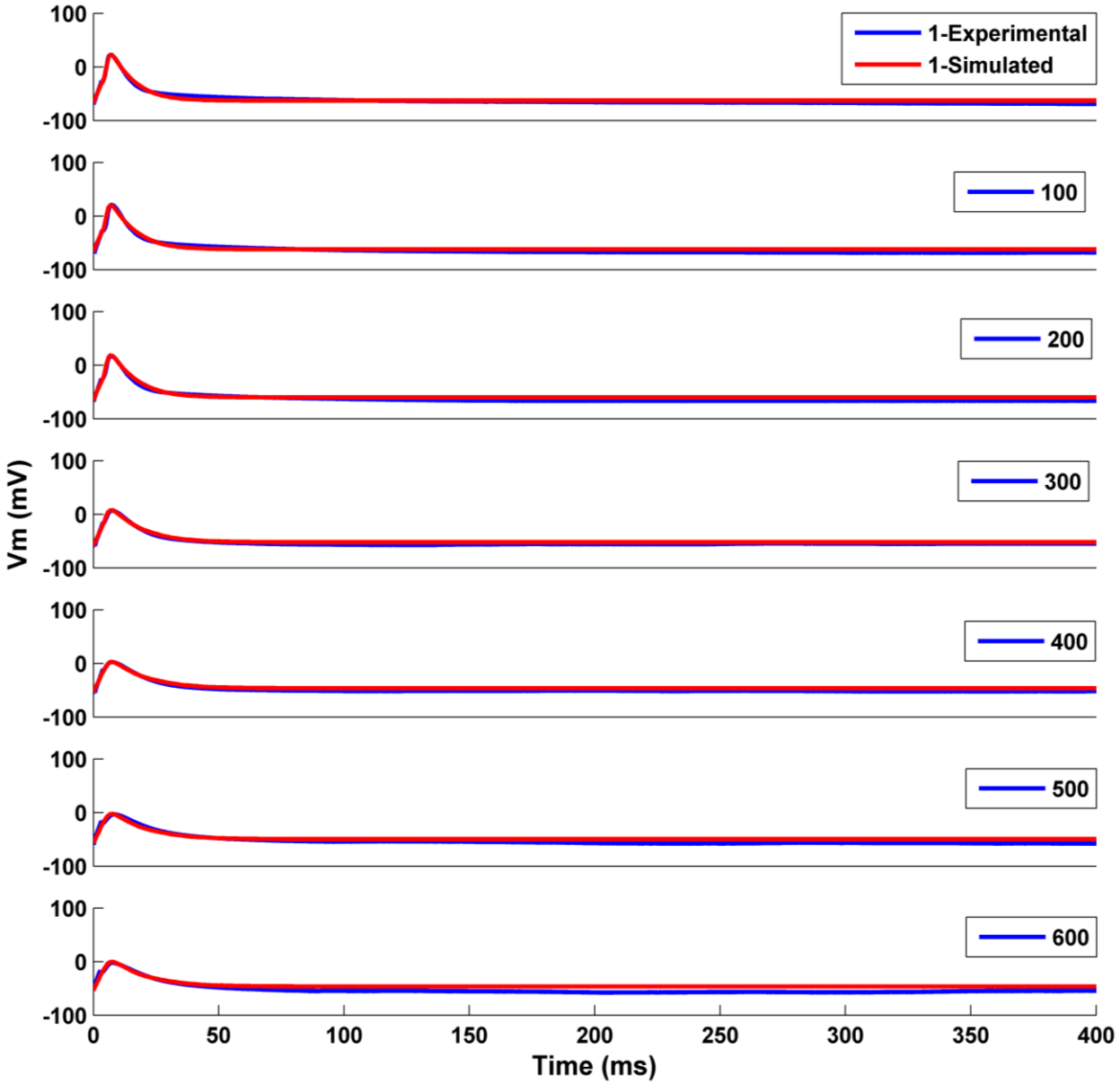

Figure 104: Predicted action potentials compared to experimental recordings exposed to 2DG and cyanide

The action potential peak height decreased and membrane potentials depolarized. The reversal potentials and cellular ATP concentrations were allowed to change during simulation. The changes in the subcellular and bulk ionic concentrations were predicted by the model. The calcium concentration initially increased linearly from 1.25e-4 mM to 2.64e-3 mM, but cellular ATP concentration did not significantly decrease (Figure 107). But after 8 minutes of exposure to 2DG and cyanide, a significant reduction in cellular ATP levels caused the calcium concentration to rise exponentially leading to a rapid influx of sodium and efflux of potassium ions. The bulk cytosolic sodium concentration increased from 10 mM to 20.4 mM (Figure 105). The potassium concentration decreased from 140 mM to 84 mM in 17 minutes (Figure 106). These results were in agreement with the ionic concentration changes found in C6 glioma cells treated with 2DG and cyanide [105].

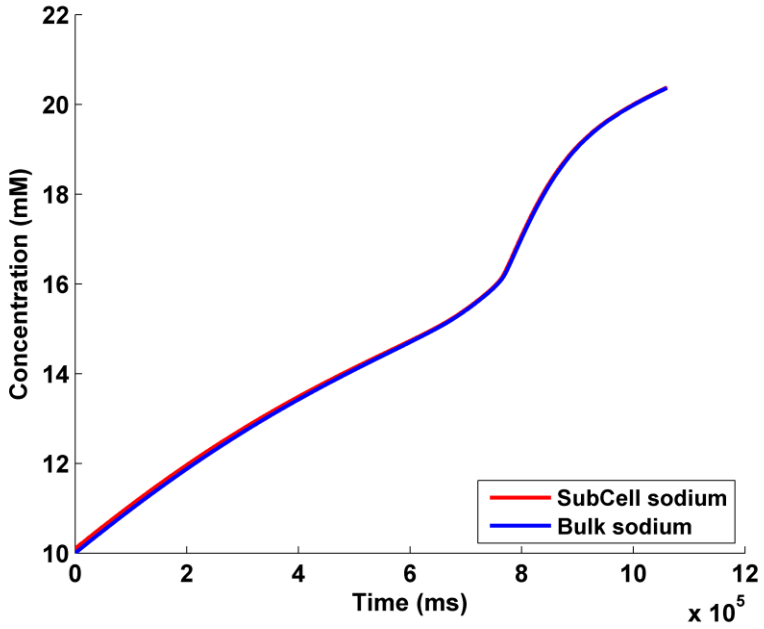

Figure 105: Predicted changes in subcellular and bulk cytosolic sodium concentrations during combinational treatment with 2DG and cyanide

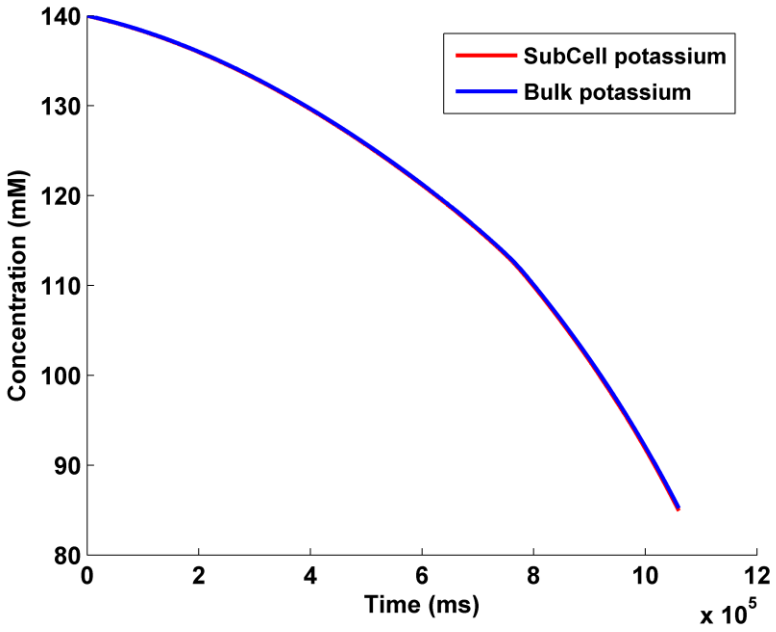

Figure 106: Predicted changes in subcellular and bulk cytosolic sodium concentrations during combinational treatment with 2DG and cyanide

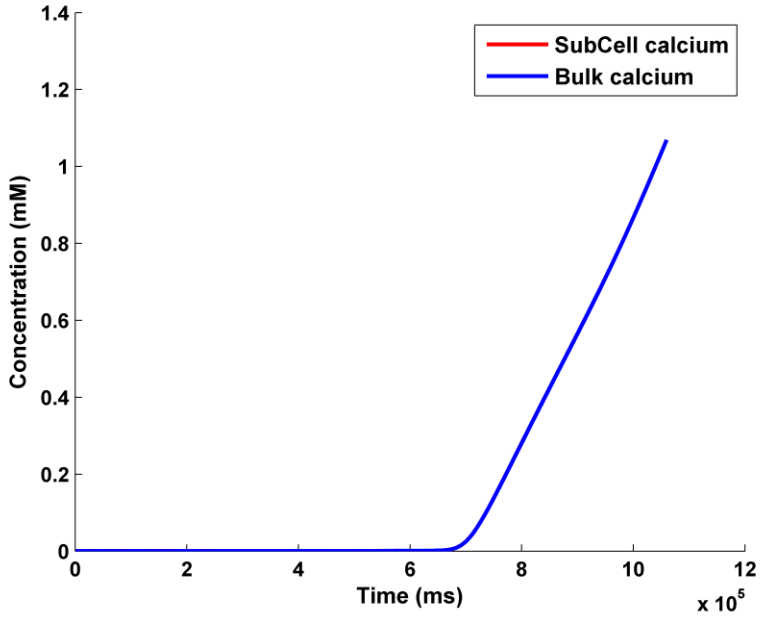

Figure 107: Predicted changes in subcellular and bulk cytosolic sodium concentrations during combinational treatment with 2DG and cyanide

5.8. Perturbing glycolysis, mitochondrial TCA cycle and electron transport chain

Inhibiting the TCA cycle by malonate had no significant effect on cellular activities as the required ATP was being generated by glycolysis. The effects of inhibiting glycolysis with 2DG and the mitochondrial TCA cycle and electron transport chain with malonate were tested. Malonate inhibits complex-II (SDH enzyme) but does not completely seize the electron transport chain as the electrons from oxidation of NADH and $FADH_2$ are directly transported into inner mitochondrial membrane. The metabolic perturbations that are due to inhibition of glycolysis and the TCA cycle were evaluated.

To simulate the effect of combination treatment of drugs, both the events representing the effect of glycolysis and TCA cycle inhibition are turned on. The scaling factors for inhibiting the pathways were obtained from the earlier obtained fitting data for standalone drugs.

5.8.1. Analysis of carbon flux

The fate of carbon was analyzed to determine the effects of combinational treatment with 2DG and malonate. The model predicted glucose flux and lactate flux were compared to the experimental data (Figure 108). The glucose flux was not measured as 2DG and glucose have a similar molecular structure and the assay kit was unable to distinguish between them. The glucose uptake and lactate production were lowered to 55% and 51% respectively in 20 min. The declines in carbon flux continued upon prolong exposure. The predicted glucose flux and lactate flux decreased to 10 and 18%, respectively, after 80 min.

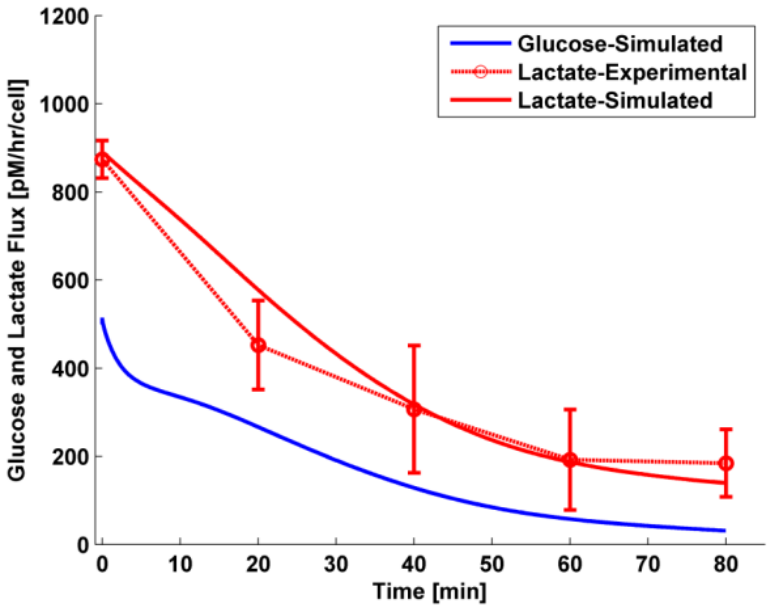

Figure 108: Simulated glucose and lactate flux compared to experimental lactate flux of NG108-15 cell during combinational treatment with 2DG and malonate

The cytosolic and mitochondrial pyruvate concentrations decreased over time (Figure 109). Unlike malonate treatment where accumulation of pyruvate was observed, the combinational treatment caused only a small increase in cytosolic and mitochondrial pyruvate levels. 2DG inhibited glucose flux which resulted in the transport of carbon to the mitochondria. The mitochondrial pyruvate slowly decreased as the cytosolic pyruvate was preferably being converted into lactate. The extracellular pyruvate flux initially remained unaltered but was completely inhibited after 80 min.

Carbon flux analysis has identified the percent of carbon being used by different pathways within the cell. Although the total carbon flux decreased, around 91% of carbon was routed through glycolysis and converted to lactate and only 8% of the carbon entered the mitochondria. The carbon flux towards the pentose phosphate pathway and extracellular

pyruvate were 0.01% and 0.7%. The decrease of carbon flux to PPP was significantly lowered as the reduction in glycolytic metabolites favored the carbon to route towards lactate generation by producing ATP for cellular functions.

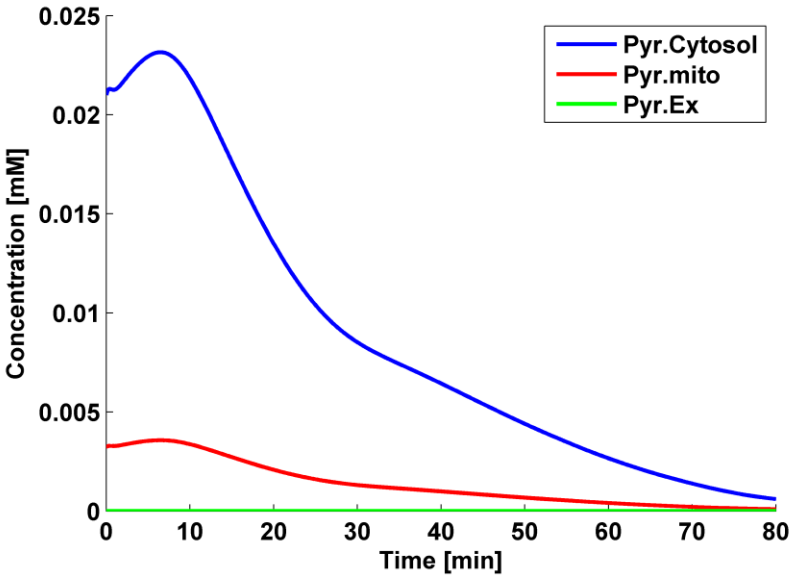

Figure 109: Predicted pyruvate flux during simulating the effects of combinational treatment of 2DG and malonate

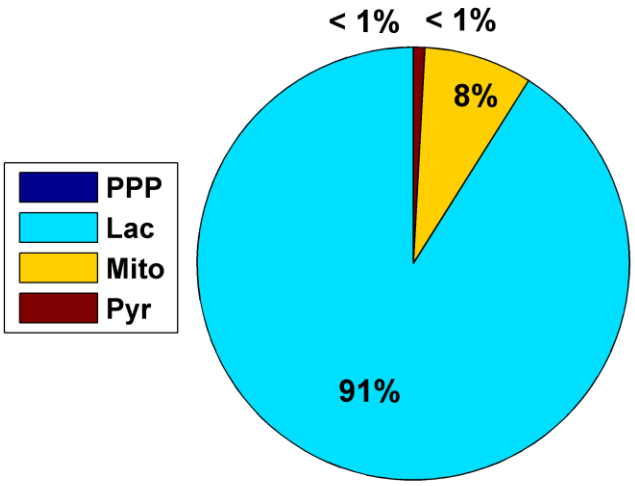

Figure 110: Carbon flux analysis of NG108-15 cell exposed to 2DG and malonate

5.8.2. ATP production and utilization

The cellular ATP and ADP levels were measured by exposing the cells to 2DG and malonate simultaneously. The predicted ATP (Figure 111) and ADP (Figure 112) concentrations were in good agreement with the experimental data. A 40 min exposure to these drugs lowered the cellular ATP levels to 21%. The model predicted cellular ATP levels declined further after exposure to 2DG and malonate for 60 min. The experimental results have shown cellular ATP levels to remain at a plateau probably due to the production of ATP by other endogenous factors such as fatty acids. The decrease in cellular ATP levels caused the ADP levels to rise initially. The AMP levels (Figure 113) increased as the cellular ATP levels were decreasing. An uninterrupted exposure lowered the cellular ADP level, and subsequently increased the intracellular AMP level.

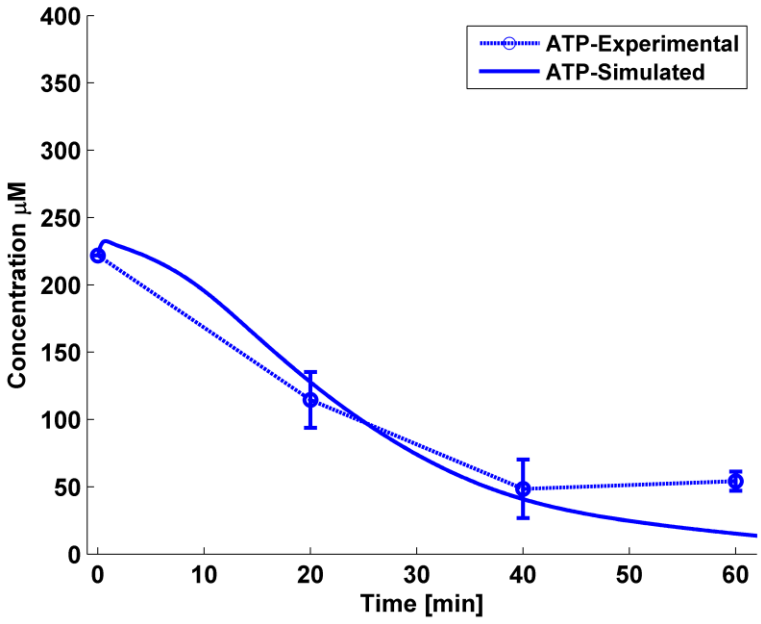

Figure 111: Measured and simulated ATP concentrations in NG108-15 cell exposed to a combinational treatment of 2DG and malonate

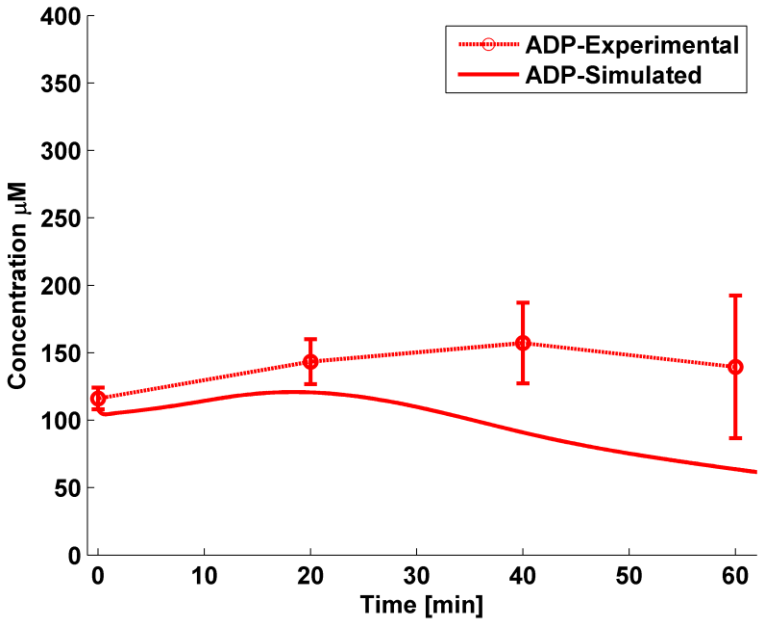

Figure 112: Measured and simulated ADP concentrations in NG108-15 cell exposed to a combinational treatment of 2DG and malonate

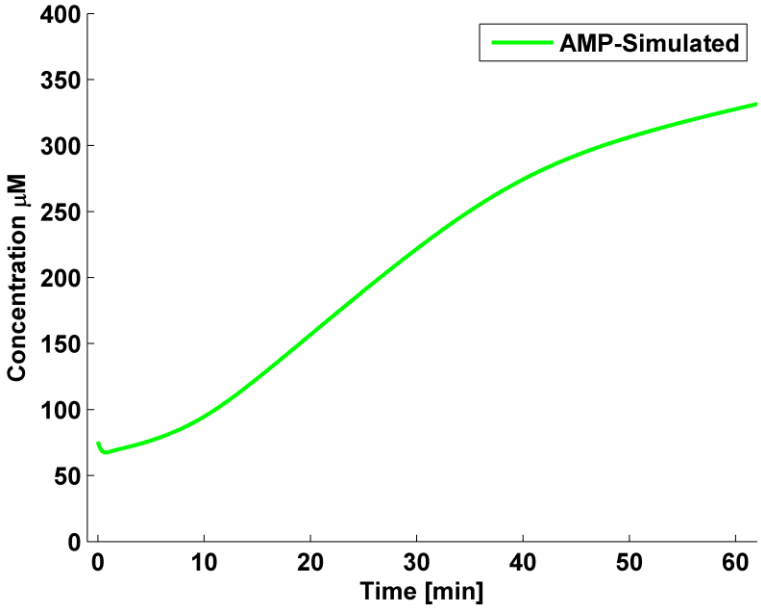

Figure 113: Simulated AMP concentrations in NG108-15 cell exposed to a combinational treatment of 2DG and malonate

The mitochondrial membrane potential became more sensitive when treated with 2DG

and malonate. Treatment with malonate alone had reduced the mitochondrial membrane potential by -4 mV, but when the cells were treated with malonate in the presence of 2DG, the mitochondrial membrane potential depolarized to -32 mV (Figure 114). The reason behind this significant depletion of the mitochondrial membrane potential was due to lowered transport of high energy electrons generated during glycolytic inhibition. The G3P shuttle was unable to transfer the electrons as sufficient electron equivalents were not generated. On the other hand, malonate has lowered the TCA cycle activity, thereby obstructing the generation and transfer of electrons. Malonate has been shown to reduce cellular functions by depolarizing the mitochondrial membrane potential and increasing the oxidative stress in SH-SY5Y neuroblastoma cells [110].

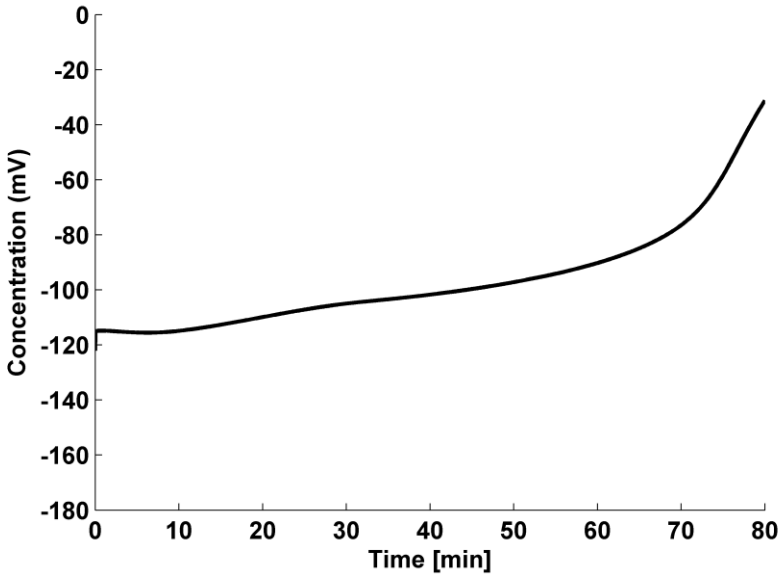

Figure 114: Predicted mitochondrial membrane potential during treatment combinational treatment with 2DG and malonate

ATP production and usage by different pathways in NG108-15 cell after 60 min exposure

to 2DG and malonate was analyzed. The ATP production from glycolysis and the mitochondria were 96% and 4% respectively (Figure 115). Although the total amount of ATP produced by the cell decreased to 21%, the glycolytic pathway was still active generating ATP. The low amount of ATP present in the cell was mainly used by hexokinase (HK), NaK-ATPase, Ca-ATPase and general ATPases (Figure 116). The activity of the HK enzyme increased due to lowered ATP and G6P levels. The lowered G6P levels triggered the influx of glucose and, more importantly, 2DG into the cell. 2DG was preferentially metabolized in the cell leading to an accumulation of 2DG6P, a metabolitite that could not be metabolized futher down the glycolysis pathway. The next highest ATP consuming process was the NaK-ATPase and Ca-ATPase proteins. These proteins bind to free-cytosolic ATP and transfer ions across the memebrane to restore ionic balance.

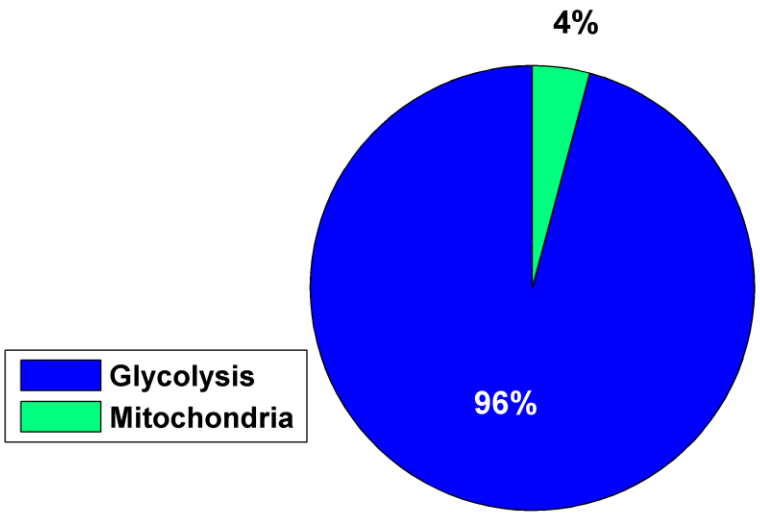

Figure 115: Analysis of ATP production by glycolysis and mitochondrial process during 2DG and malonate

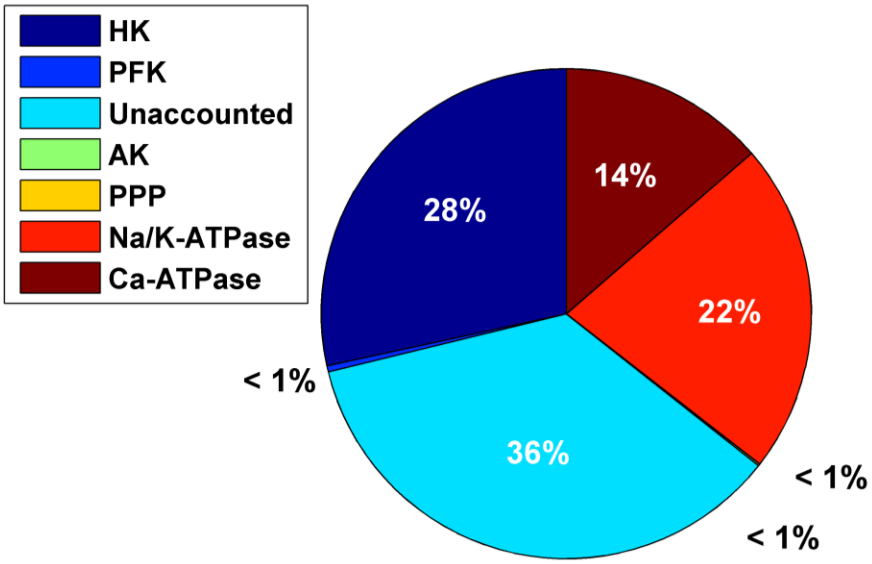

Figure 116: ATP utilization by different cellular process exposed to 2DG and malonate

5.8.3. Predicting action potentials and ionic concentrations

The time dependent changes in action potential peak shapes were predicted by the neuronal-metabolic model. The action potentials generated by the model were plotted against the experimental recordings (Figure 117). An excellent fit was obtained between the simulated and experimental recordings. The fit to tail of an action potential was acceptable. A prolonged exposure to 2DG and malonate has caused the cellular action potentials to alter significantly.

The intracellular ionic concentrations were predicted by the neuronal-metabolic model. The sodium, potassium and calcium ionic concentrations changed rapidly. The intracellular sodium reached a peak concentration of 21.1 mM in 18 min (Figure 118). The potassium concentration decreased to 90 mM in 18 min (Figure 119). The changes in ionic concentrations, and even cellular ATP levels, have caused a rapid exponential increase in calcium concentration after 15 min (Figure 120). The calcium concentration increased to 0.92 mM.

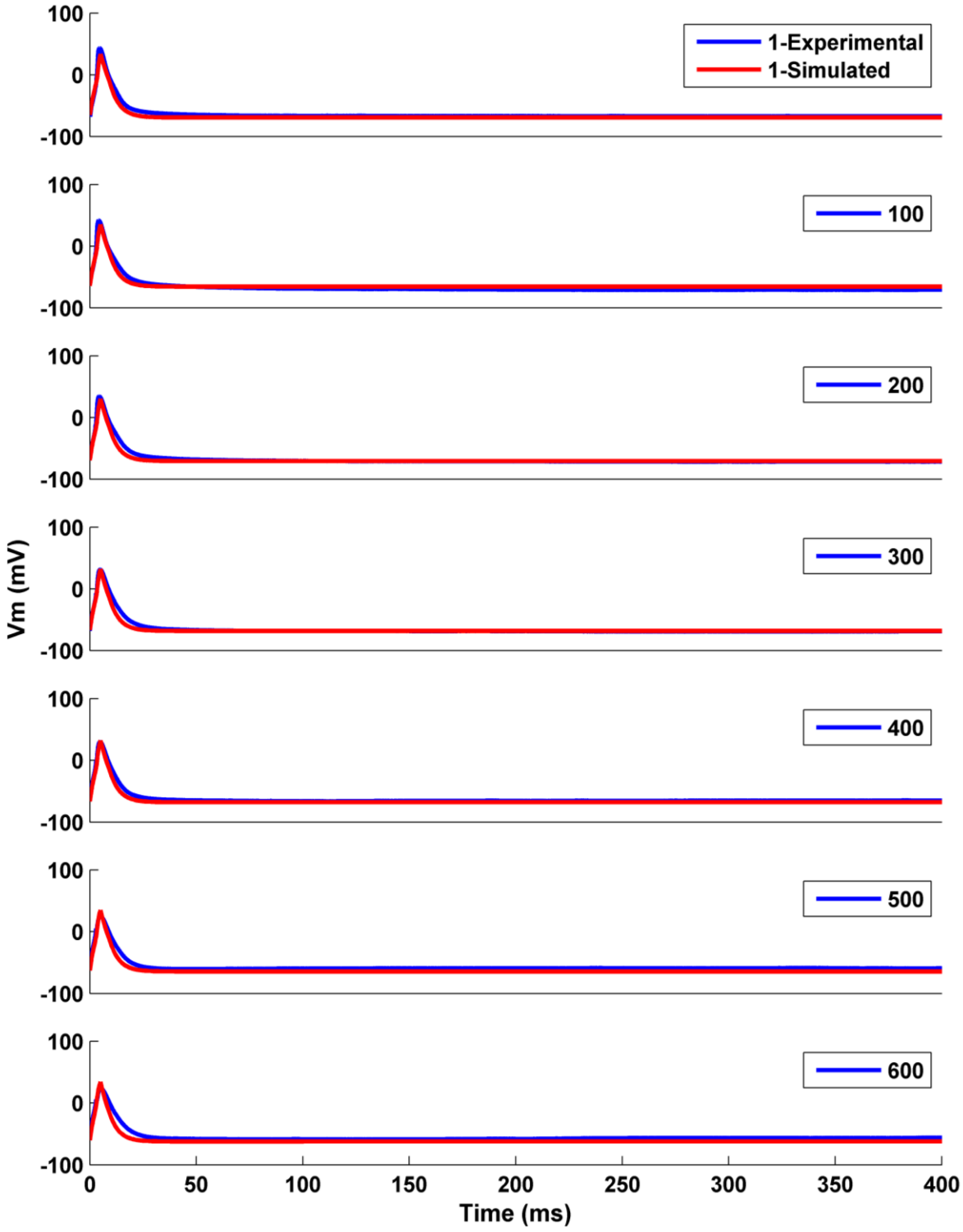

Figure 117: Predicted action potentials compared to experimental recordings exposed to 2DG and cyanide

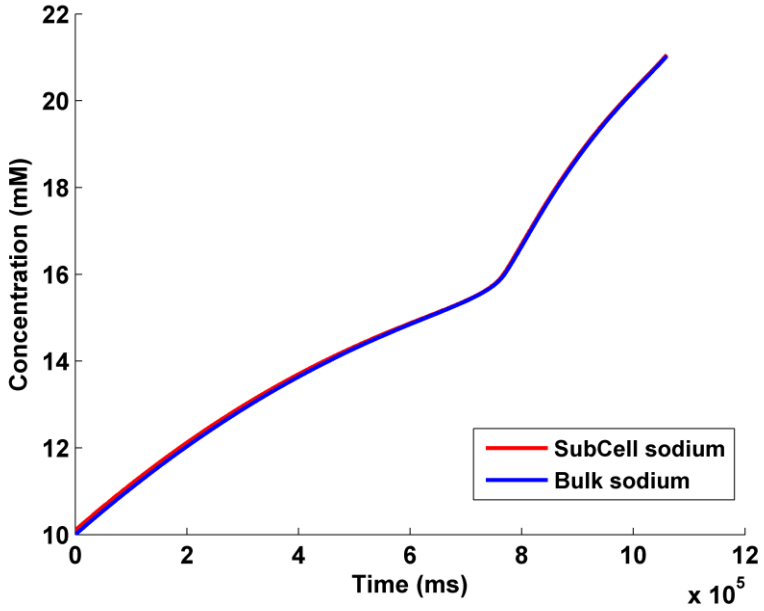

Figure 118: Predicted changes in subcellular and bulk cytosolic sodium concentrations during combinational treatment with 2DG and malonate

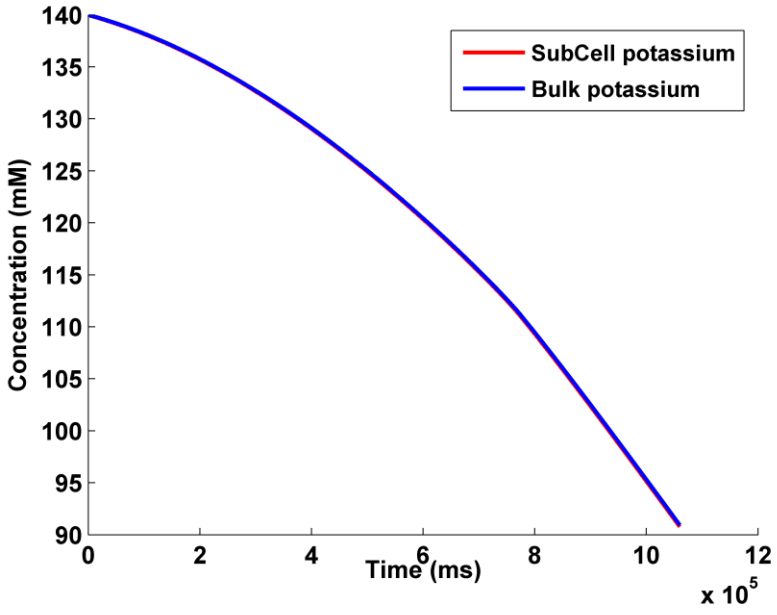

Figure 119: Predicted changes in subcellular and bulk cytosolic potassium concentrations during combinational treatment with 2DG and malonate

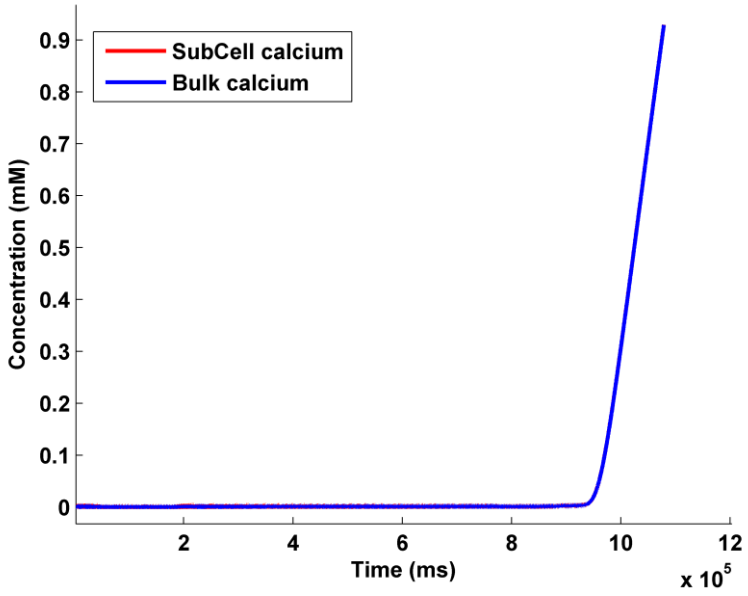

Figure 120: Predicted changes in subcellular and bulk cytosolic calcium concentrations during combinational treatment with 2DG and malonate

5.9. Distinguishing the effects of metabolic inhibitors

We hypothesized that the rate of change in action potentials would be characteristic to the pathway being inhibited and their deconvolution would enable the ability to back tract the effected pathways and allow continuous monitoring of the protein functions. Metabolic perturbations and changes in cellular proteins activities occur in the cellular network at different rates. The metabolic inhibitors tested act by lowering the cellular ATP levels, which cause impaired cellular homeostasis leading to alterations in the membrane electrical activity.

Although the model was able to accurately predict the changes in action potential peaks shapes based on the pathways being inhibited, an analysis of the characteristic changes would enable us to gain a deeper insight. To characterize and differentiate the effects of the metabolic inhibitors, changes in cellular action potential time series and ATP levels were compared.

5.9.1. Analysis of action potentials

The time dependent changes in action potentials were determined by measuring the rate of change in the action potential peak amplitude, holding potential, area and half-width at the peak amplitude. The data were normalized to compare the effects of different inhibitors.

5.9.1.1. Action potential peak height

The normalized rate of change in action potential peak amplitude for different drugs is shown in Figure 121. The peak height in control recordings remained stable and unaltered. The mitochondrial inhibitors had the least effect on cellular metabolic activity which was reflected in the AP peak height.

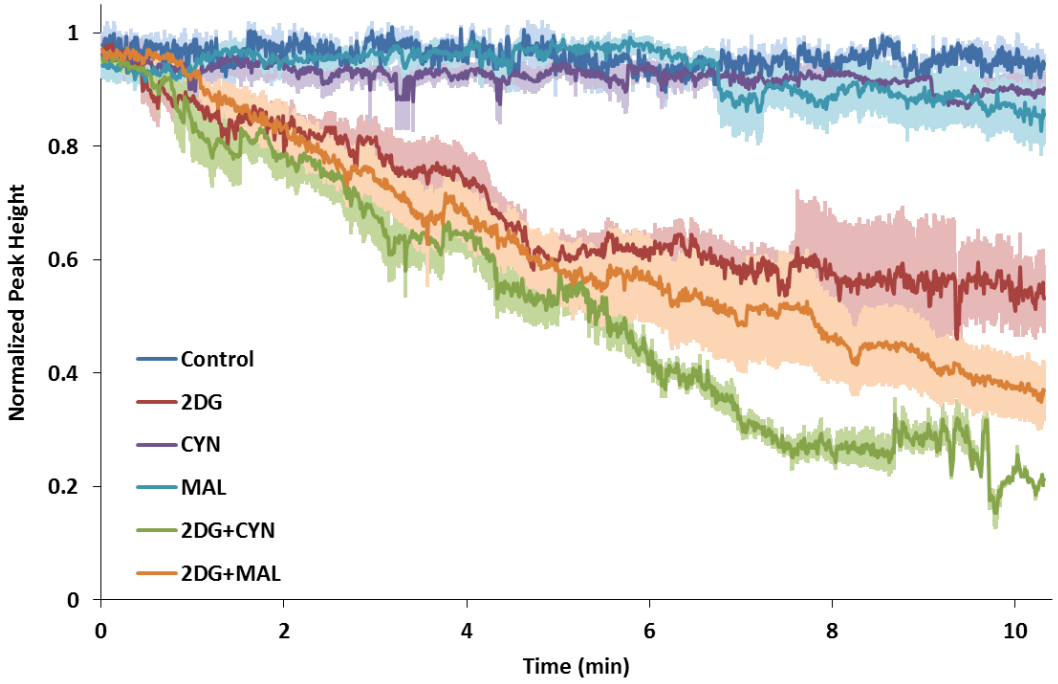

Figure 121: Normalized action potential peak height of cells exposed to different metabolic inhibitors

Cyanide and malonate lowered the action potential peak height by only 9% and 15%

respectively whereas 2DG lowered the peak height to 54%. The rate of decline in 2DG treated and combinational treatment was similar for the first 5 min. Prolonged exposure to the drugs changed the peak height in a time-dependent manner. The combinational treatment of 2DG with cyanide and malonate reduced the peak height to 21% and 37%. The reduction in action potential is due to the reduction in cellular ATP levels. The reduced ATP levels failed to restore the ionic concentrations, which resulted in huge changes in the intracellular ionic concentrations. The intracellular accumulation of sodium concentrations reduced the drive for the sodium ions to enter into the cell, which caused a decrease in sodium current.

5.9.1.2. Holding potential

The membrane potential was altered by injecting the cell initially with a sufficent current to hyperpolarize the membrane to -70 mV. Although a stimulus pulse was given to generate action potential. The current required to hold the membrane potential was not altered during the course of the experiment. The holding potential reached the initial state in one second and assuming that cellular machinery was functional, the ionic balances would have also been restored. The holding potentials in the controls recordings did not change significantly (Figure 122). The holing potential of cyanide was slightly depolarized by 9% but the change was very small. The activity of cyanide had varied depending on the resting membrane potential of the cell. Cyanide exposed to the cells with a resting membrane potential less than -38 mV caused the membrane potential to hyperpolarize and deplolarize in cells with resting membrane potentials between -38 mV and -50 mV [111]. This result was in agreement with the cyanide experiments perfomed on hippocampal pyrimidal neurons.

During the first five minutes of exposure to Malonate, a slight decline in ATP levels and changes in the intracellular ionic concentrations caused a decrease in the holding potential by 13% (Figure 122). Similar to the effects on peak amplitude, the holding potetnial of the cells treated with 2DG alone and 2DG in combination with another drug had an immense effect. The holding potential of 2DG, 2DG with cyanide and 2DG with malonate was lowered by 38%, 65% and 88% (Figure 122). In accordance with the metabolic data, 2DG+cyanide treatement had an extensive effect on AP.

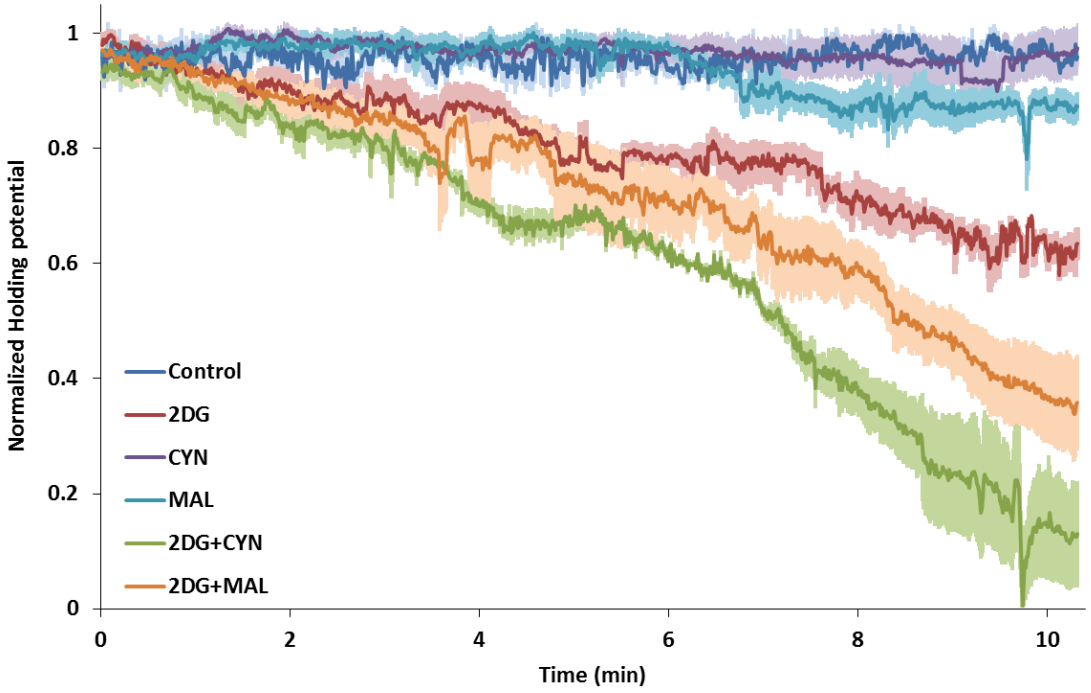

Figure 122: Normalized initial holding potential of cells exposed to different metabolic inhibitors

5.9.1.3. Area of an action potential

The area under an action potential was also measured to characterize the drug effects (Figure 123). The area in the control, 2DG, cyanide, malonate, 2DG+cyanide and 2DG+malonate

had decreased to 96%, 51%, 90%, 82%, 25% and 34%. The treatment of the NG108-15 cell with 2DG and cyanide had the highest decline in the area. The area for malonate recording had increased as the K_{ATP} channel was activated leading to a prolong depolarization of the action potential.

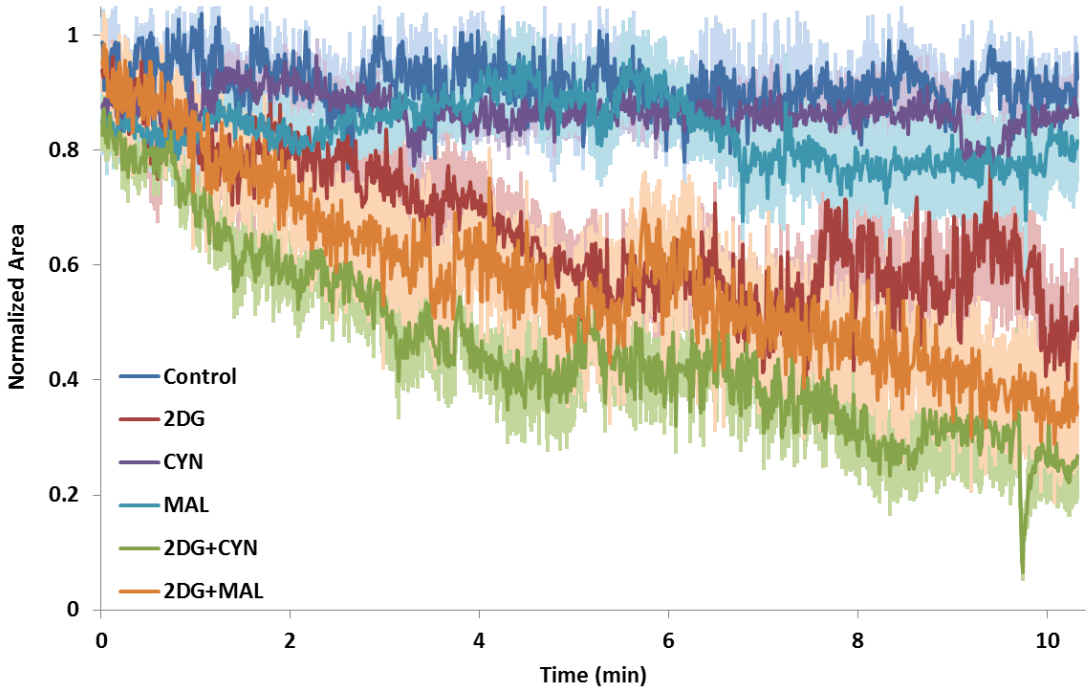

Figure 123: Normalized area of an action potential of cells exposed to different metabolic inhibitors

5.9.1.4. Half-width at peak amplitude

The half width at peak amplitude (HWPA) varied in all conditions (Figure 124). The HWPA for 2DG treated cells decreased as the peak was shortened. After five minutes, the half width of the combinational treated 2DG and cyanide has increased due to elevated intracellular calcium concentration. The calcium flux is usually responsible for the hump generated in the action potential during depolarization. Combinational treatment with 2DG and malonate had

no initial effect but reduced the HWPA after 5 minutes. Cyanide and malonate had showed no significant effect on action potential peak height, holding potential and area of action potential. Instead the HWPA of cells treated with cyanide and malonate showed a 20% and 19% decline in amplitude. These results demonstrated that the changes in action potential are characteristic to the pathway being inhibited.

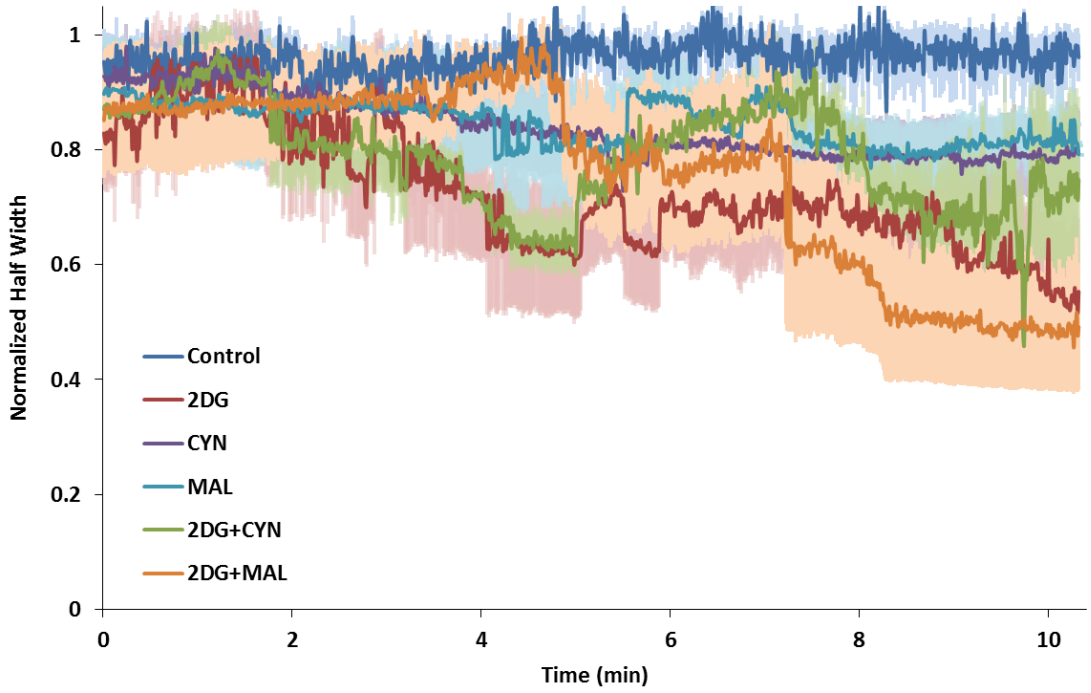

Figure 124: Normalized action potential half-width at maximum peak height of cells exposed to different metabolic inhibitors

5.9.2. Comparison of cellular ATP levels

Intracellular ATP levels act as indicators of cellular health. Since neurons are sensitive to ATP levels, the effect of energy depletion on neuronal damage was studied [93]. Several cell viability assays have been developed based on the determination of the cellular ATP levels. The ATP levels in cells exposed to mitochondrial inhibitors, namely cyanide and malonate are

reduced to 81% and 85% respectively (Figure 125).

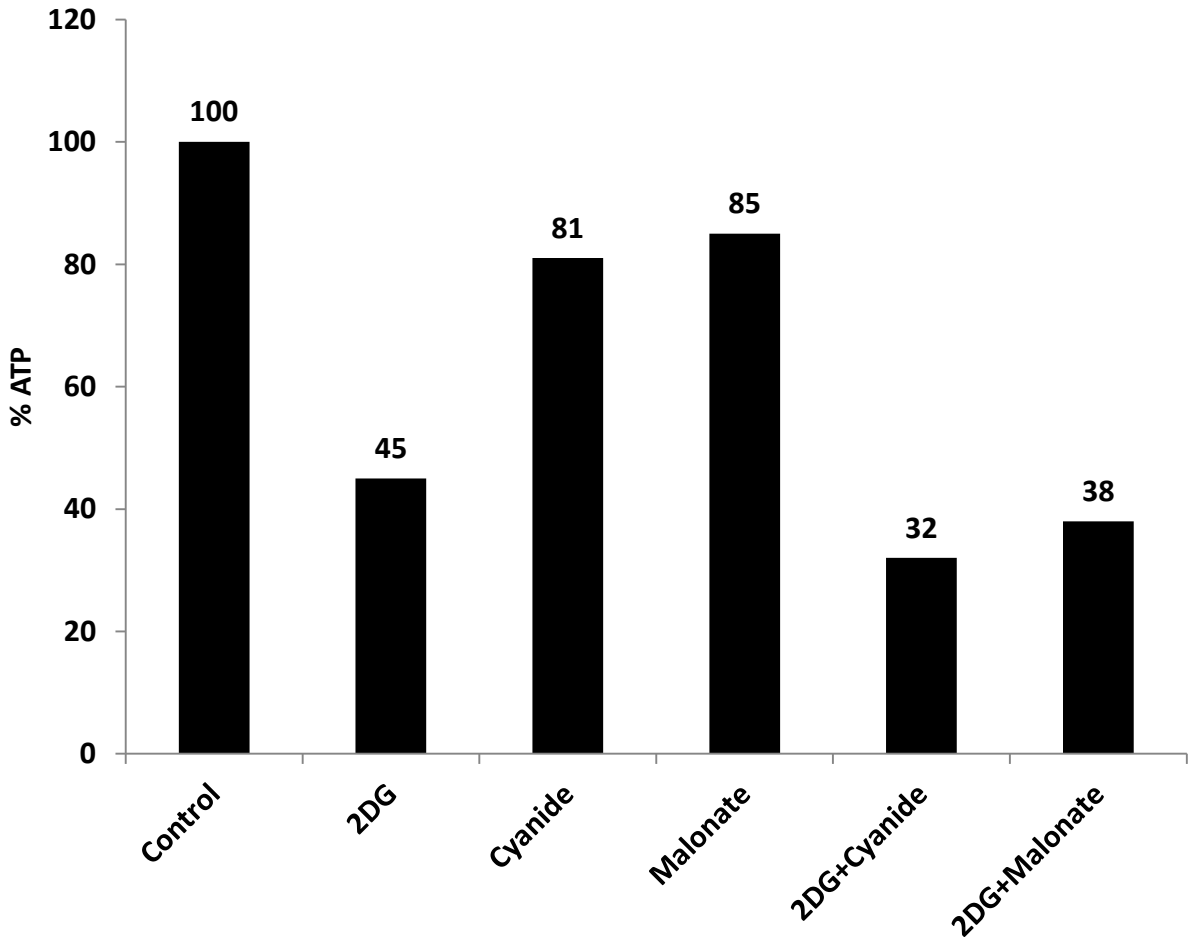

Figure 125: Percent ATP levels after 20 min exposure to metabolic inhibitors

Primary neuronal cells incubated with cyanide have been shown to lower the ATP level to 33% [89] and the clonal pheochromocytoma PC12 cell line has also been shown to be sensitive to cyanide [89]. Treatment of cells with 2DG had lowered cellular ATP levels to 45%. The combinational treatment had the highest effect on NG108-15 cellular ATP levels. After a 20 min exposure ATP levels were reduced in 2DG with cyanide and 2DG with malonate treated cells to 32 and 38% respectively. These results clearly indicated that NG108-15 cells were more

sensitive to 2DG. Ray et al. have demonstrated that pre-treatment of NG108-15 cells with $CoCl_2$ prevented the depletion of ATP during the combinational treatment with 2DG and cyanide [89].

5.10. Temporal proteomic analysis

Proteomics deals with the identification of protein expression profiles and their interactions within the cell. Most proteins are not only expressed at various concentrations, their activities also differ in the cell. A certain subset of proteins synthesized in the cell might be inactive due to several rate limiting steps governing their activation. So, it is important to chronically monitor the activities of these proteins and their interactions in a large network. The overall goal of this dissertation is to be able to perform temporal proteomic analysis.

5.10.1. Heat map of predicted protein activities

The experimentally validated neuronal-metabolic model was able to predict the changes in neuronal action potentials and cellular metabolism. The predicted activity of all the proteins was analyzed to gain a deeper insight into the protein functions. The activities of the proteins involved in the core metabolic pathways were analyzed at different time points. Figure 126 shows the changes in the proteins after a 10 minute exposure to metabolic perturbation. The first column indicates the activity of proteins in a steady state. The activity of these proteins has been normalized based on their activity. The activities of glycolytic proteins exposed to 2DG were reduced and the mitochondrial enzyme activities were slightly increased which was in accordance with the metabolic flux analysis of carbon (Figure 126).

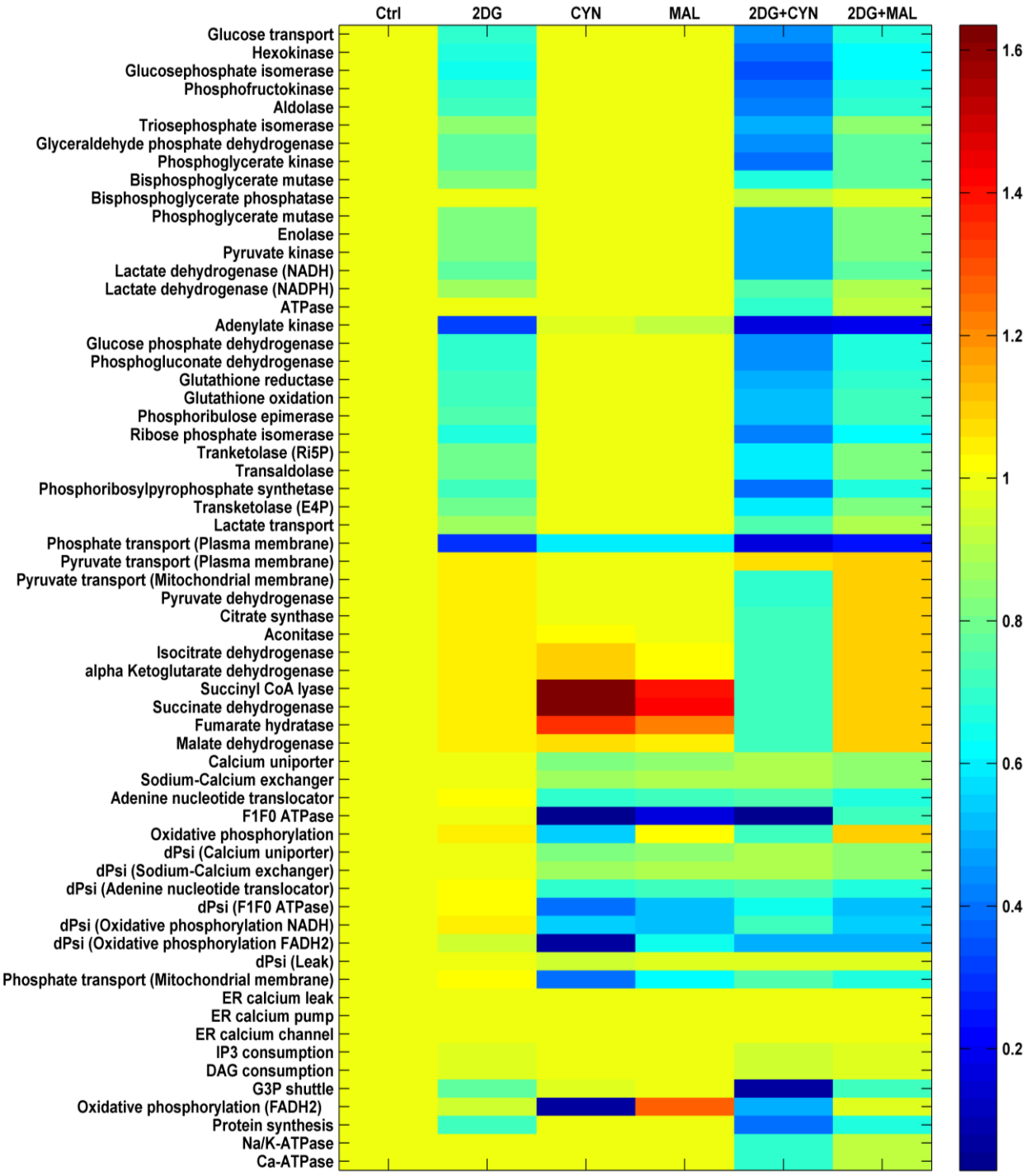

Figure 126: Heat map of cellular proteins activities exposed to different metabolic inhibitors after 10 min

The activity of glycerol-3 phosphate dehydrogenase (G3P shuttle) was also lowered as sufficient amount of electrons were not generated due to a decline in cellular glycolysis. The lowered

transport of electrons also resulted in decreased $FADH_2$ oxidative phosphorylation. The activity of phosphoribosyl pyrophosphate synthase (PRPPs) also decreased along with a decreased flux into PPP.

Cyanide inhibited the mitochondrial respiration and caused a drop in oxidative phosphotylation. The activity of F_1F_0 ATPase also deteriorated due to a lowered mitochondrial potential. The activity of the F_1F_0 ATPase protein was compared between the malonate and cyanide treatments. The inhibition of cellular respiration by cyanide increased the activity of the TCA cycle as sufficient amounts of ATP were not being produced the by mitochondria. Malonate had a mild effect on the TCA cycle and showed similar effects of cyanide induced perturbations. The effect of the combinational treatment on protein activies was also determined. The effect of 2DG and cyanide treatment had lowered protein activites in both the pathways. Whereas, the treatment with 2DG and malonate had slighly lowered the glycolytic activity compared to the 2DG and cyanide treatment. The activities of the metabolic proteins were also lowered during 2DG and cyanide treatment wheres 2DG and malonate treatment had a very low effect (Figure 126).

A snapshot of the protein activities after 60 minutes exposure to specific drugs was analysed for changes in protein activites (Figure 127). Exposure to metabolic inhibitors varied protein activities. Prolonged exposure to 2DG lowered the activity of all glycolytic proteins and, specifically, reduced the actvity of phosphoglycerate kinase (PGK). The primary function of PGK is to generate ATP by obtaining phosphate from 1,3 biphosphoglycerate.

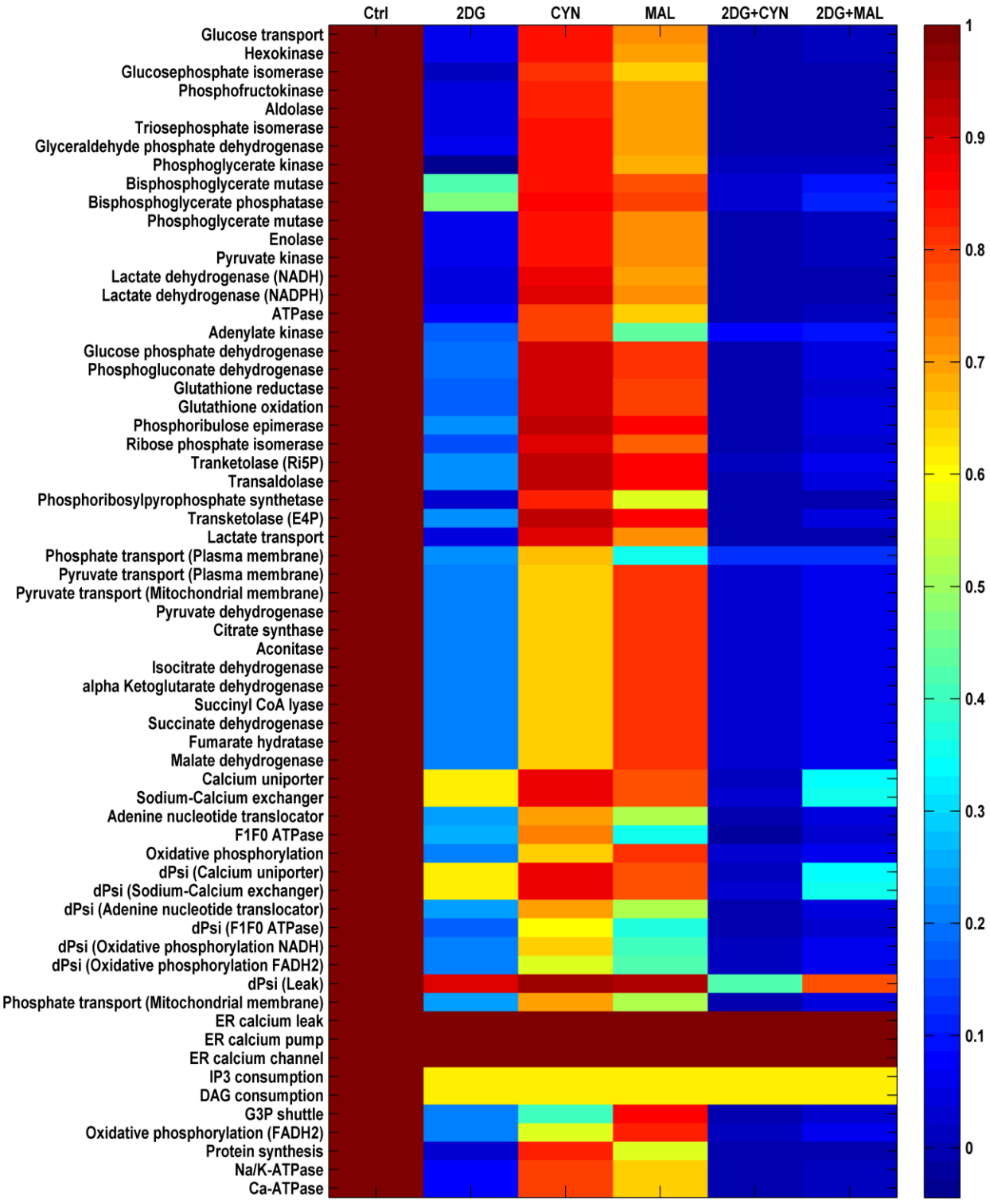

Figure 127: Heat map of cellular proteins activities exposed to different metabolic inhibitors after 60 min

This is an important reaction where glycycolytic ATP is generated and inhibition could be a viable option for cancer treatment. The acitvity of PRPPs also decreased as most of the carbon ended up as lactate. Cyanide had lowered the activity of all glycolytic poteins by ~10% and mitochondial TCA cycle proteins activities were lowered by ~40%. Malonate effected protein activities in both the glycolysis and mitochondrial pathways. The activity of G3P protein activity was significantly decreased during malonate treatment as the transport of electrons from glycolysis has decreased. The activities of all proteins decreased significantly after a 60 min combinational treatment of 2DG+ cyanide and 2DG+malonate.

5.10.2. Time-dependent functional activities of proteins

The activation and inactivation of proteins occurs in a time-dependent manner. Current proteomic tools lack the resolution to predict the changes in a large network simultaneously. The model's ability to chronically monitor functional changes in cellular protein activities of the core metabolic pathways was demonstrated. Since the perturbations were induced using cellular bioenergetic inhibitors, the activities of the proteins with respect to changes in cellular ATP fluxes were investigated. The protein activities involved in carbon usage, ATP production and usage are shown below (Figure 128, 129 and 130).

Temporal analysis of proteins involved in the cellular ATP consumption was determined (Figure 128). The activities of proteins that depend on cellular ATP levels are ATP dependent plasma membrane calcium transporter (Ca-ATPase), sodium-potassium ATPase (Na/K-ATPase), phosphoribosyl pyrophosphate synthase (PRPPS), general ATPase's (ATPase), phosphofructokinase (PFK) and hexokinase (HK). The activities were normalized to the total ATP

consumption. These protein activities were in agreement with the results obtained from the metabolic flux analysis. Analysis of cellular proteins between treatments with 2DG, cyanide, malonate, 2DG+Cyanide and 2DG+malonate was performed. Similar to the metabolic flux analysis, the activities of the proteins decreased when the cells were exposed to 2DG alone or combinational treatment involving 2DG.

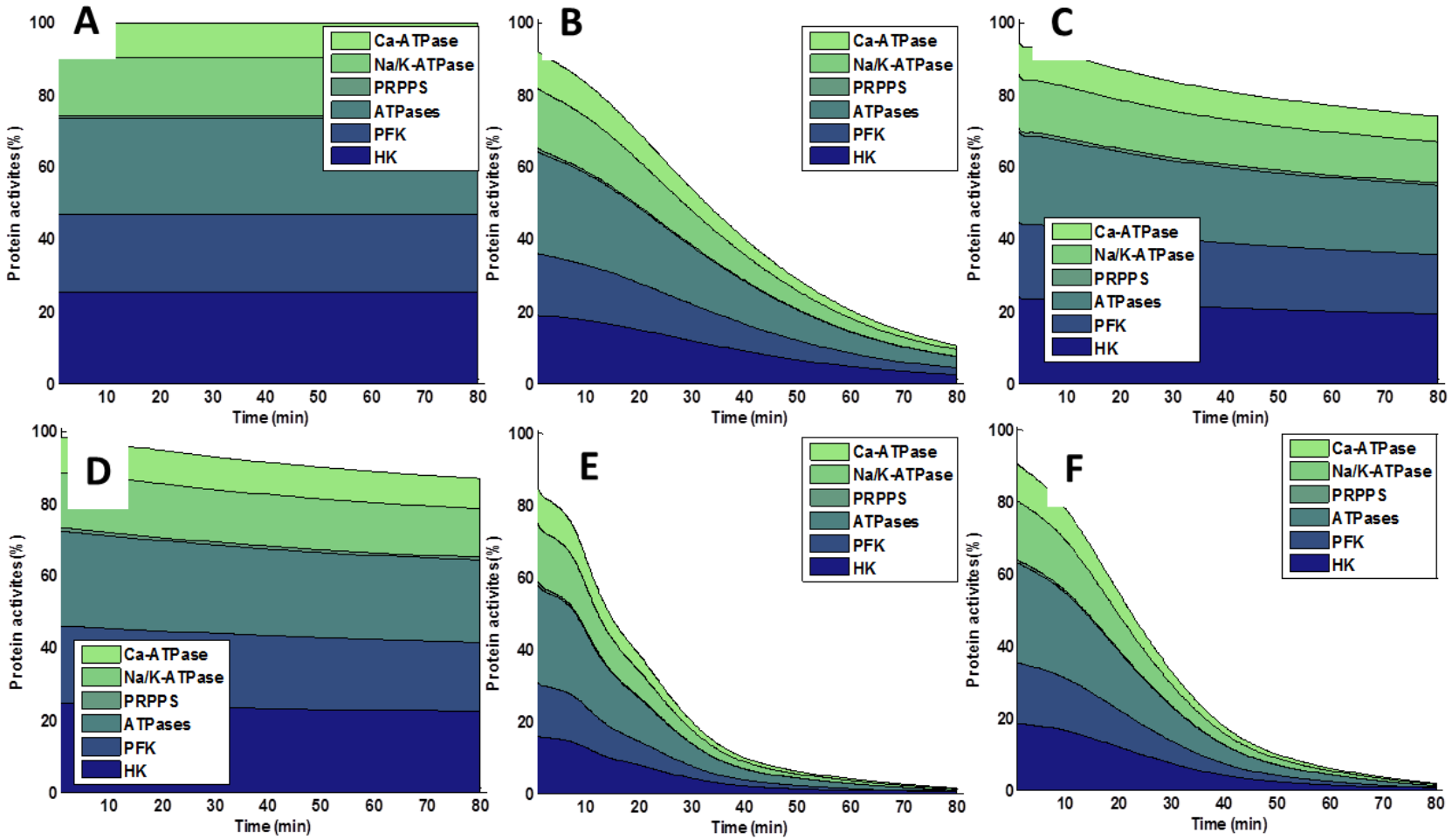

Figure 128: Predicted activities of Calcium ATPase (Ca-ATPase), Sodium-potassium-ATPase (Na/K-ATPase), phosphoribosyl pyrophosphate synthase (PRPPS), general ATPases (ATPase), phosphofructokinase (PFK) and hexokinase (HK) during (A) control, (B) 2DG, (C) cyanide, (D) malonate, (E) 2DG+cyanide and (F) 2DG+malonate exposure. Their activities are normalized to total ATP usage by NG108-15

The time dependent changes of the major proteins involved in determining carbon fluxes is shown in Figure 129. Although all the enzymes are important in maintaining a proper carbon flux throughout the cell, a few proteins were chosen to demonstrate the predictive capabilities of the model. The activities of glucose transporter, pyruvate dehydrogenase, monocarboxylate transporter and ribose-5 phosphate isomerase were analyzed. The glucose transporter senses the intracellular concentration of glucose in the cell and imports glucose. The monocarboxylate transporter (MCT) is responsible for transporting the intracellular lactate outside. These transporters are diffusion based and exchange metabolites by sensing the intracellular concentrations. The MCT's have been shown to be highly active in cells with elevated glycolysis especially in astrocytes and cancer cells. Pyruvate dehydrogenase metabolizes the carbon entering the mitochondria so that it can be used in the TCA cycle. Several inhibitors have been designed to impede the activity of these enzymes in order to modulate and create a shift in cellular metabolism.

The temporal analysis of proteins engaged in ATP production is shown in Figure 130. The major proteins involved in glycolytic ATP production are phosphoglycerate kinase (PGK) and pyruvate kinase (PK). These enzymes have lowered significantly upon exposure to 2DG (figure 130 B). The PGK protein activity was completely inhibited after 60 min. The mitochondrial proteins were still actively generating ATP. The combinational exposure of 2DG with cyanide and malonate inhibited the protein activities completely. The protein activities were inhibited on a different time scale by a different metabolic inhibitor. For example, PGK activity was completely inhibited in 70 min when exposed to 2DG whereas the activity of the same enzyme decreased much faster when exposed to a combinational treatment with 2DG and cyanide.

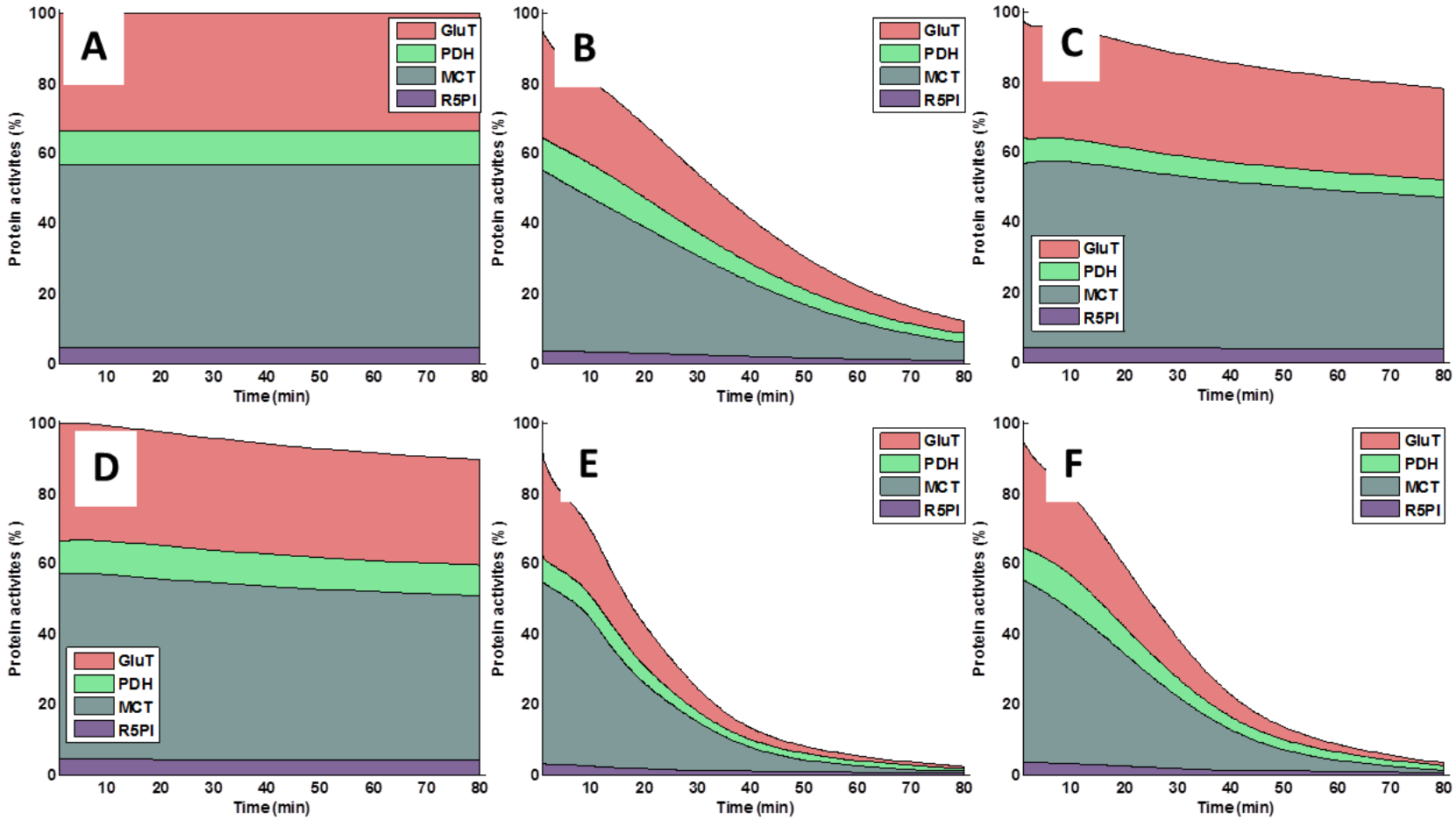

Figure 129: Predicted activities of glucose transporter (GluT), pyruvate dehydrogenase (PDH), monocarboxylate transporter (MCT) and ribose-5-phosphate isomerase (Ri5PI) during (A) control, (B) 2DG, (C) cyanide, (D) malonate, (E) 2DG+cyanide and (F) 2DG+malonate exposure. The protein activities are normalized based on total carbon utilization in NG108-15 cell

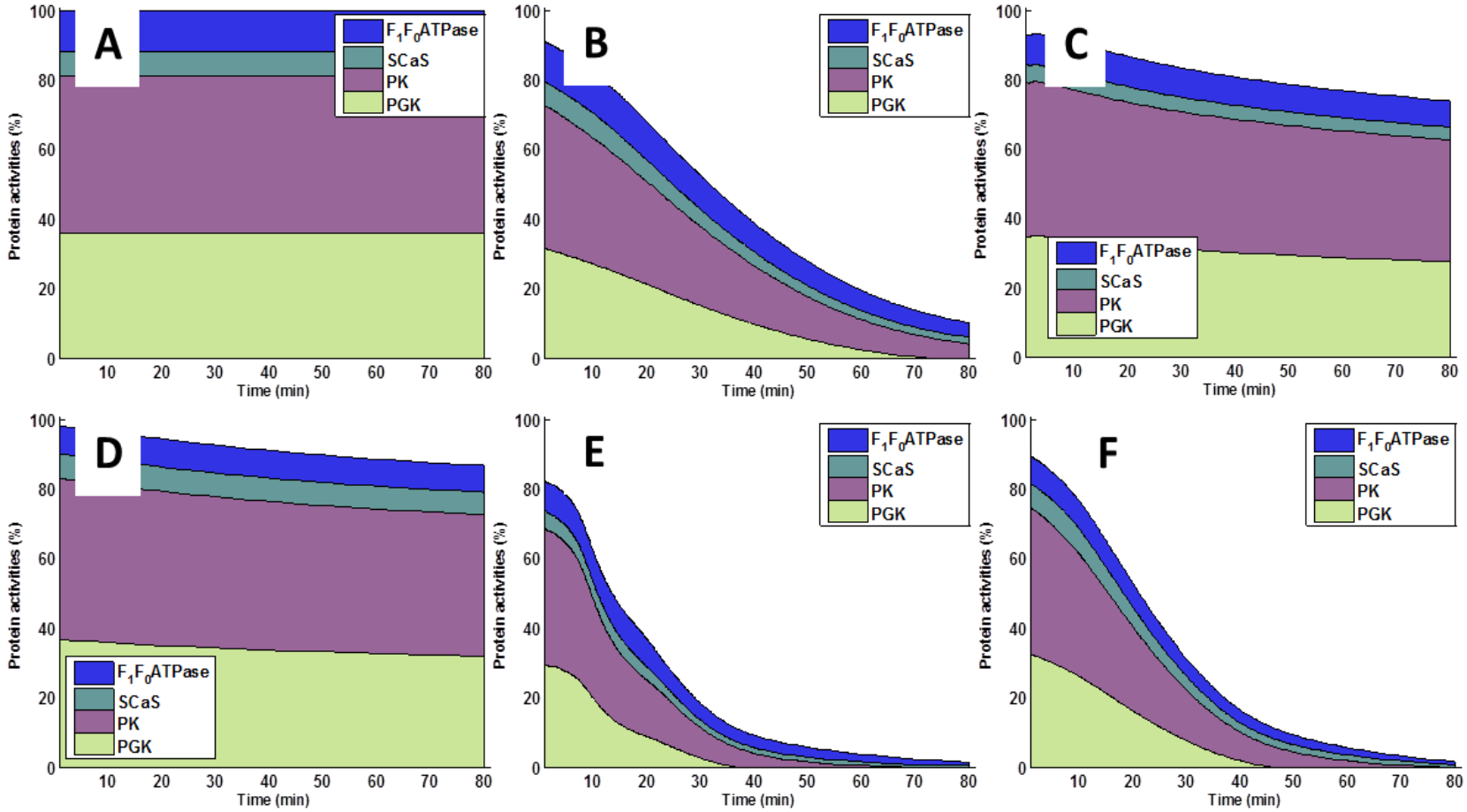

Figure 130: Predicted activities of phosphoglycerate kinase (PGK), pyruvate kinase (PK), succinyl CoA synthase (SCaS) and F-type ATP synthase (F_1F_0ATPase) during (A) control, (B) 2DG, (C) cyanide, (D) malonate, (E) 2DG+cyanide and (F) 2DG+malonate exposure. The protein activities are normalized based on the amount total amount of ATP generated by NG108-15 cell

CHAPTER-6: CONCLUSIONS AND FUTURE WORK

6.1. Conclusions

Proteomics is a dynamic and rapidly growing field where many advances have occurred during the past decade. Several high-throughput and high content screening technologies such as MS have been developed but none of them have the capability to perform non-invasive temporal analysis of cellular protein on a large-scale. The determination of protein activities over time would enable us to better understand disease progression and also analyze perturbations of pharmacologically active compounds. Pharmaceutical companies are in great need of tools capable of characterizing perturbations induced by active compounds in cellular networks. The work presented in this dissertation addresses this need with the development and experimental validation of a novel *in silico* model capable of predicting the changes in cellular protein activities and action potentials over time.

To accurately predict protein activities, a validated *in silico* model is a prerequisite. Hence, the basal metabolism and cellular bioenergetics of NG108-15 cells were first experimentally determined to validate the metabolic model. The analysis of cellular carbon fluxes and ATP levels showed that metabolic pathways in a NG108-15 cell are reprogrammed. The reconstructed metabolic module included the core metabolic pathways, namely, glycolysis, pentose phosphate pathway, mitochondria and endoplasmic reticulum, which are essential to study energy metabolism. The model calibration was accomplished using a parameter estimation algorithm to simulate steady state by concurrently constraining the model to control experimental data. The metabolic model produced an excellent fit to experimental data and

predicted the activities of cellular proteins. A detailed analysis of cellular protein activities revealed that NG108-15 cells are utilizing the 'Warburg effect'.

A more realistic neuronal module was also constructed by incorporating additional ion channels and exchangers to predict the membrane electrical properties of NG108-15 cell. The electrophysiological readout from the NG108-15 cell was complex and deconvoluted by employing a custom algorithm to estimate ion channel parameters and exchanger activities. Deconvolution of the electrophysiological readout provided an excellent fit to voltage clamp and current clamp recordings. This estimation of ion channel parameters was important as these parameters determine ion fluxes. The developed neuronal module was coupled with a metabolic model to build a more comprehensive neuronal-metabolic model. The coupled neuronal-metabolic model accurately predicted cellular metabolic and neuronal protein activities along with the changes in intracellular ionic and metabolite concentrations. The model was capable of generating multiple action potentials over time. The neuronal module also included a subcellular compartment, a distinct feature that provides a more physiological representation of ionic fluxes during action potential generation in a neuron.

The predictive capability of the neuronal-metabolic activity was confirmed by performing a series of known perturbations by inhibiting cellular proteins and simulating model behavior. The model predictions were supported with experimental measurements. The proteins involved in major energy producing pathways were perturbed. Initially, *in silico* perturbations of glycolytic enzymes were analyzed. Glycolytic perturbations identified a significant effect on cellular protein activities, leading to a decrease in carbon flux, cellular ATP levels and action

potentials. The experimental determination of metabolic and neuronal activity to glycolysis perturbations were in very good agreement with the model predictions. The glycolytic inhibition lowered the activities of several proteins which lead to time-dependent changes in neuronal AP.

The inhibition of mitochondrial protein activities was also evaluated by exposing cells to cyanide and malonate. These mitochondrial inhibitors induced changes in metabolic and electrophysiological activity and were measured experimentally and simulated using the neuronal-metabolic model. The changes in neuronal APs predicted by the model were in good agreement with the experimental recordings. In addition, the carbon and adenosine fluxes were also in good agreement. The model predicted that the mitochondrial protein activity in the NG108-15 cells was lower compared to the activity of glycolytic proteins. This lower mitochondrial activity was reflected in metabolic and electrophysiological experiments where no significant changes were found upon cyanide and malonate exposure. A combinational perturbation in the neuronal-metabolic model showed that the sensitivity of the NG108-15 cells could be enhanced. An experimental determination of neuronal electrophysiological recordings and metabolic measurements showed that the model predictions were in good agreement.

Analysis of AP time series data revealed that the shape of APs varies based on the pathway being inhibited. The characterization of these AP changes enabled the distinguishing of the pathways being affected. The developed model also allowed temporal analysis of cellular protein activities involved in core energy producing pathways. Thus, the developed model and validated results demonstrate the use of a system biology driven electrophysiological model as

an attractive platform for functional temporal proteomic analysis based on an electrophysiology readout.

6.2. Future work

Future work could focus on extending the current model by incorporating additional pathways representing all functional categories. The functional categories can be broadly divided into 6 categories, namely, 1) energy metabolism, 2) biosynthesis of aminoacids, 3) cellular processes, 4) fatty acid metabolism, 5) transcriptional regulation, 6) trasporters and binding proteins [26]. Currently, the energy metabolism has been incorporated and tied to neuronal actvitiy. A top-down model development approach has been followed that allows the flexibility of incorporating any new functional modules later on.

The short-term future goals of the project could be to include cell-cycle to develop nuclear-signaling process, followed by a more precise implementation of calcium handling. At present the neuronal module is capable of predicting the ion concentration changes over time. In future work, the incorporation of secondary messenger systems and its activation based on altered ion concentrations would be useful to predict modifications in cellular activities. The model would have to be adapted and validated for NG108-15 cells followed by electrophysiological characterization, since time-scale of activities and corresponding AP peak shapes could be different.

The long-term goal would be to include cellular process of functional categories listed above and experimentally validate them followed by building a database of their effects. This

would then enable analysis of APs after being treated with a compound to predict pathway perturbations. For understanding disease progression or identification of long-term effects of a drug, it is necessary to analyze APs on a longer time-scale. Long-term electrophysiological recordings obtained from MEAs would have to be deconvoluted using a custom algorithm. Although the resolutions of signals obtained from MEAs are not as high as compared to patch-clamp electrophysiology, they could still be deconvoluted. In the event of complexity, other viable approaches can be adapted. Recent advances in electrophysiological recordings have enabled researchers to culture cells on carbon nanotubes [112] for achieving whole-cell recordings on a longer time scale. But these techniques need to be validated confirming that no other cellular mechanisms were triggered while using carbon nanotubes.

Further, advancement in model development would allow cellular APs to be measured directly from a microfluidic system, followed by deconvolution of AP time-series to predict protein-protein interaction and changes in protein activities for performing high-throughput, non-invasive temporal proteomics.

APPENDIX A: METABOLIC MODEL DIFFERENTIAL EQUATIONS

Mitochondrial pyruvate	$\frac{d(Pyrm)}{dt} = \frac{1}{mitochondrial} * (v35 - v36)$
Mitochondrial NAD	$\frac{d(NADm)}{dt} = \frac{1}{mitochondrial} * (-v36 - v39 - v40 - v44 + v49)$
Acetyl-CoA	$\frac{d(AcCoA)}{dt} = \frac{1}{mitochondrial} * (v36 - v37)$
Mitochondrial NADH	$\frac{d(NADHm)}{dt} = \frac{1}{mitochondrial} * (v36 + v39 + v40 + v44 - v49)$
Oxaloacetate	$\frac{d(OAA)}{dt} = \frac{1}{mitochondrial} * (-v37 + v44)$
Citrate	$\frac{d(Cit)}{dt} = \frac{1}{mitochondrial} * (v37 - v38)$
Isocitrate	$\frac{d(IsoCit)}{dt} = \frac{1}{mitochondrial} * (v38 - v39)$
α-Ketoglutarate	$\frac{d(aKG)}{dt} = \frac{1}{mitochondrial} * (v39 - v40)$
Mitochondrial ADP	$\frac{d(ADPm)}{dt} = \frac{1}{mitochondrial} * (-v41 + v47 - v48)$
Mitochondrial calcium	$\frac{d(Cam)}{dt} = \frac{1}{mitochondrial} * (v45 - v46)$
Succinyl CoA	$\frac{d(SucCoA)}{dt} = \frac{1}{mitochondrial} * (v40 - v41)$
Mitochondrial phosphate	$\frac{d(Pim)}{dt} = \frac{1}{mitochondrial} * (-v41 - v48 + v57)$
Succinate	$\frac{d(Suc)}{dt} = \frac{1}{mitochondrial} * (v41 - v42)$

Mitochondrial ATP	$\frac{d(ATPm)}{dt} = \frac{1}{mitochondrial} * (v41 - v47 + v48)$
Fumarate	$\frac{d(Fum)}{dt} = \frac{1}{mitochondrial} * (v42 - v43)$
Malate	$\frac{d(Mal)}{dt} = \frac{1}{mitochondrial} * (v43 - v44)$
Mitochondrial membrane potential	$\frac{d(dPsi)}{dt} = \frac{1}{mitochondrial} * (-2 * v50 - v51 - v52 - v53 + v54 + v55 - v56)$
Mitochondrial FAD	$\frac{d(FAD)}{dt} = \frac{1}{mitochondrial} * (-v42 - v64 + v65)$
Mitochondrial $FADH_2$	$\frac{d(FADH2)}{dt} = \frac{1}{mitochondrial} * (v42 + v64 - v65)$
Endoplasmic reticulum calcium	$\frac{d(Caer)}{dt} = \frac{1}{er} * (-v59 + v60 - v61)$
Cytosolic Glucose	$\frac{d(Glc)}{dt} = \frac{1}{cellular} * (v1 - v2)$
Magnesium bound ATP	$\frac{d(MgATP)}{dt} = \frac{1}{cellular} * (-v2 - v4 + v8 + v13 - v16 - v17 - v26 - v31 - v67 - v68)$
Glucose-6-phosphate	$\frac{d(G6P)}{dt} = \frac{1}{cellular} * (v2 - v3 - v18)$
Magnesium bound ADP	$\frac{d(MgADP)}{dt} = \frac{1}{cellular} * (v2 + v4 - v8 - v13 + v16 + v17 - v32 + v67 + v68)$
2,3-bisphosphoglycerate	$\frac{d(BPG23)}{dt} = \frac{1}{cellular} * (v9 - v10 + v34)$
Magnesium	$\frac{d(Mg)}{dt} = \frac{1}{cellular} * (v31 + v32 + v33 + v34)$

Magnesium bound 2,3-bisphosphoglycerate	$\frac{\mathrm{d(MgBPG23)}}{\mathrm{dt}} = \frac{1}{\mathrm{cellular}} * (-\mathrm{v34})$
Fructose 6-phosphate	$\frac{\mathrm{d(F6P)}}{\mathrm{dt}} = \frac{1}{\mathrm{cellular}} * (\mathrm{v3} - \mathrm{v4} + \mathrm{v25} + \mathrm{v27})$
AMP	$\frac{\mathrm{d(AMP)}}{\mathrm{dt}} = \frac{1}{\mathrm{cellular}} * (-\mathrm{v17} + \mathrm{v33})$
ATP	$\frac{\mathrm{d(ATP)}}{\mathrm{dt}} = \frac{1}{\mathrm{cellular}} * (\mathrm{v31} + \mathrm{v47})$
Fructose 1,6-biphosphate	$\frac{\mathrm{d(F16BP)}}{\mathrm{dt}} = \frac{1}{\mathrm{cellular}} * (\mathrm{v4} - \mathrm{v5})$
Magnesium bound AMP	$\frac{\mathrm{d(MgAMP)}}{\mathrm{dt}} = \frac{1}{\mathrm{cellular}} * (\mathrm{v26} - \mathrm{v33})$
Glyceraldehyde-3-phosphate	$\frac{\mathrm{d(GAP)}}{\mathrm{dt}} = \frac{1}{\mathrm{cellular}} * (\mathrm{v5} + \mathrm{v6} - \mathrm{v7} + \mathrm{v24} - \mathrm{v25} + \mathrm{v27})$
Dihydroxyacetone phosphate	$\frac{\mathrm{d(DHAP)}}{\mathrm{dt}} = \frac{1}{\mathrm{cellular}} * (\mathrm{v5} - \mathrm{v6})$
Cytosolic phosphate	$\frac{\mathrm{d(Pi)}}{\mathrm{dt}} = \frac{1}{\mathrm{cellular}} * (-\mathrm{v7} + \mathrm{v10} + \mathrm{v16} + \mathrm{v29} - \mathrm{v57} + \mathrm{v67} + \mathrm{v68})$
Cytosolic NAD	$\frac{\mathrm{d(NAD)}}{\mathrm{dt}} = \frac{1}{\mathrm{cellular}} * (-\mathrm{v7} + \mathrm{v14} + \mathrm{v64})$
1,3-bisphosphoglycerate	$\frac{\mathrm{d(BPG13)}}{\mathrm{dt}} = \frac{1}{\mathrm{cellular}} * (\mathrm{v7} - \mathrm{v8} - \mathrm{v9})$
Cytosolic NADH	$\frac{\mathrm{d(NADH)}}{\mathrm{dt}} = \frac{1}{\mathrm{cellular}} * (\mathrm{v7} - \mathrm{v14} - \mathrm{v64})$
3-Phosphoglycerate	$\frac{\mathrm{d(PG3)}}{\mathrm{dt}} = \frac{1}{\mathrm{cellular}} * (\mathrm{v8} + \mathrm{v10} - \mathrm{v11})$

2-Phosphoglycerate	$\frac{\mathrm{d(PG2)}}{\mathrm{dt}} = \frac{1}{\mathrm{cellular}} * (\mathrm{v11} - \mathrm{v12})$
Phosphoenolpyruvate	$\frac{\mathrm{d(PEP)}}{\mathrm{dt}} = \frac{1}{\mathrm{cellular}} * (\mathrm{v12} - \mathrm{v13})$
Cytosolic pyruvate	$\frac{\mathrm{d(Pyr)}}{\mathrm{dt}} = \frac{1}{\mathrm{cellular}} * (\mathrm{v13} - \mathrm{v14} - \mathrm{v15} + \mathrm{v30} - \mathrm{v35})$
Cytosolic lactate	$\frac{\mathrm{d(Lac)}}{\mathrm{dt}} = \frac{1}{\mathrm{cellular}} * (\mathrm{v14} + \mathrm{v15} + \mathrm{v28})$
Cytosolic NADPH	$\frac{\mathrm{d(NADPH)}}{\mathrm{dt}} = \frac{1}{\mathrm{cellular}} * (-\mathrm{v15} + \mathrm{v18} + \mathrm{v19} - \mathrm{v20})$
Cytosolic NADP	$\frac{\mathrm{d(NADP)}}{\mathrm{dt}} = \frac{1}{\mathrm{cellular}} * (\mathrm{v15} - \mathrm{v18} - \mathrm{v19} + \mathrm{v20})$
ADP	$\frac{\mathrm{d(ADP)}}{\mathrm{dt}} = \frac{1}{\mathrm{cellular}} * (\mathrm{v17} + \mathrm{v32} - \mathrm{v47})$
6-phosphoglucono-δ-lactone	$\frac{\mathrm{d(PGL)}}{\mathrm{dt}} = \frac{1}{\mathrm{cellular}} * (\mathrm{v18} - \mathrm{v19})$
Ribuloase-5-phosphate	$\frac{\mathrm{d(Ru5P)}}{\mathrm{dt}} = \frac{1}{\mathrm{cellular}} * (\mathrm{v19} - \mathrm{v22} - \mathrm{v23})$
Glutathione disulphide	$\frac{\mathrm{d(GSSG)}}{\mathrm{dt}} = \frac{1}{\mathrm{cellular}} * (-\mathrm{v20} + \mathrm{v21})$
Glutathione	$\frac{\mathrm{d(GSH)}}{\mathrm{dt}} = \frac{1}{\mathrm{cellular}} * (2 * \mathrm{v20} - -2 * \mathrm{v21})$
Xyulose-5-phosphate	$\frac{\mathrm{d(X5P)}}{\mathrm{dt}} = \frac{1}{\mathrm{cellular}} * (\mathrm{v22} - \mathrm{v24} - \mathrm{v27})$
Ribose-5-phosphate	$\frac{\mathrm{d(Ri5P)}}{\mathrm{dt}} = \frac{1}{\mathrm{cellular}} * (\mathrm{v23} - \mathrm{v24} - \mathrm{v26})$

Sedoheptulose 7-phosphate	$\frac{\mathrm{d(S7P)}}{\mathrm{dt}} = \frac{1}{\mathrm{cellular}} * (\mathrm{v24} - \mathrm{v25})$
Erythrose 4-phosphate	$\frac{\mathrm{d(E4P)}}{\mathrm{dt}} = \frac{1}{\mathrm{cellular}} * (\mathrm{v25} - \mathrm{v27})$
Phosphoribosyl pyrophosphate	$\frac{\mathrm{d(PRPP)}}{\mathrm{dt}} = \frac{1}{\mathrm{cellular}} * (\mathrm{v26} - \mathrm{v66})$
Cytosolic calcium	$\frac{\mathrm{d(Ca)}}{\mathrm{dt}} = \frac{1}{\mathrm{cellular}} * (-\mathrm{v45} + \mathrm{v46} + \mathrm{v59} - \mathrm{v60} + \mathrm{v61})$
Phosphatidylinositol 4,5-bisphosphate	$\frac{\mathrm{D(PIP2)}}{\mathrm{dt}} = \frac{1}{\mathrm{cellular}} * (-\mathrm{v58})$
Inositol triphosphate	$\frac{\mathrm{d(IP3)}}{\mathrm{dt}} = \frac{1}{\mathrm{cellular}} * (\mathrm{v58} - \mathrm{v62})$
Diacyl-glycerol	$\frac{\mathrm{d(DAG)}}{\mathrm{dt}} = \frac{1}{\mathrm{cellular}} * (\mathrm{v58} - \mathrm{v63})$
Extracellular glucose	$\frac{\mathrm{d(Glce)}}{\mathrm{dt}} = \frac{1}{\mathrm{extracellular}} * (-\mathrm{v1})$
Extracellular lactate	$\frac{\mathrm{d(Lace)}}{\mathrm{dt}} = \frac{1}{\mathrm{extracellular}} * (-\mathrm{v28})$
Extracellular phosphate	$\mathrm{d(Pie)/dt} = 1/\mathrm{extracellular} * (-\mathrm{v29})$
Extracellular pyruvate	$\frac{\mathrm{d(Pyre)}}{\mathrm{dt}} = \frac{1}{\mathrm{extracellular}} * (-\mathrm{v30})$

APPENDIX B: METABOLIC MODEL FLUXES

Glucose transporter

$$v1 = \frac{Vmax_{gt}}{KmGlcout_{gt}} * \frac{Glce - \frac{Glc}{Keq_{gt}}}{1 + \frac{Glce}{KmGlcout_{gt}} + \frac{Glc}{KmGlcin_{gt}} + \frac{Glce * Glc}{KmGlcout_{gt} * KmGlcin_{gt}}}$$

Hexokinase

$$v2 = \frac{Glc}{Glc + KmGlc_{hk}} * \left(\frac{Vmax1_{hk}}{KmMgATP_{hk}}\right) * \frac{MgATP + \frac{Vmax2_{hk}}{Vmax1_{hk}} MgATP \frac{Mg}{KmMgATPMg_{hk}} - G6P * \frac{MgADP}{Keq_{hk}}}{\left(\left(1 + \frac{MgATP}{KmMgATP_{hk}}\right)\left(1 + \frac{Mg}{KmMgATPMg_{hk}}\right) + \frac{Mg}{KmMg_{hk}} + \left(1.55 + \frac{G6P}{KmG6P_{hk}}\right)\left(1 + \frac{Mg}{KmMg_{hk}}\right) + \frac{BPG23 + MgBPG23}{KmBPG23_{hk}} + Mg\frac{BPG23 + MgBPG23}{KmMg_{hk} * KmMgBPG23_{hk}}\right)}$$

Glucosephosphate isomerase

$$v3 = Vmax_{gpi} * \frac{G6P - \frac{F6P}{Keq_{gpi}}}{G6P + KmG6P_{gpi} * \left(1 + \frac{F6P}{KmF6P_{gpi}}\right)}$$

Phosphofructokinase

$$v4 = Vmax_{pfk} * \frac{F6P * MgATP - F16BP * \frac{MgADP}{Keq_{pfk}}}{\left(F6P + KmF6P_{pfk}\right) * \left(MgATP + KmMgATP_{pfk}\right) * \left(\left(1 + Lo_{pfk} * \left(\left(1 + \frac{ATP}{KmATP_{pfk}}\right) * \frac{1 + \frac{Mg}{KmMg_{pfk}}}{\left(1 + \frac{AMP + MgAMP}{KmAMP_{pfk}}\right) * \left(1 + \frac{F6P}{KmF6P_{pfk}}\right)}\right)^4\right)\right)}$$

Aldolase

$$v5 = \frac{Vmax_{ald}}{KmF16BP_{ald}} * \frac{F16BP - GAP * \frac{DHAP}{Keq_{ald}}}{1 + \frac{F16BP}{KmF16BP_{ald}} + \frac{GAP}{KiGAP_{ald}} + DHAP * \frac{GAP + KmGAP_{ald}}{KmDHAP_{ald} * KiGAP_{ald}} + F16BP * \frac{GAP}{KmF16BP_{ald} * KiiGAP_{ald}}}$$

Triosephosphate isomerase

$$v6 = Vmax_{tpi} * \frac{DHAP - \frac{GAP}{Keq_{tpi}}}{DHAP + KmDHAP_{tpi} * \left(1 + \frac{GAP}{KmGAP_{tpi}}\right)}$$

Glyceraldehyde phosphate dehydrogenase

$$v7 = \frac{Vmax_{gapdh}}{KmNAD_{gapdh} * KmGAP_{gapdh} * KmPi_{gapdh}} * \frac{NAD * GAP * Pi - BPG13 * \frac{NADH}{Keq_{gapdh}}}{\left(1 + \frac{NAD}{KmNAD_{gapdh}}\right) * \left(1 + \frac{GAP}{KmGAP_{gapdh}}\right) * \left(1 + \frac{Pi}{KmPi_{gapdh}}\right) + \left(1 + \frac{NADH}{KmNADH_{gapdh}}\right) * \left(1 + \frac{BPG13}{KmBPG13_{gapdh}}\right) - 1}$$

Phosphoglycerate kinase

$$v8 = \frac{Vmax_{pgk}}{KmMgADP_{pgk} * KmBPG13_{pgk}} * \frac{MgADP * BPG13 - MgATP * \frac{PG3}{Keq_{pgk}}}{\left(1 + \frac{MgADP}{KmMgADP_{pgk}}\right) * \left(1 + \frac{BPG13}{KmBPG13_{pgk}}\right) + \left(1 + \frac{MgATP}{KmMgATP_{pgk}}\right) * \left(1 + \frac{PG3}{KmPG3_{pgk}}\right) - 1}$$

Bisphosphoglycerate mutase

$$v9 = Kd_{bpgm} * \frac{BPG13 - \frac{BPG23 + MgBPG23}{Keq_{bpgm}}}{1 + \frac{BPG23 + MgBPG23}{KmBPG23_{bpgm}}}$$

Bisphosphoglycerate phosphatase

$$v10 = Vmax_{bpgp} * \frac{BPG23 + MgBPG23 - \frac{PG3}{Keq_{bpgp}}}{BPG23 + MgBPG23 + KmBPG23_{bpgp}}$$

Phosphoglycerate mutase

$$v11 = Vmax_{pgm} * \frac{PG3 - \frac{PG2}{Keq_{pgm}}}{PG3 + KmPG3_{pgm} * \left(1 + \frac{PG2}{KmPG2_{pgm}}\right)}$$

Enolase

$$v12 = Vmax_{eno} * \frac{PG2 - \frac{PEP}{Keq_{eno}}}{PG2 + KmPG2_{eno} * \left(1 + \frac{PEP}{KmPEP_{eno}}\right)}$$

Pyruvate kinase

$$v13 = Vmax_{pk} * \frac{PEP * MgADP - Pyr * \frac{MgATP}{Keq_{pk}}}{\left(PEP + KmPEP_{pk}\right) * \left(MgADP + KmMgADP_{pk}\right) * \left(1 + Lo_{pk} * \frac{\left(1 + \frac{ATP + MgATP}{KmATP_{pk}}\right)^4}{\left(\left(1 + \frac{PEP}{KmPEP_{pk}}\right)^4\right) * \left(\left(1 + \frac{F16BP}{KmF16BP_{pk}}\right)^4\right)}\right)}$$

Lactate dehydrogenase (NADH)

$$v14 = Vmax_{ldh} * \left(Pyr * NADH - Lac * \frac{NAD}{[\text{Lactate dehydrogenase (NADH)}]} . Keq_{ldh}\right)$$

Lactate dehydrogenase (NADPH)

$$v15 = k_{ldh} * \left(Pyr * NADPH - Lac * \frac{NADP}{[\text{Lactate dehydrogenase (NADPH)}]} . Keq_{ldh}\right)$$

ATPase

$$v16 = k_{ATPase} * MgATP$$

Adenylate kinase

$$v17 = = \frac{\frac{Vmax_{ak}}{KmATP_{ak} * KmAMP_{ak}} * \left(MgATP * AMP - MgADP * \frac{ADP}{Keq_{ak}}\right)}{\left(1 + \frac{MgATP}{KmATP_{ak}}\right) * \left(1 + \frac{AMP}{KmAMP_{ak}}\right) + \frac{MgADP + ADP}{KmADP_{ak}} + MgADP * \left(\frac{ADP}{(KmADP_{ak})^2}\right)}$$

Glucose phosphate dehydrogenase

$$v18 = \frac{Vmax_{gpdh}}{KmG6P_{gpdh} * KmNADP_{gpdh}} * \frac{G6P * NADP - PGL * \frac{NADPH}{Keq_{gpdh}}}{1 + NADP * \frac{1 + \frac{G6P}{KmG6P_{gpdh}}}{KmNADP_{gpdh}} + \frac{ATP + MgATP}{KmATP_{gpdh}} + \frac{NADPH}{KmNADPH_{gpdh}} + \frac{BPG23 + MgBPG23}{KmBPG23_{gpdh}}}$$

Phosphogluconate dehydrogenase

$$v19 = \frac{Vmax_{pgldh}}{KmPGL1_{pgldh} * KmNADP_{pgldh}} * \frac{PGL * NADP - Ru5P * \frac{NADPH}{Keq_{pgldh}}}{\left(\left(1 + \frac{NADP}{KmNADP_{pgldh}}\right) * \left(1 + \frac{PGL}{KmPGL1_{pgldh}} + \frac{BPG23 + MgBPG23}{KmBPG23_{pgldh}}\right) + \frac{ATP + MgATP}{KmATP_{pgldh}} + \right.}$$
$$\left. NADPH * \frac{1 + \frac{PGL}{KmPGL2_{pgldh}}}{KmNADPH_{pgldh}}\right)$$

Glutathione reductase

$$v20 = Vmax_{gr} * \frac{GSSG * \frac{NADPH}{KmGSSG_{gr} * KmNADPH_{gr}} - \frac{(GSH)^2}{(KmGSH_{gr})^2} * \frac{NADP}{KmNADP_{gr} * Keq_{gr}}}{1 + NADPH * \frac{1 + \frac{GSSG}{KmGSSG_{gr}}}{KmNADPH_{gr}} + \frac{NADP}{KmNADP_{gr}} * \left(1 + GSH * \frac{1 + \frac{GSH}{KmGSH_{gr}}}{KmGSH_{gr}}\right)}$$

Glutathione oxidation

$$v21 = K_{go} * GSH$$

Phosphoribulose epimerase

$$v22 = Vmax_{pre} * \frac{Ru5P - \frac{X5P}{Keq_{pre}}}{Ru5P + KmRu5P_{pre} * \left(1 + \frac{X5P}{KmX5P_{pre}}\right)}$$

Ribose phosphate isomerase

$$v23 = Vmax_{rpi} * \frac{Ru5P - \frac{Ri5P}{Keq_{rpi}}}{Ru5P + KmRu5P_{rpi} * \left(1 + \frac{Ri5P}{KmRi5P_{rpi}}\right)}$$

Tranketolase (Ri5P)

$$v24 = \frac{[\text{Tranketolase (Ri5P)}].Vmax_{tk} * * \ Ri5P * X5P - \frac{GAP * S7P}{[\text{Tranketolase (Ri5P)}].Keq_{tk}}}{\left(\begin{array}{c}([\text{Tranketolase (Ri5P)}].K1_{tk} + Ri5P) * X5P + \\ ([\text{Tranketolase (Ri5P)}].K2_{tk} + [\text{Tranketolase (Ri5P)}].K6_{tk} * S7P) * Ri5P + \\ ([\text{Tranketolase (Ri5P)}].K3_{tk} + [\text{Tranketolase (Ri5P)}].K5_{tk} * S7P) * GAP + \\ [\text{Tranketolase (Ri5P)}].K4_{tk} * S7P + @[\text{Tranketolase (Ri5P)}].K7_{tk} * X5P * GAP\end{array}\right)}$$

Transaldolase

$$v25 = Vmax_{ta} * \frac{S7P * GAP - E4P * \frac{F6P}{Keq_{ta}}}{(K1_{ta} + GAP) * S7P + (K2_{ta} + K6_{ta} * F6P) * GAP + (K3_{ta} + K5_{ta} * F6P) * E4P + K4_{ta} * F6P + K7_{ta} * S7P * E4P}$$

Phosphoribosylpyrophosphate synthetase

$$v26 = Vmax_{prpps} * \frac{Ri5P * MgATP - PRPP * \frac{MgAMP}{Keq_{prpps}}}{(KmATP_{prpps} + MgATP) * (KmRi5P_{prpps} + Ri5P)}$$

Transketolase (E4P)

$$v27 = \frac{\left([\text{Transketolase (E4P)}]Vmax_{tk} * E4P * X5P - GAP * \frac{F6P}{[\text{Transketolase (E4P)}]Keq_{tk}}\right)}{\left(\begin{array}{c}([\text{Transketolase (E4P)}]K1_{tk} + E4P) * X5P + \\ ([\text{Transketolase (E4P)}]K2_{tk} + [\text{Transketolase (E4P)}]K6_{tk} * F6P) * E4P + \\ ([\text{Transketolase (E4P)}]K3_{tk} + [\text{Transketolase (E4P)}]K5_{tk} * F6P) * GAP + \\ [\text{Transketolase (E4P)}]K4_{tk} * F6P + \\ [\text{Transketolase (E4P)}]K7_{tk} * X5P * GAP\end{array}\right)}$$

Monocarboxylate transporter, Lactate transport

$$v28 = Vmax_{lt} * \left(Lace - \frac{Lac}{Keq_{lt}}\right)$$

Phosphate transporter on plasma membrane

$$v29 = [\text{Phosphate transport (Plasma membrane)}].Vmax_{pt} * \left(Pie - \frac{Pi}{[\text{Phosphate transport (Plasma membrane)}]}.Keq_{pt}\right)$$

Pyruvate transporter on plasma membrane

$$v30 = [\text{Pyruvate transport (Plasma membrane)}].Vmax_{pt} * \left(Pyre - \left(\frac{Pyr}{[\text{Pyruvate transport (Plasma membrane)}]}.Keq_{pt}\right)\right)$$

MgATP dissociation

$$v31 = EqMgATP * \left(MgATP - Mg * \frac{ATP}{KdMgATP}\right)$$

MgADP dissociation

$$v32 = EqMgADP * \left(MgADP - Mg * \frac{ADP}{KdMgADP}\right)$$

MgAMP dissociation

$$v33 = EqMgAMP * (MgAMP - Mg * AMP/KdMgAMP))$$

MgBPG23 dissociation

$$v34 = EqMgBPG23 * (MgBPG23 - Mg * BPG23/KdMgBPG23))$$

Pyruvate transport
(Mitochondrial membrane)

$$v35 = [\text{Pyruvate transport (Mitochondrial membrane)}].Vmax_{pt} * \left(Pyr - \frac{Pyrm}{[\text{Pyruvate transport (Mitochondrial membrane)}]}.Keq_{pt}\right)$$

Pyruvate dehydrogenase

$$v36 = k_{pdh} * \left(Pyrm - \frac{AcCoA}{K_{pdh_{EQ}}}\right) * CoA * NADm$$

Citrate synthase

$$v37 = \frac{Kcat_{cs} * Et_{cs}}{1 + \frac{KmAcCoA_{cs}}{AcCoA} + \frac{KmOAA_{cs}}{OAA} + KmAcCoA_{cs} * \frac{KmOAA_{cs}}{AcCoA * OAA}}$$

Aconitase

$$v38 = Kf_{aco} * \left(Cit - \frac{IsoCit}{Keq_{aco}}\right)$$

Isocitrate dehydrogenase

$$v39 = \frac{Kcat_{idh}\, Et_{idh}}{\left(\begin{array}{c} 1 + \left(\frac{Hm}{kH1_{idh}}\right) + \left(\frac{kH2_{idh}}{Hm}\right) + \frac{\left(\frac{KmIsoCit_{idh}}{IsoCit}\right)^{n_{idh}}}{\left(1 + \frac{ADPm}{KaADP_{idh}}\right) * \left(1 + \frac{Cam}{KaCa_{idh}}\right)} + \frac{KmNAD_{idh}}{NADm} * \left(1 + \frac{NADHm}{KiNADH_{idh}}\right) + \\ \left(\frac{KmIsoCit_{idh}}{IsoCit}\right)^{n_{idh}} * \frac{KmNAD_{idh}}{NADm} * \frac{1 + \frac{NADHm}{KiNADH_{idh}}}{\left(1 + \frac{ADPm}{KaADP_{idh}}\right) * \left(1 + \frac{Cam}{KaCa_{idh}}\right)} \end{array}\right)}$$

α-Ketoglutarate dehydrogenase

$$v40 = \frac{Kcat_{akgdh} Et_{akgdh}}{1 + \frac{\frac{KmaKG_{akgdh}}{aKG}}{\left(1 + \frac{Mgm}{KaMg_{akgdh}}\right) * \left(1 + \frac{Cam}{KaCa_{akgdh}}\right)} + \frac{\left(\frac{KmNAD_{akgdh}}{NADm}\right)^{n_{akgdh}}}{\left(1 + \frac{Mgm}{KaMg_{akgdh}}\right) * \left(1 + \frac{Cam}{KaCa_{akgdh}}\right)}}$$

Succinyl CoA lyase

$$v41 = Kf_{scl} * \left(SucCoA * ADPm - Suc * ATPm * \frac{CoA}{Keq_{scl}}\right)$$

Succinate dehydrogenase

$$v42 = \frac{Kcat_{sdh} * Et_{sdh}}{1 + \frac{KmSuc_{sdh}}{Suc} * \left(1 + \frac{OAA}{KiOAA_{sdh}}\right) * \left(1 + \frac{Fum}{KiFum_{sdh}}\right)}$$

Fumarate hydratase

$$v43 = Kf_{fh} * \left(Fum - \frac{Mal}{Keq_{fh}}\right)$$

Malate dehydrogenase

$$v44 = Kcat_{mdh}\, Et_{mdh} \left(\frac{1}{1 + \frac{Hm}{kH1_{mdh}} + \frac{Hm^2}{kH1_{mdh} * kH2_{mdh}}} + koffset\right) * \frac{\frac{1}{\left(1 + \frac{kH3_{mdh}}{Hm} + kH3_{mdh} * \frac{kH4_{mdh}}{Hm}\right)^2}}{1 + \frac{KmMal_{mdh}}{Mal} * \left(1 + \frac{OAA}{KiOAA_{mdh}}\right) + \frac{KmNAD_{mdh}}{NADm} + \frac{KmMal_{mdh}}{Mal} * \left(1 + \frac{OAA}{KiOAA_{mdh}}\right) * \left(\frac{KmNAD_{mdh}}{NADm}\right)}$$

Calcium uniporter

$$v45 = \frac{\mathrm{Vmax_{uni}} * \left(\frac{Ca}{Ktrans}\right) * \left(1 + \frac{Ca}{Ktrans}\right)^3}{\left(1 + \frac{Ca}{Ktrans}\right)^4 + \left(\frac{L}{\left(1 + \frac{Ca}{Kact}\right)^{na_{uni}}}\right) * \frac{2F(dPsi - dPsio)}{R * T} * \left(1 - \exp\left(-2F\frac{dPsi - dPsio}{R * T}\right)\right)}$$

Sodium-Calcium exchanger

$$v46 = \frac{\left(\mathrm{Vmax_{ex}} * \exp\left(bF\frac{dPsi - dPsio}{R * T}\right) * \left(\frac{Cam}{Ca}\right)\right)}{\left(1 + \frac{KNa}{Na}\right)^{n_{ex}} * \left(1 + \frac{KCa}{Cam}\right)}$$

Adenine nucleotide translocator

$$v47 = \mathrm{Vmax_{ant}} * \frac{1 - 0.018 * ATP * \frac{ADPm}{0.0225 * ADP * ATPm} * \exp\left(-F * \frac{dPsi}{R * T}\right)}{\left(1 + 0.05 * \frac{ATP}{0.45 * ADP} * \exp\left(-h * F * \frac{dPsi}{R * T}\right)\right) * \left(1 + 0.36 * \frac{ADPm}{0.05 * ATPm}\right)}$$

F1F0 ATPase

$$v48 = -rhoF1 * \frac{\left(\begin{array}{c}\left(100 * pa + pc1 * \exp\left(3F * \frac{dPsiB}{R * T}\right)\right) * KF1 * \frac{Cm - ADPm}{ADPm * Pim} - \\ \left(pa - pc2 * KF1 * \frac{Cm - ADPm}{ADPm * Pim}\right) * \exp\left(3F * \frac{R * T * \frac{dpH}{F} + dPsi}{R * T}\right)\end{array}\right)}{\left(\begin{array}{c}\left(1 + p1 * KF1 * \frac{Cm - ADPm}{ADPm * Pim}\right) * \exp\left(3F * \frac{dPsiB}{R * T}\right) + \\ \left(p2 + p3 * KF1 * \frac{Cm - ADPm}{ADPm * Pim}\right) * \exp\left(3F * \frac{R * T * \frac{dpH}{F} + dPsi}{R * T}\right)\end{array}\right)}$$

Oxidative phosphorylation

$$v49 = 0.5 * rhoNADH * \frac{\left(\left(ra + rc1 * \exp\left(6F\frac{dPsiB}{R*T}\right)\right) * KNADH * sqrt\left(\frac{NADHm}{NADm}\right) - ra * \exp\left(g * 6F\frac{R*T*\frac{dpH}{F} + dPsi}{R*T}\right) + rc2 * KNADH * sqrt\left(\frac{NADHm}{NADm}\right) * \exp\left(g * 6F\frac{R*T*\frac{dpH}{F} + dPsi}{R*T}\right)\right)}{\left(\left(1 + r1 * KNADH * sqrt\left(\frac{NADHm}{NADm}\right)\right) * \exp\left(6F\frac{dPsiB}{R*T}\right) + \left(r2 + r3 * KNADH * sqrt\left(\frac{NADHm}{NADm}\right)\right) * \exp\left(g * 6F\frac{R*T*\frac{dpH}{F} + dPsi}{R*T}\right)\right)}$$

dPsi (Calcium uniporter)

$$v50 = \frac{Vmax_{uni}}{C_{mito}} * \frac{\left(\frac{Ca}{Ktrans}\right) * \left(1 + \frac{Ca}{Ktrans}\right)^3}{\left(1 + \frac{Ca}{Ktrans}\right)^4 + \left(\frac{L}{\left(1 + \frac{Ca}{Kact}\right)^{na_{uni}}}\right) * \frac{2F(dPsi - dPsio)}{R*T} * \left(1 - \exp\left(-2F\frac{dPsi - dPsio}{R*T}\right)\right)}$$

dPsi (Sodium-Calcium exchanger)

$$v51 = \frac{Vmax_{ex}}{C_{mito}} \frac{\left(\exp\left(bF\frac{dPsi - dPsio}{R*T}\right) * \left(\frac{Cam}{Ca}\right)\right)}{\left(1 + \frac{KNa}{Na}\right)^{n_{ex}} * \left(1 + \frac{KCa}{Cam}\right)}$$

dPsi (Adenine nucleotide translocator)

$$v52 = \frac{Vmax_{ant}}{C_{mito}} * \frac{1 - 0.018 * ATP * \frac{ADPm}{0.0225 * ADP * ATPm} * \exp\left(-F * \frac{dPsi}{R*T}\right)}{\left(1 + 0.05 * \frac{ATP}{0.45 * ADP} * \exp\left(-h * F * \frac{dPsi}{R*T}\right)\right) * \left(1 + 0.36 * \frac{ADPm}{0.05 * ATPm}\right)}$$

dPsi (F1F0 ATPase)

$$v53 = -\left(\frac{3 * rhoF1}{C_{mito}}\right) * \frac{100 * pa * \left(1 + KF1\frac{Cm - ADPm}{ADPm * Pim}\right) - (pa + pb) * \exp\left(3F\frac{R * T * \frac{dpH}{F} + dPsi}{R * T}\right)}{\left(\begin{array}{c}\left(1 + p1 * \left(KF1\frac{Cm - ADPm}{ADPm * Pim}\right)\right) * \exp\left(3F\frac{dPsiB}{R * T}\right) + \\ \left(p2 + p3\left(KF1\frac{Cm - ADPm}{ADPm * Pim}\right)\right) * \exp\left(3F\frac{R * T * \frac{dpH}{F} + dPsi}{R * T}\right)\end{array}\right)}$$

dPsi (Oxidative phosphorylation NADH)

$$v54 = \frac{6 * rhoNADH}{C_{mito}} * \frac{ra * KNADH * sqrt\left(\frac{NADHm}{NADm}\right) - (ra + rb) * \exp\left(g * 6 * F * \frac{R * T * \frac{dpH}{F} + dPsi}{R * T}\right)}{\left(\begin{array}{c}\left(1 + r1 * KNADH * sqrt\left(\frac{NADHm}{NADm}\right)\right) * \exp\left(6 * F * \frac{dPsiB}{R * T}\right) + \\ \left(r2 + r3 * KNADH * sqrt\left(\frac{NADHm}{NADm}\right)\right) * \exp\left(g * 6 * F * \frac{R * T * \frac{dpH}{F} + dPsi}{R * T}\right)\end{array}\right)}$$

dPsi (Oxidative phosphorylation FADH2)

$$v55 = \frac{4 * rhoFADH2}{C_{mito}} * \frac{ra * KFADH2 * sqrt\left(\frac{FADH2}{FAD}\right) - (ra + rb) * \exp\left(g * 4F\frac{R * T * \frac{dpH}{F} + dPsi}{R * T}\right)}{\left(\begin{array}{c}\left(1 + r1 * KFADH2 * sqrt\left(\frac{FADH2}{FAD}\right)\right) * \exp\left(4F\frac{dPsiB}{R * T}\right) + \\ \left(r2 + r3 * KFADH2 * sqrt\left(\frac{FADH2}{FAD}\right)\right) * \exp\left(g * 4F\frac{R * T * \frac{dpH}{F} + dPsi}{R * T}\right)\end{array}\right)}$$

dPsi (Leak)

$$v56 = gh * \frac{R * T * \frac{dpH}{F} + dPsi}{C_{mito}}$$

Phosphate transport
(Mitochondrial membrane)

$$v57 = [\text{Phosphate transport (Mitochondrial membrane)}].\text{Vmax}_{pt} * \left(\text{Pi} - \frac{\text{Pim}}{[\text{Phosphate transport (Mitochondrial membrane)}]}.\text{Keq}_{pt}\right)$$

Phospholipase C

$$v58 = \left(\text{PLC} * \left(\text{Vmax}_{plc} * \frac{\text{PIP2}}{\text{KmPIP2}_{plc} + \text{PIP2}}\right)\right)$$

ER calcium leak

$$v59 = \left(\text{kLeak} * (\text{Caer} - \text{Ca})\right) * \text{er}$$

ER calcium pump

$$v60 = (\text{kPump} * \text{Ca}) * \text{cellular}$$

ER calcium channel

$$v61 = \left(\text{L}_{channel} + \text{P}_{channel} * (\text{IP3}^3) * \frac{\text{Ca}^3}{(\text{IP3} + \text{KmIP3}_{channel})^3 * (\text{Ca} + \text{KmCa}_{channel})^3}\right) * (\text{Caer} - \text{Ca})$$

IP3 consumption

$$v62 = kIP3 * IP3$$

DAG consumption

$$v63 = kDAG * DAG$$

G3P shuttle

$$v64 = Vmax_{G3P} * FAD * NADH$$

Oxidative phosphorylation
FADH2

$$v65 = 0.5 * rhoFADH2 * \frac{\left(\left(ra + rc1 * \exp\left(4F\frac{dPsiB}{R*T}\right)\right) * KFADH2 * sqrt\left(\frac{FADH2}{FAD}\right) - ra * \exp\left(g4F\frac{R*T*\frac{dpH}{F} + dPsi}{R*T}\right) + rc2 * KFADH2 * sqrt\left(\frac{FADH2}{FAD}\right) * \exp\left(g*4*F*\frac{R*T*\frac{dpH}{F} + dPsi}{R*T}\right)\right)}{\left(\left(1 + r1 * KFADH2 * sqrt\left(\frac{FADH2}{FAD}\right)\right) * \exp\left(4F\frac{dPsiB}{R*T}\right) + \left(r2 + r3 * KFADH2 * sqrt\left(\frac{FADH2}{FAD}\right)\right) * \exp\left(g*4F\frac{R*T*\frac{dpH}{F} + dPsi}{R*T}\right)\right)}$$

Sink for protein synthesis

$$v66 = \mathrm{Vmax}_{\mathrm{proteinsyn}} * \mathrm{PRPP}$$

Na/K-ATPase

$$v67 = \left(\frac{1}{\left(\left(1 + \frac{\mathrm{KmK}}{\mathrm{Ke}}\right)^{2}\right) * \left(\left(1 + \frac{\mathrm{KmNa}}{\mathrm{Na}}\right)^{3}\right) * \left(\left(1 + \frac{\mathrm{KATP}}{\mathrm{MgATP}}\right)\right)} \right)$$

Ca-ATPase

$$v68 = \frac{1}{\left(1 + \left(\frac{Km_{Ca}}{\mathrm{Ca}}\right)\right) * \left(1 + \left(\frac{\mathrm{KATP}}{\mathrm{MgATP}}\right)\right)}$$

APPENDIX C: METABOLIC MODEL PARAMETERS

Description	Symbol	Value	Units	Ref
Faraday constant	F	96480	C mol^{-1}	[59]
Activation constant	Kact	0.00038	mM	[59]
K_d for translocated Ca^{+2}	Ktrans	0.019	mM	[59]
Keq for conformational transitions in uniporter	L	110	-	[59]
Gas constant	R	8.3145	V C mol^{-1} $^0K^{-1}$	[59]
Temperature	T	302.15	^0K	[59]
Vmax uniport Ca+2 transport	Vmax_uni	0.625	uM s^{-1}	[59]
Offset membrane potential	dPsio	0.091	Volts	[59]
Uniporter activation cooperativity	na_uni	2.8	-	[59]
Antiporter Ca+ constant	KCa	0.000375	mM	[59]
Antiporter Na+ constant	KNa	9.4	mM	[59]
V_{max} of Na^+/Ca^{+2} antiporter	Vmax_ex	$9 * 10^{-7}$	mM s^{-1}	Fitted
dPsi dependence on Na^+/Ca^{+2} antiporter	b	0.5	-	[59]
Na^+/Ca^{+2} antiporter cooperativity	n_ex	3	-	[59]
Maximal rate of ANT	Vmax_ant	0.005	mM	[59]

Description	Symbol	Value	Units	Ref
Fraction of ΔdPsi	h	0.5	-	[59]
Total sum of mitochondrial adenine nucleotides	Cm	2.5	mM	Fitted
Equilibrium constant of ATP hydrolysis	KF1	1.71e+06	-	[59]
Phase boundary potential	dPsiB	0.05	V	[59]
pH gradient across the inner membrane	dpH	-0.6	pH units	[59]
Sum of products of rate constants	p1	1.346e-08	-	[59]
Sum of products of rate constants	p2	7.739e-07	-	[59]
Sum of products of rate constants	p3	6.65e-15	-	[59]
Sum of products of rate constants	pa	1.656e-05	s^{-1}	[59]
Sum of products of rate constants	pc1	9.651e-14	s^{-1}	[59]
Sum of products of rate constants	pc2	4.585e-14	s^{-1}	[59]
Concentration of electron carriers (respiratory complexes II-III-IV)	rhoF1	0.003	mM	Fitted
Equilibrium constant of respiration	KNADH	1.35e+18	-	[59]
Correction factor for voltage	g	0.85	-	[59]
Sum of products of rate constants	r1	2.077e-18	-	[59]

Description	Symbol	Value	Units	Ref
Sum of products of rate constants	r2	1.728e-09	-	[59]
Sum of products of rate constants	r3	1.059e-26	-	[59]
Sum of products of rate constants	ra	6.394e-10	s^{-1}	[59]
Sum of products of rate constants	rc1	2.656e-19	s^{-1}	[59]
Sum of products of rate constants	rc2	8.632e-27	s^{-1}	[59]
Concentration of electron carriers (respiratory complexes I-III-IV)	rhoNADH	0.005	mM	[59]
Inner membrane capacitance	Cmito	1.812	mM V^{-1}	[59]
Sum of products of rate constants	pb	2.023e-05	s^{-1}	[59]
Sum of products of rate constants	rb	1.762e-13	s^{-1}	[59]
Equilibrium constant of FADH2 oxidation	KFADH2	5.497e+13	-	[59]
Concentration of electron carriers (respiratory complexes II-III-IV)	rhoFADH2	0.06	mM	Fitted
Ionic conductance of the inner membrane	gh	0.01	mM s^{-1} V^{-1}	[59]
Equilibrium constant for PDH	K_pdh_EQ	8.0	-	[75]
Rate constant G3P shuttle	Vmax_G3P	0.031	s^{-1}	Fitted
Rate constant for protein synthesis/degradation	Vmax_proteinsyn	3.084	s^{-1}	Fitted

Description	Symbol	Value	Units	Ref
Michaelis constant for ATP in NaK-ATPase	KATP	5	mM	Fitted
Michaelis constant for K+ in NaK-ATPase	KmK	3.5	mM	[78]
Michaelis constant for Na in NaK-ATPase	KmNa	10	mM	[78]
Equilibrium constant of glucose transporter	Keq_gt	0.25	-	[58]
Michaelis constant for forward glucose transporter	KmGlcin_gt	6.9	mM	[58]
Michaelis constant for reverse glucose transporter	KmGlcout_gt	1.7	mM	[58]
Maximal rate of glucose transporter	Vmax_gt	0.0953	$mM\ s^{-1}$	Fitted
Equilibrium constant of HK	Keq_hk	3900	mM	[58]
Michaelis constant for HK	KmBPG23_hk	2.7	mM	[58]
Michaelis constant for HK	KmG6P_hk	0.0045	mM	[58]
Michaelis constant for HK	KmGlc_hk	0.1	mM	[58]
Michaelis constant for HK	KmMgATPMg_hk	1.14	mM	[58]
Michaelis constant for HK	KmMgATP_hk	1.44	mM	[58]
Michaelis constant for HK	KmMgBPG23_hk	3.44	mM	[58]
Michaelis constant for HK	KmMg_hk	1.02	mM	[58]

Description	Symbol	Value	Units	Ref
Maximal rate of HK	Vmax1_hk	0.045	mM s^{-1}	Fitted
Maximal rate of HK	Vmax2_hk	1.1067	mM s^{-1}	[58]
Equilibrium constant of GPI	Keq_gpi	0.3925	-	[58]
Michaelis constant for GPI	KmF6P_gpi	0.071	mM	[58]
Michaelis constant for GPI	KmG6P_gpi	0.182	mM	[58]
Maximal rate for GPI	Vmax_gpi	2.652	mM s^{-1}	Fitted
Equilibrium constant of PFK	Keq_pfk	1e+05	mM	[58]
Michaelis constant for PFK	KmAMP_pfk	0.033	mM	[58]
Michaelis constant for PFK	KmATP_pfk	0.01	mM	[58]
Michaelis constant for PFK	KmF6P_pfk	0.1	mM	[58]
Michaelis constant for PFK	KmMgATP_pfk	0.068	mM	[58]
Michaelis constant for PFK	KmMg_pfk	0.44	mM	[58]
Lo for PFK	Lo_pfk	0.001072	-	[58]
Maximal rate of PFK	Vmax_pfk	0.6779	mM s^{-1}	Fitted
Equilibrium constant of ALD	Keq_ald	0.114	mM	[58]

Description	Symbol	Value	Units	Ref
Inhibition constant for ALD	KiGAP_ald	0.0572	mM	[58]
Inhibition constant for ALD	KiiGAP_ald	0.176	mM	[58]
Michaelis constant for ALD	KmDHAP_ald	0.0364	mM	[58]
Michaelis constant for ALD	KmF16BP_ald	0.0071	mM	[58]
Michaelis constant for ALD	KmGAP_ald	0.1906	mM	[58]
Maximal rate of ALD	Vmax_ald	0.2857	mM	Fitted
Equilibrium constant of TPI	Keq_tpi	0.0407	mM	[58]
Michaelis constant for TPI	KmDHAP_tpi	0.838	mM	[58]
Michaelis constant for TPI	KmGAP_tpi	0.428	mM	[58]
Maximal rate of TPI	Vmax_tpi	15.4784	mM s^{-1}	[58]
Equilibrium constant of GADPH	Keq_gapdh	0.000192	mM	[58]
Michaelis constant for GADPH	KmBPG13_gapdh	0.0035	mM	[58]
Michaelis constant for GADPH	KmGAP_gapdh	0.005	mM	[58]
Michaelis constant for GADPH	KmNADH_gapdh	0.0083	mM	[58]
Michaelis constant for GADPH	KmNAD_gapdh	0.05	mM	[58]

Description	Symbol	Value	Units	Ref
Michaelis constant for GADPH	KmPi_gapdh	3.9	mM	[58]
Maximal rate of GADPH	Vmax_gapdh	12.197	mM s^{-1}	Fitted
Equilibrium constant of PGK	Keq_pgk	1455	mM	[58]
Michaelis constant for PGK	KmBPG13_pgk	0.002	mM	[58]
Michaelis constant for PGK	KmMgADP_pgk	0.35	mM	[58]
Michaelis constant for PGK	KmMgATP_pgk	0.48	mM	[58]
Michaelis constant for PGK	KmPG3_pgk	1.2	mM	[58]
Maximal rate of PGK	Vmax_pgk	14.184	mM s^{-1}	Fitted
Dissociation constant of bPGM	Kd_bpgm	215.5866	Fitted	[58]
Equilibrium constant of bPGM	Keq_bpgm	1e+05	mM	[58]
Michaelis constant for bPGM	KmBPG23_bpgm	0.04	mM	[58]
Equilibrium constant of bPGM	Keq_bpgp	1e+05	mM	[58]
Michaelis constant for bPGM	KmBPG23_bpgp	0.2	mM	[58]
Maximal rate of bPGM	Vmax_bpgp	0.0015	mM s^{-1}	Fitted
Equilibrium constant of PGM	Keq_pgm	0.145	mM	[58]

Description	Symbol	Value	Units	Ref
Michaelis constant for PGM	KmPG2_pgm	1	mM	[58]
Michaelis constant for PGM	KmPG3_pgm	5	mM	[58]
Maximal rate of PGM	Vmax_pgm	5.673	$mM\ s^{-1}$	Fitted
Equilibrium constant of ENO	Keq_eno	1.7	mM	[58]
Michaelis constant for ENO	KmPEP_eno	1	mM	[58]
Michaelis constant for ENO	KmPG2_eno	1	mM	[58]
Maximal rate of ENO	Vmax_eno	4.255	$mM\ s^{-1}$	Fitted
Equilibrium constant of PK	Keq_pk	13790	mM	[58]
Michaelis constant for PK	KmATP_pk	3.39	mM	[58]
Michaelis constant for PK	KmF16BP_pk	0.005	mM	[58]
Michaelis constant for PK	KmMgADP_pk	0.474	mM	[58]
Michaelis constant for PK	KmPEP_pk	0.225	mM	[58]
Lo for PK	Lo_pk	19	-	[58]
Maximal rate of PK	Vmax_pk	1.617	mMs^{-1}	Fitted
Equilibrium constant of LDH (Lactate dehydrogenase-NADH)	Keq_ldh	9090	mM	[58]

Description	Symbol	Value	Units	Ref
Maximal rate of LDH (NADH)	Vmax_ldh	104.99	mM s^{-1}	[58]
Equilibrium constant of LDH (Lactate dehydrogenase-NADPH)	Keq_ldh	32	mM	[58]
Maximal rate of LDH (NADPH)	k_ldh	2	mM s^{-1}	[58]
Maximal rate of ATPase	k_ATPase	0.015	mM s^{-1}	Fitted
Equilibrium constant of AK	Keq_ak	0.25	mM	[58]
Michaelis constant for AK	KmADP_ak	0.11	mM	[58]
Michaelis constant for AK	KmAMP_ak	0.08	mM	[58]
Michaelis constant for AK	KmATP_ak	0.09	mM	[58]
Maximal rate of AK	Vmax_ak	46	mM s^{-1}	Fitted
Equilibrium constant of GPDH	Keq_gpdh	2000	mM	[58]
Michaelis constant for GPDH	KmATP_gpdh	0.749	mM	[58]
Michaelis constant for GPDH	KmBPG23_gpdh	2.289	mM	[58]
Michaelis constant for GPDH	KmG6P_gpdh	0.0667	mM	[58]
Michaelis constant for GPDH	KmNADPH_gpdh	0.00312	mM	[58]
Michaelis constant for GPDH	KmNADP_gpdh	0.00367	mM	[58]

Description	Symbol	Value	Units	Ref
Maximal rate of GPDH	Vmax_gpdh	0.108	mM s^{-1}	Fitted
Equilibrium constant of PGLDH	Keq_pgldh	141.7	mM	[58]
Michaelis constant for PGLDH	KmATP_pgldh	0.154	mM	[58]
Michaelis constant for PGLDH	KmBPG23_pgldh	0.12	mM	[58]
Michaelis constant for PGLDH	KmNADPH_pgldh	0.0045	mM	[58]
Michaelis constant for PGLDH	KmNADP_pgldh	0.018	mM	[58]
Maximal rate of PGLDH	Vmax_pgldh	1.05	mM s^{-1}	Fitted
Michaelis constant for PGLDH	KmPGL1_pgldh	0.01	mM	[58]
Michaelis constant for PGLDH	KmPGL2_pgldh	0.058	mM	[58]
Equilibrium constant of Glutathione reduction	Keq_gr	1.04	mM	[58]
Michaelis constant for Glutathione reduction (GR)	KmGSH_gr	20	mM	[58]
Michaelis constant for GR	KmGSSG_gr	0.0652	mM	[58]
Michaelis constant for GR	KmNADPH_gr	0.00852	mM	[58]
Michaelis constant for GR	KmNADP_gr	0.07	mM	[58]
Maximal rate of GR	Vmax_gr	3	mM s^{-1}	[58]

Description	Symbol	Value	Units	Ref
Rate constant for Glutathione oxidation (GO)	K_go	0.01	mM	[58]
Equilibrium constant of GO	Keq_pre	2.7	mM	[58]
Michaelis constant for PRE	KmRu5P_pre	0.19	mM	[58]
Michaelis constant for PRE	KmX5P_pre	0.5	mM	[58]
Maximal rate of PRE	Vmax_pre	3.0894	mM s^{-1}	Fitted
Equilibrium constant of RPI	Keq_rpi	3	mM	[58]
Michaelis constant for RPI	KmRi5P_rpi	2.2	mM	[58]
Michaelis constant for RPI	KmRu5P_rpi	0.78	mM	[58]
Maximal rate of RPI	Vmax_rpi	0.4866	mM	Fitted
Constant for Tranketolase (Ri5P)	K1_tk	0.4177	mM	[58]
Constant for Tranketolase (Ri5P)	K2_tk	0.3055	mM	[58]
Constant for Tranketolase (Ri5P)	K3_tk	12.432	mM	[58]
Constant for Tranketolase (Ri5P)	K4_tk	0.00496	mM	[58]
Constant for Tranketolase (Ri5P)	K5_tk	0.41139	mM	[58]
Constant for Tranketolase (Ri5P)	K6_tk	0.00774	mM	[58]

Description	Symbol	Value	Units	Ref
Constant for Tranketolase (Ri5P)	K7_tk	48.8	mM	[58]
Equilibrium constant of Tranketolase (Ri5P)	Keq_tk	1.05	mM	[58]
Maximal rate of Tranketolase (Ri5P)	Vmax_tk	0.0157	mM	Fitted
Constant for Transaldolase (TA) (Ri5P)	K1_ta	0.00823	mM	[58]
Constant for TA (Ri5P)	K2_ta	0.04765	mM	[58]
Constant for TA (Ri5P)	K3_ta	0.1733	mM	[58]
Constant for TA (Ri5P)	K4_ta	0.006095	mM	[58]
Constant for TA (Ri5P)	K5_ta	0.8683	mM	[58]
Constant for TA (Ri5P)	K6_ta	0.4653	mM	[58]
Constant for TA (Ri5P)	K7_ta	2.524	mM	[58]
Equilibrium constant of TA (Ri5P)	Keq_ta	1.05	mM	[58]
Maximal rate of Transaldolase (Ri5P)	Vmax_ta	0.01813	mM s^{-1}	Fitted
Equilibrium constant of PRPPS	Keq_prpps	1e+05	mM	[58]
Michaelis constant for PRPPS	KmATP_prpps	0.03	mM	[58]
Michaelis constant for PRPPS	KmRi5P_prpps	0.57	mM	[58]

Description	Symbol	Value	Units	Ref
Maximal rate of PRPPS	Vmax_prpps	0.001	mM s^{-1}	Fitted
Constant for Transketolase (E4P)	K1_tk	0.00184	mM	[58]
Constant for Transketolase (E4P)	K2_tk	0.3055	mM	[58]
Constant for Transketolase (E4P)	K3_tk	0.0548	mM	[58]
Constant for Transketolase (E4P)	K4_tk	0.0003	mM	[58]
Constant for Transketolase (E4P)	K5_tk	0.0287	mM	[58]
Constant for Transketolase (E4P)	K6_tk	0.122	mM	[58]
Constant for Transketolase (E4P)	K7_tk	0.215	mM	[58]
Equilibrium constant of Transketolase (E4P)	Keq_tk	1.2	mM	[58]
Maximal rate of Transketolase (E4P)	Vmax_tk	0.0157	mM s^{-1}	Fitted
Equilibrium constant of LT	Keq_lt	0.5	mM	[58]
Maximal rate for LT	Vmax_lt	0.0015	mM s^{-1}	Fitted
Equilibrium constant of phosphate transport (Plasma membrane)	Keq_pt	1	mM	[58]
Maximal rate of phosphate transport (Plasma membrane)	Vmax_pt	3.3333	mMs^{-1}	Fitted
Equilibrium constant of pyruvate transport (Plasma membrane)	Keq_pt	1	mM	Fitted

Description	Symbol	Value	Units	Ref
Maximal rate of pyruvate transport (Plasma membrane)	Vmax_pt	0.0003	mM	Fitted
Equilibrium constant of MgATP	EqMgATP	$3.3333 * 10^5$	s^{-1}	[58]
Dissociation constant for MgATP	KdMgATP	0.072	mM	[58]
Equilibrium constant of MgADP	EqMgADP	$3.3333 * 10^5$	s^{-1}	[58]
Dissociation constant for MgADP	KdMgADP	0.76	mM	[58]
Equilibrium constant of MgAMP	EqMgAMP	$3.3333 * 10^5$	s^{-1}	[58]
Dissociation constant for MgAMP	KdMgAMP	16.64	mM	[58]
Equilibrium constant of MgBPG23	EqMgBPG23	$3.3333 * 10^5$	s^{-1}	[58]
Dissociation constant for MgBPG23	KdMgBPG23	1.667	mM	[58]
Equilibrium constant of pyruvate transport (Mito membrane)	Keq_pt	2	-	Fitted
Maximal rate of pyruvate transport (Mito membrane)].	Vmax_pt	0.04	s^{-1}	Fitted
Rate constant of PDH	k_pdh	1.2	-	[75]
Concentration of CS	Et_cs	0.0258	mM	Fitted
Catalytic constant of CS	Kcat_cs	3.2	s^{-1}	[59]
Michaelis constant for AcCoA	KmAcCoA_cs	0.0126	mM	[59]

Description	Symbol	Value	Units	Ref
Michaelis constant for OAA	KmOAA_cs	0.00063	mM	[59]
Equilibrium constant of ACO	Keq_aco	2.22	-	[59]
Forward rate constant of ACO	Kf_aco	12.5	s^{-1}	[59]
Concentration of IDH	Et_idh	0.007	mM	Fitted
Activation constant by ADP	KaADP_idh	0.062	mM	[59]
Activation constant for Ca^{+2}	KaCa_idh	0.00141	mM	[59]
Rate constant of IDH	Kcat_idh	16.3	s^{-1}	[59]
Inhibition constant by NADH	KiNADH_idh	0.19	mM	[59]
Michaelis constant for isocitrate	KmIsoCit_idh	1.52	mM	[59]
Michaelis constant for NAD	KmNAD_idh	0.923	mM	[59]
Ionization constant of IDH	kH1_idh	8.1e-05	mM	[59]
Ionization constant of IDH	kH2_idh	5.98e-05	mM	[59]
Hill coefficient of IDH	n_idh	2	-	[59]
Concentration of α-KGDH	Et_akgdh	0.0323	mM	Fitted
Activation constant for Ca^{+2}	KaCa_akgdh	0.00127	mM	[59]

Description	Symbol	Value	Units	Ref
Activation constant for Mg^{+2}	KaMg_akgdh	0.0308	mM	[59]
Rate constant of KGDH	Kcat_akgdh	5	s^{-1}	[59]
Michaelis constant for NAD	KmNAD_akgdh	38.7	mM	[59]
Michaelis constant for αKG	KmaKG_akgdh	1.94	mM	[59]
Hill coefficient of KGDH for αKG	n_akgdh	1.2	-	[59]
Equilibrium constant of SL	Keq_scl	3.115	-	[59]
Forward rate constant of SL	Kf_scl	0.127	mM^{-1} s^{-1}	[59]
Concentration of SDH	Et_sdh	0.0323	mM	Fitted
Rate constant of SDH	Kcat_sdh	1	s^{-1}	[59]
Inhibition constant by fumarate	KiFum_sdh	1.3	mM	[59]
Inhibition constant by oxalacetate	KiOAA_sdh	0.15	mM	[59]
Michaelis constant for succinate	KmSuc_sdh	0.03	mM	[59]
Equilibrium constant of FH	Keq_fh	1	-	[59]
Forward rate constant for FH	Kf_fh	1.83	s^{-1}	[59]
Total MDH enzyme concentration	Et_mdh	0.001	mM	Fitted

Description	Symbol	Value	Units	Ref
Rate constant of MDH	Kcat_mdh	27.75	s^{-1}	[59]
Inhibition constant by oxalacetate	KiOAA_mdh	0.0015	mM	[59]
Michaelis constant for malate	KmMal_mdh	1.493	mM	[59]
Michaelis constant for NAD^+	KmNAD_mdh	0.2244	mM	[59]
Ionization constant of MDH	kH1_mdh	1.131e-05	mM	[59]
Ionization constant of MDH	kH2_mdh	26.7	mM	[59]
Ionization constant of MDH	kH3_mdh	6.68e-09	mM	[59]
Ionization constant of MDH	kH4_mdh	5.62e-06	mM	[59]
pH-independent term in the pH activation factor of MDH	koffset	0.0399	-	[59]
Equilibrium constant of phosphate transport (Mito membrane)	Keq_pt	20	-	Fitted
Maximal rate of phosphate transport (Mito membrane)	Vmax_pt	5.002	s^{-1}	Fitted
Michaelis constant for PLC	KmPIP2_plc	0.00045	mM	[74]
Maximum flux across PMCA	Vmax_plc	0.001	mM s^{-1}	[74]
Maximal rate of IP3 production	kPump	20	s^{-1}	[74]
Dissociation constant of IP3 sites on IP3R	KmIP3_channel	0.001	mM	[74]

Description	Symbol	Value	Units	Ref
Ca2+ leak from ER to cytoplasm	L_channel	0.00093	s^{-1}	[74]
Maximal total permeability of IP3 channels	P_channel	66.6	s^{-1}	[74]
Dissociation constant of Ca2+-activation sites on IP3R	KmCa_channel	0.0004	mM	[74]
Half maximal inhibitory concentration for 2DG	2DG IC_{50}	23.34	mM	Fitted
Half maximal inhibitory concentration for cyanide	CYN IC_{50}	0.005	mM	Fitted
Half maximal inhibitory concentration for malonate	MAL IC_{50}	24.17	mM	Fitted

APPENDIX D: METABOLIC MODEL INITIAL VALUES

Description	Symbol	Value (mM)
Mitochondrial pyruvate	Pyrm	0.0032449
Mitochondrial NAD	NADm	10
Acetyl-CoA	AcCoA	0.00013565
Mitochondrial NADH	NADHm	5.4748e-07
Oxaloacetate	OAA	0.0046568
Citrate	Cit	0.025474
Isocitrate	IsoCit	0.054419
α-Ketoglutarate	aKG	0.00060511
Mitochondrial ADP	ADPm	0.27199
Mitochondrial calcium	Cam	0.00013734
Succinyl CoA	SucCoA	0.3477
Mitochondrial phosphate	Pim	19.99
Succinate	Suc	0.00078309
Mitochondrial ATP	ATPm	2.228
Fumarate	Fum	0.037381

Description	Symbol	Value (mM)
Malate	Mal	0.030819
Mitochondrial FAD	FAD	5.25
Mitochondrial $FADH_2$	FADH2	3.2402e-05
Endoplasmic reticulum calcium	Caer	0.044987
Mitochondrial membrane potential	dPsi	0.12203
Cytosolic Glucose	Glc	5.8843
Magnesium bound ATP	MgATP	0.20011
Glucose-6-phosphate	G6P	0.0014076
Magnesium bound ADP	MgADP	0.070602
2,3-bisphosphoglycerate	BPG23	0.31498
Magnesium	Mg	1.0641
Magnesium bound 2,3-bisphosphoglycerate	MgBPG23	0.20106
Fructose 6-phosphate	F6P	0.00050133
AMP	AMP	0.071164
ATP	ATP	0.013541

Description	Symbol	Value (mM)
Fructose 1,6-biphosphate	F16BP	0.06041
Magnesium bound AMP	MgAMP	0.0045507
Glyceraldehyde-3-phosphate	GAP	0.016302
Dihydroxyacetone phosphate	DHAP	0.40075
Cytosolic phosphate	Pi	0.9999
Cytosolic NAD	NAD	0.062889
1,3-bisphosphoglycerate	BPG13	7.4997e-05
Cytosolic NADH	NADH	0.0026113
3-Phosphoglycerate	PG3	0.036012
2-Phosphoglycerate	PG2	0.0045566
Phosphoenolpyruvate	PEP	0.0056698
Cytosolic pyruvate	Pyr	0.02099
Cytosolic lactate	Lac	1.4259
Cytosolic NADPH	NADPH	3.0797e-07
Cytosolic NADP	NADP	0.004

Description	Symbol	Value (mM)
ADP	ADP	0.050427
6-phosphoglucono-δ-lactone	PGL	0.00032077
Ribuloase-5-phosphate	Ru5P	0.02701
Glutathione disulphide	GSSG	1.4447
Glutathione	GSH	0.225
Xyulose-5-phosphate	X5P	0.072808
Ribose-5-phosphate	Ri5P	0.079043
Sedoheptulose 7-phosphate	S7P	0.00085122
Erythrose 4-phosphate	E4P	0.00045071
Phosphoribosyl pyrophosphate	PRPP	3.4337e-05
Cytosolic calcium	Ca	0.00012546
Phosphatidylinositol 4,5-bisphosphate	PIP2	2000
Inositol triphosphate	IP3	3.7369e-12
Diacyl-glycerol	DAG	3.7369e-12
Extracellular glucose	Glce	25

Description	Symbol	Value (mM)
Extracellular lactate	Lace	3.3388e-05
Extracellular phosphate	Pie	1
Extracellular pyruvate	Pyre	1.1601e-07
Extracellular potassium	Ke	5.4
Extracellular calcium	Cae	1.8
Extracellular magnesium	Mge	0.8
Extracellular sodium	Nae	130.2
CoA	CoA	0.02
Mitochondrial proton	Hm	2.5e-05
Mitochondrial magnesium	Mgm	0.4

REFERENCES

1. Liebler DC (2002) Introduction to proteomics : tools for the new biology. Totowa, NJ: Humana Press. ix, 198 p. p.

2. Venter JC, Adams MD, Myers EW, Li PW, Mural RJ, et al. (2001) The sequence of the human genome. Science 291: 1304-+.

3. Graves PR, Haystead TA (2002) Molecular biologist's guide to proteomics. Microbiol Mol Biol Rev 66: 39-63; table of contents.

4. Abbott A (1999) A post-genomic challenge: learning to read patterns of protein synthesis. Nature 402: 715-720.

5. Arab S, Gramolini AO, Ping P, Kislinger T, Stanley B, et al. (2006) Cardiovascular proteomics: tools to develop novel biomarkers and potential applications. J Am Coll Cardiol 48: 1733-1741.

6. Mishra NC (2010) Introduction to proteomics : principles and applications. Hoboken, N.J.: John Wiley & Sons. xx, 180 p. p.

7. Rothman S (2010) How is the balance between protein synthesis and degradation achieved? Theor Biol Med Model 7: 25.

8. Wheatley DN (1984) Intracellular Protein-Degradation - Basis of a Self-Regulating Mechanism for the Proteolysis of Endogenous Proteins. Journal of Theoretical Biology 107: 127-149.

9. Radivojac P, Clark WT, Oron TR, Schnoes AM, Wittkop T, et al. (2013) A large-scale evaluation of computational protein function prediction. Nat Meth 10: 221-227.

10. Schaffner AE, Barker JL, Stenger DA, Hickman JJ (1995) Investigation of the factors necessary for growth of hippocampal neurons in a defined system. J Neurosci Methods 62: 111-

119.

11. Twyman RM (2004) Principles of proteomics. New York: BIOS Scientific Publishers. xiii, 241 p. p.

12. Shedden K, Posada MM, Chang YT, Li Q, Rosania G (2007) Prospecting for Live Cell BioImaging Probes With Cheminformatic Assisted Image Arrays (CAIA). Proc IEEE Int Symp Biomed Imaging: 1108-1111.

13. Kubitscheck U, Peters R (2013) Fluorescence microscopy. Weinheim: Wiley-Blackwell. 1 volume p.

14. Zetterberg H, Ruetschi U, Portelius E, Brinkmalm G, Andreasson U, et al. (2008) Clinical proteomics in neurodegenerative disorders. Acta Neurol Scand 118: 1-11.

15. Alzate O (2010) Neuroproteomics. Boca Raton, FL: Taylor & Francis. xix, 322 p. p.

16. Moxon JV, Padula MP, Herbert BR, Golledge J (2009) Challenges, current status and future perspectives of proteomics in improving understanding, diagnosis and treatment of vascular disease. Eur J Vasc Endovasc Surg 38: 346-355.

17. Jia L, Lu Y, Shao J, Liang XJ, Xu Y (2013) Nanoproteomics: a new sprout from emerging links between nanotechnology and proteomics. Trends Biotechnol 31: 99-107.

18. Ray S, Reddy PJ, Choudhary S, Raghu D, Srivastava S (2011) Emerging nanoproteomics approaches for disease biomarker detection: a current perspective. J Proteomics 74: 2660-2681.

19. Chandramouli K, Qian PY (2009) Proteomics: challenges, techniques and possibilities to overcome biological sample complexity. Hum Genomics Proteomics 2009.

20. Wu CC, MacCoss MJ (2002) Shotgun proteomics: tools for the analysis of complex biological

systems. Curr Opin Mol Ther 4: 242-250.

21. Banks RE, Dunn MJ, Hochstrasser DF, Sanchez JC, Blackstock W, et al. (2000) Proteomics: new perspectives, new biomedical opportunities. Lancet 356: 1749-1756.

22. Villaamil VM, Gallego GA, Cainzos IS, Valladares-Ayerbes M, Aparicio LMA (2012) State of the Art in Silico Tools for the Study of Signaling Pathways in Cancer. International Journal of Molecular Sciences 13: 6561-6581.

23. Weston AD, Hood L (2004) Systems biology, proteomics, and the future of health care: Toward predictive, preventative, and personalized medicine. Journal of Proteome Research 3: 179-196.

24. Palsson B (2011) Systems biology : simulation of dynamic network states. Cambridge, UK ; New York: Cambridge University Press. xiii, 317 p. p.

25. Moore JB, Weeks ME (2011) Proteomics and Systems Biology: Current and Future Applications in the Nutritional Sciences. Advances in Nutrition 2: 355-364.

26. Hickman J, Molnar P, Sommerhage F, Hood J, Jenkins J (2013) Model and methods for identifying points of action in electrically active cells. Google Patents.

27. Mohan DK, Molnar P, Hickman JJ (2006) Toxin detection based on action potential shape analysis using a realistic mathematical model of differentiated NG108-15 cells. Biosens Bioelectron 21: 1804-1811.

28. Offenhausser A, Knoll W (2001) Cell-transistor hybrid systems and their potential applications. Trends Biotechnol 19: 62-66.

29. Haynes RK, Ho WY, Chan HW, Fugmann B, Stetter J, et al. (2004) Highly antimalaria-active artemisinin derivatives: biological activity does not correlate with chemical reactivity.

Angew Chem Int Ed Engl 43: 1381-1385.

30. Gross GW, Harsch A, Rhoades BK, Gopel W (1997) Odor, drug and toxin analysis with neuronal networks in vitro: extracellular array recording of network responses. Biosens Bioelectron 12: 373-393.

31. Morefield SI, Keefer EW, Chapman KD, Gross GW (2000) Drug evaluations using neuronal networks cultured on microelectrode arrays. Biosens Bioelectron 15: 383-396.

32. Armstrong DL, Rossie S (1999) Ion channel regulation. Introduction. Advances in second messenger and phosphoprotein research 33: ix-xx.

33. Orlov SN, Hamet P (2006) Intracellular monovalent ions as second messengers. Journal of Membrane Biology 210: 161-172.

34. Rosati B, McKinnon D (2004) Regulation of ion channel expression. Circulation Research 94: 874-883.

35. Selivanov VA, Alekseev AE, Hodgson DM, Dzeja PP, Terzic A (2004) Nucleotide-gated K(ATP) channels integrated with creatine and adenylate kinases: Amplification, tuning and sensing of energetic signals in the compartmentalized cellular environment. Molecular and Cellular Biochemistry 256: 243-256.

36. Hsiao CF, Wu NP, Chandler SH (2005) Voltage-dependent calcium currents in trigeminal motoneurons of early postnatal rats: Modulation by 5-HT receptors. Journal of Neurophysiology 94: 2063-2072.

37. Soundarapandian MM, Zhong XF, Peng LS, Wu D, Lu YM (2007) Role of K-ATP channels in protection against neuronal excitatory insults. Journal of Neurochemistry 103: 1721-1729.

38. van Soest PF, Kits KS (1998) Conopressin affects excitability, firing, and action potential shape through stimulation of transient and persistent inward currents in mulluscan neurons. Journal of Neurophysiology 79: 1619-1632.

39. Spencer CI, Yuill KH, Borg JJ, Hancox JC, Kozlowski RZ (2001) Actions of pyrethroid insecticides on sodium currents, action potentials, and contractile rhythm in isolated mammalian ventricular myocytes and perfused hearts (vol 298, pg 1067, 2001). Journal of Pharmacology and Experimental Therapeutics 299: 399-399.

40. Martin-Caraballo M, Greer JJ (2000) Development of potassium conductances in perinatal rat phrenic motoneurons. Journal of Neurophysiology 83: 3497-3508.

41. Akanda N, Molnar P, Stancescu M, Hickman JJ (2009) Analysis of toxin-induced changes in action potential shape for drug development. J Biomol Screen 14: 1228-1235.

42. Gleeson P, Crook S, Cannon RC, Hines ML, Billings GO, et al. (2010) NeuroML: a language for describing data driven models of neurons and networks with a high degree of biological detail. PLoS Comput Biol 6: e1000815.

43. Lewis A, Trudel BK, Belore RC, Mullin JV (2010) Large-scale dispersant leaching and effectiveness experiments with oils on calm water. Mar Pollut Bull 60: 244-254.

44. Zhou L, Solhjoo S, Millare B, Plank G, Abraham MR, et al. (2014) Effects of regional mitochondrial depolarization on electrical propagation: implications for arrhythmogenesis. Circ Arrhythm Electrophysiol 7: 143-151.

45. Le Masson G, Przedborski S, Abbott LF (2014) A computational model of motor neuron degeneration. Neuron 83: 975-988.

46. Cortassa S, Aon MA, O'Rourke B, Jacques R, Tseng HJ, et al. (2006) A computational model

integrating electrophysiology, contraction, and mitochondrial bioenergetics in the ventricular myocyte. Biophys J 91: 1564-1589.

47. Greenstein JL, Winslow RL (2002) An integrative model of the cardiac ventricular myocyte incorporating local control of Ca2+ release. Biophysical Journal 83: 2918-2945.

48. Slepchenko BM, Schaff JC, Macara I, Loew LM (2003) Quantitative cell biology with the virtual cell. Trends in Cell Biology 13: 570-576.

49. Winslow RL, Cortassa S, Greenstein JL (2005) Using models of the myocyte for functional interpretation of cardiac proteomic data. Journal of Physiology-London 563: 73-81.

50. Karr JR, Sanghvi JC, Macklin DN, Gutschow MV, Jacobs JM, et al. (2012) A whole-cell computational model predicts phenotype from genotype. Cell 150: 389-401.

51. Lehninger AL, Nelson DL, Cox MM (2008) Lehninger principles of biochemistry. New York: W.H. Freeman.

52. Huang P, Pelicano H, Martin DS, Xu RH (2006) Glycolysis inhibition for anticancer treatment. Oncogene 25: 4633-4646.

53. Zubay GL (1998) Biochemistry. Dubuque, IA: Wm.C. Brown Publishers. 990, 995 p. p.

54. Siegel G, Agranoff B, Albers R, Fisher S, Uhler M (2006) Basic Neurochemistry: Molecular, Cellular and Medical Aspects. Philadelphia: Lippincott Williams and Wilkins. Copyright by American Society for Neurochemistry. www. ncbi. nlm. nih. gov/books/bv. fcgi.

55. Fall CP (2002) Computational cell biology. New York: Springer. xx, 468 p. p.

56. Rodriguez-Enriquez S, Marin-Hernandez A, Gallardo-Perez JC, Carreno-Fuentes L, Moreno-Sanchez R (2009) Targeting of cancer energy metabolism. Molecular Nutrition & Food Research 53: 29-48.

57. Porporato PE, Dhup S, Dadhich RK, Copetti T, Sonveaux P (2011) Anticancer targets in the glycolytic metabolism of tumors: a comprehensive review. Front Pharmacol 2: 49.

58. Schuster R, Holzhutter HG (1995) Use of Mathematical-Models for Predicting the Metabolic Effect of Large-Scale Enzyme-Activity Alterations - Application to Enzyme Deficiencies of Red-Blood-Cells. European Journal of Biochemistry 229: 403-418.

59. Cortassa S, Aon MA, Marban E, Winslow RL, O'Rourke B (2003) An integrated model of cardiac mitochondrial energy metabolism and calcium dynamics. Biophysical Journal 84: 2734-2755.

60. Karp PD, Paley SM, Krummenacker M, Latendresse M, Dale JM, et al. (2010) Pathway Tools version 13.0: integrated software for pathway/genome informatics and systems biology. Briefings in Bioinformatics 11: 40-79.

61. Hucka M, Finney A, Sauro HM, Bolouri H, Doyle JC, et al. (2003) The systems biology markup language (SBML): a medium for representation and exchange of biochemical network models. Bioinformatics 19: 524-531.

62. Becker SA, Feist AM, Mo ML, Hannum G, Palsson BO, et al. (2007) Quantitative prediction of cellular metabolism with constraint-based models: the COBRA Toolbox. Nat Protoc 2: 727-738.

63. Weiss TF (1996) Cellular Biophysics: Electrical properties: MIT Press.

64. Lodish H (2008) Molecular Cell Biology: W. H. Freeman.

65. Weiss TF (1996) Cellular biophysics: Transport. Vol. 1: MIT Press.

66. Hodgkin AL, Huxley AF (1952) A quantitative description of membrane current and its application to conduction and excitation in nerve. J Physiol 117: 500-544.

67. Destexhe A, Huguenard JR (2000) Nonlinear thermodynamic models of voltage-dependent currents. J Comput Neurosci 9: 259-270.

68. Hamprecht B (1977) Structural, electrophysiological, biochemical, and pharmacological properties of neuroblastoma-glioma cell hybrids in cell culture. Int Rev Cytol 49: 99-170.

69. Ravenscroft MS, Bateman KE, Shaffer KM, Schessler HM, Jung DR, et al. (1998) Developmental neurobiology implications from fabrication and analysis of hippocampal neuronal networks on patterned silane-modified surfaces. Journal of the American Chemical Society 120: 12169-12177.

70. Shannon TR, Wang F, Puglisi J, Weber C, Bers DM (2004) A mathematical treatment of integrated Ca dynamics within the ventricular myocyte. Biophys J 87: 3351-3371.

71. Deutsch C, Erecinska M, Werrlein R, Silver IA (1979) Cellular energy metabolism, trans-plasma and trans-mitochondrial membrane potentials, and pH gradients in mouse neuroblastoma. Proc Natl Acad Sci U S A 76: 2175-2179.

72. Holzhutter HG (2004) The principle of flux minimization and its application to estimate stationary fluxes in metabolic networks. Eur J Biochem 271: 2905-2922.

73. Marhl M, Haberichter T, Brumen M, Heinrich R (2000) Complex calcium oscillations and the role of mitochondria and cytosolic proteins. Biosystems 57: 75-86.

74. Chen XF, Li CX, Wang PY, Li M, Wang WC (2008) Dynamic simulation of the effect of calcium-release activated calcium channel on cytoplasmic Ca2+ oscillation. Biophys Chem 136: 87-95.

75. Nazaret C, Heiske M, Thurley K, Mazat JP (2009) Mitochondrial energetic metabolism: a simplified model of TCA cycle with ATP production. J Theor Biol 258: 455-464.

76. Rouzaire-Dubois B, Dubois JM (2004) Calcium-dependent proliferation of NG108-15 neuroblastoma cells. Gen Physiol Biophys 23: 231-239.

77. Cunningham MO, Pervouchine DD, Racca C, Kopell NJ, Davies CH, et al. (2006) Neuronal metabolism governs cortical network response state. Proc Natl Acad Sci U S A 103: 5597-5601.

78. Kager H, Wadman WJ, Somjen GG (2000) Simulated seizures and spreading depression in a neuron model incorporating interstitial space and ion concentrations. J Neurophysiol 84: 495-512.

79. Chander BS, Chakravarthy VS (2012) A computational model of neuro-glio-vascular loop interactions. PLoS One 7: e48802.

80. Courtemanche M, Ramirez RJ, Nattel S (1998) Ionic mechanisms underlying human atrial action potential properties: insights from a mathematical model. Am J Physiol 275: H301-321.

81. Kager H, Wadman WJ, Somjen GG (2007) Seizure-like afterdischarges simulated in a model neuron. J Comput Neurosci 22: 105-128.

82. Lo YH, Peachey T, Abramson D, McCulloch A, Michailova A (2013) Sensitivity of rabbit ventricular action potential and Ca(2)(+) dynamics to small variations in membrane currents and ion diffusion coefficients. Biomed Res Int 2013: 565431.

83. Müller M, Somjen GG (2000) Na+ and K+ Concentrations, Extra- and Intracellular Voltages, and the Effect of TTX in Hypoxic Rat Hippocampal Slices. 735-745 p.

84. Mirams GR, Davies MR, Cui Y, Kohl P, Noble D (2012) Application of cardiac electrophysiology simulations to pro-arrhythmic safety testing. Br J Pharmacol 167: 932-

945.

85. Yang CD, Sudderth J, Dang TY, Bachoo RG, McDonald JG, et al. (2009) Glioblastoma Cells Require Glutamate Dehydrogenase to Survive Impairments of Glucose Metabolism or Akt Signaling. Cancer Research 69: 7986-7993.

86. Volk C, Kempski B, Kempski OS (1997) Inhibition of lactate export by quercetin acidifies rat glial cells in vitro. Neuroscience Letters 223: 121-124.

87. Ozturk SS, Palsson BO (1991) Growth, Metabolic, and Antibody-Production Kinetics of Hybridoma Cell-Culture .1. Analysis of Data from Controlled Batch Reactors. Biotechnology Progress 7: 471-480.

88. Maldonado EN, Lemasters JJ (2014) ATP/ADP ratio, the missed connection between mitochondria and the Warburg effect. Mitochondrion.

89. Ray P, Monroe FL, Berman JD, Fiedler J (1991) Cyanide Sensitive and Insensitive Bioenergetics in a Clonal Neuroblastoma X Glioma Hybrid Cell-Line. Neurochemical Research 16: 1121-1124.

90. Heiden MGV, Cantley LC, Thompson CB (2009) Understanding the Warburg Effect: The Metabolic Requirements of Cell Proliferation. Science 324: 1029-1033.

91. Vrbacky M, Krijt J, Drahota Z, Melkova Z (2003) Inhibitory effects of Bcl-2 on mitochondrial respiration. Physiological Research 52: 545-554.

92. Storch A, Burkhardt K, Ludolph AC, Schwarz J (2000) Protective effects of riluzole on dopamine neurons: Involvement of oxidative stress and cellular energy metabolism. Journal of Neurochemistry 75: 2259-2269.

93. Ray P, Ray R, Broomfield CA, Berman JD (1994) Inhibition of Bioenergetics Alters

Intracellular Calcium, Membrane-Composition, and Fluidity in a Neuronal Cell-Line. Neurochemical Research 19: 57-63.

94. Bower J, Beeman D (1998) Ion Channels in Bursting Neurons. The Book of GENESIS: Springer New York. pp. 97-130.

95. Platkiewicz J, Brette R (2010) A Threshold Equation for Action Potential Initiation. PLoS Comput Biol 6: e1000850.

96. Bekkers JM (2000) Distribution and activation of voltage-gated potassium channels in cell-attached and outside-out patches from large layer 5 cortical pyramidal neurons of the rat. Journal of Physiology-London 525: 611-620.

97. Loussouarn G, Pike LJ, Ashcroft FM, Makhina EN, Nichols CG (2001) Dynamic Sensitivity of ATP-sensitive K+Channels to ATP. Journal of Biological Chemistry 276: 29098-29103.

98. Kowtha VC, Bryant HJ, Pancrazio JJ, Stenger DA (1998) Influence of extracellular matrix proteins on membrane potentials and excitability in NG108-15 cells. Neurosci Lett 246: 9-12.

99. Takahashi Y, Kawajiri H, Yoshimoto T, Hoshi N, Higashida H (1999) 12-lipoxygenase overexpression in rodent NG108-15 cells enhances membrane excitability by inhibiting M-type K+ channels. Journal of Physiology-London 521: 567-574.

100. Schulze ED (1994) Flux control in biological systems : from enzymes to populations and ecosystems. San Diego: Academic Press. xv, 494 p. p.

101. Schmitz JP, van Riel NA, Nicolay K, Hilbers PA, Jeneson JA (2010) Silencing of glycolysis in muscle: experimental observation and numerical analysis. Exp Physiol 95: 380-397.

102. Lehninger AL, Nelson DL, Cox MM (2005) Lehninger principles of biochemistry. New York:

W.H. Freeman.

103. Griffiths EJ, Rutter GA (2009) Mitochondrial calcium as a key regulator of mitochondrial ATP production in mammalian cells. Biochimica Et Biophysica Acta-Bioenergetics 1787: 1324-1333.

104. Israel M, Tomasi M, Bostel S, Meunier FM (2001) Cellular resistance to Evans blue toxicity involves an up-regulation of a phosphate transporter implicated in vesicular glutamate storage. J Neurochem 78: 658-663.

105. Silver IA, Deas J, Erecinska M (1997) Ion homeostasis in brain cells: differences in intracellular ion responses to energy limitation between cultured neurons and glial cells. Neuroscience 78: 589-601.

106. Thangaraju M, Carswell KN, Prasad PD, Ganapathy V (2009) Colon cancer cells maintain low levels of pyruvate to avoid cell death caused by inhibition of HDAC1/HDAC3. Biochem J 417: 379-389.

107. Peters GJ, Laurensse E, Leyva A, Pinedo HM (1984) Fluctuations in Phosphoribosyl Pyrophosphate Levels in Monolayer Tumor-Cell Lines - Effects of Drugs. Febs Letters 170: 277-280.

108. Pelicano H, Carney D, Huang P (2004) ROS stress in cancer cells and therapeutic implications. Drug Resistance Updates 7: 97-110.

109. Fernandez-Gomez FJ, Galindo MF, Gomez-Lazaro M, Yuste VJ, Comella JX, et al. (2005) Malonate induces cell death via mitochondrial potential collapse and delayed swelling through an ROS-dependent pathway. British Journal of Pharmacology 144: 528-537.

110. Gadoth N, Goebel HH (2011) Oxidative stress and free radical damage in neurology. New

York: Humana Press. viii, 323 p. p.

111. Englund M, Hyllienmark L, Brismar T (2001) Chemical hypoxia in hippocampal pyramidal cells affects membrane potential differentially depending on resting potential. Neuroscience 106: 89-94.

112. Keefer EW, Botterman BR, Romero MI, Rossi AF, Gross GW (2008) Carbon nanotube coating improves neuronal recordings. Nat Nano 3: 434-439.